

THE UNIVERSITY OF HULL

**INDUSTRIAL APPLICATION OF CFD TO  
PREDICT HIGH FREQUENCY NOISE  
FROM AUTOMOTIVE ACOUSTIC  
DEVICES**

being a Thesis submitted for the Degree of

**Doctor of Philosophy**

to The University of Hull

by

**Imran Khan (MEng)**

August 2014



## **i. Table of Contents**

1	Introduction .....	20
1.1	Motivation.....	20
1.2	Aims.....	23
1.3	Objectives.....	24
1.4	Automotive Noise Control Techniques .....	24
1.4.1	Helmholtz Resonators .....	26
1.4.2	Closed Quarter Wave Tube Side-branch Resonator .....	29
1.5	Aero-Acoustic Cavity Flows .....	32
1.6	Vortex Shedding .....	41
1.7	Methodology .....	46
2	Experimental Work.....	48
2.1	Experimental Configuration .....	48
2.2	Validation Experiments .....	57
2.3	VVH Resonator Noise Generation Experiments.....	63
2.4	QWT Protrusion Experiments .....	77
2.5	Charge Air Cooler Experiments .....	87
2.6	Experimental Work Summary .....	99
3	Computational Fluid Dynamics .....	101
3.1	Turbulence Modelling .....	105
3.1.1	RANS Solvers .....	115
3.1.2	LES Solvers.....	119
3.2	Numerical Investigations into Cavity Flows .....	125
3.2.1	Aero-acoustic models.....	131
3.2.2	Mesh.....	133

3.2.3	Time Step.....	137
3.2.4	Boundary Conditions.....	138
3.2.5	Convergence Criteria.....	140
3.3	Computational Fluid Dynamics Summary.....	141
4	Modelling and Simulation Work.....	143
4.1	RANS Simulations.....	143
4.1.1	VVH Resonator Pipe Simulation.....	146
4.1.2	VVH Resonator with a 1000 Hz Sine Wave Pulse.....	154
4.1.3	VVH Resonator with a 200 Hz Sine Wave Pulse.....	159
4.1.4	VVH Resonator U-RANS Noise Generation Simulation.....	162
4.1.5	Summary.....	166
4.2	Large Eddy Simulations.....	166
4.2.1	LES Validation Simulations.....	167
4.2.2	VVH Resonator LES Noise Generation.....	185
4.2.3	QWT Simulations.....	189
4.2.4	Charge Air Cooler Resonator Simulations.....	204
4.3	Modelling and Simulation Summary.....	228
5	Conclusion.....	230
5.1	Thesis Summary.....	230
5.2	Recommendations and Future Work.....	234
6	Appendix.....	236
6.1	Appendix 1.....	236
6.2	Appendix 2.....	238
7	Bibliography.....	240

## ii. Table of Figures

Figure 1: A typical exhaust with closed side-branch (Go Tuning Unlimited, 2010) .....	21
Figure 2: Photograph of a production intake duct with a side-branch resonator attached (Harrison, 2004) .....	22
Figure 3: QWT with radius $a$ , and length $L$ as a side-branch (Barron, 2001).....	30
Figure 4: Production of flow-excited cavity resonance (Lawson & Barakos, 2011).....	42
Figure 5: Principal elements of self-sustaining oscillation of turbulent flow past a cavity associated with purely hydrodynamic effects (Rockwell, et al., 2003).....	44
Figure 6: Diagram of experimental set up.....	49
Figure 7: Photograph of experimental configuration .....	50
Figure 8: Resonator with adjustable volume via movable piston, showing dimensions .....	51
Figure 9: Ideal profile for fully developed turbulent and laminar flows in a circular pipe (Mathieu & Scott, 2000).....	52
Figure 10: Fan velocity profile. Each line represents the velocity profile of the flow from the fan at various power inputs (measured in Hz at the controller). .....	53
Figure 11: Mass flow comparison 10 m (Resonator Port) and 20 m (Anechoic Termination) downstream at various flow velocities. Black line = trendline.....	54
Figure 12: Inlet signal – Amplitude in mV against sample number. ....	58
Figure 13: FFT plot of inlet signal. SPL (dB) against Frequency (Hz). ....	59
Figure 14: FFT comparison between inlet signal (red) and attenuated signal using a VVH resonator tuned to 200 Hz (blue). SPL (dB) against Frequency (Hz).....	60
Figure 15: FFT comparison between modified inlet signal (red) and attenuated signal using a VVH resonator tuned to 400 Hz (blue). SPL (dB) against Frequency (Hz). ....	61
Figure 16: FFT comparison between modified inlet signal (red) and two VVH resonators simultaneously tuned to 200 Hz and 400 Hz (blue). SPL (dB) against Frequency (Hz). ....	62
Figure 17: Resonator Noise Generation Experiment set-up. VVH Resonator with an upstream, a downstream and an internal volume microphone connected up to the amplifying hardware. ....	65
Figure 18: FFT plot – Experiment of VVH resonator tuned to 460 Hz and flow velocity of 20 m/s .....	66
Figure 19: FFT plot - Experiment of VVH resonator tuned to 358 Hz and flow velocity of 50 m/s. ....	67

Figure 20: FFT plot - Experiment of VVH resonator tuned to 284 Hz and flow velocity of 50 m/s .....	68
Figure 21: FFT plot - Experiment of VVH resonator tuned to 242 Hz and flow velocity of 50 m/s .....	68
Figure 22: FFT plot - Experiment of VVH resonator tuned to 215 Hz and flow velocity of 50 m/s .....	69
Figure 23: FFT plot - Experiment of VVH resonator tuned to 358 Hz and flow velocity of 60 m/s .....	69
Figure 24: FFT plot - Experiment of VVH resonator tuned to 284 Hz and flow velocity of 60 m/s .....	70
Figure 25: FFT plot - Experiment of VVH resonator tuned to 242 Hz and flow velocity of 60 m/s .....	70
Figure 26: FFT plot - Experiment of VVH resonator tuned to 215 Hz and flow velocity of 60 m/s .....	71
Figure 27: FFT plot - Experiment of VVH resonator tuned to 358 Hz and flow velocity of 70 m/s .....	71
Figure 28; FFT plot - Experiment of VVH resonator tuned to 284 Hz and flow velocity of 70 m/s .....	72
Figure 29: FFT plot - Experiment of VVH resonator tuned to 242 Hz and flow velocity of 70 m/s .....	72
Figure 30: FFT plot - Experiment of VVH resonator tuned to 215 Hz and flow velocity of 70 m/s .....	73
Figure 31: Dominant tone frequency (Hz) plotted against flow velocity (m/s) for various resonator piston heights (resonator volumes). 50 mm piston height configurations are not shown due to insignificant tones produced.....	74
Figure 32: FFT plot showing response at the sensor door-gap and representing the vehicle interior as a function of the incoming flow velocity (Pachebat, et al., 2008).....	75
Figure 33: A photograph showing the QWT and Variable Volume Helmholtz Resonator .....	78
Figure 34: Experiment configuration showing upstream and downstream microphone locations as well as the resonator port in the centre of the photograph.....	78
Figure 35: FFT plot showing three monitor locations at a flow velocity of 30 m/s and a Quarter Wave Tube protrusion of 0 mm .....	80
Figure 36: FFT plot showing three monitor locations at a flow velocity of 30 m/s and a Quarter Wave Tube protrusion of 2.5 mm .....	80

Figure 37: FFT plot showing three monitor locations at a flow velocity of 30 m/s and a Quarter Wave Tube protrusion of 5 mm .....	81
Figure 38: FFT plot showing frequency distributions at the downstream monitor location for three protrusions at 30 m/s.....	82
Figure 39: FFT plot showing three monitor locations at a flow velocity of 60 m/s and a Quarter Wave Tube protrusion of 0 mm .....	83
Figure 40: FFT plot showing three monitor locations at a flow velocity of 60 m/s and a Quarter Wave Tube protrusion of 2.5 mm .....	83
Figure 41: FFT plot showing three monitor locations at a flow velocity of 60 m/s and a Quarter Wave Tube Protrusion of 5 mm .....	84
Figure 42: FFT plot showing frequency distributions at the downstream monitor location for three protrusions at 60 m/s.....	85
Figure 43: FFT plot showing frequency distributions at the downstream monitor location for 5 mm protrusion at 30 m/s and 60 m/s .....	86
Figure 44: CAC Resonator in the Pre-Production (whistle) layout. Flow from right to left. ....	88
Figure 45: Isometric cut-away view of the CAC Resonator in the Production layout. Flow from left to right.....	89
Figure 46: CAC Resonator microphone and pipework set-up.....	89
Figure 47: FFT plot - CAC Resonator experiment comparison between production and Pre-Production geometries with a 30 m/s flow velocity .....	91
Figure 48: FFT plot - CAC Resonator experiment comparison between production and Pre-Production geometries with a 40 m/s flow velocity .....	92
Figure 49: FFT plot - CAC Resonator experiment comparison between production and Pre-Production geometries with a 45 m/s flow velocity .....	93
Figure 50: FFT plot - CAC Resonator experiment comparison between production and Pre-Production geometries with a 50 m/s flow velocity .....	94
Figure 51: FFT plot - CAC Resonator experiment comparison between production and Pre-Production geometries with a 60 m/s flow velocity .....	95
Figure 52: Experiment Insertion Loss at 30 m/s between Production and Pre-Production CAC Resonators .....	96
Figure 53: Experiment Insertion Loss at 40 m/s between Production and Pre-Production CAC Resonators .....	96
Figure 54: Experiment Insertion Loss at 45 m/s between Production and Pre-Production CAC Resonators .....	97

Figure 55: Experiment Insertion Loss at 50 m/s between Production and Pre-Production CAC Resonators ..... 97

Figure 56: Experiment Insertion Loss at 60 m/s between Production and Pre-Production CAC Resonators ..... 98

Figure 57: A diagram to show how turbulence is calculated in Direct Numerical Simulation (DNS), Large Eddy Simulation (LES) and Reynolds averaged Navier-Stokes (RANS) solvers..... 103

Figure 58: Energy cascade process where  $l$  denotes the size of eddies in the inertial sub-range. (Davidson, 2013) ..... 107

Figure 59: Example of turbulent flow (Dyke, 1982) ..... 108

Figure 60: Turbulent Energy Spectrum (Hinze, 1975) ..... 111

Figure 61: Turbulence energy wavenumber spectrum ..... 112

Figure 62: Velocity profile for a fully developed wall-bounded flow (Villiers, 2006)..... 113

Figure 63: Steady state fully developed profile ..... 114

Figure 64: Volume mesh example. Left – Polyhedral, right – Hexahedral (CD-Adapco, 2011). 135

Figure 65: Prism layer example (CD-Adapco, 2011)..... 136

Figure 66: Pressure monitor probe located centrally in the region of interest against inner iteration number. The blue arrows give an indication of when convergence within tolerance has occurred for each timestep – marked with green dashed line. .... 141

Figure 67: Pressure (Pa) in relation to time (s) at 1.5 m along the length of the pipe ..... 145

Figure 68: Resonator and Pipe Layout ..... 146

Figure 69: Resonator pipe initial volume mesh - neck close-up ..... 147

Figure 70: Velocity magnitude vectors around the neck ..... 147

Figure 71: Velocity magnitude around the VVH resonator neck ..... 148

Figure 72: Pressure (gauge) around the VVH resonator neck..... 148

Figure 73: VVH resonator and pipe simulation - pressure (Pa) against time (s) ..... 149

Figure 74: Mesh Frequency cut-off contour ..... 150

Figure 75: VVH resonator refined mesh..... 151

Figure 76: Refined mesh around neck close-up ..... 151

Figure 77: Re-mesh - Mesh Frequency cut-off contour ..... 152

Figure 78: VVH resonator and pipe re-mesh simulation - pressure (Pa) against time (s)..... 153

Figure 79: A pressure scene to show the sine wave pulse moving along the pipe..... 155

Figure 80: A pressure scene to show the sine wave pulse leaving the pipe ..... 155

Figure 81: Simulation of a sinusoidal wave - A plot to show Pressure (Pa) at points along the pipe against time (s)..... 156

Figure 82: Refined trimmer mesh ..... 157

Figure 83: 1000 Hz pulse simulation re-run - A plot to show Gauge Pressure (Pa) at points along the pipe against Time (s). ..... 158

Figure 84: 1000 Hz pulse, time step: 1E-5 s, 2 periods - A plot to show pressure (Pa) at points along the pipe against time (s)..... 159

Figure 85: Pressure monitor points plot - 200 Hz pulse simulation, no resonator. Pressure (Pa) against Time (s)..... 160

Figure 86: Monitor points plot - 200 Hz pulse simulation with resonator tuned to 200 Hz. Pressure (Pa) against Time (s) ..... 161

Figure 87: Monitor point locations ..... 162

Figure 88: Scalar acoustic pressure scene showing vortex shedding on the trailing edge of the resonator neck. .... 163

Figure 89: Monitor points plot - Simulation whistle with inlet, outlet, downstream edge, neck and resonator monitor points ..... 163

Figure 90: FFT plot – U-RANS Simulation of VVH resonator tuned to 460 Hz. Experimental and simulation results shown for inlet and outlet points. .... 165

Figure 91: Straight pipe showing a developing turbulent flow using LES ..... 169

Figure 92: Turbulent fully developed flow ..... 170

Figure 93: Geometric inlet section limits (CD-Adapco, 2011) ..... 171

Figure 94: FFT plot of simulations showing SPL (dB) against logarithmic frequency for three inlet conditions on a straight pipe with a side-branch QWT and a flow velocity of 30 m/s ..... 172

Figure 95: A close-up region of an FFT plot showing simulations three inlet conditions on a straight pipe with a side-branch QWT and a flow velocity of 30 m/s..... 173

Figure 96: Steady State RANS 'uu' Reynolds Stress distribution in a radial direction at four points, evenly spaced, along the pipe. .... 175

Figure 97: LES 'uu' Reynolds Stress distribution in a radial direction at four points, evenly spaced, along the pipe. .... 175

Figure 98: Boundary layer velocity distribution near a solid wall (Schlichting, 1979) ..... 177

Figure 99: Turbulent Energy Spectrum for Standard and Dynamic SGS models along with the Kolmogorov 5/3's law. .... 179

Figure 100: Volume mesh - 2 mm base size, with 50 % further refinement around area of interest ..... 181

Figure 101: Volume mesh - 1 mm base size, no refined areas ..... 182

Figure 102: Volume mesh - 2 mm base size, no refined areas ..... 182

---

Figure 103: FFT plot - Simulation downstream edge monitoring point of a QWT with three different meshes .....	183
Figure 104: LES simulation of the QWT geometry at 30 m/s mean flow velocity .....	184
Figure 105: U-RANS simulation of the QWT geometry at 30 m/s mean flow velocity .....	184
Figure 106: FFT plot - Outlet monitor point comparison between LES and U-RANS.....	185
Figure 107: Acoustic pressure plot 1 - Shear layer about to roll up and enter the resonator..	186
Figure 108: Acoustic pressure plot 2 - Vortex entering resonator and creating high pressure internally .....	187
Figure 109: Acoustic pressure plot 3 - Vortex exiting resonator, about to be entrained downstream .....	187
Figure 110: LES Simulation of VVH resonator tuned to 460 Hz. Experimental and simulation results shown for inlet and outlet points. ....	188
Figure 111: QWT geometry with a 5 mm neck protrusion .....	190
Figure 112: QWT also showing monitor point locations. The inlet and outlet monitor locations approximately five QWT diameters upstream and downstream of the QWT resonator.....	191
Figure 113: QWT mesh also showing monitor point locations. ....	191
Figure 114: Velocity scalar - QWT with no neck protrusion. 60m/s flow. ....	192
Figure 115: Velocity scalar - QWT with 2.5 mm neck protrusion. 60m/s flow. ....	193
Figure 116: FFT plot CFD simulation frequency distribution comparison at 30 m/s flow velocity showing straight pipe against QWT with no neck protrusion .....	194
Figure 117: FFT plot showing CFD simulation results of QWT protruding into the main pipe by 0 mm with a flow velocity of 30 m/s. ....	195
Figure 118: QWT scalar velocity (m/s) scene - 30 m/s in-flow velocity, 5 mm neck protrusion.....	196
Figure 119: QWT acoustic pressure (Pa) scalar scene - 30 m/s in-flow velocity, 5 mm neck protrusion.....	197
Figure 120: Simulation comparisons at the downstream edge point of the QWT protruding into the main pipe by 0 mm, 2.5 mm and 5 mm with a flow velocity of 30 m/s. ....	197
Figure 121: Simulation comparisons at the downstream edge point of the QWT protruding into the main pipe by 0 mm, 2.5 mm and 5 mm with a flow velocity of 60 m/s. ....	199
Figure 122: QWT 5 mm protrusion at 60 m/s FFT plot – Downstream monitor point comparison between simulation and experiment. ....	200

Figure 123: Simulation Outlet Monitor of 20, 30 and 40 mm diameter QWTs with a 30 m/s grazing flow .....	202
Figure 124: Simulation Outlet Monitor of 20, 30 and 40 mm diameter QWTs with a 60 m/s grazing flow .....	202
Figure 125: CAC tract geometry - CAD representation .....	205
Figure 126: Pre-Production CAC resonator section view. Flow from right to left. ....	206
Figure 127: Production CAC resonator section view. Flow from right to left. ....	206
Figure 128: CAC resonator upstream pipe and inlet volume mesh .....	207
Figure 129: CAC Resonator geometry showing location of monitor points .....	207
Figure 130: Pre-Production CAC Resonator – 45 m/s acoustic pressure scalar scene.....	208
Figure 131: Pre-Production CAC Resonator – Acoustic Pressure in the resonator at two points in time .....	209
Figure 132: Pre-Production CAC Resonator - Velocity Magnitude scalar scene .....	210
Figure 133: Pre-Production CAC Resonator - Vorticity Vector Scalar Scene.....	210
Figure 134: Pressure (Pa) against time (s) plot for Pre-Production CAC Resonator simulation monitor points.....	212
Figure 135: Pre-Production CAC Resonator FFT - Outlet and Resonator Section 2 Monitor points (30 m/s).....	212
Figure 136: Pre-Production CAC Resonator Simulation - Outlet and Resonator Section 2 Monitor points (45 m/s).....	213
Figure 137: Pre-Production CAC Resonator Simulation - Outlet and Resonator Section 2 Monitor points (60 m/s).....	213
Figure 138: Pre-Production CAC Resonator Simulation - Outlet and Resonator Section 2 Monitor point comparison: 30 m/s, 45 m/s and 60 m/s.....	214
Figure 139: Production CAC Resonator - Velocity Magnitude scalar scene.....	216
Figure 140: Pressure (Pa) against time (s) plot for Production CAC Resonator monitor points - 45 m/s mean inlet velocity.....	217
Figure 141: Production CAC Resonator - Velocity Vector scene for Production geometry (top) and Non-Production (bottom).....	218
Figure 142: 30 m/s CAC Resonator Simulation Downstream Location - Production/Pre-Production Comparison .....	220
Figure 143: 45 m/s CAC Resonator Simulation Downstream Location - Production/Pre-Production Comparison .....	220

Figure 144: 60 m/s CAC Resonator Simulation Downstream Location - Production/Pre-Production comparison..... 221

Figure 145: FFT plot - Immediate Downstream location at 30 m/s, simulation and experiment comparison. .... 222

Figure 146: FFT plot - Immediate Downstream and Resonator Section 2 locations at 45 m/s, simulation and experiment comparison. .... 223

Figure 147: FFT plot - Immediate Downstream location at 60 m/s, simulation and experiment comparison. .... 223

Figure 148: CAC Resonator volume mesh section view ..... 225

Figure 149: CAC Mesh Independence – FFT of section immediately downstream of the resonator ..... 226

### **iii. Declaration**

No portion of the work referred to in the thesis has been submitted in support of an application for another degree or qualification of this or any other university or other institution of learning.

#### **iv. Acknowledgments**

I would like to express my gratitude to my Supervisor, Dr. Philip A. Rubini, Department of Engineering, for his invaluable suggestions, careful supervision and constant availability during my research work.

I would like to thank Jaguar Land Rover for sponsoring this research with a particular mention to Steven Pierson, Andrew Daghish, Raymond Cheung and Karamjit Sandhu.

I am also thankful to Dr. Qin Qin for his advice and support in experimental planning and to all my colleagues - Brian, Carl, Esther, Nishant, Haydar, amongst others during this project for their friendship and collaboration. I would like to thank Mr. Steve Coopland for his help in obtaining software licences and hardware related issues on various occasions along with the CD-Adapco Star CCM+ support team for their continued software support.

Special thanks go to my family, partner and friends for their continuous support throughout these years of research.

Finally, I would like to acknowledge the Department of Engineering for granting me this opportunity and the facilities to complete the project successfully.

## v. Abstract

NVH (noise, vibration and harshness) of automotive systems is receiving an ever increasing level of interest. Industry sectors are facing increasing pressure from customers as well as government authorities to reduce flow noise and its transmission to the interior environment or propagated externally to by passers. The NVH levels are not the only important factor. The *quality* of the noise produced such as the engine note or the exhaust rasp is also a key market area, particularly for luxury/sports car consumers. Resonators play a large part in NVH and sound quality in modern automotive flow system design. An excellent understanding of the complex interaction between the resonators and the effect on the incoming flow is crucial to be able to predict the performance of the designs of these configurations.

The objective of this thesis is to establish the feasibility of industrial application of Large Eddy Simulation (LES) to practical automotive acoustic problems. A Computer Aided Engineering (CAE) tool based around CFD would be utilised in premium automotive applications to allow upfront assessments of the intake/exhaust systems and facilitate cost effective optimisation early on in the vehicle development programme. Furthermore, a CAE tool could be used to aid failure mode resolution later on in the development programme. As a contribution to knowledge, the primary aim of this study is to gain understanding and scientific insight into the advantages and concerns surrounding the application of LES to practical acoustic problems for premium automotive applications. In turn, the flow processes which are responsible for the unwanted high frequency noise can be analysed visually and analytically in greater detail than is possible through experimental studies alone.

The majority of existing studies in industry tend to be Reynolds Averaged Navier Stokes (RANS) based, primarily due to cost associated with LES. Many of the assumptions and limitations of these models can be overcome by specialised modifications, such as those available for in-cylinder studies. However, for aero-acoustic studies, by solving the full compressible Navier–Stokes equations, the nonlinearities in the acoustic waves can be solved, thereby circumventing the constraint of linear wave amplitude treatments. Furthermore, many studies tend to have a strong theoretical focus with limited industrial transfer. This study combines theoretical, experimental and computational based findings of predicting high frequency tones in flows using LES to be applied to real world complex

geometries. A commercial CFD solver has been utilised in this thesis to replicate the CFD usage within the premium automotive company.

The LES solutions have been proved to be more useful in providing a greater insight into the processes involved inside and around the resonator. The Large Eddy Simulations have enabled the opportunity to visually inspect the flow processes which are the cause of the noise generated in many of the experimental studies carried out in this thesis.

With the use of LES, this study has produced, with encouraging accuracy, the high frequency flow-generated noise present in several resonating geometries present in many industrial contexts, particularly in the automotive sector. The Large Eddy Simulations have produced acoustic results which are generally within 5% agreement of the experimental validation results.

Thus, the work carried out in this thesis has enabled a greater understanding of the underlying physical phenomena in automotive cavity flows. It has been recognised the application of LES is suitable for use as a design tool, and thus could be utilised early on in the product design phase. However, from a practical viewpoint, it is suggested the LES function of CFD, as opposed to RANS solvers, should be limited to cases of interest due to the increased resource needed to obtain robust results.

## vi. Nomenclature

$\overline{u}_i$  = Mean 'u' velocity component

$u'_i$  = Fluctuating (turbulent) 'u' velocity component

$u_i$  = Component of 'u' velocity vector

$\Delta t$  = Time step

$\Delta x$  = Grid spacing

$\mu$  = Dynamic viscosity

$a'$  = Cylinder radius

$A$  = Cross-sectional area of neck opening

$C$  = SGS universal constant

$c$  = Speed of sound

$d$  = Wall distance

$E$  = Energy

$F$  = Pulsation amplitude

$f$  = Frequency

$f_c$  = Resonant frequency

$f_{mc}$  = Maximum resolved frequency

$f_v$  = Van Driest damping function

$f_D$  = Darcy–Weisbach friction factor

$I$  = Sound Intensity

$k$  = Eddy Position

$K$  = Kinetic energy

$K$  = Wave number =  $\frac{2\pi f}{c}$

$l$  = Cavity length

$L$  = Characteristic length

$L'$  = Effective neck length

$m$  = Integer value (1,2,3,...)

$M$  = Mach number

$n$  = Harmonic number

$\eta$  = Stiffness of the air in the neck

$P(t)$  = Time-dependent power

$p$  = Pressure

$P_{rms}$  = Root mean squared sound pressure

$p_{ref}$  = Reference sound pressure ( $2 \times 10^{-5}$  Pa)

$R$  = Impedance

$R_e$  = Reynolds number

$R_s$  = Flow resistance

$S$  = Expansion ratio

$S_p$  = Cross-sectional area of the pipe

$S_r$  = strain rate tensor

$S_t$  = Strouhal number

$T_p$  = Period of oscillation

$T$  = Time

$T_i$  = Turbulence intensity

$T_t$  = Turbulent stress tensor

$T_0$  = Temperature

$U_{ref.}$  = Reference mean flow velocity

$T_\pi$  = Power transmission coefficient

$U_e$  = Free-stream velocity

$u$  = Mean velocity

$u^*$  = Friction velocity

$u_i$  = Component of 'u' velocity vector

$\overline{u_i}$  = Mean velocity determined by either time, spatial or ensemble averaging

$u'_i$  = Fluctuating (turbulent) velocity component

$u_l$  = Velocity scale

$u_{ac}$  = Acoustic velocity

$U_f$  = Characteristic velocity at the cell face

$U_{max}$  = Maximum velocity

$v$  = Cell volume

$V$  = Volume of the Helmholtz resonator

$w$  = Mass of the fluid in the neck

$X_A$  = Acoustic reactance

$x$  = End correction multiplication factor

$Y^+$  = Wall distance

$\gamma$  = Dimensionless lag between passage of vortex and radiation of a pressure wave

$\delta$  = Boundary layer thickness

$\Delta$  = Length scale/grid filter width

$\kappa$  = Ratio between convection velocity of vortices and  $U$

$\kappa$  = Von Karman constant (default value = 0.41)

$\lambda$  = Wavelength

$\mu$  = Turbulent viscosity

$v$  = Total velocity

$\nu$  = Kinematic viscosity

$\rho$  = Density

$\sigma$  = Attenuation coefficient

$\omega$  = Angular frequency

$\omega_o = \nabla \times v$  = Vorticity of the flow

# 1 Introduction

## 1.1 Motivation

The interest for aero-acoustics mainly in the aerospace and automotive industries has increased during the last few years, primarily because of customer surveys that show wind noise to be a common complaint. Luxury vehicles are constantly in search for class leading attributes. Therefore, NVH (noise, vibration and harshness) of automotive systems is receiving an ever increasing level of interest. Furthermore, industry sectors are facing pressure from customers as well as government authorities to reduce flow noise and its transmission to the interior environment or propagated externally to by passers. The NVH levels are not the only important factor. The *quality* of the noise produced such as the engine note or the exhaust rasp is also a key market area, particularly for luxury/sports car consumers. Resonators play a large part in NVH and sound quality in modern automotive flow system design. Therefore, the acoustic prediction during development is particularly important, not just in terms of sound pressure levels but also in quality.

Resonators are often used in engine breathing systems such as intake piping, charge cooler piping, HVAC (cabin ventilation) ducting and exhausts which all have a combination of an incoming noise and mean flow to 'tune' the noise content by enhancing or reducing certain frequencies. In these cases, resonators are used as band-stop filters to suppress certain frequencies. Therefore, the interest for the aero-acoustic aspects of resonator and cavity flows has increased dramatically in recent times, to fully understand and optimise these systems.

In many cases, such as in automotive applications, there are limitations on the physical size and the shape of the muffler. This requirement often interacts with the acoustic requirements. A typical exhaust system with a closed side branch resonator is provided in Figure 1. An excellent understanding of the complex interaction between the resonators and the effect on the incoming flow is crucial to be able to predict the performance of the designs of these configurations. Another example of such a configuration is provided in Figure 2.

Through the design and development of automotive powertrain systems, unusual engine noises, often of high (>1000 Hz) frequency are systematic issues and often discovered late on during a vehicle development programme. Failure mode resolution at this stage in the programme tends to be costly as the vehicle package has been frozen and parts released. Computer Aided Engineering (CAE) is proving to be an increasingly valuable tool to

help understand the flow noise generation propagation and transmission mechanisms. Consequently, engineers are able to design against them either by reducing the source or minimising its propagation in the aerodynamic/hydrodynamic domain and the transmission through structures.



Figure 1: A typical exhaust with closed side-branch (Go Tuning Unlimited, 2010)

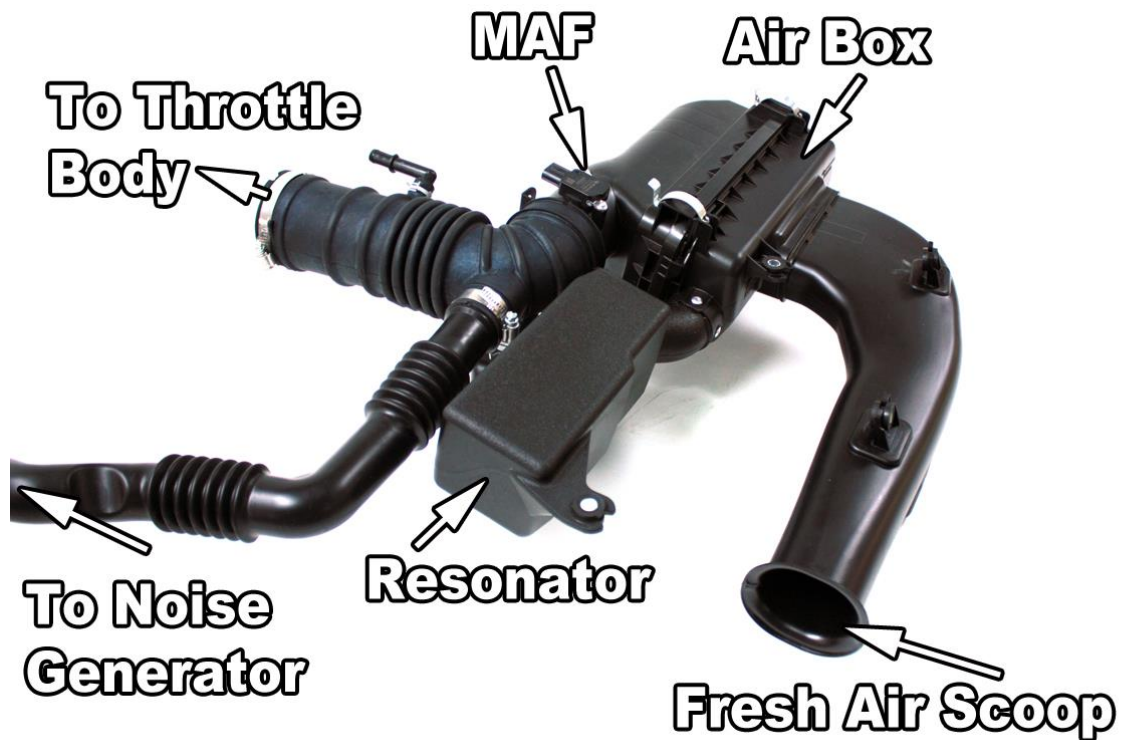


Figure 2: Photograph of a production intake duct with a side-branch resonator attached (Harrison, 2004)

Aero-acoustics, or the sound generated by fluid flows, is an area of research that has primarily been aimed at high-Mach number flows with jet noise being a common case of interest - for example the studies by Chaudhari et al (Chaudhari, et al., 2009) and Vikramaditya & Kurian (Vikramaditya & Kurian, 2013). In vehicle applications, the Mach numbers of the flows are typically small and the flows are often heavily separated because of the complex geometries present. Acoustics and fluid flow are intrinsically coupled as acoustic waves are essentially compressions of the fluid which create periodic pressure fluctuations.

Historically, automotive aero-acoustic investigations were carried out in an experimental design iteration process. This is very time consuming, labour intensive and expensive. Cattafesta et al. (Cattafesta III, et al., 2008) provides a substantial literature review of experimental cavity flows. Numerical characterisation has the clear benefit of reducing the need for experimental rigs, and potentially provides far greater insight into the flow phenomena involved. The flow can be studied in detail, providing a better understanding. Also many simulations with changing variables can be simulated in a relatively short amount of time in comparison to real-life. CAE is now often utilised in the form of 1-dimensional wave codes but acoustics is inherently a fluid dynamics problem. With

increasing computational resource and technology, computational simulations of acoustics (CAA) with Computational Fluid Dynamics (CFD) are becoming ever more popular design and problem solving tools (Versteeg & Malalasekera, 2007). The majority of automotive CFD studies utilise time-averaged solvers which provide a reasonable level of detail to assess areas of high pressure or regions of low heat transfer, etc. However, for acoustic problems, the spatial complex nature of the shear layers and the complex array of evolving energy flow scales make point-wise measurements and time or phase averaged data not fully adequate to describe their dynamics and complexity. In order to search for sound sources which can be generated by the flow inside and around a resonator or cavity, the unsteady nature of the flow needs to be observed in detail.

Before the last decade, low levels of computational work for production-type geometries were carried out due to the prohibitive computational cost of performing time varying (unsteady) CFD calculations (Mendonca, 2005). With the continued decrease in hardware cost and the increase in performance, Computational Aero-acoustics (CAA) calculations are now being performed by an ever-increasing number of industrial CFD engineers. Large Eddy Simulations (LES) is the next stage of this technology advancement (Piomelli, 2001). LES solutions are more useful in providing a greater insight into the detailed turbulent flow processes involved inside and around the resonator cavity. In turn, it is able to capture the high frequency unwanted noise which can be created in certain geometries and flows. Time-averaged solvers are unable to capture the high level of turbulence detail required.

## **1.2 Aims**

The aim of this thesis is to establish the feasibility of industrial application of Large Eddy Simulation (LES) to practical automotive acoustic problems. A Computer Aided Engineering (CAE) tool based around CFD would be utilised in premium automotive applications to allow upfront assessments of the intake/exhaust systems and facilitate cost effective optimisation early on in the vehicle development programme. Furthermore, a CAE tool could be used to aid failure mode resolution later on in the development programme. As a contribution to knowledge, the primary aim of this study is to gain understanding and scientific insight into the advantages and concerns surrounding the application of LES to practical acoustic problems for premium automotive applications. In turn, the flow processes which are responsible for the unwanted high frequency noise can be analysed

visually and analytically in greater detail than is possible through experimental studies alone. The majority of studies in industry are RANS based with unique developed models for specific problems, primarily due to cost associated with LES. Others are strongly theoretical focused with limited industrial transfer. This study combines theoretical, experimental and computational based findings to be applied in the real world.

### **1.3 Objectives**

Flow rig experiments are carried out with several resonator geometries to provide a validation baseline for which the CFD simulations can be validated against. Several parameters are varied such as in-flow rate, resonator volume and resonator neck geometry. The main objective of this thesis is to assess the capability of LES to predict high frequency noise in complex geometries, with the view to utilise LES as a practical design tool in an industrial context. A Variable Volume Helmholtz resonator a Quarter Wave Tube with an adjustable protruding neck and a Charge Air Cooler resonator are tested experimentally with corresponding CFD simulations. The LES capability of CFD is assessed by carried out equivalent simulations of the flow rig experiments to model how the acoustic spectrum of turbulent fluid flows can be affected by a resonator inserted in a pipe or attached as a side-branch.

A commercial CFD solver is utilised in this thesis to replicate the CFD usage within the premium automotive company. This thesis does not aim to code a new solver, nor does it aim to create a theoretical model. The objective of this thesis is to assess the capability of LES to predict high frequency noise in complex geometries, with the view to utilise LES as a practical design tool in an industrial context.

### **1.4 Automotive Noise Control Techniques**

To remove unwanted noise and certain tones from automotive powertrain set-ups, silencers are often used in intake and exhaust pipe work tracts. Noise control is of great importance for premium car manufacturers. Customers want a certain noise from a V6 or a V8 engine, with minimal undesirable tones. Forced induction parts and certain shapes in the engine breathing components can lead to unwanted and unpleasant tones. Silencers and

other flow devices inserted into the intake/exhaust tract can help reduce or even eliminate these undesirable sounds.

Flow noise can be both tonal and broadband in nature, with broadband flow noise having frequency components predominantly over 500 Hz. Conversely, pulsating intake and exhaust noise is relatively low frequency. Therefore silencer research and development tends to focus on the lower end of the frequency spectrum such as in Munjal's paper (Munjal, 1998). In general, as stated by Barron (Barron, 2001), a silencer may be defined as an element in the flow duct that acts to reduce the sound transmitted along the duct whilst allowing free flow of the gas through the flow passage. A silencer can be active in which the noise is cancelled by electronic feed-forward and feedback techniques. This is a relatively recent addition to silencer design where a loudspeaker, together with a feedback/feed-forward loops superimposes on an unwanted tone with one which is of the opposite phase - effectively noise cancellation. Mechanical or electrical active noise control is also possible with movable lips and spoilers via an actuator to reduce cavity tones. A comprehensive literature review has been carried out in this area by Cattafesta (Cattafesta III, et al., 2008).

Another technique to utilise for a silencer is passive, in which the sound is attenuated by reflection and absorption of the acoustic energy within the geometry. The detailed design procedures and theoretical explanations for mufflers have been well documented by Munjal (Munjal, 1987). Passive silencers may be of the reactive or dissipative type which is generally achieved by reflection or absorption respectively. Depending on the frequency of interest, the attenuation technique is selected. Generally, reflection is used at low frequencies or for removal of tones, while absorption by damping (or mass) is used for high frequencies. Acoustic, aerodynamic, mechanical/material, economic and geometric requirements are all important when designing silencers and automotive pipe work tracts. The latter two requirements are becoming ever more important with the increasing packaging restraints for efficiency and the decreasing economic margins for manufacturers.

This thesis focuses on the reactive type whereby a side branch or resonator section reflects sound waves passing through the pipe work tract back to the acoustic energy source. Generally speaking, a resonator is tuned to a specific frequency. The wavelength of this frequency corresponds to the dimensions of the resonator. As the sound wave is reflected off the walls, it is reflected back 180 degrees out of phase to the incoming wave, effectively cancelling out this particular frequency.

### 1.4.1 Helmholtz Resonators

A Helmholtz resonator is a special type of resonator which consists of a rigid-walled cavity of volume,  $V$  and a neck of length,  $L$  and area,  $S_p$  (Kinsler, et al., 2000) Each resonator has its own resonating frequency due to the mass of air in the resonator and neck. Following the lumped model approach, the Helmholtz resonator can be compared to simple harmonic motion of a mechanical system. The gas in the closed cavity acts like a spring as the compression of the fluid in the cavity provides stiffness and the gas in the neck acts like a mass therefore the gas in the resonator can be compared to a simple oscillator. This is the condition for Simple Harmonic Motion. It is effectively a mass on a spring and can be treated so mathematically.

The impedance,  $R$  of the Helmholtz resonator can be determined. The impedance of a system is defined as the ratio of the driving force and the velocity of the system at the driving point. Acoustic reactance is the opposition to the flow of sound through the resonator. Acoustic resistance is the real component of acoustic impedance and acoustic reactance is the imaginary component. The resonator resistance,  $\alpha$  is defined as in Equation [1] (Whitehead, 2005):

$$\alpha = \frac{S_p R}{A \rho c} \quad [1]$$

The resonator reactance,  $\beta$  is defined as in Equation [2] (Whitehead, 2005):

$$\beta = \frac{S_p c}{2\pi f_c V} \quad [2]$$

According to the simple harmonic motion analogy between Helmholtz resonator and mass-spring-damper system (vibration absorber), the impedance of a Helmholtz resonator is obtained by replacing mass and damping from Helmholtz resonator system. At the resonant frequency, large velocity amplitudes exist in the neck of the resonator, but all the acoustic energy transmitted to the resonator from the incident wave during one part of the acoustic

cycle is returned to the pipe later in the cycle (Kinsler, et al., 2000). Russel (Russel, 2005) states the phase relationship is such that all the absorbed energy is returned back towards the source, it does not get sent down the pipe. Since no energy is removed from the system, just returned, then the real part of impedance,  $\alpha$  is minimum.

The neck length,  $L$  has an extra term in the equations below called the effective neck length  $L'$ . This can be explained as so: each sound wave within the air flow cannot abruptly change its form to fit into the small cross section of the opening, nor can it assume its original shape immediately after leaving the neck aperture. Instead, the flow will gradually contract and at the same time, it is accelerated. After passing through the neck, the same process takes place in the reverse direction. This 'effective' elongation on the neck length is taken into account with the end correction factor (Kuttruff, 2007). If the neck has a finite length, the effective length with an end correction factor is given by Equation [3]:

$$L' = L + x\alpha \quad [3]$$

The multiplication factor,  $x$  varies depending on the shape of the neck and how it is terminated. At low frequencies, an extra mass termed a radiation mass is loaded in the neck equal to that of the fluid contained in a cylinder of a radius and length equal to  $1.6a$  in the case of a cylindrical opening, where 'a' is the radius of the cylinder (Everest & Pohlmann, 2009). The mass of the fluid in the neck,  $w$  can be expressed as shown in Equation [4].

$$w = \rho L' A \quad [4]$$

The stiffness of the air in the neck,  $\eta$  can be thought of as an air-tight piston with a mass. The mass,  $w$  is moved by the difference in pressure between the top and bottom of the neck. The variation of the pressure due to the movement of the piston and the force required to maintain the displacement provides the effective stiffness of the resonator, see Equation [5] (Ingard, 1953).

$$\eta = \frac{\rho c^2 S_b^2}{V} \quad [5]$$

The theory applies Newton's second law to a lumped mass in the resonator neck acting between an adiabatically compressed volume at one end and the forcing function which is the incident pressure on the resonator at the other. From Equation [6], the restoring force is proportional to the displacement. Two sources of damping in the Helmholtz resonator can be considered; sound radiation from the neck and viscous losses in the neck, which in many cases can be neglected compared to the overall radiation losses of the system. The fundamental resonant frequency of a Helmholtz resonator is the frequency for which the acoustic reactance is zero. Equation [6] below from Kinsler et al (Kinsler, et al., 2000) shows the relationship between the fundamental resonant frequency,  $f_c$  of the resonator and these 'lumped model' parameters:

$$f_c = \left(\frac{c}{2\pi}\right) \sqrt{\left(\frac{S_b}{L'V}\right)}$$

[6]

This lumped element mode approach, which approximates the acoustic behaviour to simple one-dimensional components, holds when the characteristic dimension of the resonator is much smaller than the wavelength. Changing the length and width of the neck and resonator can change the resonating frequency. Clearly, increasing the Neck area,  $S_b$ , will increase the resonant frequency of the Helmholtz resonator, whereas, increasing effective neck length,  $L'$ , and/or volume,  $V$ , will decrease the resonant frequency. Doria (Doria, 2000) shows the lumped mass approach of Equation [6] creates acceptable results as long as any characteristic dimension of the resonator is much smaller than the wavelength.

Transmission loss ( $TL$ ) is the difference in sound power between waves entering the resonator and waves transmitted past the resonator, assuming an anechoic termination. It is therefore a property of the resonator itself and is independent of upstream and downstream conditions. The transmission loss ( $TL$ ) in decibels (dB) of a Helmholtz resonator can be expressed as in Equation [7] (Embleton, 1971).

$$TL = 10 \log_{10} \left[ 1 + \frac{\alpha + 0.25}{\alpha^2 + \beta^2 \left( \frac{f}{f_c} - \frac{f_c}{f} \right)^2} \right] \quad [7]$$

As described above, at resonance, the reactance,  $\beta$  of the resonator is reduced to zero. Therefore, Equation [7] simplifies to Equation [8] (Whitehead, 2005):

$$TL = 20 \log_{10} \left( \frac{\alpha + 0.5}{\alpha} \right) \quad [8]$$

It should be noted that in order to minimize the effects of standing waves within the device, the dimensions do not exceed a quarter wavelength of the resonator natural frequency. Exceeding the quarter wavelength threshold can set up large self-sustaining oscillating pressure fields within the resonator which can create audible tones beyond the resonator geometry.

#### 1.4.2 Closed Quarter Wave Tube Side-branch Resonator

A closed Quarter Wave Tube (QWT) is an alternative type of resonator which is also utilised for noise attenuation in marine and automotive applications amongst others. For automotive applications, QWT's are utilised in air intake tracts and exhaust pipe work. Consider a rigid length of pipe which is closed at both ends. Any harmonic sound field within the pipe consists of a standing wave with maximum pressure amplitude occurring at its terminations. This is only possible if an integral number of half-wavelengths fit into the pipe length,  $L_c$ . This requirement defines the allowed frequencies (eigen-frequencies) in Equation [9] (Kuttruff, 2007):

$$f_c = n \frac{c}{2L_c}$$

[9]

If the pipe has one open end and one end closed, with a forced excitation, the resulting standing wave has a pressure maximum at its closed end and a pressure node at the open end. Thus, the pipe length must be equal to an integral number of half-wavelengths plus one quarter-wavelength

Therefore, the sound field in a pipe of this geometry only exists at certain discrete frequencies. Each resonant frequency corresponds with a characteristic standing wave known as a normal mode.

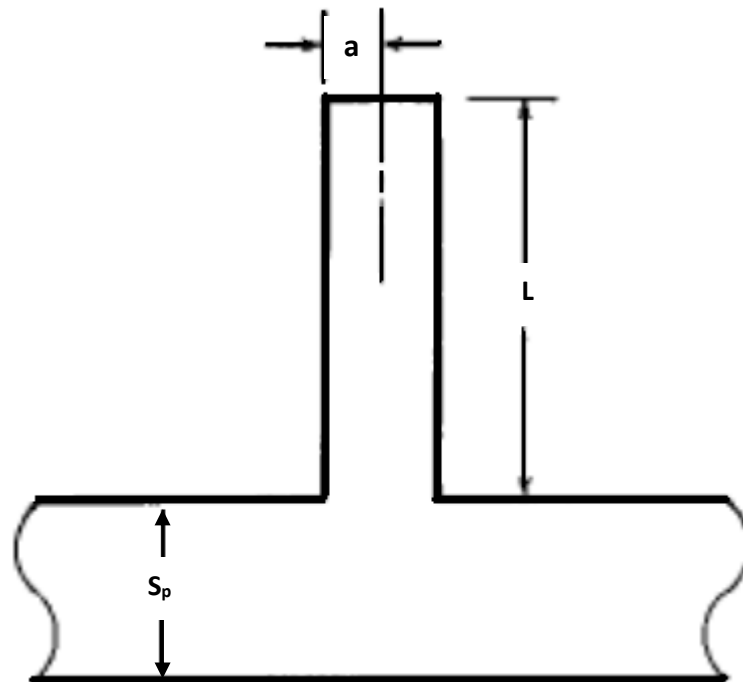


Figure 3: QWT with radius  $a$ , and length  $L$  as a side-branch (Barron, 2001)

From Barron, (Barron, 2001)  $L_c$ , the equivalent length of the QWT is given by taking into account the open end. From Figure 3,  $L$  is the length and  $a$  is the radius of the QWT is used to calculate  $L_c$  as shown in Equation [10]

$$L_c = L + \left(\frac{8}{3\pi}\right)a$$

[10]

A sound wave travelling to the right is reflected from the right end, returning as a sound wave out of polarity with itself (delayed by half a period), travelling to the left. The returning waves react with the oncoming waves to create, by superposition, a standing wave at the natural modal frequency of the pipe or one of its multiples. This standing wave has areas of cancellation (nodes) and reinforcement (antinodes) between the reflecting surfaces (Everest & Pohlmann, 2009).

The nodes and antinodes can be observed at higher order harmonic frequencies. At any point along the QWT, the particle displacement is exactly out of phase with the particle velocity. Particle displacement is always zero at the closed end of a pipe. For any mode, the first particle displacement is maximum at the centre point. This centre position from the end of the pipe corresponds to  $\lambda/4$  (Everest & Pohlmann, 2009). Thus, the fundamental frequency ( $n=1$ ) at which the QWT will resonate is when the wavelength is approximately four times the length of the QWT. Therefore, in the time taken for the acoustic wave to travel down the QWT and back to the main duct, the acoustic wave in the main duct has moved along half a wavelength and is 180 degrees out of phase with the acoustic wave coming from the side branch (QWT resonator). This results in destructive interference and removal of the frequency corresponding to the wavelength.

A pipe of finite length shows several pronounced resonances and the resonance frequencies are identical to the eigen-frequencies of the pipe. Unlike Helmholtz resonators, the primary response of a QWT is a standing wave. Several standing waves are often present to give numerous harmonic resonant frequencies due to the wavelengths intersecting, creating the nodes and anti-nodes. The resonant frequencies rarely produce the same amplitude or attenuation due to the dynamic nature of fluid flows. The following expression (Kinsler, et al., 1982) shown in Equation [11] predicts these resonant frequencies:

$$f_c = \frac{(n - 0.5)c}{2L_c}$$

Where  $n = 1, 2, 3, \dots$

[11]

The transmission loss,  $TL$  is defined for a QWT in Equation [12]. This allows the acoustic attenuation or amplification of noise to be defined.

$$TL = 10 \log_{10} \left[ \left( 1 + \frac{\rho c}{2R_s S} \right)^2 \right]$$

[12]

If there are tones which correspond to the tuned resonant frequencies, the maximum attenuation produced from the QWT is achieved when the cross-section of the QWT matches that of the main duct.

This section has described Helmholtz Resonators, Quarter Wave Tube Resonators and their function in real world applications. The lumped element model approach for a Helmholtz resonator has been explained and is found to be a satisfactory approach to define the expected resonant frequencies in the majority of resonator applications and investigations, including the one here. The following section, Section 1.5, provides an overview of previous work carried out, surrounding this area of cavity flow noise.

## 1.5 Aero-Acoustic Cavity Flows

According to Gloerfelt (Gloerfelt, 2009 (1)), low Mach number flows are involved in automotive applications. Therefore, the density is considered constant along particle paths thus, the flow is considered to be incompressible from a fluid mechanics perspective. Mach number is defined by Equation [13]. Whilst the fluid dynamics can be considered incompressible, the acoustics must consider the fluid to be compressible.

$$M = \frac{u}{c}$$

[13]

The first and most important non-dimensional parameter influencing the properties of a turbulent flow is the Reynolds number,  $Re$  which is based on  $u$ , length scale  $L$  and the kinematic viscosity,  $\nu$  as provided in Equation [14]:

$$Re = \frac{\rho u L}{\mu} = \frac{u L}{\nu}$$

[14]

The Reynolds number determines the ratio between inertial forces and viscous forces. For a low Reynolds number the viscous forces are dominant, and for a high Reynolds number, such as investigations in this paper (in the region of  $10^5 - 10^6$ ), the inertial forces are dominant. Turbulent flow is only possible at high Reynolds number as this is when inertial forces can overcome the influence of viscous forces which are used to damp down the small initial perturbations. Turbulence is discussed in more detail in Section 3.1.

It is well known that when exhaust gas passes through succeeding silencing components and exits the exhaust pipe as a high velocity jet, a significant level of turbulence is generated which is responsible for broadband self-generated noise. Thus the silencer itself can behave like a noise source and sound pressure level can be comparable to that of the engine source (Winterbone & Pearson, 2001). Further to this, under certain flow and geometry conditions the acoustic resonances inside closed side-branches can couple with the shear layer instabilities at the opening. Grazing flow can excite these resonant frequencies. As discussed by Radavich (Radavich, et al., 2001), a shear layer is created between the moving fluid in the main duct and the stationary fluid in the side branch. The instability in the shear layer creates oscillations, which can then go on to excite acoustic resonances in the side branch. The acoustic resonances then amplify the oscillations in the shear layer and the whole process continues to amplify until large-amplitude vortices are formed. Such coupling can produce very high-pressure amplitudes in both the side-branch and the main duct, leading to significant fluctuations inside the side-branch along with the pressure fluctuations being transferred upstream and downstream of the source. This can lead to a disturbing noise outside the main duct. Thus, this interaction causes the resonator to become a noise source rather than an acoustic silencer. There are a large number of

practical examples of this phenomenon in the induction and exhaust systems of combustion engines with oscillating gas flow as well as exterior fluid flows such as automotive sunroofs and door seals. This phenomenon is also prevalent in aircraft amongst other scenarios. The coupling is dictated by a selective mechanism between the discrete vortex modes and the discrete resonant modes, generating the pure tones usually known as a 'whistle' noise.

There have been many attempts to accurately simulate aero-acoustic flow with varying degrees of success and a concise summary is presented as follows. High frequency noise in exhaust/intake systems are difficult to predict. Many investigations, primarily through experimental analysis and more recently, computational based research have been conducted to study the flow fields of resonant cavities. Investigations have been conducted at speeds ranging from subsonic through hypersonic, with the largest amount of effort concentrated on supersonic speeds since military aircraft generally operate supersonically, as highlighted by Tracy and Plentovich (Tracy & Plentovich, 1997). However, many studies have been focused on the theory of resonant cavity flows to help understand the mechanisms behind it. An early paper by Davis (Davis, et al., 1954) largely discusses the basic principles of muffler dynamics but includes a section about resonators. The experiments carried out with branch resonators show the significant attenuation resonators can produce at their resonant frequency and the effects of varying the volume. Davis also describes how the attenuation falls off rapidly at deviations from the tuned frequency. The attenuation frequency region is varied by adjusting the resonator dimensions. The paper concludes that increasing the cross sectional area of the resonator increases the width of the attenuation region, whereas increasing the length of the neck decreases the width of the attenuation region.

Side branches are generally categorised as cavities with a length/diameter (L/D) ratio of  $\geq 1$  or  $\leq 1$ . Selamet (Selamet, et al., 1999) states that shallow cavity literature is significantly larger than that of deep cavities. Flow over cavity-backed openings often results in high-amplitude pressure fluctuations inside the cavity. This phenomenon is thought to be caused by periodic shear-layer vortex shedding from the upstream edge of the opening becoming coupled to a resonance frequency of the cavity (Zoccola, 2004). This phenomenon has been explained further in Section 1.6.

Numerous studies have been carried out concentrating primarily on the effect of resonator shape on acoustic performance. This is often carried out in a one-dimensional methodology and in the absence of grazing flow. For example, an early paper by Bies (Bies & Wilson, 1957) investigated a resonator as a side branch with an incoming sound source

between 100 – 170 dB which produced a standing wave in a tube with no incoming flow. Bies & Wilson found, as the excitation pressure level increased, the absorption coefficient peak shifted to lower value and with a broader bandwidth. The resonance frequency also shifted upwards slightly. The author's view was this non-linear effect was due to thermal and viscous dissipation.

Bruggeman's thesis (Bruggeman, 1987) on flow induced pulsations in pipe systems is a detailed experimental and theoretical study of pipe flow induced pulsations with relatively low Mach number flow – a similarly low Mach number to the range investigated in this thesis. Flow in a T – joint is the focus of the study with the aim being trying to describe, quantitatively, the flow instability as a model of the acoustic field. Bruggeman (Bruggeman, 1987) concludes the model proposed is useful to design flow systems with low pulsation levels. The author also suggests other theoretical model studies for different scenarios, such as the ones described by Powell (Powell, 1964), Howe (Howe, 1975) and Rockwell (Rockwell, 1983) – Howe (Howe, 1975) being the most popular theoretical acoustic analogy for which more recent studies are based upon. Kriesels et al. (Kriesels, et al., 1995) through another gas pipe flow problem analysed the model by Bruggeman (Bruggeman, 1987) along with the Vortex blob method developed by Chorin and Bernard (Chorin & Bernard, 1973) with good end results. These studies have largely concentrated on mean static-pressure distributions and/or unsteady-pressure spectra in cavities as the problem can be split into two separate parts to concentrate on the far-field noise. However, to be able to accurately predict the tonal amplitudes and frequencies in the far-field, the sound source must be predicted in a robust and detailed manner. For pipe systems with high amplitude pulsations, the strength of the aero-acoustic source and the resonance condition are not independent of the pulsation amplitude. Although theoretical work on the fundamental mechanisms surrounding aero-acoustic cavity flows is extremely important for a fundamental understanding of resonant devices, this thesis focuses more on the practical application of a tool to predict, from an engineering perspective, unwanted high frequency resonating activity within these devices. These devices can be built into very complex piping systems, the likes of which, especially for high frequency tones, cannot be accurately predicted with theoretical models. The geometries which the tool is envisaged to be utilised with can be very different shapes to others studied for theoretical purposes. More recent studies of cavity flows and flow-noise has produced a considerable amount of literature perhaps because of the increasing importance of noise reduction to societies in transportation

systems around the world. The most relevant studies to this thesis are cited in the following section.

Some of the early experimental work on deep cavities was performed by East (East, 1966) who examined low Mach number flows over a two-dimensional rectangular cross sectional cavities. East showed that these deep cavities excite primarily discrete frequencies that occur near the fundamental acoustic resonance frequency of the side branch, and concluded that the tones are produced when oscillations are amplified by coupling between the shear layer fluctuations and the cavity acoustic modes. He also noted that the peak excitation occurred in two discrete ranges of Strouhal number, 0.3 - 0.4 and 0.6 - 0.9, suggesting two different modes of shear layer excitation. Later experimental work by Jungowski (Jungowski, et al., 1989) for a circular side branch mounted to a circular duct showed excitation in similar ranges of Strouhal number. Jungowski also showed that increasing the diameter of the side-branch, with respect to that of the main pipe, increases the radiation losses into the main pipe and reduces the amplitude of the tone at resonance.

Ziada (Ziada, 1994) and (Ziada & Shine, 1999) studied the flow-excited acoustic resonances of cavity flows. Ziada's earlier paper (Ziada, 1994), performed a flow visualization study of the coupling between a shear layer with the sound field of a resonant side-branch. Ziada's study showed that the excitation near a Strouhal number of 0.4 is characterized by a single vortex in the branch mouth, while the excitation near a Strouhal number of 0.8 is characterized by two simultaneous vortices in the branch mouth. In the second paper (Ziada & Shine, 1999), the authors carried out experimental investigations into piping systems containing closed side-branches to be able to predict critical flow velocities at which acoustic resonances are initiated with three different configurations of side-branches (single, tandem, and coaxial branches). Ziada and Shine found the maximum amplitude at resonance increases with the diameter ratio. The resonance range, and in particular the onset of resonance was found to shift to lower Strouhal numbers (i.e. to higher velocities) as the diameter ratio ( $d/D$ ) is decreased. The critical Strouhal number is reduced, i.e., the onset of resonance is delayed, when  $d/D$  is decreased. The effect of  $d/D$  on the Strouhal number is seen to be quite strong and is suggested by the authors to be taken into account when evaluating the liability of a system to resonance. Although radiation and viscous losses were found to strongly influence the maximum amplitude during resonance and the width of the resonant frequency range, they are found to have a negligible effect on the Strouhal number at the onset of resonance.

The dimensionless Strouhal number is given in Equation [15] (Zoccola, 2004). As was shown by Ziada (Ziada, 1994) and Jungowski (Jungowski, et al., 1989), this range is strongly dependent on the ratio between the side branch and the pipe diameter.

$$S_t = \frac{fL}{u}$$

[15]

Numerous studies have been conducted on with varying L/D (length/depth) ratios of resonant cavities. These configurations have generally been categorized into two groups: deep cavities and shallow cavities. Studies have generally found; firstly, deep cavities tend to excite primarily the discrete frequencies in several ranges of the Strouhal number near the fundamental acoustic resonance frequency of the side-branch and secondly, the tones are produced only when the shear layer oscillations are amplified by coupling between the shear layer fluctuations and the cavity acoustic modes. It is worth noting here that the cross-section of the resonant cavity, i.e. round or square makes negligible/no difference to the resonant frequency or amplitude (Peters & Riezebos, 2001). See also Equation [17].

Selamet has published several papers surrounding this subject around the turn of the century. One of the first, (Selamet, et al., 1999) was to investigate, experimentally, the whistle noise generation in the obstructed flow of the throttle body adaptor in vehicle intake systems. The author attempted to identify the ranges physical parameters including Strouhal number and Mach number which characterise the resonance conditions. The coupling of shear layer instabilities with the acoustic resonances at the interference of two ducts - a main duct and a connecting side-branch, leads to whistle noise. A generic side-branch adapter was fabricated and attached downstream of a throttle body in the induction system of a production engine. The length and diameter could be adjusted. Experiments were conducted both in a flow facility and an engine dynamometer facility for the same set of flow rates. The distinct resonance particularly higher amplitudes appear in two discrete Strouhal number bands; 0.3-0.9 for first vortex mode and 1-1.6 for second. This is higher than other studies of unobstructed flows, as admitted by the author. The first vortex mode in other studies is around 0.45. However, when the throttle plate is taken into account, the results are said to be valid. Regardless of throttle position, the 1st band is dominant with the

second typically 10-15 dB lower. The number of distinct resonant tones tends to increase with increasing Mach number.

Selamet et al (Selamet, et al., 2001) investigates the insertion loss using a Helmholtz resonator in the intake tract of a V6 internal combustion engine. Experimental and 1D computational modelling were compared with a prototype inlet tract, with and without a Helmholtz resonator. Pressure data was analysed at wide open throttle ranging from 1000-5000 rpm. The influence of the resonator was found to be most noticeable when the fundamental firing frequency was near the resonant frequency of the resonator. High frequency unwanted noise from the resonator was not explored in this paper as the authors mainly concentrated on the one-dimensional approach which is most useful at low acoustic frequencies. The results presented are expected to somewhat depend on the design of the resonator, its location, the intake system, and the engine.

A further study by Selamet (Selamet, et al., 2002) in Partnership with Ford motor company powertrain department investigated experimentally the production and suppression of whistle noise resulting from the shear layer instabilities coupled with the acoustic resonances at the interface of two ducts, a main duct and connecting side-branch. Using a similar set up described above in Selamet's earlier paper (Selamet, et al., 1999), the experiment also investigates a number of suppression methods such as ramps before the side-branch opening, rotation of the throttle body and distance to the side branch opening. The results are compared with results on an engine dynamometer facility. Again, no computational comparisons were made. Selamet's literature review found deep cavities at low Mach numbers tend to be excited by several resonance frequencies corresponding to Strouhal numbers around 0.3, 0.8 and 1.6 respectively for each resonant tone. The author states that the resonances tend to coincide with the quarter-wave frequencies, particularly at higher amplitudes and lower frequencies. The sound pressure level is shown to exceed 130 dB for some resonances close to the source which is thought to be the main duct interaction at the immediate opening of the side-branch. The ramps were found to reduce the amplitudes of the tones by up to 30 dB, though not completely eliminating them. Interestingly, the 2<sup>nd</sup> and 3<sup>rd</sup> harmonic frequencies were eliminated although it is difficult to understand how the flow mechanism is being affected from the results presented. The paper doesn't state whether the function of the resonator is impaired with these changes. Rotating the throttle body and/or using a spacer to extend the distance between the throttle plate and resonator also noticeable reduced resonant tones. The explanation given suggests the local turbulent velocities are reduced near the resonator opening.

Meissner, (Meissner, 2002) discusses air flow through a pipe with two closed side-branches. The acoustic coupling between the branches was investigated and the paper concluded – as flow velocity is increased, “the succeeding resonant modes are excited and the acoustic response of the system occurs at a specific range of a Strouhal number.” (Meissner, 2002) This agrees with other Authors on the subject such as Rossiter (Rossiter, 1964), Zaida (S Ziada, 1999) and Selamet, (Selamet, et al., 2002) amongst others. Meissner also states the change from one acoustic mode to the next is gradual, thus, two excited frequency modes can appear together. The results showed that a strong sound excitation is possible when a resonant frequency of the whole system is close to resonant frequencies of the resonators. However, Meissner makes a valid point in that the noise generation is a product of the whole pipe system and the excited frequency modes can differ considerably from the resonant frequencies of the resonators.

Kook (Kook, 2001) investigated reduction techniques of flow excitation over side-branch Helmholtz resonators. A feedback loop consisting of a microphone located in the cavity and a loudspeaker feeding a movable spoiler located on the leading edge of the cavity was utilised to help actively reduce flow-generated noise. A reduction in amplitude of up to 20 dB was achieved over a range of flow velocities but the noise was not completely attenuated. This method is possibly of use to reduce the unwanted high frequency noise found in some automotive designs. However, designing the problem out beforehand such as moving the resonator to another location would be preferable as this will reduce costs and complexity. This is one of the main reasons a CFD tool is being investigated in this thesis.

Doria, (Doria, 2000) discusses an improved method of determining resonator natural frequencies with accuracy. Although this is not a subject covered directly in this thesis, the paper does hold some relevant and useful information. The effect of geometry on the resonance frequency of Helmholtz resonators is of interest here. Large ratio resonators (long and thin or short and wide) do not follow the simple 1D formulation very accurately (see Equation [6]). Doria suggests shape functions to predict these large ratio resonators more accurately with good success.

Zoccola (Zoccola, 2004) investigated the subject of noise reduction techniques for the flow-excited response of Helmholtz resonators. Unwanted tones produced by resonators, described in Section 1.6 are often suppressed in practice by installing a grid in the opening. The Zoccola (Zoccola, 2004) states, “Analysis of results from large-scale model tests has revealed that even with a grid present, under some circumstances these fluctuations continue to occur at amplitudes and frequencies similar to those that would be

observed for an unobstructed opening". The study by Zoccola was experiment based to understand why and under what circumstances this flow-excited resonance continues to occur despite the presence of a grid. Measurements of cavity pressure due to flow over a cavity with obstructions or grids of varying dimensions in the opening were obtained. Measurements were also carried out to capture the flow field in the cavity opening for selected configurations. The experiments confirmed tones can be created by resonant cavity openings. It was also found that although a grid does have a positive effect on the amplitude of the tones, the frequency of the excitation and the amplitude of the response at the large length scale are altered in various ways, depending on the configuration of the grid. Of particular interest is the distinct difference between the results obtained with coarse and fine grids. Flow field results show the effects that a grid has on the flow, including effects on the vortex convection velocity and the energy production distribution. Overall, this paper highlighted the complexity of grazing flow control from an acoustic perspective.

Kannan, et al (Kannan, et al., 2004) investigated the suppression of a 2.2 kHz frequency whistle noise in an automotive intake manifold. The root cause of this whistle was a resonant cavity present in the geometry downstream of a throttle plate. Kannan, et al confirmed the whistle was produced purely from air-flow related phenomena and was not related to structural resonance or engine firing frequency. A ramp with a sharp radius was introduced on the upstream edge with a clay mould. This, the author's state, was an attempt to de-couple or weaken the resonance between the shear flow instabilities and the acoustic modes of the sump cavity. The study found the ramp reduced the 2.2 kHz tone by more than 20 dB. Kannan et al. Concludes, for a future direction, Computational Fluid Dynamics has been initiated in an attempt to gain better insights into the mechanism of whistle production/suppression. This is a similar route to the one taken in this thesis.

Duben, et al (Duben, et al., 2012) carried out a study of acoustic flow in the Helmholtz resonator throat. The results compare data from physical experiment, mathematical modelling and comparison with theoretical estimation. The experiment uses a Laser Doppler Velocimeter and a condenser microphone to control pressure level. Simulation of nonlinear effects and generation of acoustic flow in the throat is carried out with the Navier–Stokes equations. Detailed flow images as well as quantitative data is gathered with incoming excitation sound waves but with no grazing air flow at resonant frequencies. Three different amplitudes are monitored to provide an image of the acoustic flow formation, mainly the averaged velocity components in the throat of a resonator. The

results showed that computational modelling of complex flow structures is useful in understanding the underlying phenomena.

Aero-acoustic cavity noise has been attenuated and amplified. Different shapes (shallow/deep/square/round) of resonating cavities have been investigated. However, from the literature review, very few studies have investigated unwanted high frequency noise with complex geometries. Noise created from the neck edge, welds, manufacturing process, bends upstream of resonators are all real problems to be understood and investigated. Being able to predict designs which exhibit high frequency flow-generated tones through numerical methods would reduce the need to carry out expensive experimental analysis of these systems.

## 1.6 Vortex Shedding

This section provides further detail into the fundamental mechanisms of resonant cavity flows. As Section 1.5 revealed, fluid passing the resonator neck can induce turbulent flow oscillations and unwanted high frequency noise mainly due to vortex shedding. The overall process produces resonant frequencies, which are referred to as cavity tones. The acoustic resonances of side-branches are caused by a feedback excitation mechanism which is often referred to in the literature as fluid-resonant mechanism. The amplitude spectrum is generally dominated by high-amplitude, discrete-frequency tones and large broadband levels. In many cases, multiple tones are observed, and these are often accompanied by their harmonics.

Flow tones can be generated in a wide variety of configurations. In essence, they arise due to favourable coupling between an inherent instability of a separated shear layer and a resonant acoustic mode of the flow system (Tam, et al., 2008). The fundamental mechanism for this generation of flow-excited cavity resonance is well understood. In the context of cavity flows, the flow acoustic coupling which leads to resonance is commonly called the *Rossiter mechanism* as described by Rossiter (Rossiter, 1964). He identified an acoustic feedback mechanism for cavities and flow regimes. The period of the fluctuations was found to be the the same as the time it takes for a disturbance to travel the length of the cavity at roughly half of the free-stream velocity and then to traverse back up the cavity at sonic speed. A visual representation of this mechanism is provided below in Figure 4.

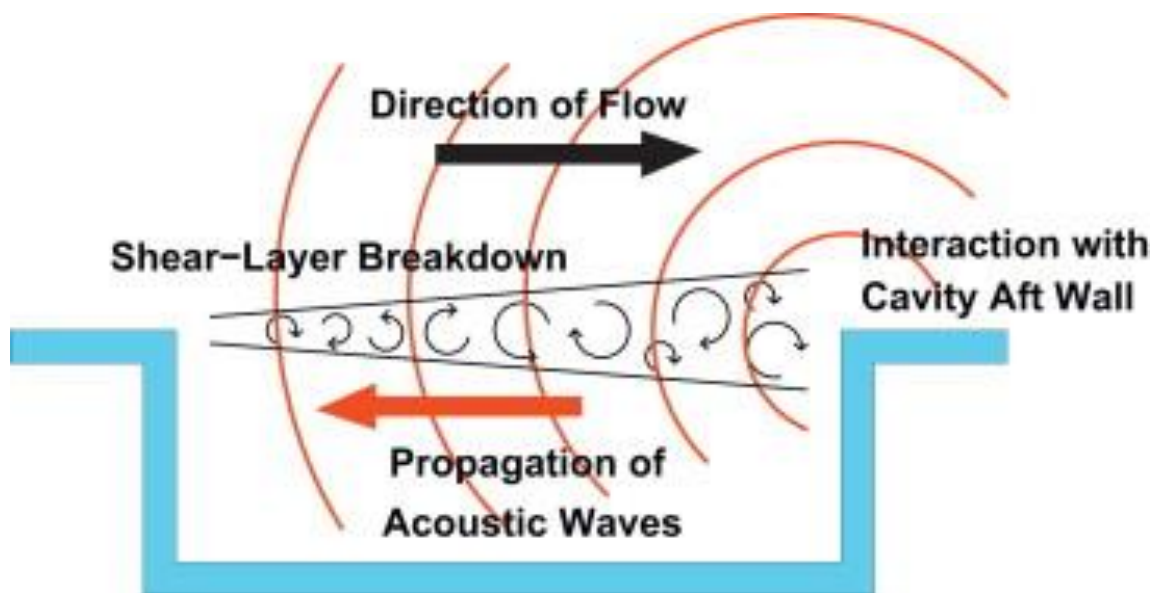


Figure 4: Production of flow-excited cavity resonance (Lawson & Barakos, 2011)

Rossiter also looked at the amplitude spectra of the pressure fluctuations at the rear of the cavities for varying  $L/D$  ratios. For deep cavities, the fluctuations occurred at specific frequencies. It was determined that as the  $L/D$  ratio of the cavity increased, the pressure fluctuations inside the cavity became more random and so the tones were replaced with a wider range of frequencies (Lawson & Barakos, 2011). Rossiter (Rossiter, 1964) derived an empirical formula to predict the onset of the pressure fluctuation modes, given in Equation [16]. The Rossiter mechanism relates the two mechanisms (i.e., vortex shedding and acoustic radiation) by taking into account a phase difference by which a vortex is downstream of the rear wall when the acoustic wave leaves the rear wall in the upstream direction. The frequency of the organized flow is proportional to the free-stream velocity,  $V$ , of the flow and inversely proportional to the length,  $L$ , of the opening, resulting in a constant Strouhal number for a given configuration. Rossiter also identified a resonant model which occurs when the flow oscillations in the cavity contain wavelengths equal to that of the cavity length or smaller. The Rossiter model and similar theories, some of which are provided in the review article by Rockwell & Naudascher (Rockwell & Naudascher, 1978) empirically formulate pressure fluctuating feedback mechanisms to predict dominant frequencies are very successful with a low  $L/D$  (length/depth) cavity ratio and moderately high Mach and Reynolds numbers. However, as discussed in Section 1.5, when the  $L/D$  ratio is increased, the solutions do not hold true.

$$f = \frac{U_e(m - \gamma)}{l(M + 1/\kappa)}$$

[16]

Rossiter and others found good agreement between the proposed empirical formula and experimental results for  $\gamma = 0.25$  and  $1/K = 1.75$ . In Rossiter's formula, the free shear layer is viewed as two-dimensional, and the re-circulating flow is neglected. At high Mach numbers, this simple formula succeeds in predicting the admissible Strouhal numbers, although it provides no information on the amplitude of the self-sustained oscillations nor it indicates which of the multiple modes will be dominant. It can be noted that almost no other theoretical models are available for high-speed cavity flows (Gloerfelt, 2009 (2)).

The production of flow-excited cavity resonance is further described by Bruggeman (Bruggeman, 1987), Rockwell & Naudascher (Rockwell & Naudascher, 1978), Stoneman et al. (Stoneman, et al., 1988) Ziada (Ziada, 1994), Kook (Kook & Mongeau, 2002), (Kook, 2001), Meissner (Meissner, 2002) and others but is summarised here. The processes that leads to stable, sustained flow oscillations can be described as follows: The unstable shear layer across the resonator orifice, shown in Figure 5, periodically rolls up into discrete vortices. These vortices are convected downstream at a speed of approximately half the main flow velocity, on average. The vortex core path is not straight. Vortices are often entrained into the resonator near the leading edge, and ejected further downstream. The presence of the downstream edge causes these structures to become highly organized at a discrete frequency (Rockwell & Knisely, 1979). The total net circulation of the flow over the resonator orifice fluctuates as the vortices are discharged past the downstream orifice edge. The fluctuations in the total circulation strength for the flow region in the vicinity of the resonator orifice give rise to external pressure fluctuations, which excite acoustic modes within the resonator. The acoustic pressure fluctuations inside the resonator, in turn, trigger discrete vortex shedding near the separation point at the upstream edge, synchronised with the nearly sinusoidal flow fluctuations. New vortices are initiated immediately after the moment where the cavity pressure is a minimum, and the air mass within the resonator orifice (treated as a lumped mass) is being displaced towards the interior of the resonator (Kook, 2001). The amplitude of the resonant modes is not only a function of the growth of instabilities in the shear layer, but depends also on the conversion of turbulent disturbances

into acoustic waves at the trailing edge, the propagation of the waves and their re-conversion to turbulent disturbances at the leading edge or along the shear layer in a distributed way (Rowley, et al., 2000). At the trailing edge, a conversion of fluctuating flow energy to the energy of resonant acoustic field takes place. When a balance between acoustic energy losses and the energy extracted from flow fluctuations is reached, the stable pulsations with frequencies close to resonant modes are generated (Meissner, 2002).

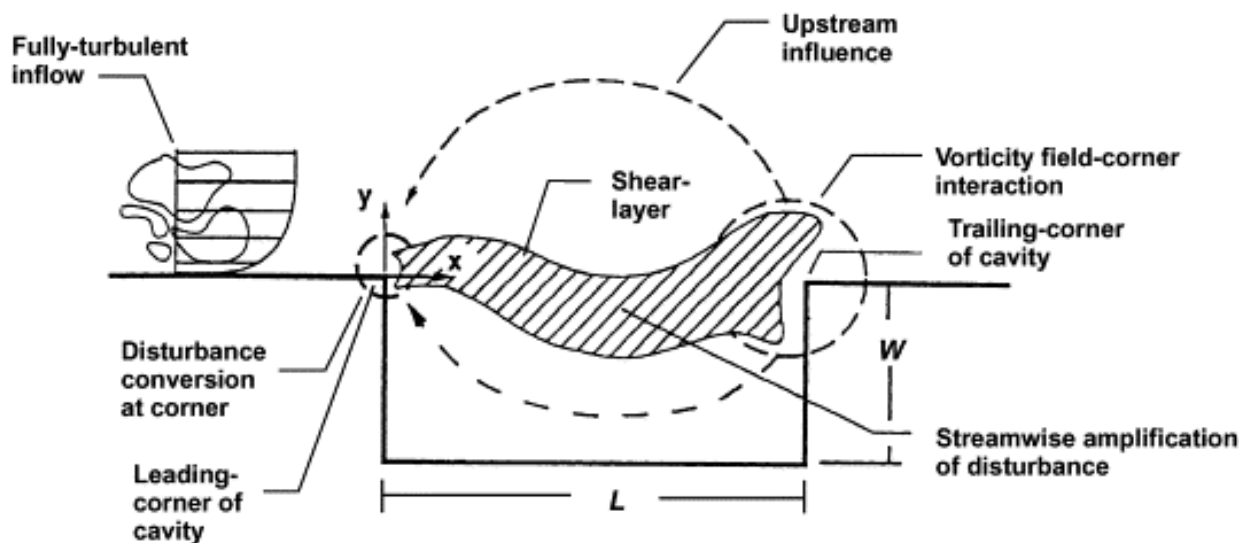


Figure 5: Principal elements of self-sustaining oscillation of turbulent flow past a cavity associated with purely hydrodynamic effects (Rockwell, et al., 2003)

This phenomenon may be observed in measurements of fluctuating pressure beneath the opening/inside the resonator. These speed-dependent tones are referred to as shear-tones. The terms ‘first shear-tone’ and ‘second shear-tone’ are used to refer to the presence of one and two vortices, respectively in the cavity opening. When the shear-tone frequency approaches a resonance frequency, which may be the Helmholtz resonance or an acoustic standing wave, the vortex formation process and the resonant response become coupled, forming a flow induced cavity resonance. The terms flow-induced cavity resonance or resonant shear-tone are used to describe the tone measured in the cavity pressure spectrum at speeds where the vortex shedding is coupled with the cavity response; non-resonant shear-tone describes these tones where coupling is not present. A flow-induced cavity resonance results in high-amplitude pressure fluctuations in the cavity. It also alters

the dependence of frequency on velocity and, hence, alters the Strouhal number. (Zoccola, 2004)

Flow-excited cavity resonance causes nearly sinusoidal cavity pressure fluctuations. In an attempt to quantify this aero-acoustic response, the non-linear coupling between the acoustic response of the side branch and the vortical flow excitation can be modelled using a describing function theory (Kook & Mongeau, 1997). The time-averaged source strength,  $P^*$  of this aero-acoustic response is, according to Howe (Howe, 1975) is given by Equation [17].

$$P^* = \frac{\bar{P}}{\rho U_o^3 A} = \frac{1}{\rho U_o^3 T_p} \int_0^T P(t) dt$$

[17]

Both the velocity and the vorticity field have to be known as a function of time and space to be able to quantify the aero-acoustic source. Various levels of sophistication have been applied both experimentally and numerically to determine the source strength as a function of amplitude ( $u_{ac}/U_o$ ), edge radius ( $R/D$ ) and Strouhal Number. Several of these methods are referenced in the paper by Peters & Riezebos (Peters & Riezebos, 2001). Hofmans (Hofmans, 1999) used a 'vortex blob' method to describe the unsteady separated flow in a side branch T-joint. From the Power Source,  $P^*$  obtained from numerical simulation, it appears that for moderate amplitudes, which is common for most applications,  $0.05 < u_{ac}/U_o < 0.3$ , the source strength increases linearly with the pulsation amplitude (Peters & Bokhorst, 2000) and as a result it can be assumed that the ratio is constant. From this, the amplitude of the pulsations can be estimated by Equation [18].

$$F = \frac{P^*}{u_{ac}/U_o} = \frac{\bar{P}}{\rho U_o^2 u_{ac} A}$$

[18]

The value,  $F$  of the aero-acoustic source in the moderate amplitude region has been determined numerically as a function of Strouhal number for a number of configurations with sharp edges by Hofmans (Hofmans, 1999). The results can be used to predict the amplitude of flow-induced pulsations in configurations with a T-joint with sharp edges. (Peters & Riezebos, 2001)

This section has described the fundamental flow processes in resonant cavity flows. The fundamental phenomena for both Helmholtz resonators and QWT's have been represented through simple harmonic motion analogy and a combination of standing waves respectively. An explanation is given of resonators with grazing flow, both the acoustic properties within the resonator geometry and further downstream, thus its effect on the overall acoustic properties contained in the flow. It is clear from the literature, a very complex phenomenon is occurring around the leading edge, cavity entrance, inside the cavity and the downstream edge to create high amplitude tones. The problem of unwanted high frequency tones originating from resonating cavities has been shown to occur in many configurations across many engineering sectors. Clearly, further analysis is required to fully understand and eliminate these problems at an early design stage. The functions and principal elements of these oscillations have been detailed along with function theories to help analyse numerically the aero-acoustic response. The knowledge gained here helps to give a fundamental understanding into the flow processes present in the experimental and computational findings throughout the following chapters of this study.

## **1.7 Methodology**

This study will conduct several experimental tests to re-create the unwanted high frequency tones from resonators found in the literature examples discussed in the section above, as well as the examples found during the production phases within the premium automotive sector. The experiments will analyse several resonator geometries at various flow velocities. The tests will be re-created as numerical Large-Eddy Simulations using a commercial Computational Fluid Dynamics (CFD) code. The results will be analysed and compared with the experiments to deduce whether the CFD code is suitable for use as a design tool, and thus could be utilised early on in the product design phase.

Chapter 2 introduces the experimental set up and validation of the equipment and flow rig. The validation includes the use of acoustic signals and air flow as it passes the opening of various side branch configurations. A side branch consisting of a Variable Volume

Helmholtz (VvH) resonator and an adjustable Quarter Wave Tube (QWT) will be analysed in terms of the noise generating effect on the acoustic field in a straight section of pipe. An automotive resonator is flowed which has been shown to produce high amplitude high frequency tones. For Chapter 4, a literature study on numerical investigations into cavity flows is undertaken to understand the state-of-the-art in CFD usage. The focus is to re-create the experiments as numerical simulations using a commercial Computational Fluid Dynamics (CFD) code. Computational validations are carried out and further studies are undertaken with the increased information and variability available through CFD. The results are analysed and compared with the experiments. Chapter 5 summarises the thesis to deduce whether the CFD code is suitable for use as a design tool, and thus could be utilised early on in the product design phase.

## 2 Experimental Work

This chapter introduces the experimental work which aims to gain further understanding into how a resonator behaves under various flow conditions, geometries and acoustic signals. Several validation experiments will be conducted to investigate the effect of acoustic signals and the air flow as it passes the opening of various side branch configurations. A side branch consisting of a VVH Helmholtz resonator and an adjustable Quarter Wave Tube (QWT) will be analysed in terms of the effect on the acoustic field in a straight section of pipe. Various parameters will be explored including; inlet signal, multiple resonators in series, inlet flow rate, resonator geometry, resonator volume and side branch neck protrusion length. Later, an automotive section of charge inlet tract is flowed which has been shown as creating high amplitude high frequency tones at certain mass flow rates.

The following section will describe the experimental work carried out which will be used as a comparison for the CFD simulations described in later chapters of this thesis.

### 2.1 Experimental Configuration

The experiment layout for the first series of experiments, including validation tests with a Variable Volume Helmholtz (VVH) resonator are shown in Figure 6 and Figure 7. A photograph of the VVH resonator is also provided in Figure 33. The flow test facility (wind tunnel) is predominantly an aluminium thin-walled pipe, 74 mm in internal diameter and approximately 20 metres in length. Each section, approximately 2 m long is connected via a flange. Four bolts equally spaced ensure a smooth and sealed transition. The fan at the inlet – a 22kW TEC Electric Motors has a smooth conical 130 - 74 mm aluminium reducer with 1 m of flexible smooth-walled tubing to reduce noise and vibration. The working cross-section and the resonator proportions used throughout this study have been chosen to closely relate to real world automotive intake and exhaust parameters. A large generic dissipative silencer (not shown in Figure 6 and Figure 7) is also fixed in series downstream of the flexible tubing to further reduce the mean background noise from the axial fan. The maximum velocity of the fan is approximately 150 m/s. However, the signal-to-noise ratio, which compares the sound under test and the inherent background noise of the equipment in decibels, is acceptable up to a maximum of 60-70 m/s. The facility is anechoically terminated with an ISO 7235 design (ISO-7235, 1991) to reduce acoustic reflections to a minimum.

The cylindrical VVH resonator has a movable piston which allows the volume of the resonator to be varied. By varying the volume, the resonant frequency of the resonator can be tuned anywhere between 200-3000 Hz. The dimensions of this VVH resonator are provided in Figure 8. Figure 7 shows the VVH resonator situated towards the outlet end of the pipe. This can be removed to create the original signal and thus isolate the effect of the silencer. In the foreground is the loudspeaker which creates the signal and in the background, the microphone is shown, which picks up the signal ready for processing. A large fan to provide an incoming air flow is situated approximately 10 m upstream of the test section. Using such a long upstream length, it is expected the flow will become a fully developed turbulent profile. A long downstream length, approximately 8 m and an anechoic termination is situated at the outlet to dissipate and reduce noise reflection.

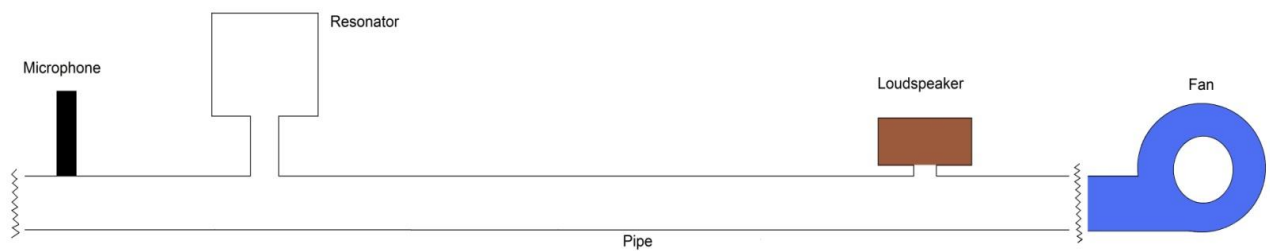


Figure 6: Diagram of experimental set up



Figure 7: Photograph of experimental configuration

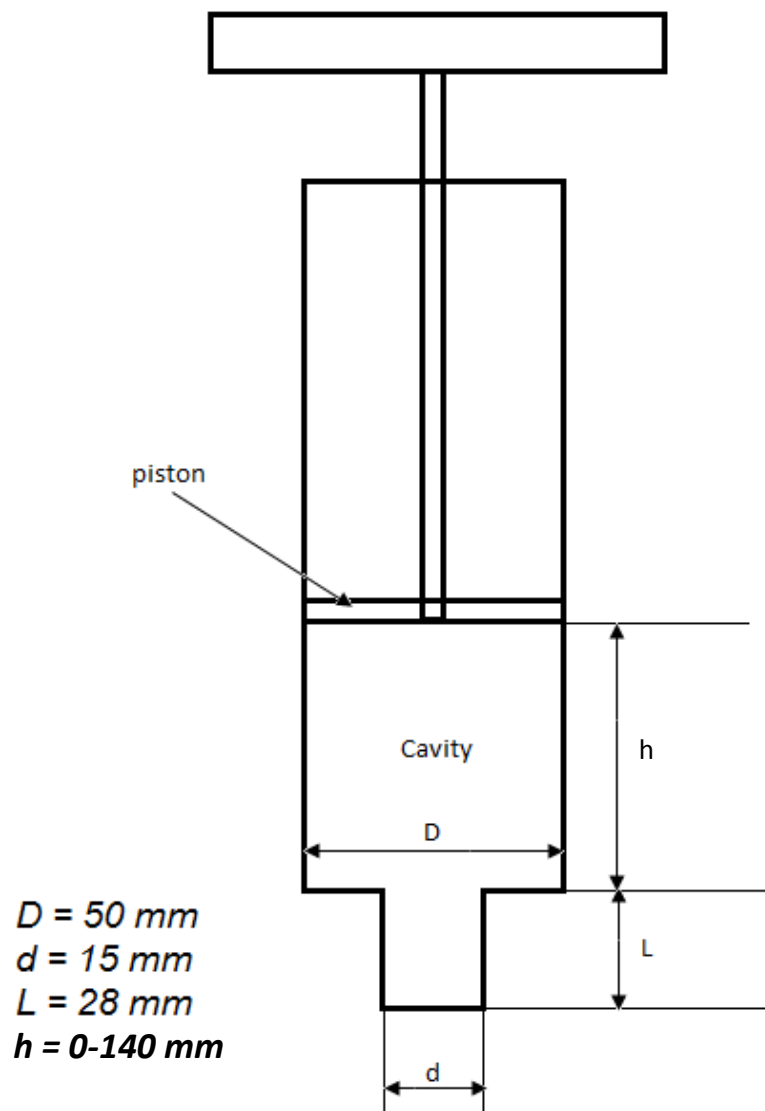


Figure 8: Resonator with adjustable volume via movable piston, showing dimensions

Most 'real' flows are turbulent including the scenario analysed in this thesis. Therefore, the experimental flow set-up must contain a realistic level of turbulence i.e. a fully developed turbulent flow. Figure 10 shows a plot of velocity (m/s) against distance from the wall (mm) of the fan situated at the pipe inlet. An electronic handheld EXTECH manometer, which measures to the nearest Pascal with 0.5% repeatability, is used to obtain a radial profile of the air velocity in the pipe. In a fully developed channel, a logarithmic flow profile is typical. The profile is the result of the friction generated between the fluid and the pipe wall, which results in the fluid layer in direct contact with the wall having a parallel

velocity-approaching zero. Due to the viscous forces present, this effect is propagated in the normal direction throughout the fluid boundary layer, as shown in Figure 9.

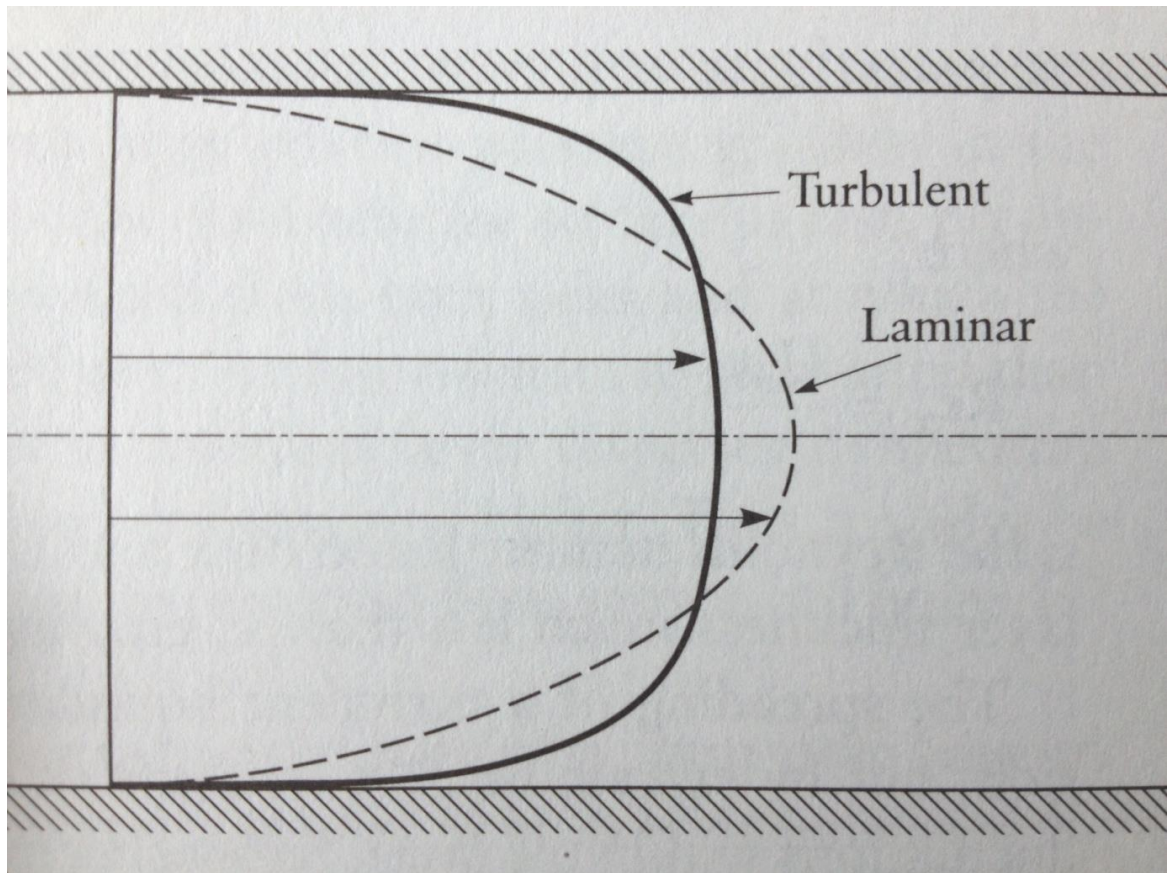


Figure 9: Ideal profile for fully developed turbulent and laminar flows in a circular pipe (Mathieu & Scott, 2000)

Three layers exist within the boundary layer of flow within a pipe. The first is the viscous sub-layer that is extremely small, whereby turbulent fluctuations are present but dominated by viscous forces. The layer above is the remainder of the boundary layer that is known as the transition layer. This acts as a buffer layer between the viscous dominated sub-layer and the turbulent dominated outer layer known as the wake region. This layer contains small turbulent eddies and more turbulence kinetic energy than the outer layer. Further information of fully developed turbulent flow can be found in Section 3.1. To analyse the flow profile within the experiment, six points, evenly spread radially across the pipe are plotted for various flow velocities in Figure 10. These points were made only as a coarse measure of the flow velocity with no further investigation of accuracy. The velocity profile appears to be fairly flat with a small boundary layer with resembles the expected profile

shape – see Figure 9. The measuring point is located at the side branch port. This is 10 metres from the outlet from the fan, thus the profile is expected to be fully turbulent.

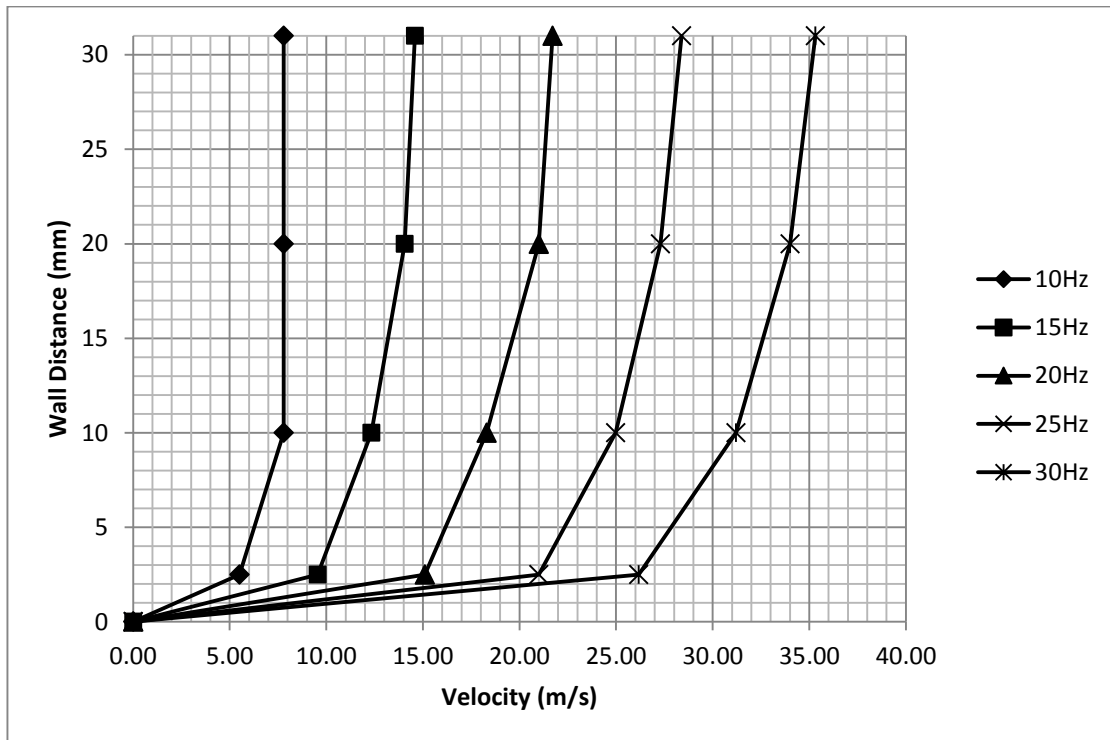


Figure 10: Fan velocity profile. Each line represents the velocity profile of the flow from the fan at various power inputs (measured in Hz at the controller).

To ensure the measurements were repeatable, the mass flow rate was calculated at the side branch port as well as towards the anechoic termination – a further 10 m downstream. The results provided in Figure 11 show a very good correlation. The mass flow error between measurement locations is within 1%. This gives confidence to the accuracy and repeatability of the velocity profile measurements.

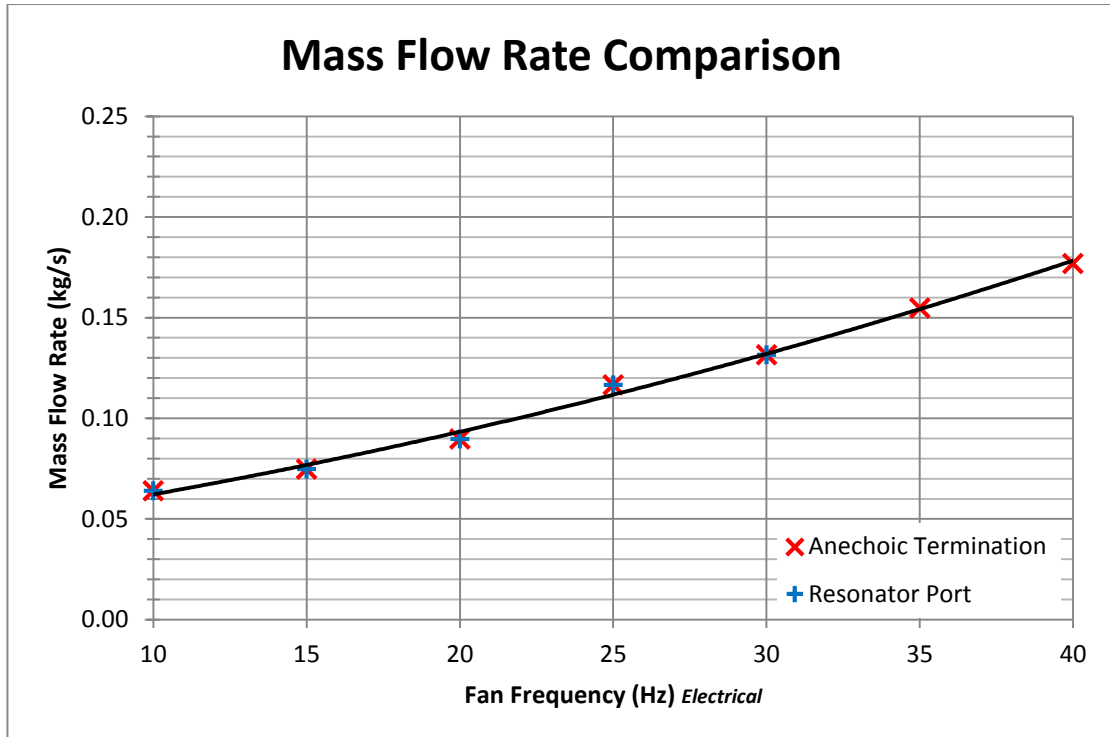


Figure 11: Mass flow comparison 10 m (Resonator Port) and 20 m (Anechoic Termination) downstream at various flow velocities. Black line = trendline

The purpose of the experimental studies is to determine how different resonator shapes and positions change the noise produced with grazing airflow. To see the relative effect of a particular resonator, it is necessary to have a benchmark with which to compare. This benchmark is the test rig without a resonator. For all cases apart from the CAC resonator section, the resonator can be completely removed with a smooth nylon bung, shaped to the curvature of the pipe which is placed in the resulting opening. A grub screw placed on the side of the port is used to position the bung accurately, allowing for smooth pipe airflow. The background noise spectrum is provided for each resonator test set-up in the relevant chapter section.

A Brüel & Kjaer  $\frac{1}{4}$ " microphone (Type 4939-A-011) is placed flush with the pipe wall approximately 300 mm downstream of the resonator/test section to measure pressure fluctuations. The microphone is mounted flush to the pipe wall to reduce the effects of self-generated noise. Only tones which are in the human hearing range are of interest, particularly tones which can be heard by the car's occupants. The linearity (11 mV/Pa), flat frequency response over a wide frequency range of 4 – 100,000 Hz, small size and their large dynamic range of 28 – 164 dB make these microphones ideal for capturing the aero-acoustic results.

Agilent software along with Agilent Measurement Manager Amplifier equipment (U2761A/U2542A/U2781A) amplifies and extracts usable high resolution data from the microphone output ready for post-processing. The Agilent equipment has a 16-bit resolution, simultaneous analog input channels, up to 500 kSa/s/ch, 2 12-bit analog output channels, 1 MSa/s analog output update rate and 24-bit programmable TTL input/output channels.

Each test produces 20,000 useable samples to capture the wave forms accurately with a sampling rate of 100,000 Hz. The tests are carried out 20 times and the results are averaged to reduce background noise errors. The uncertainty of the measurements is demonstrated in Appendix 2. The statistical measurement error of the microphone outputs is calculated for all presented experimental data. After recording the time-pressure data for the background noise spectrum and the noise spectrum for the resonator test sections, it is imported from Agilent software into MATLAB 2010 in order to convert the time-pressure signal to the frequency-amplitude spectrum by using a Fast-Fourier Transform (FFT) algorithm.

An FFT frequency analysis can be thought of as a process which transforms a time varying signal in the time domain to its frequency components in the frequency domain. Frequency analysis can be used for noise source identification will help determine the effectiveness of a silencer or resonator for example. There are two ways of transforming a signal from the time domain to the frequency domain. The first involves the use of band limited digital or analogue filters. The second involves the use of Fourier analysis where the time-domain signal is transformed using a Fourier series. The expression of the Fourier Integral Transform theorem for a non-periodic signal  $f(t)$  is given in Equation [19] (Kinsler, et al., 2000).

$$F(\omega) = \int_{-\infty}^{\infty} f(t)e^{-j\omega t} dt$$

[19]

This is implemented in practice digitally (referred to as the DFT - Digital Fourier Transform) by dividing the initial signal into several pure sinusoidal signals. These sinusoids are then converted into a frequency-amplitude spectrum. The MATLAB code used to post-process the data in this thesis is provided in Appendix 1, Chapter 6.1. The results are examined in terms of Sound Pressure Level (SPL) in decibels as a function of Frequency (in

Hz) for a given flow rate. The acoustic frequency range captured is 20-10,000 Hz to encompass the human hearing range.

There are two commonly used useful measures to quantify an acoustic source. The sound pressure is the local change in pressure from the reference ambient pressure caused by a sound wave (a pressure fluctuation). The Sound Pressure Level (SPL), Equation [20], is a logarithmic measure of the effective sound pressure relative to a reference value and is measured in decibels (dB).

$$SPL = 10 \log_{10} \left( \frac{p_{rms}^2}{p_{ref}^2} \right) = 20 \log_{10} \left( \frac{p_{rms}}{p_{ref}} \right) \quad [20]$$

The Sound Intensity ( $I$ ) is a vector quantity determined as the product of sound pressure and the component of particle velocity in the direction of the intensity vector. It is expressed as watts per square metre ( $W/m^2$ ). It is a measure of the rate of power transmission through a surface normal to the intensity vector. In an environment with no reflected sound waves and well away from any other sound sources, the sound intensity is related to the root mean square acoustic sound pressure as follows in Equation [21].

$$I = \frac{p_{rms}^2}{\rho c} \quad [21]$$

The FFT set-up described above is implemented into the experiments with the parameters defined as follows:

- $\Delta t = 0.2$  seconds
- Amplitude Function = Sound Pressure Level
- Frequency Function = Frequency
- Analysis Blocks = 2
- Overlap Factor = 0.8
- Reference Sound Pressure =  $2E-5$  Pa

## 2.2 Validation Experiments

The design of the initial experiments is as shown in Figure 6. Initial experiments are carried out to validate the experimental procedure and configuration which is used throughout the study. The validation experiments are also of use to verify the theoretical lumped model approach used for the Helmholtz Resonator calculations.

A single Helmholtz Resonator and a pair in series, both with an adjustable volume given in Figure 8 are tested to show the function of a Helmholtz Resonator in the majority of real world situations. The acoustic response of the resonator is investigated with loudspeaker driven noise with zero incoming mean flow. To create a sinusoidal sound wave pulse for the validation tests, a noise generator (Brüel & Kjær type 1405) is utilised along with a 1.6kW power amplifier (C-Audio SR707) to power a JBL 6.5" diameter 125W RMS loudspeaker with a flat +/- 2 dB frequency response of 50 Hz – 21 KHz. The measuring equipment is as described in Section 7.1. A random broadband noise signal is created at the inlet and the signal at the outlet of the pipe, downstream of the resonator, is investigated to find any fluctuations/attenuation caused by the resonator.

The initial sound signal comes from the loudspeaker and travels through the pipe. The raw noise signal is shown in Figure 12.

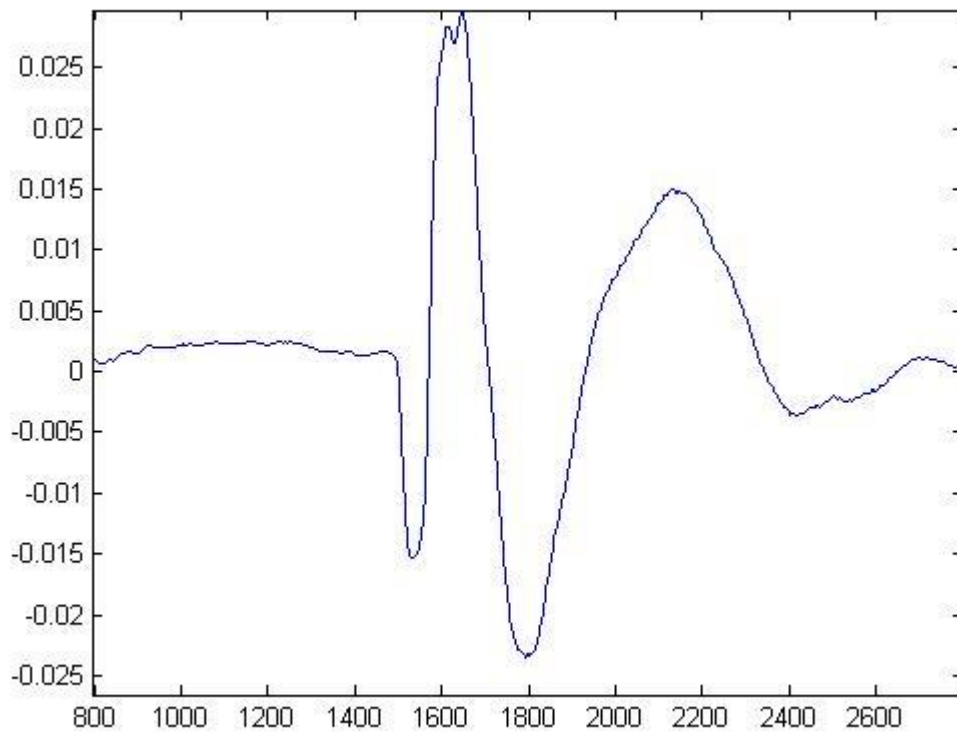


**Figure 12: Inlet signal – Amplitude in mV against sample number.**

The initial signal, without the resonator in place, has a spectrum of frequency around 100-200 Hz shown in Figure 13 which is an FFT plot of the initial signal. Figure 13 shows a FFT plot of the broadband signal driven by the loudspeaker with no resonator present as shown in Figure 12.

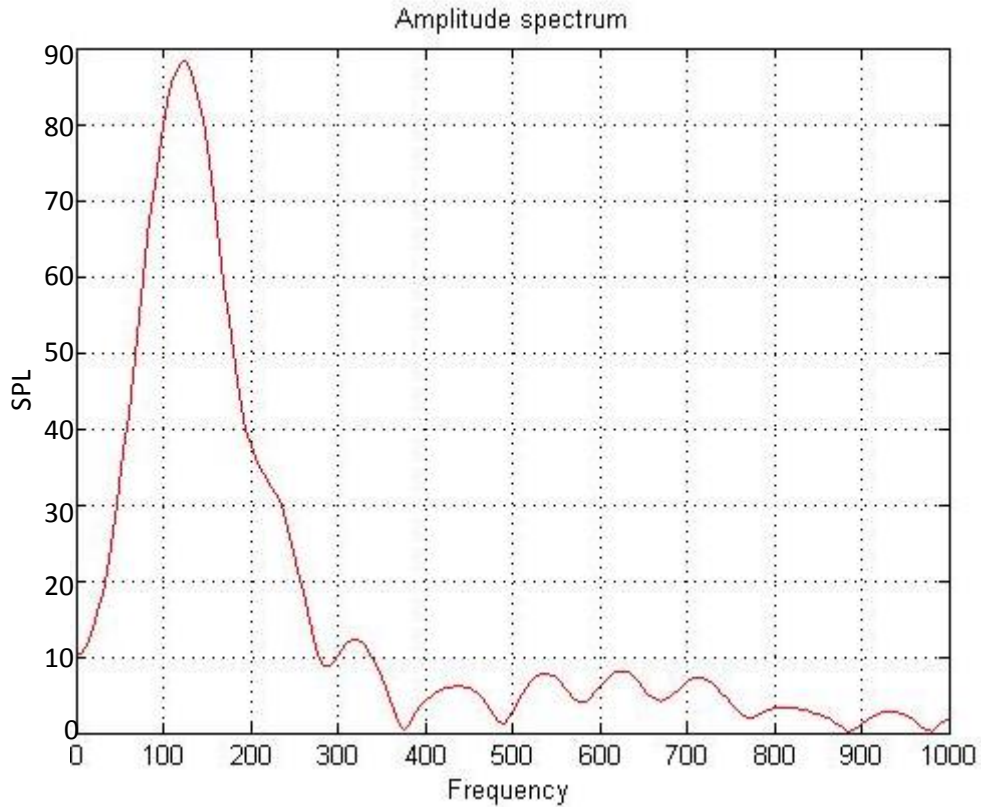


Figure 13: FFT plot of inlet signal. SPL (dB) against Frequency (Hz).

Each FFT plot in the following section measures SPL (dB) against Frequency (Hz). The sensitivity of the microphone is 11mV/Pa, thus the SPL can be calculated. The first step is to import the data and to select just one period of the signal to make the Fourier Transform. The mean pressure is calculated and subtracted to leave the pressure fluctuation from the mean at every sample in time. The attenuation of the resonator can be calculated from converted pressure values or from the SPL as shown by Equation [22] below which defines the Insertion Loss. Insertion Loss is the difference in Sound Pressure Level (SPL) at the receiver with and without the inclusion of the resonator. Since the resonator will attenuate some of the sound power created at the inlet, the pressure at the receiver with the resonator will be less. Therefore, this creates a positive insertion loss.

$$Insertion\ Loss\ (dB) = 20 \log \frac{p_{no\ resonator}}{p_{resonator}} = \frac{SPL_{no\ resonator}}{SPL_{resonator}}$$

[22]

The VVH resonator is tested with different volumes predicted to attenuate these frequencies: 200Hz and 400Hz, using Equation [6]. This will assess the influence of the volume of the cavity on the incoming noise source and any attenuated frequency.

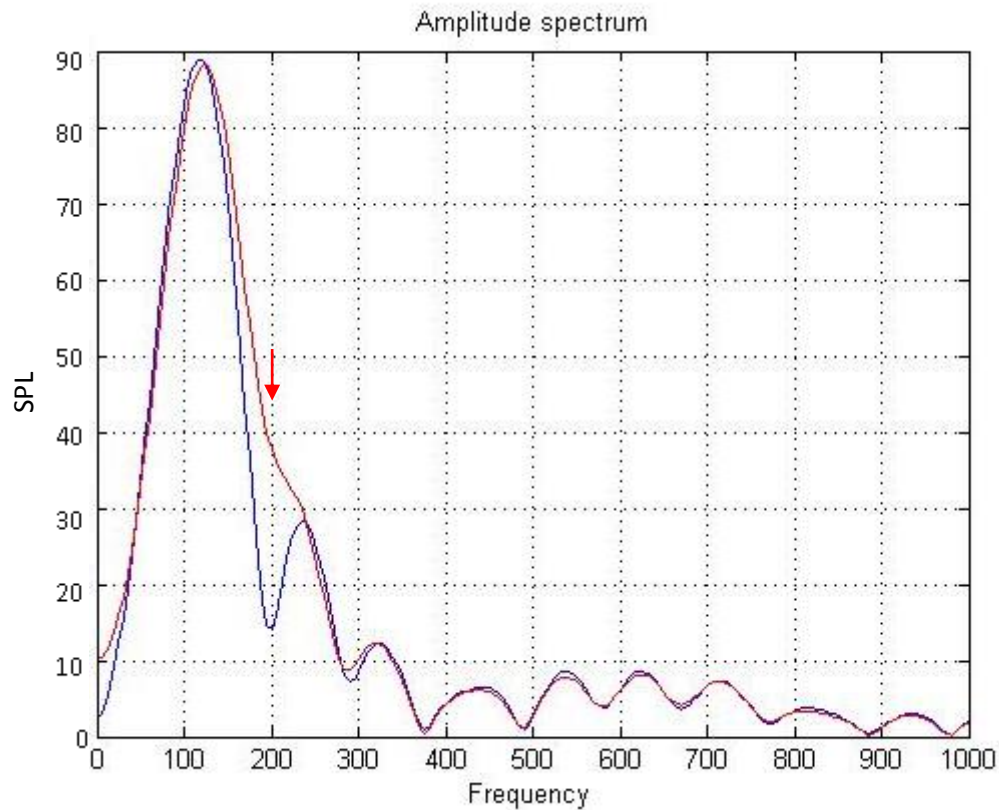


Figure 14: FFT comparison between inlet signal (red) and attenuated signal using a VVH resonator tuned to 200 Hz (blue). SPL (dB) against Frequency (Hz).

Figure 14 shows the results of the 200 Hz experiment. The red curve shows the amplitude spectrum without any resonator present and the blue curve with the resonator tuned to 200 Hz. It is shown that the spectrums overlay but with a clear attenuation at 200 Hz. Using Equation [22], the overall Insertion Loss is approximately 20 dB. As a conclusion, it can be said that the effect of the resonator on the input signal is clearly visible and the attenuation is exactly where it was expected.

Figure 15 shows an FFT plot of a modified inlet signal and an attenuated signal caused by a resonator tuned to 400 Hz. The modified inlet signal has a wider frequency spread to allow the attenuation by the resonator tuned to 400 Hz to be more clearly shown. The attenuation is created around 400 Hz which is again where it was calculated to be. Looking at the percentage of the attenuation on the initial signal for each measurement, for

both the 200Hz and 400 Hz resonator it decreases the pressure amplitude by at least 50% which, using Equation [22], this is an attenuation of 6 dB.

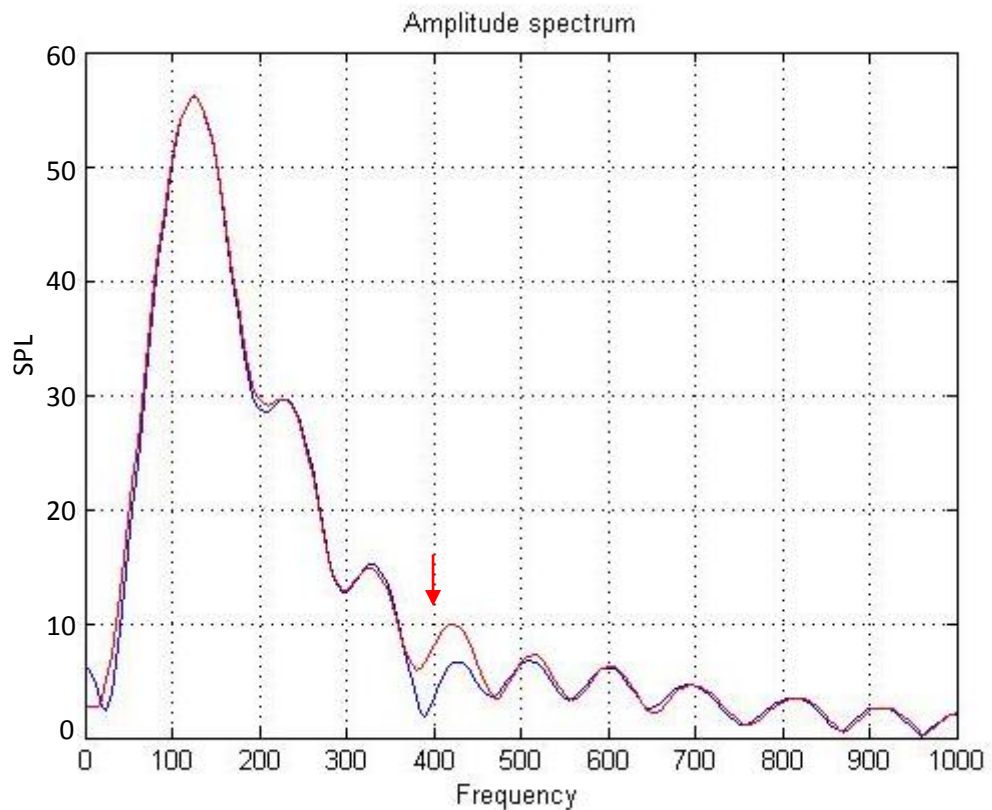


Figure 15: FFT comparison between modified inlet signal (red) and attenuated signal using a VVH resonator tuned to 400 Hz (blue). SPL (dB) against Frequency (Hz).

These experiments aim to show the major use of resonators and the effect of varying the volume of the resonator. The Helmholtz resonant frequency equation as stated in Section 1.4.1 (Equation [6]) was used to good effect (within 5% of resonant frequency) in calculating the volume required for each resonant frequency. As a conclusion, it has been shown that the attenuation properties of the resonators are substantial at their tuned frequencies whilst not having an effect on the rest of the signal. However, high frequency noise as a by-product is expected in some scenarios with grazing flow, as the premium automotive company is experiencing.

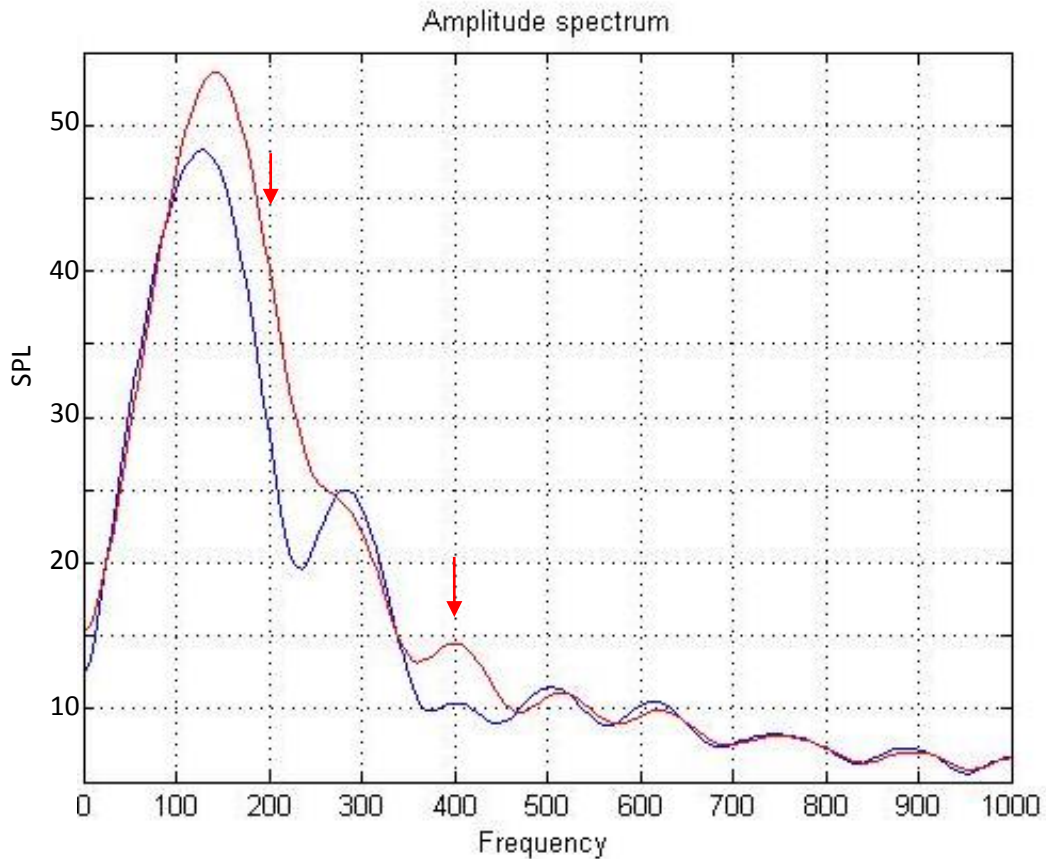


Figure 16: FFT comparison between modified inlet signal (red) and two VVH resonators simultaneously tuned to 200 Hz and 400 Hz (blue). SPL (dB) against Frequency (Hz).

Figure 16 shows an FFT plot of the modified inlet signal which again is used to show more clearly any attenuation of the signal at the outlet after passing two side-branch Helmholtz resonators 250 mm apart. The red line is the sound amplitude with respect to frequency when no resonators are present. The blue line is the sound amplitude with respect to frequency with two resonators connected in series, one tuned to  $\sim 200$  Hz and the other tuned to  $\sim 400$  Hz. As can be seen from the plot, attenuation of the noise source is created at around 200 Hz and 400 Hz proving that resonators can be run in series with minimal effect on each other. The location and order of the resonators does not appear to affect the attenuation properties. The plot broadly indicates the attenuation is of similar amplitude for both the 200 Hz resonator and 400 Hz resonator. Therefore it is possible to deduce that the resonators appear to be as efficient used in series as used singularly.

Overall, this section has shown the effect of varying the volume of the resonator on the attenuation properties on an incoming noise source. The Helmholtz resonator mechanism has been demonstrated experimentally, along with a correct theoretical

prediction of the attenuation. The location and order of more than one resonator along the length of a straight pipe is shown to have a negligible effect on attenuation performance. These experiments also help to validate the experiment set up and the equipment which will be used for the experiments in the forthcoming sections.

### **2.3 VVH Resonator Noise Generation Experiments**

From the literature and background sections, it is apparent resonators can produce noise as well as attenuate noise. The main aim of this thesis is to re-create the noise experienced by the premium automotive company and using a CFD tool, be able to predict the frequency and amplitude of the tone produced as several parameters are varied. Experiments are carried out to replicate this noise and to give a solid comparison from which to validate the CFD predictions. This section shows several experiments which attempt to create flow-generated noise using the VVH resonator as a side branch to the main pipe. Air flow via the fan shown in Figure 6 is provided for flow noise generation. Ultimately, a section of the automotive charge air cooler pipework known to produce unwanted tones will be flowed and modelled in CFD to analyse the effectiveness of the tool.

The VVH Resonator Noise Generation experiments include measurements across three microphones. For the VVH resonator, shown in Figure 17, the microphones are situated inside the resonator volume, upstream and downstream of the resonator neck. Acoustic measurements are also carried out with no resonator in place to provide a baseline comparison. The microphones are located as close as possible to the monitor points in the simulations, thus direct comparisons can be made. Experiments with this resonator are made to assess the effect of varying flow velocities and resonator volume on the frequency distribution. The flow velocity is varied between 20 m/s to 70 m/s in 10 m/s increments. The volume of the resonator is varied by adjusting the height of the piston. This is varied between 20 mm to 140 mm in 30 mm increments.

The geometries under test, along with their respective matrix of flow parameters are summarised in Table 1.

<b>Experiment</b>	<b>Resonator Type</b>	<b>Fundamental Resonant Frequency (Hz)</b>	<b>Flow Velocity (m/s)</b>	<b>Neck Protrusion</b>
Validation	VVH Resonator	200, 400	N/A	N/A
Noise Generation	VVH Resonator	215, 242, 284, 358, 460	20, 30, 40, 50, 60, 70	N/A
Neck Protrusion	QWT Resonator	343	30, 45, 60	0, 2.5, 5
Charge Air Cooler	CAC	9038, 4950	30, 45, 60	N/A

**Table 1: Summary of experiments - Geometries and flow parameters**

The experimental configuration is as described in the introduction to this chapter and the hardware is shown again in Figure 17. Each test is carried out 20 times. The raw pressure-time data is analysed to produce individual FFT's and then averaged to reduce background noise errors. Each test produces 20,000 samples to capture the wave forms accurately with a sampling rate of 100,000 Hz. The results are then examined in terms of Sound Pressure Level (SPL) in decibels as a function of Frequency (in Hz) for a given flow rate.

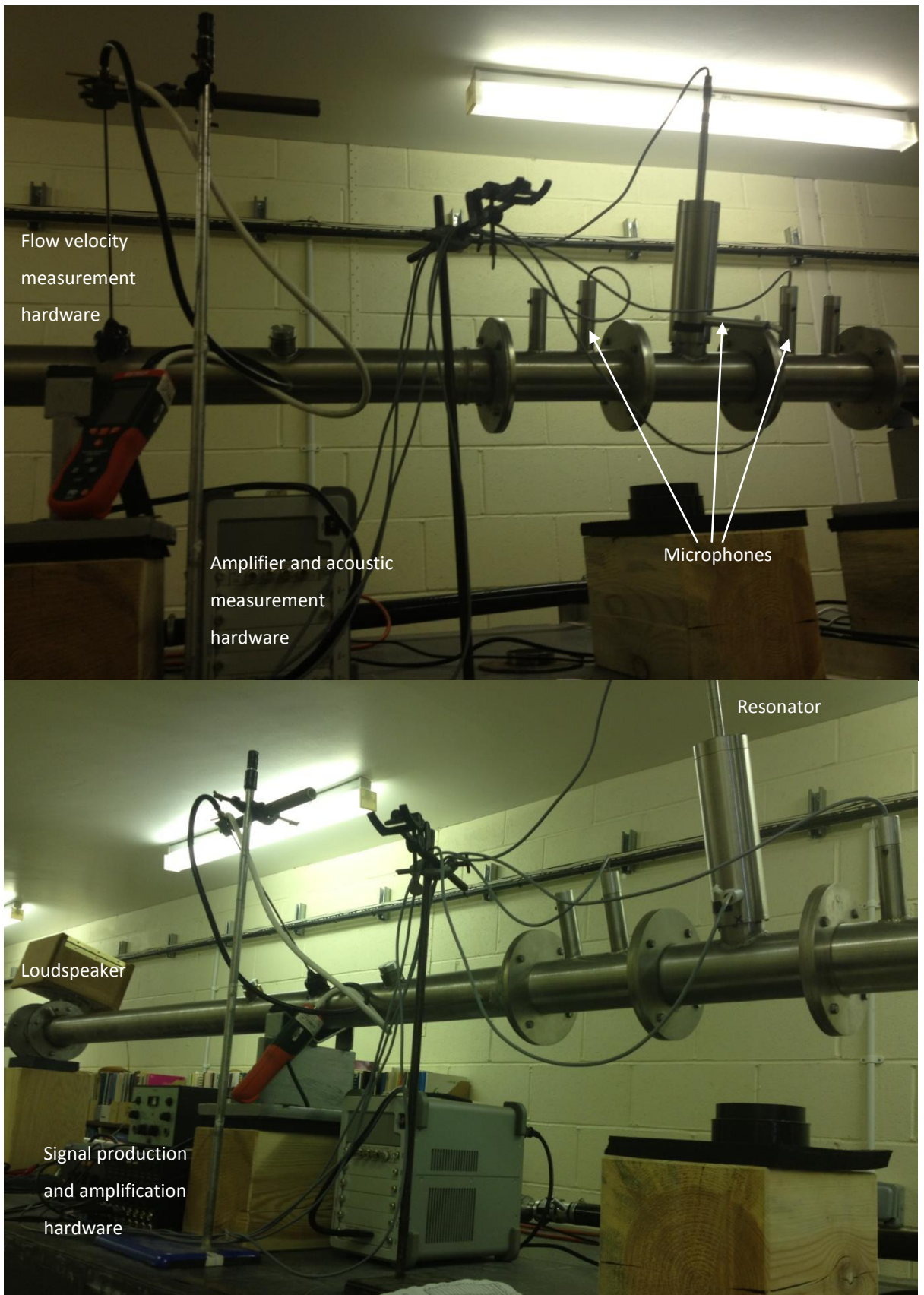
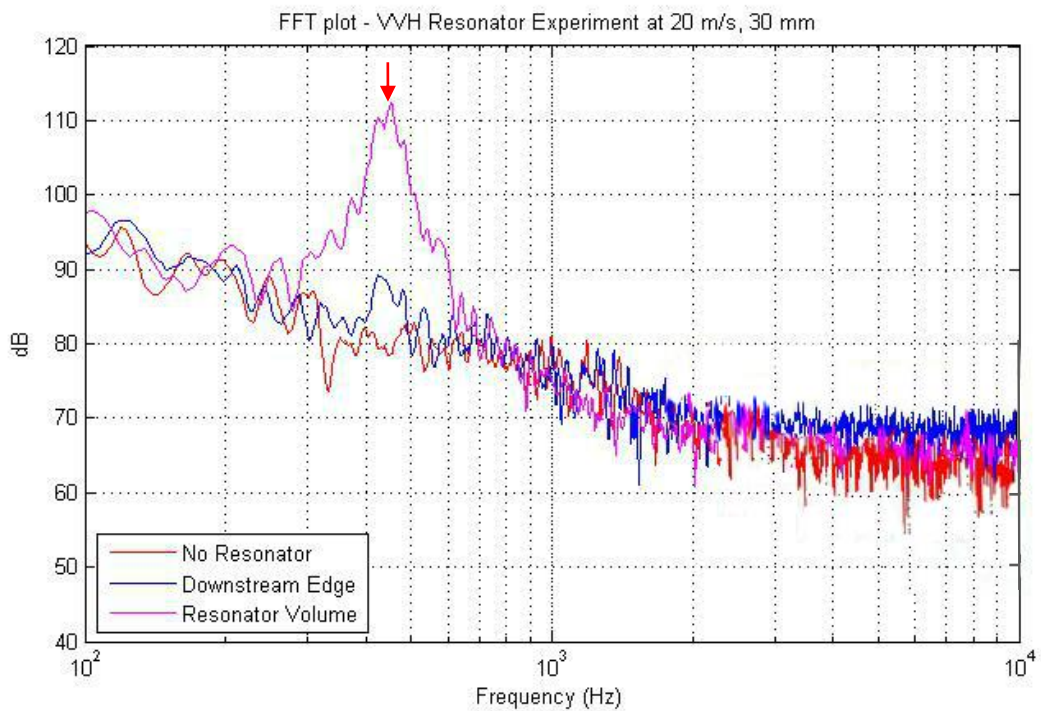


Figure 17: Resonator Noise Generation Experiment set-up. VVH Resonator with an upstream, a downstream and an internal volume microphone connected up to the amplifying hardware.

For the FFT plots, the data is presented in its raw form to preserve the very narrow-band frequency tones. Smoothing the data with a smoothing function may remove these tonal peaks from the plot. In this section, the FFT plots show Decibels (dB) against log frequency (Hz). The red line is the plotted data for the base line case, i.e. with no resonator present. The blue line shows the frequency distribution from the microphone situated immediately downstream of the resonator and the pink line shows the frequency distribution captured by the microphone inside the volume of the resonator as pictured in Figure 17.



**Figure 18: FFT plot – Experiment of VVH resonator tuned to 460 Hz and flow velocity of 20 m/s**

Loud tones are generated at specific resonator volumes and inflow velocities. Figure 18 shows the FFT plot of the experiment carried out with the VVH resonator tuned to approximately 460 Hz with a grazing mean flow of 20 m/s passing the resonator opening. The broadband noise, shown by the red line, is low-energy background noise contributed by the free-stream, the shear layer and turbulent fluctuations initiating from the flow from the fan. Most notable is a large peak within the resonator volume which appears to show a resonant frequency cavity tone. This fundamental resonant frequency of the resonator is predicted within 2% using Equation [6]. This is thought to be created from the acoustic resonances inside closed side-branches can couple with the shear layer instabilities at the opening of the resonator as described in the Introduction Section 1.5. Immediately

downstream of the resonator (blue line) is also showing propagation of the tone. This is signified by a 10 dB tone around the same frequency. The Strouhal number of this tone using Equation [15] is calculated to be 0.75. This is in a similar region to comparable studies considered in Chapter 1.

Further experiments with air flow are carried out in an attempt to create flow-generated noise by varying air flow rate and resonator length. Some combinations of resonator volume and flow velocity provided some interesting flow-generated noise and attenuation. With the exception of the example shown in Figure 18 which was a special case as described above, the majority of flow-generated noise from the resonator is produced at higher flow velocities. Results of the VVH Resonator experiments with an inflow velocity of 50, 60 and 70 m/s with varying resonator volumes are plotted below in Figure 19 through to Figure 30.

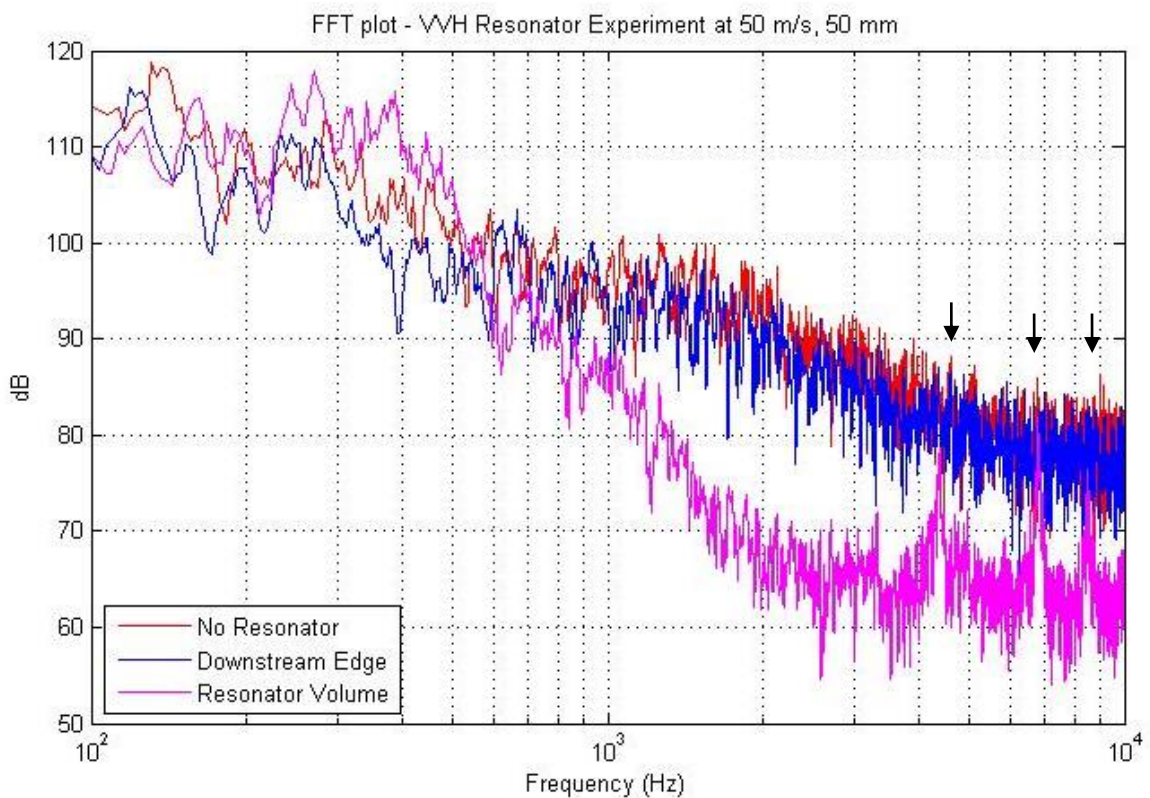


Figure 19: FFT plot - Experiment of VVH resonator tuned to 358 Hz and flow velocity of 50 m/s.

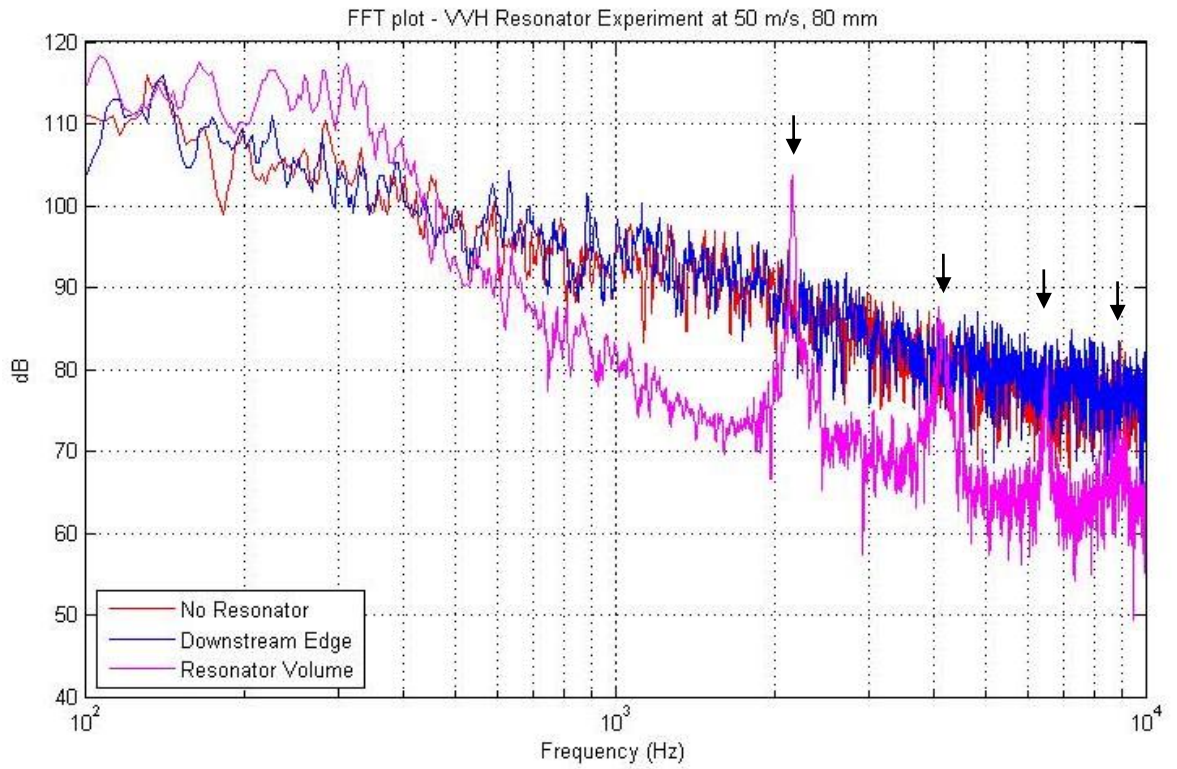


Figure 20: FFT plot - Experiment of VVH resonator tuned to 284 Hz and flow velocity of 50 m/s.

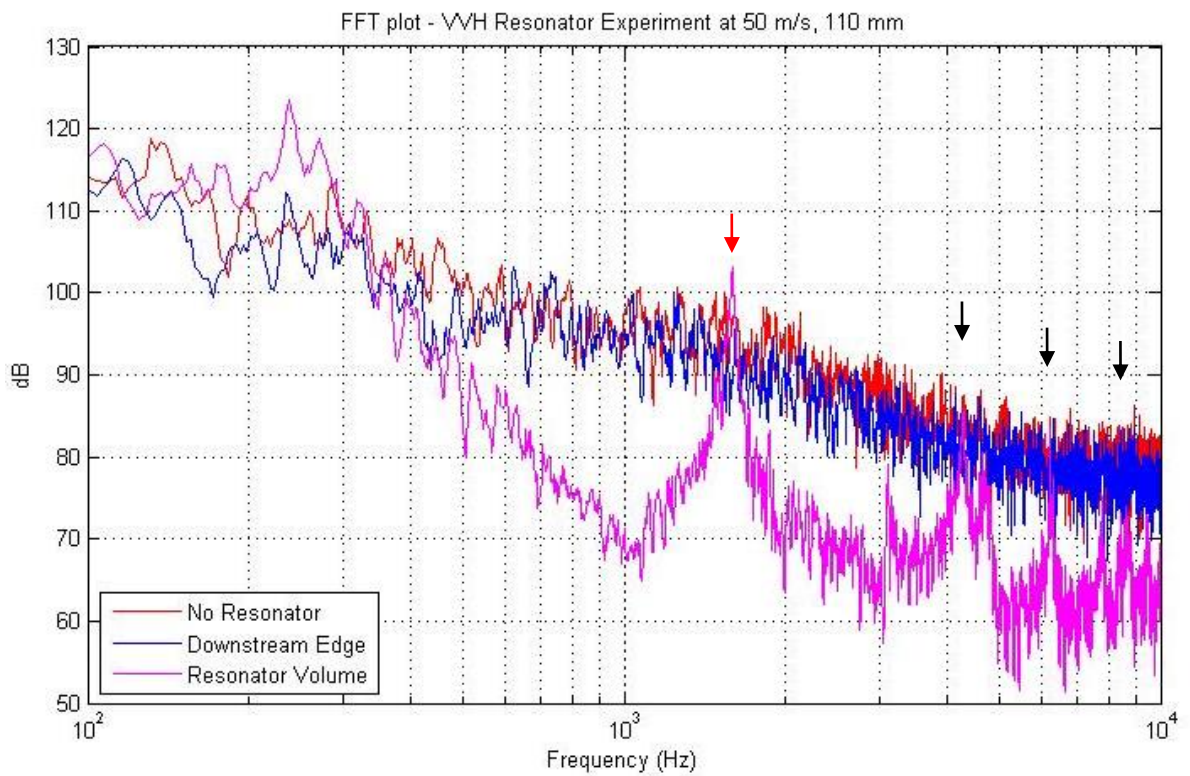


Figure 21: FFT plot - Experiment of VVH resonator tuned to 242 Hz and flow velocity of 50 m/s.

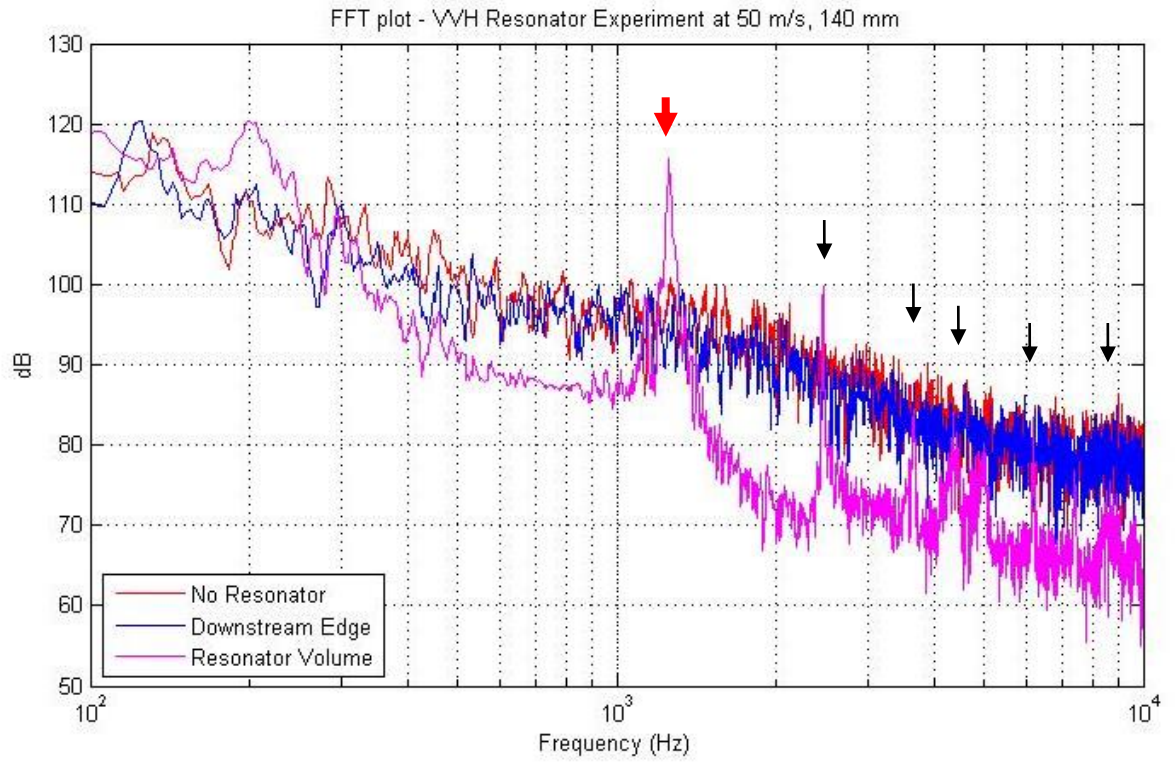


Figure 22: FFT plot - Experiment of VVH resonator tuned to 215 Hz and flow velocity of 50 m/s.

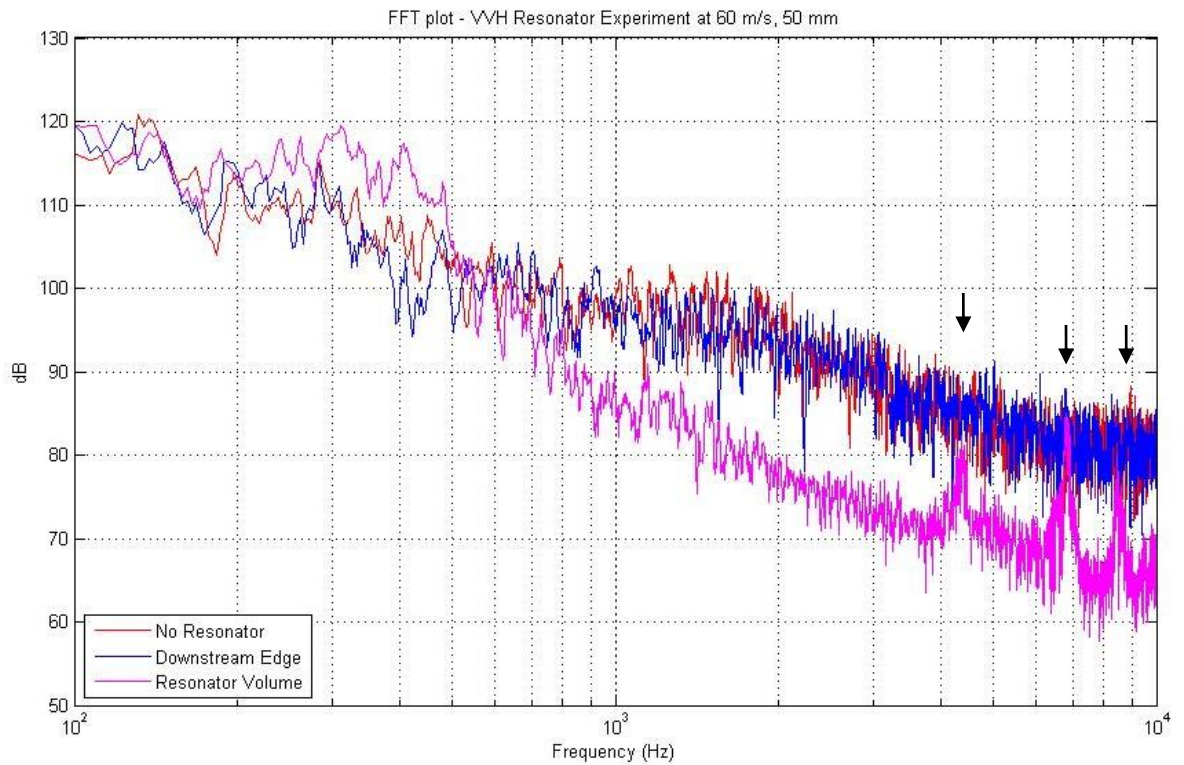


Figure 23: FFT plot - Experiment of VVH resonator tuned to 358 Hz and flow velocity of 60 m/s.

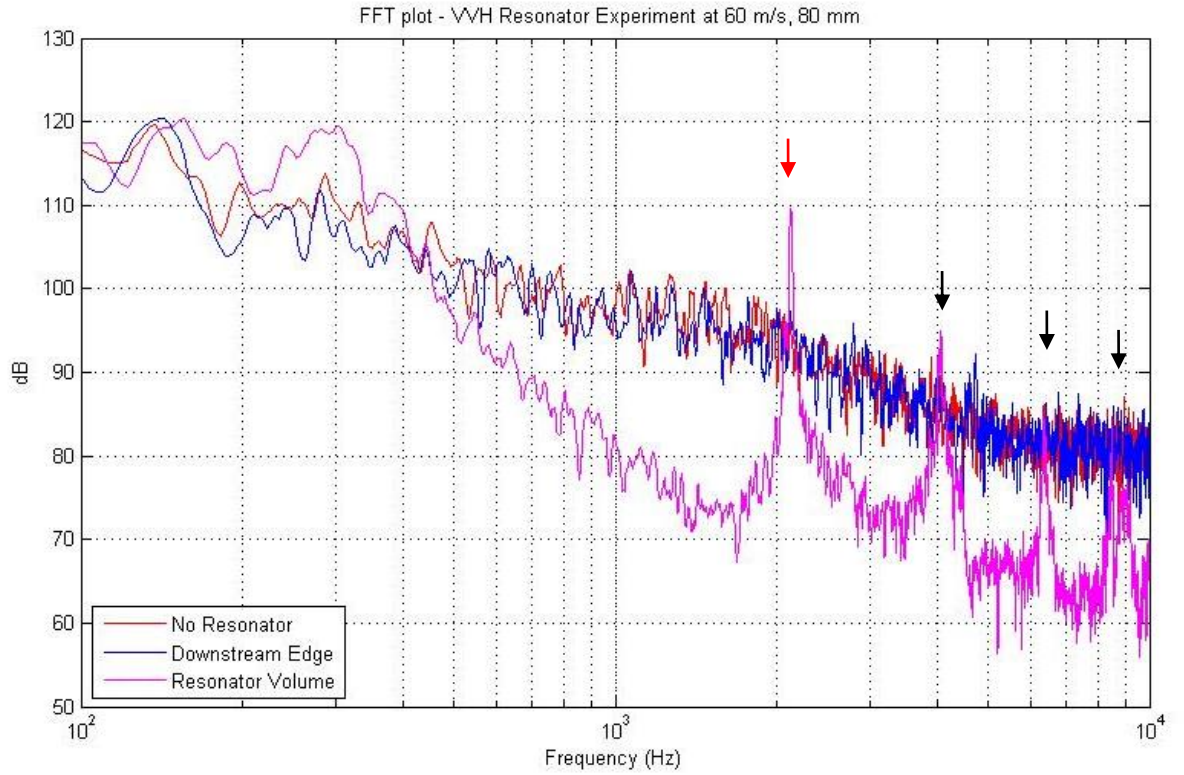


Figure 24: FFT plot - Experiment of VVH resonator tuned to 284 Hz and flow velocity of 60 m/s.

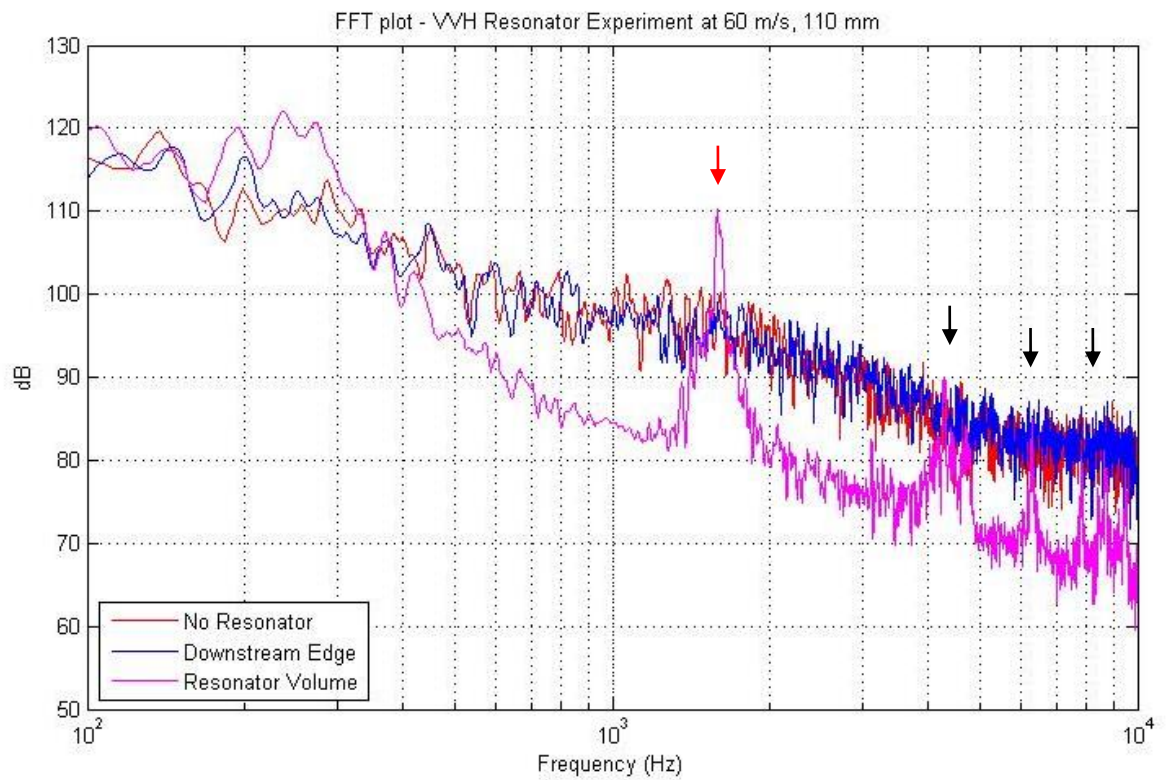


Figure 25: FFT plot - Experiment of VVH resonator tuned to 242 Hz and flow velocity of 60 m/s.

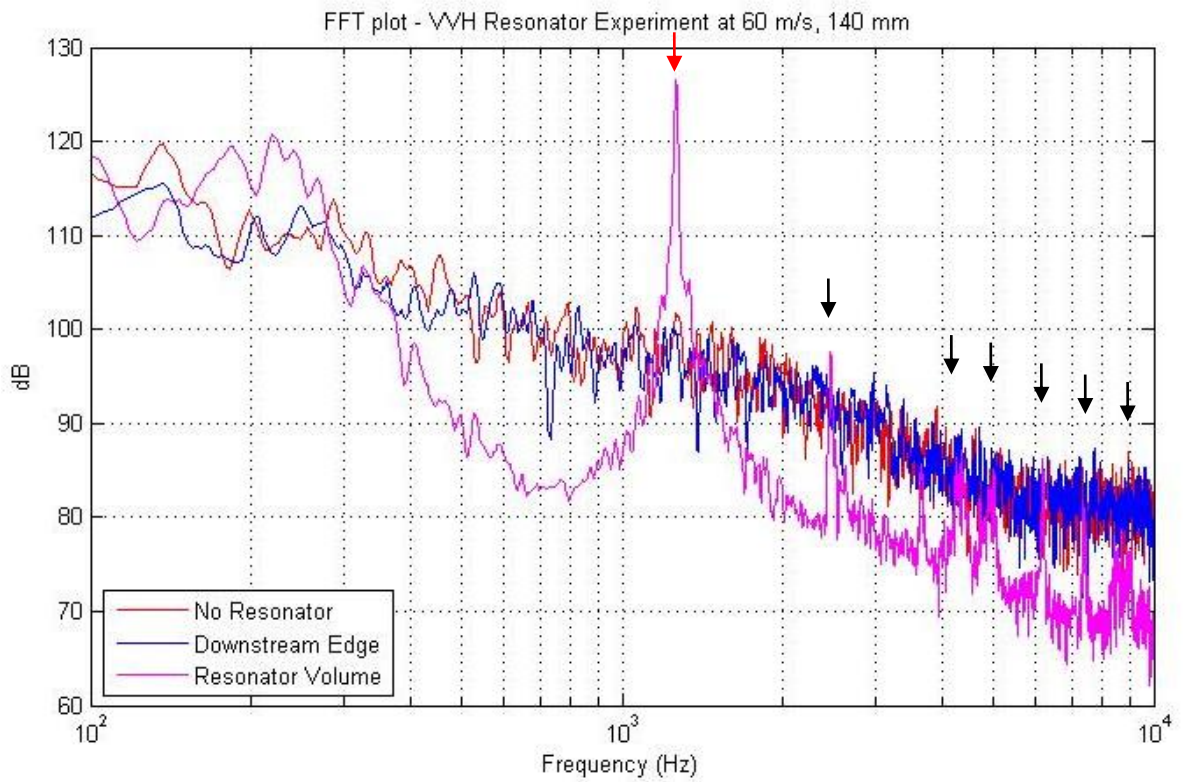


Figure 26: FFT plot - Experiment of VVH resonator tuned to 215 Hz and flow velocity of 60 m/s.

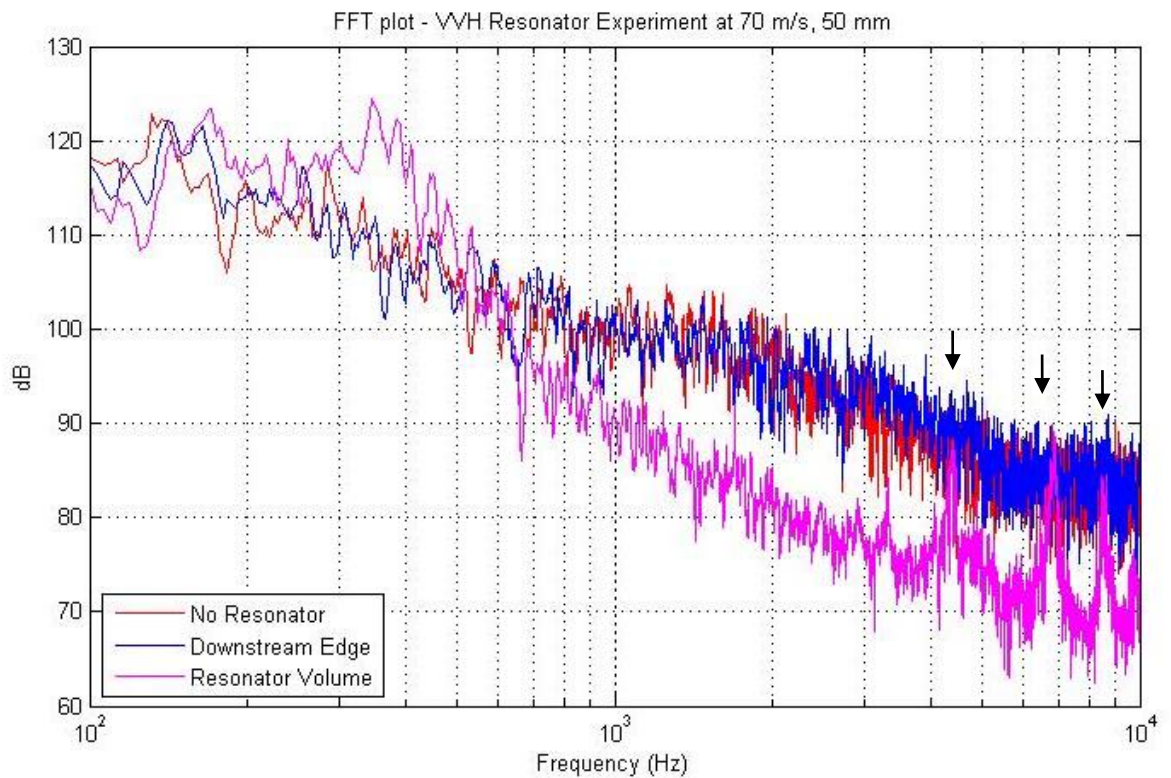


Figure 27: FFT plot - Experiment of VVH resonator tuned to 358 Hz and flow velocity of 70 m/s.

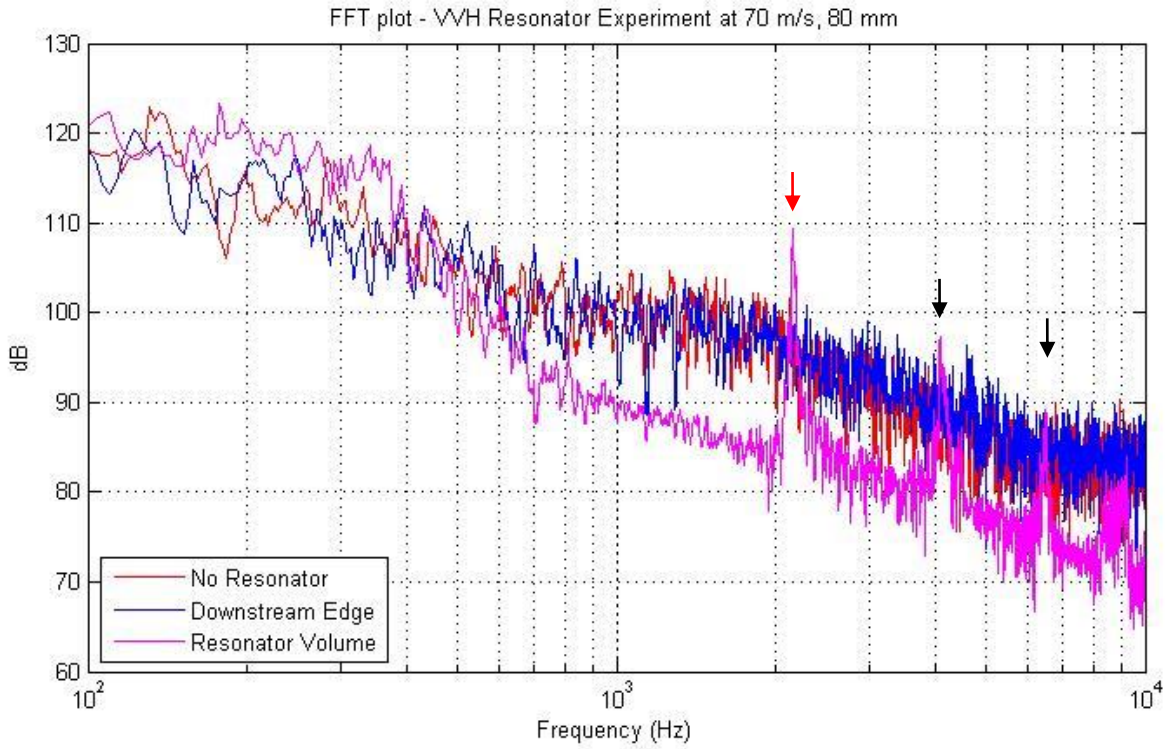


Figure 28; FFT plot - Experiment of VVH resonator tuned to 284 Hz and flow velocity of 70 m/s.

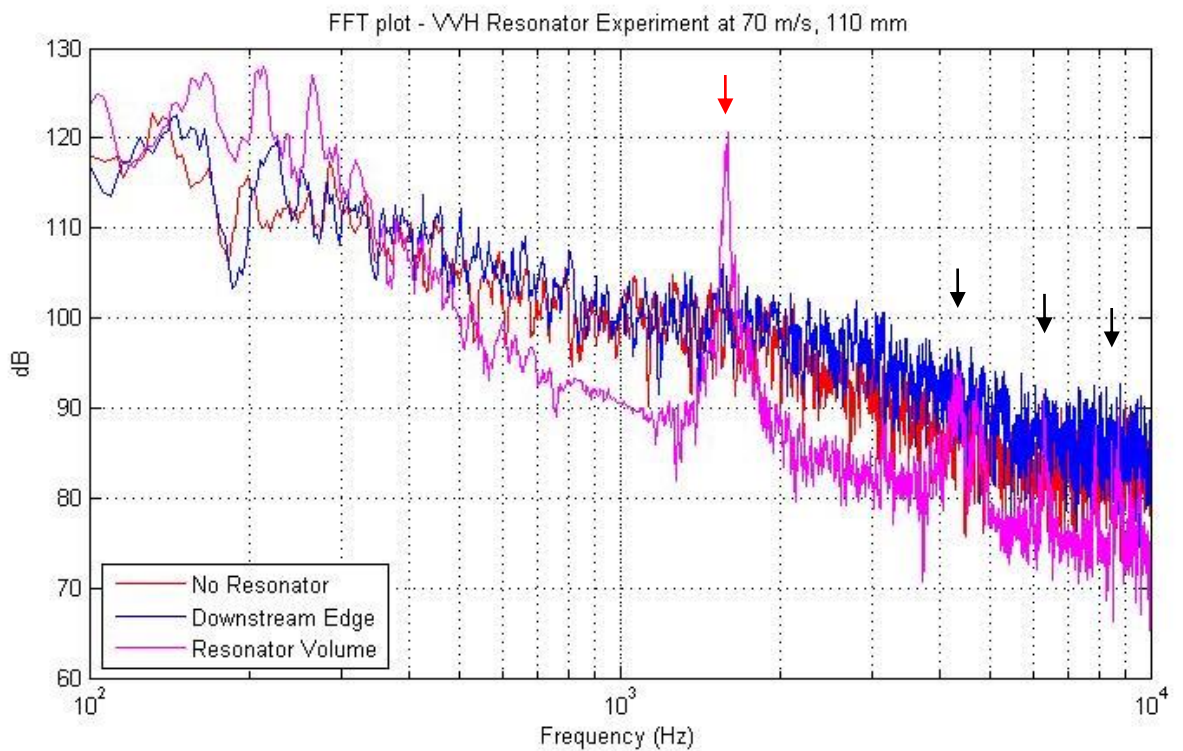


Figure 29: FFT plot - Experiment of VVH resonator tuned to 242 Hz and flow velocity of 70 m/s.

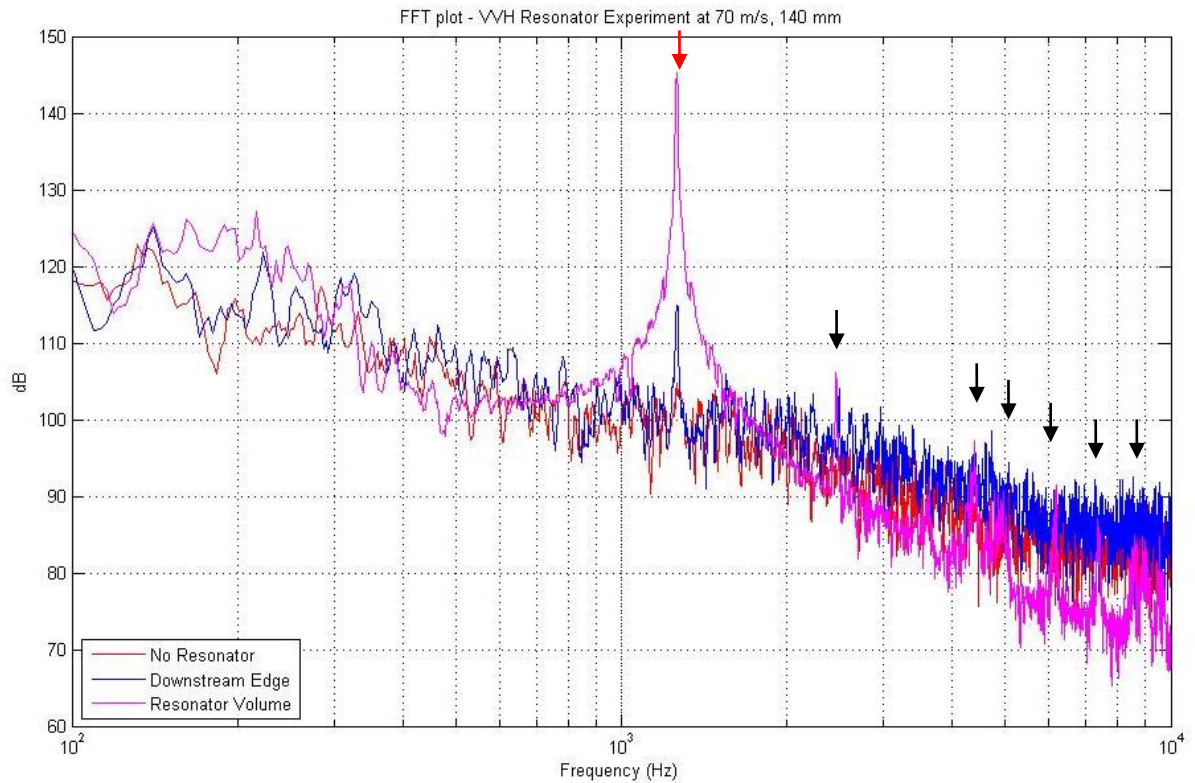


Figure 30: FFT plot - Experiment of VVH resonator tuned to 215 Hz and flow velocity of 70 m/s.

Clear tones are shown to be produced inside the volume of the resonator in the majority of combinations of in-flow velocity and resonator volumes tested. These tones tend to be stronger at higher velocities (50-70 m/s) depending on the resonator volume.

The most pronounced tone for each configuration is plotted in Figure 31. The results tend to show, as the resonator volume increases, the amplitude of the frequency peak inside the volume also increases. As the flow velocity increases, the frequency of the dominant tone does not significantly change. However these tones are not shown to be transmitted for downstream as indicated by the lack of disturbance in the frequency distribution from the Downstream Edge microphone. Tones are usually dissipated within the geometry but in two cases tested, shown in Figure 18 and Figure 30, tones are transmitted downstream. Figure 18 is explained towards the beginning of this section. The high amplitude tones apparent in Figure 30, as well as the remainder of the results plotted in Figure 31 are thought to be the result of a subtly different phenomenon as the high amplitude tone in this case is not the fundamental tuned resonant frequency. Also, as the noise is transmitted downstream, the pressure fluctuations or oscillations must be transmitted downstream. This is expected to be the formation of standing waves within the geometry as the wavelengths

are no longer significantly smaller than the characteristic length. See Section 1.4 for more information. The large pressure oscillations, in turn, create periodic vortices which are shed from the mouth of the resonator, particularly from the leading and trailing sharp edges of the resonator neck creating periodic disturbances in the bulk flow.

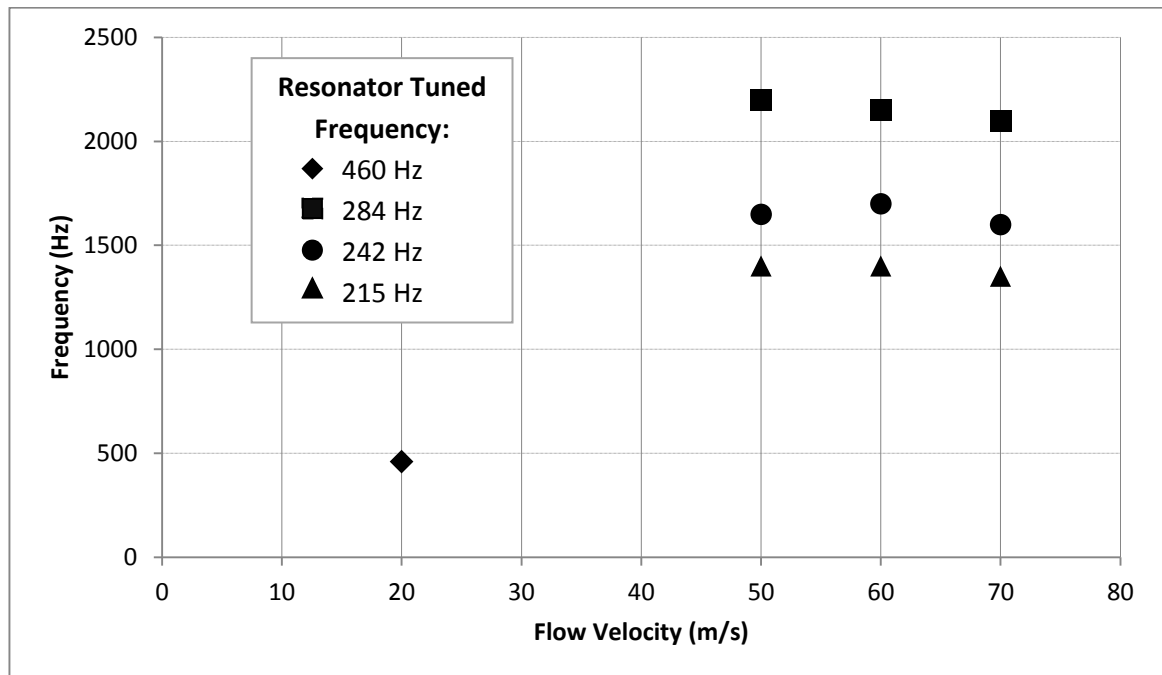


Figure 31: Dominant tone frequency (Hz) plotted against flow velocity (m/s) for various resonator piston heights (resonator volumes). 50 mm piston height configurations are not shown due to insignificant tones produced.

There is also further evidence to suggest the production of higher harmonic tones or frequency multiples on the fundamental or 1<sup>st</sup> harmonic tone. Clear examples of this can be seen in Figure 24 and Figure 28. Taking Figure 24 as an example, the Resonator Volume frequency distribution shows a large peak around 2- 2.1 KHz – 1<sup>st</sup> harmonic, a lower amplitude peak at around 4 KHz – 2<sup>nd</sup> harmonic, and a 3<sup>rd</sup> and 4<sup>th</sup> harmonic tone at 6 KHz and 8 KHz respectively. The fundamental or 1<sup>st</sup> harmonic tone is in fact a much lower frequency—that is the frequency at which the resonator is tuned to. In the 80 mm piston height case of Figure 24, the resonator is tuned to 284 Hz. There is a small peak as an indication of this looking at the Resonator Volume frequency distribution. Therefore it can be said the high amplitude tone at around 2 kHz is some frequency multiple of the fundamental resonant tone. The higher frequency tones are a multiple of this and any of the harmonic frequencies can become very high amplitude oscillations or tones with certain grazing flow conditions.

An experimental study by Pachebat et al (Pachebat, et al., 2008) was conducted by PSA, LEA, and Signal Development which looked at noise created by a door cavity. The acoustic results are displayed in Figure 32. The broadband fluctuations coming from the incoming turbulent boundary layer are passed over the cavity. An acoustic resonance is excited but a strong coupling with the flow, known as the Rossiter-type feedback mechanism is not visible. It is indeed clear from Figure 32 that the frequency peaks only increase slightly in frequency as the incoming velocity is increased, along with an increase in amplitude.

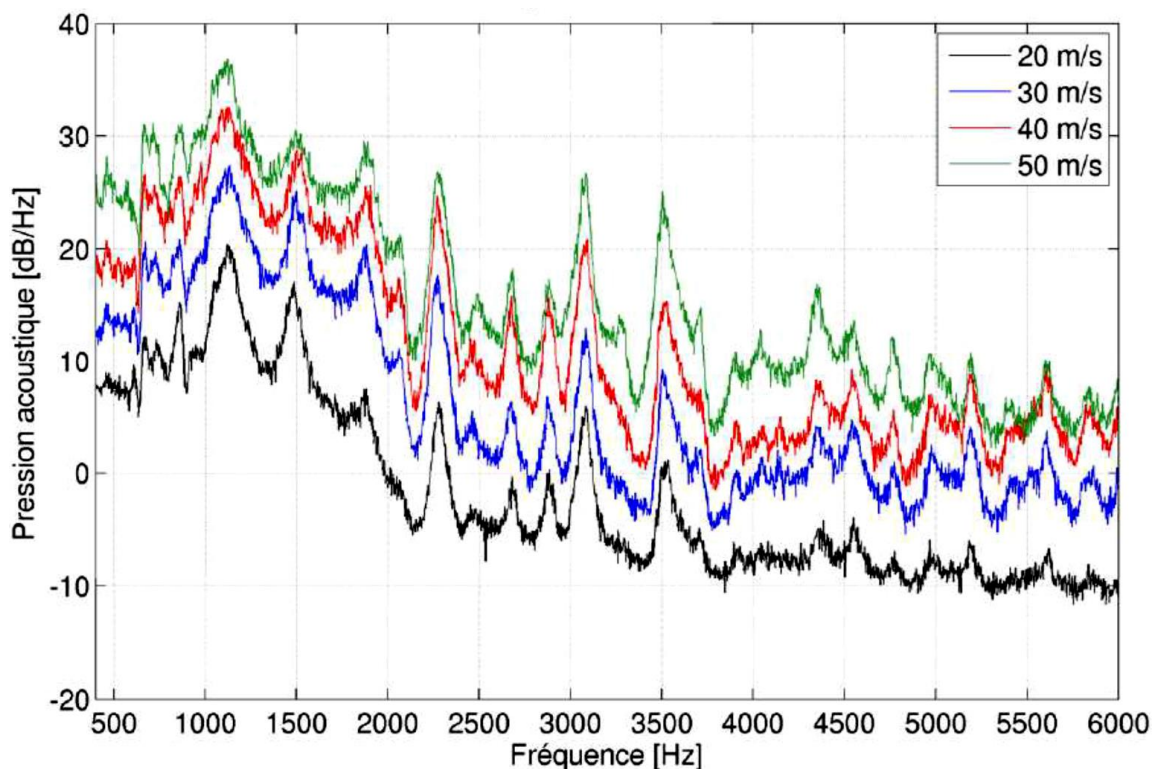


Figure 32: FFT plot showing response at the sensor door-gap and representing the vehicle interior as a function of the incoming flow velocity (Pachebat, et al., 2008).

The results from Pachebat's study shows several resonant frequency tones as found in this set of experiments. The instabilities in the air flow over the mouth of the cavity appears to excite the acoustic modes of the resonator which then couples with its resonant modes and results in self-sustained oscillations which transmit downstream through vortex shedding thus producing the acute tones. When the flow velocity is increased, the succeeding resonant modes are excited and the acoustic response of the system occurs at a specific range of a Strouhal number. A transfer from one to the next mode is gradual, so at some flow velocities two discrete frequency components appear in the sound spectrum. This

agrees with the findings from Jungowski’s work (Jungowski, et al., 1989) who observed QWT resonances at various harmonics.

The results from the VVH Resonator Noise Generation experiments are assessed against the theoretical Rossiter modal frequencies. The Rossiter modes are predicted using the Rossiter equation - Equation [16]. The predicted Rossiter modes for the VVH geometries are compared with the dominant tones from the experiment results. The results are summarised in Table 2.

Resonator Tuned Frequency (Hz)	Velocity (m/s)	Experiment Tone (Hz)	Predicted Rossiter Tone (Hz)	Difference (Hz)	Harmonic Mode
284	50	1410	1482	-72	4
242	50	1680	1723	-43	5
215	50	2220	2207	13	6
284	60	1400	1408	-8	4
242	60	1720	1784	-64	5
215	60	2150	2159	-9	6
284	70	1350	1363	-13	4
242	70	1600	1712	-112	5
215	70	2100	2091	9	6

**Table 2: VVH Resonator Noise Generation Experiments with predicted Rossiter modes**

The predicted 4<sup>th</sup>, 5<sup>th</sup> and 6<sup>th</sup> Harmonic Rossiter tones correlate to within 6.5% of the dominant tone for each VVH experiment. This suggests the Rossiter mechanism is indeed the primary cause of the high frequency, large amplitude tones which are generated by flow past the VVH resonator.

Further investigations into vortex shedding from the neck area will be carried out in the following chapter sections, as this is an interesting area of study for the high frequency unwanted noise the premium automotive company is experiencing.

Overall, a general trend has emerged from the tests. The resonator has a considerable effect on the fluid flow and the acoustic profile within. It is clear to see, as the resonator volume is increased, the large peak in the frequency distribution for the internal volume shifts to a lower frequency value. This occurs for all velocities shown. What is also clear from the experiments is the peak increases in amplitude as the flow rate is increased.

From this set of experiments which have attempted to create flow-generated noise using a resonator as a side branch to the main pipe, interesting results have been obtained. These experiment examples show that by varying volume and flow rate, several tones can be produced including the 460 Hz tone investigated earlier shown in Figure 18. To further

investigate the vortex shedding phenomenon thought to be happening across the resonator neck, the following section of this chapter will analyse the influence the neck edge of a simple Quarter Wave Tube has upon the acoustic field in a pipe. The interference between the main pipe and the resonator appear to be of great interest in terms of how it can affect the acoustic field downstream of this area. A great deal of work has been carried out to attenuate flow coupled resonance, as shown in Sections 1.5 and 1.6. Solutions to this resonance include leading edge spoilers, chamfered edges, trailing edge spoilers and active noise attenuation. This thesis will focus on shear tones which induce vortex shedding – their production and attenuation. The following section will therefore focus on the neck area of a side branch Quarter Wave Tube which is a special case of a resonator.

## 2.4 QWT Protrusion Experiments

Experiments with a cylindrical Quarter Wave Tube (QWT) test section are carried out. QWT theory and their uses are described Section 1.4.2. Experiments with the QWT comprises of the flow rate being varied as well as the neck protrusion length into the flow being adjusted. Neck protrusion lengths of 0 mm (flush to the main pipe), 2.5 mm and 5 mm at flow velocities of 20 m/s, 30 m/s, 40 m/s, 50 m/s, 60 m/s and 70 m/s are chosen. From the literature reviews carried out in the Section 1, sharp edges, particularly with joints to a T-section can cause the flow to split and create fluctuations initiating from these sharp edges. These fluctuations can eventually roll up and form vortices which are shed and can be transmitted downstream, also affecting the upstream flow. A series or a pattern of vortices can be set up which forms an acoustic resonance response. To investigate this phenomena which is thought to be a cause of tones created in automotive pipe work, the neck of the QWT is protruded into the flow to assess the effect the increasingly large sharp edges will have upon the acoustic flow field upstream and downstream of the QWT.

Work done by Tang, et al (Tang & Rockwell, 1983), indicated that the addition of a small radius to the rear edge drastically reduces the shedding vorticity from the front edge. A rear edge ramp at a lower height than the front edge (compared to a curve or sharp edge) produced the most attenuation. Additionally having ramps at both front and rear edge completely removed the tonal peaks from shallow cavity resonance, but increased broadband noise slightly. Rear edge ramps/lips and front edge spoilers/deflectors have all

been used in the literature in order to achieve effective suppression of tonal noise. Therefore, the shape of the QWT neck area has been deduced to be an excellent area to investigate, with a view to correlate these findings with CFD simulations.

The QWT is shown in Figure 33 below.  $L$ , the length of the QWT is 254 mm and  $D$ , the diameter is 40 mm. Using Equation [11] from Section 1.4.2, the fundamental resonant frequency of the QWT is calculated to be 343 Hz.

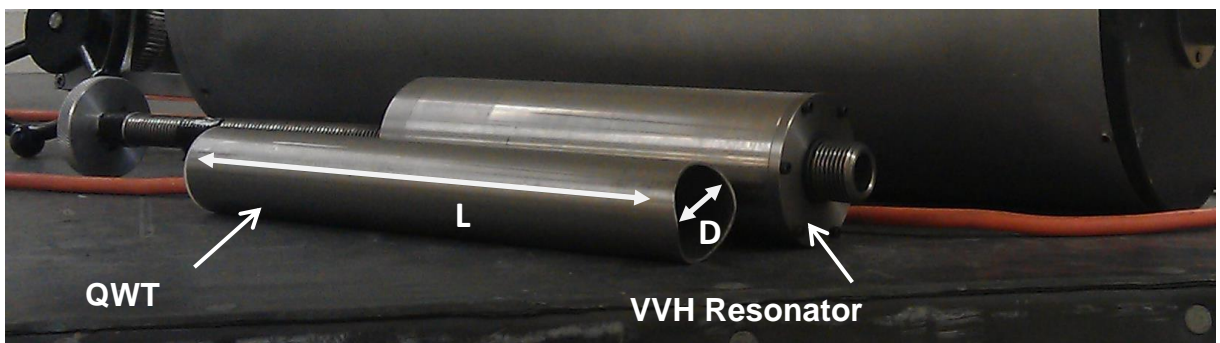


Figure 33: A photograph showing the QWT and Variable Volume Helmholtz Resonator

Two microphones are situated either side (upstream and downstream) of the QWT approximately 250 mm away. Figure 34 shows the microphone ports either side of the resonator port and the resonator neck port itself in the centre, fitted with a bung.

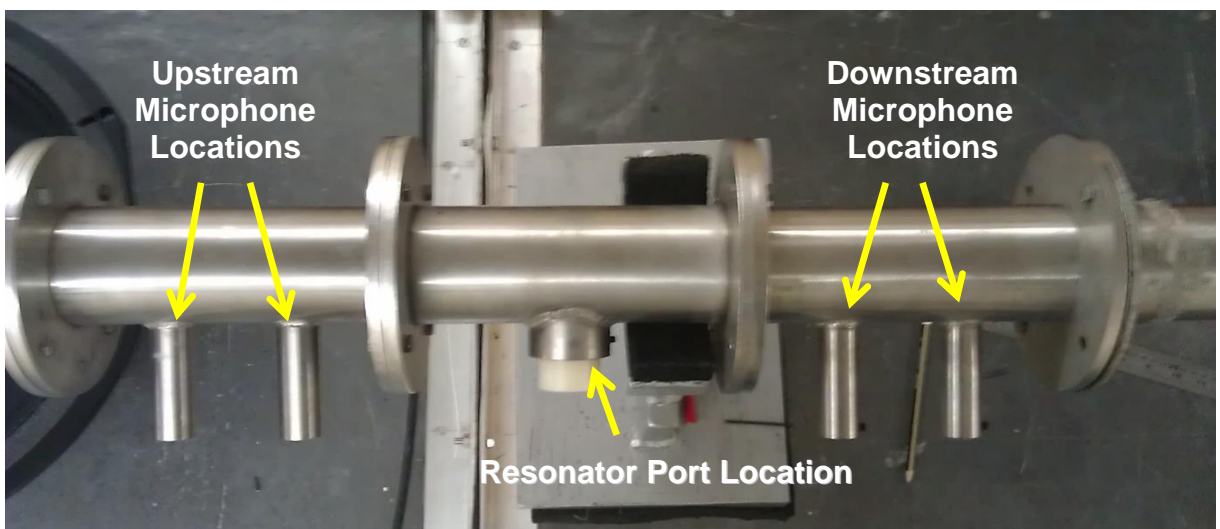


Figure 34: Experiment configuration showing upstream and downstream microphone locations as well as the resonator port in the centre of the photograph

Each experiment utilises two Brüel & Kjaer ¼" microphones (see Section 2.1 for details) – one upstream of the leading edge of the QWT and one downstream approximately 150 mm away from the trailing edge of the QWT. Monitor points are located in positions to replicate the simulations - see Figure 112, thus direct comparisons can be made. The QWT can be inserted into the port and fixed by a grub screw located on the side of the port as shown in Figure 34. This allows the position of the QWT to be accurately placed in the vertical direction whilst maintaining a good air seal join to the main duct. The open end of the QWT is shaped to the profile of the main duct and the QWT is maintained at zero degrees to the incoming flow direction. The experimental hardware and software configuration is as described in Section 2.1.

The QWT is protruded into the main duct by three lengths and each length is tested at two flow velocities of 30 m/s and 60 m/s. The QWT is placed flush to the main duct (0 mm protrusion) to create a sharp 90° edge. It is also tested with a 2.5 mm and 5 mm protrusion into the main duct to create a sharp protruding lip. This lip attempts to replicate a welded joint which is often the case, particularly in automotive exhaust systems. Figure 35, Figure 36 and Figure 37 shows FFT plots of mean flow air velocity of 30 m/s passing a Quarter Wave Tube (QWT) with the neck of the QWT protruding into the main flow by 0 mm, 2.5 mm and 5 mm respectively. For all FFT plots shown in this section, the vertical axis is the amplitude (SPL) measured in decibels and the horizontal axis is the logarithmic frequency measured in Hertz. The blue line represents the frequency spectrum near the upstream edge of the QWT. The red line represents the frequency spectrum near the downstream edge of the QWT. The green line represents the frequency spectrum with no QWT present, i.e. a straight pipe at the same location as the downstream edge monitor. The black arrows highlight the frequency at which the main tones are produced for each configuration.

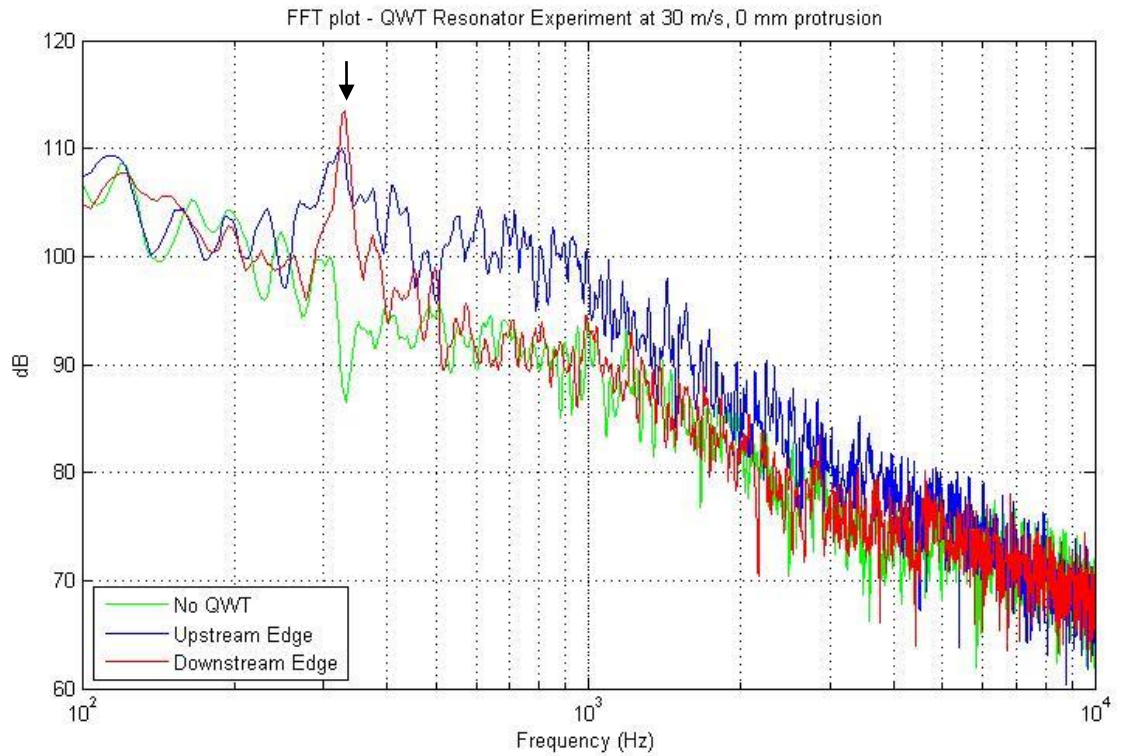


Figure 35: FFT plot showing three monitor locations at a flow velocity of 30 m/s and a Quarter Wave Tube protrusion of 0 mm

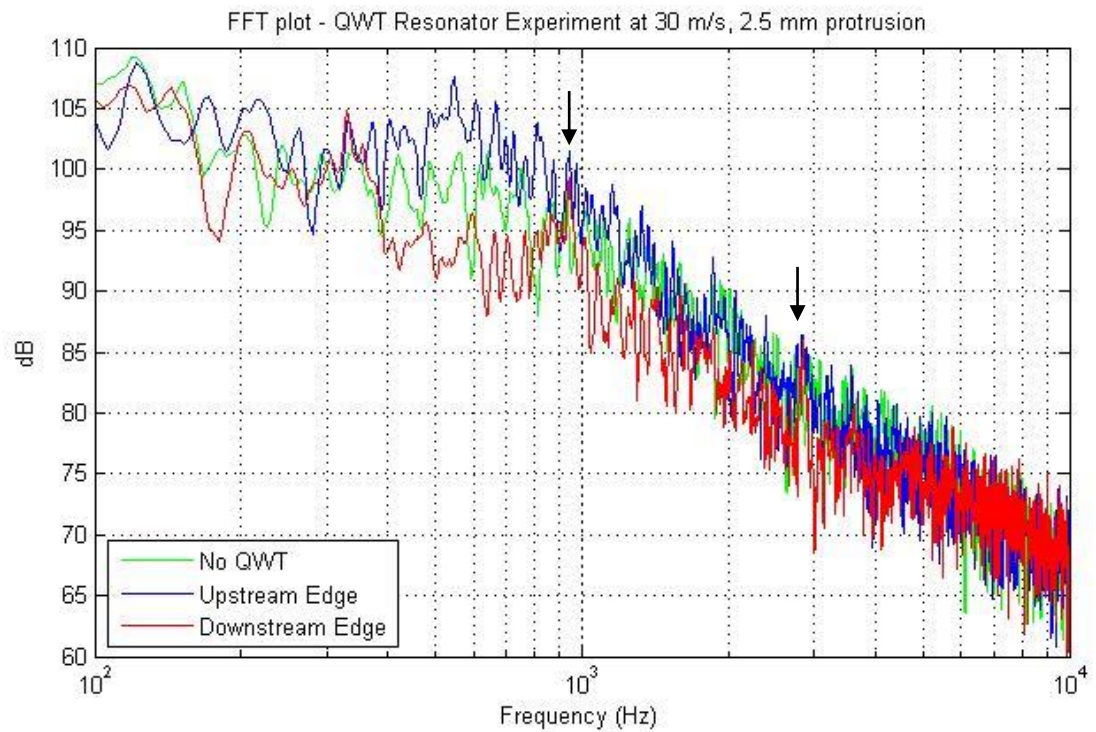
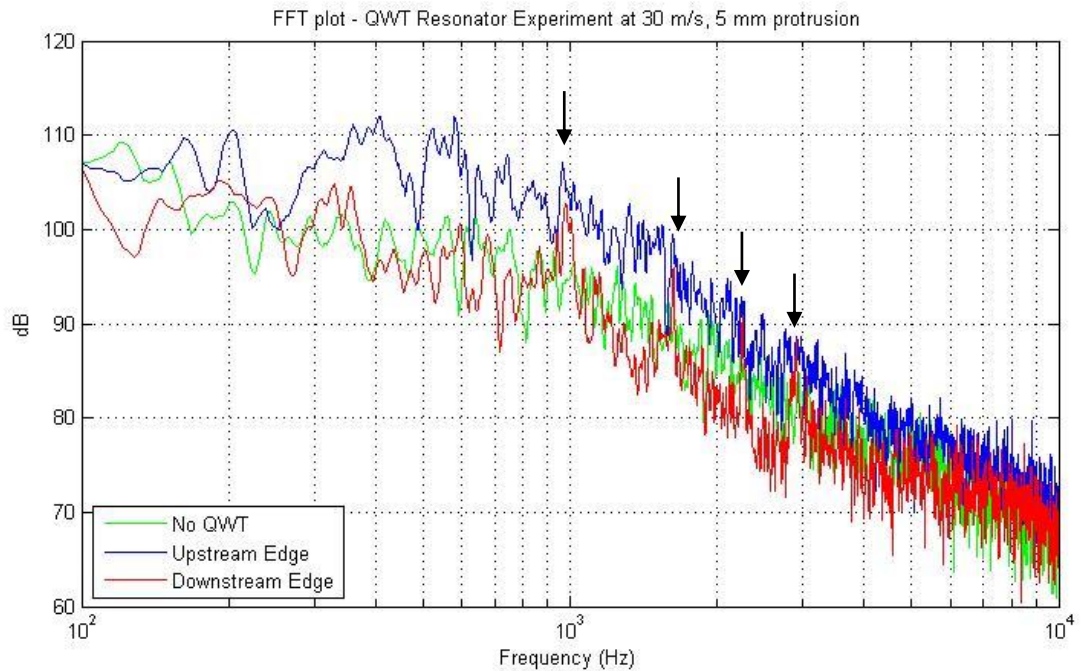
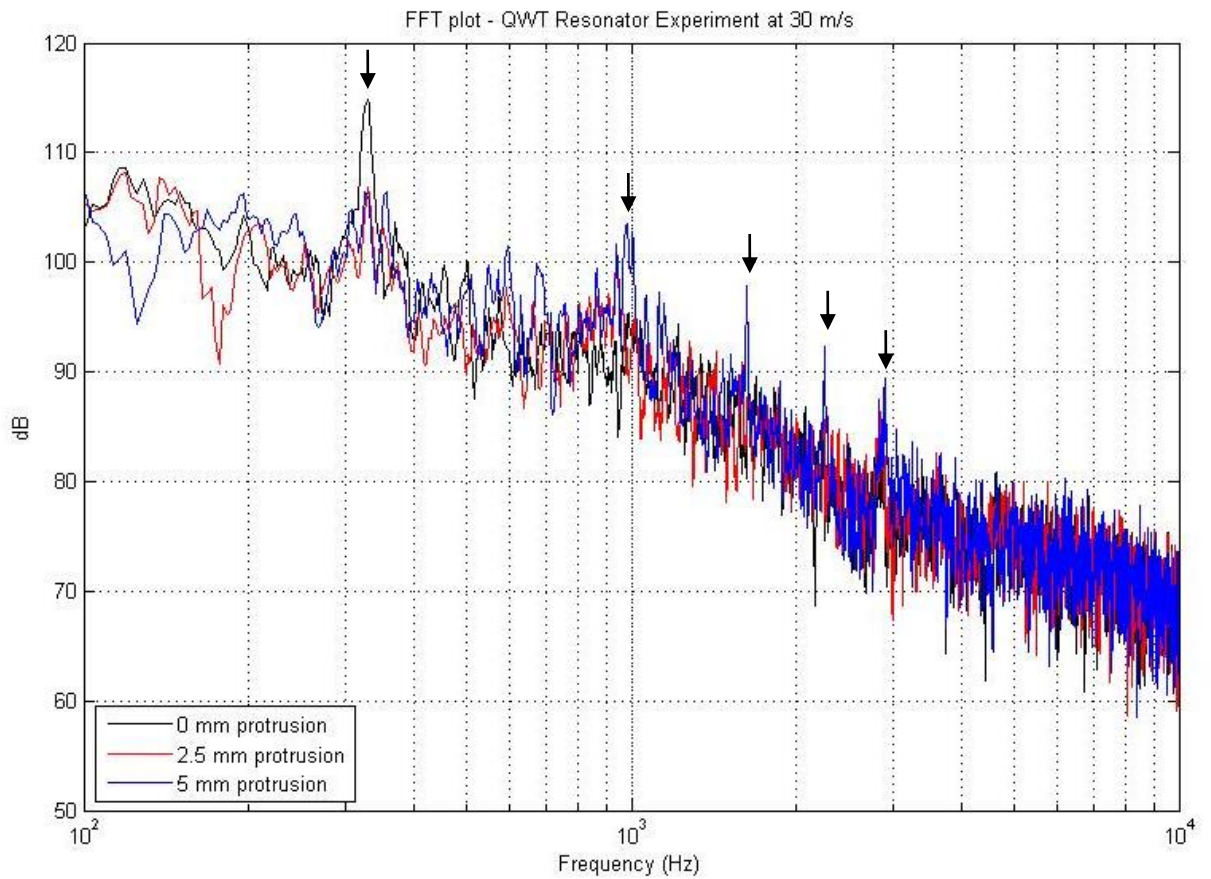


Figure 36: FFT plot showing three monitor locations at a flow velocity of 30 m/s and a Quarter Wave Tube protrusion of 2.5 mm



**Figure 37: FFT plot showing three monitor locations at a flow velocity of 30 m/s and a Quarter Wave Tube protrusion of 5 mm**

As expected, the Upstream Edge microphone captures higher mean SPL compared to the microphone port further downstream with and without the QWT (red and green lines respectively). This is due to the natural pressure loss between the two locations. For the 0 mm protrusion case (Figure 35), a small peak of around 15 dB is present with 0 mm protrusion at around 350-400 Hz with the QWT in place. This is the natural resonating frequency of the QWT. Although not easily visible in the plots, Figure 38 shows higher frequency tones are present at the downstream edge monitor point with the 2.5 and 5 mm protrusion lengths shown in Figure 36 and Figure 37. The tones have frequencies of approximately 950 Hz, 1600 Hz, 2250 Hz and 2900 Hz and are approximately 10-15 dB higher than the mean dB values. Again, as found with the VVH Resonator, see Section 2.3, these higher frequency tones appear to be equally spaced frequency multiples, possibly related to the fundamental QWT resonant frequency tone. Figure 38 also shows a small increase in amplitude (2-3 dB) for the higher frequency tones as the protrusion into the main duct is increased.



**Figure 38: FFT plot showing frequency distributions at the downstream monitor location for three protrusions at 30 m/s**

Figure 39, Figure 40 and Figure 41 shows FFT plots of mean flow air velocity of 60 m/s passing a Quarter Wave Tube (QWT) with the neck of the QWT protruding into the main flow by 0 mm, 2.5 mm and 5 mm respectively.

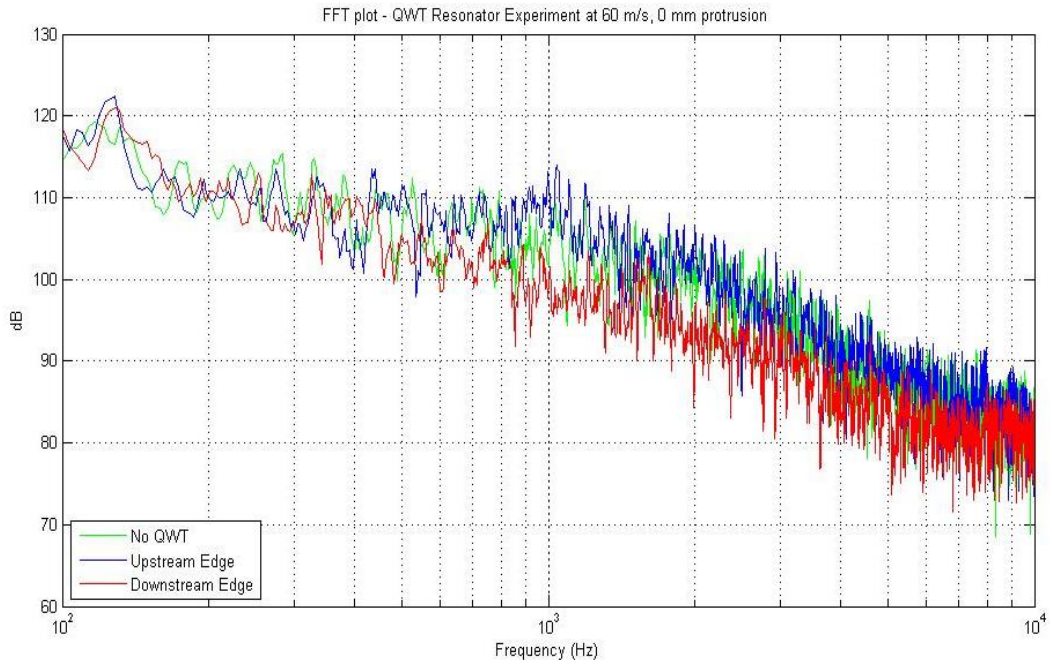


Figure 39: FFT plot showing three monitor locations at a flow velocity of 60 m/s and a Quarter Wave Tube protrusion of 0 mm

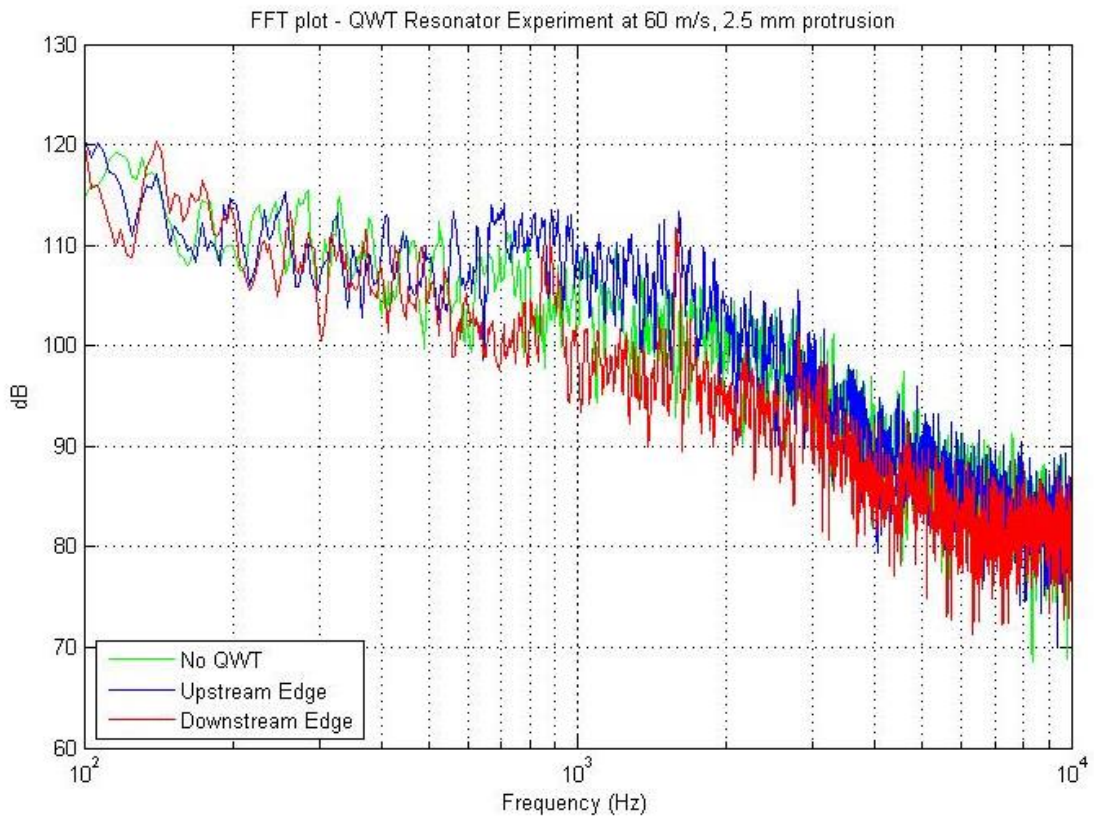
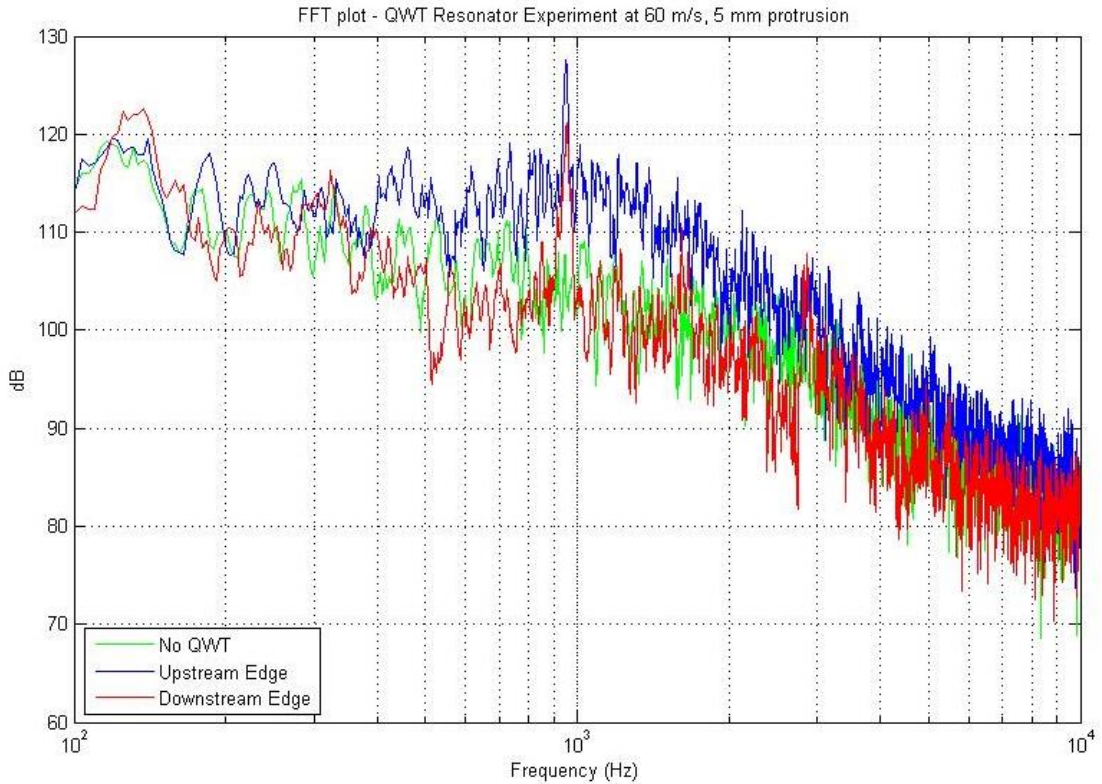


Figure 40: FFT plot showing three monitor locations at a flow velocity of 60 m/s and a Quarter Wave Tube protrusion of 2.5 mm



**Figure 41: FFT plot showing three monitor locations at a flow velocity of 60 m/s and a Quarter Wave Tube Protrusion of 5 mm**

For the 60 m/s cases, no tone is produced at the QWT's fundamental resonant frequency (343 Hz). However, as the protrusion length is increased, tones of similar frequencies to the 30 m/s cases start to be produced. This is particularly clear with the 5 mm protrusion case given in Figure 41. High amplitude noise, approximately 15-20 dB higher than the mean dB value is created around 950 Hz. It is present on the downstream edge and upstream edge of the QWT which suggests the pressure fluctuations are transmitted upstream as well as downstream.

Figure 42 shows an FFT plot of the Downstream Edge frequency distributions for the 60 m/s QWT cases protruding into the main flow by 0 mm, 2.5 mm and 5 mm respectively.

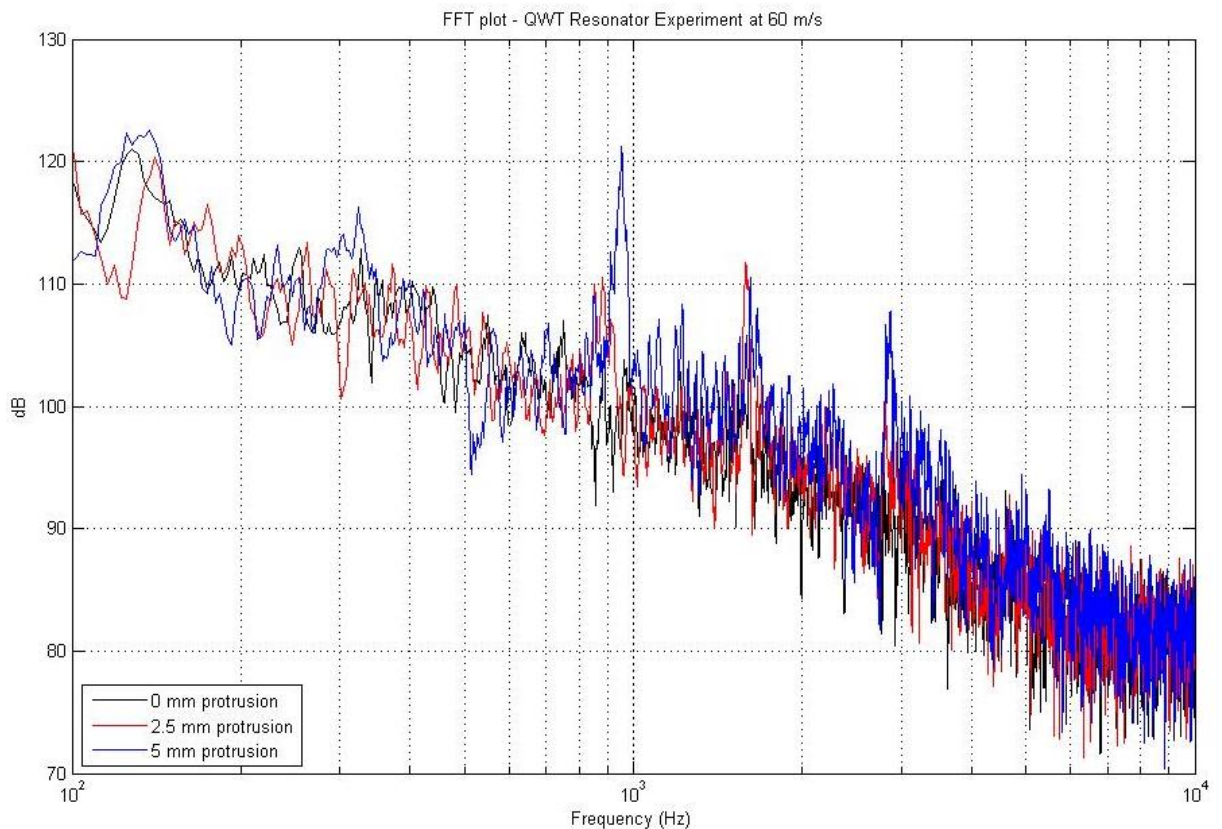


**Figure 42: FFT plot showing frequency distributions at the downstream monitor location for three protrusions at 60 m/s**

Figure 42 clearly demonstrates how, in general, as the protrusion length increases, the amplitude of the tones (signified by the peaks) increase. Again, the amplitude between each harmonic tone varies due to the inherent random nature of the flow. Therefore, the most dominant tone tends to change with differing conditions. It is also interesting to note that as the protrusion length increases, the high amplitude peaks increase in frequency. For example, the tone around 850 Hz for the 0 mm protrusion case (black line) has increased in frequency to approximately 950 Hz with the larger 5 mm protrusion signified by the blue line.

The largest protrusion length, 5 mm is compared at the two flow velocities tested in Figure 43. The FFT plot gives the frequency distribution at the Downstream Edge microphone location for both 30 m/s (blue line) and 60 m/s (red line) cases.

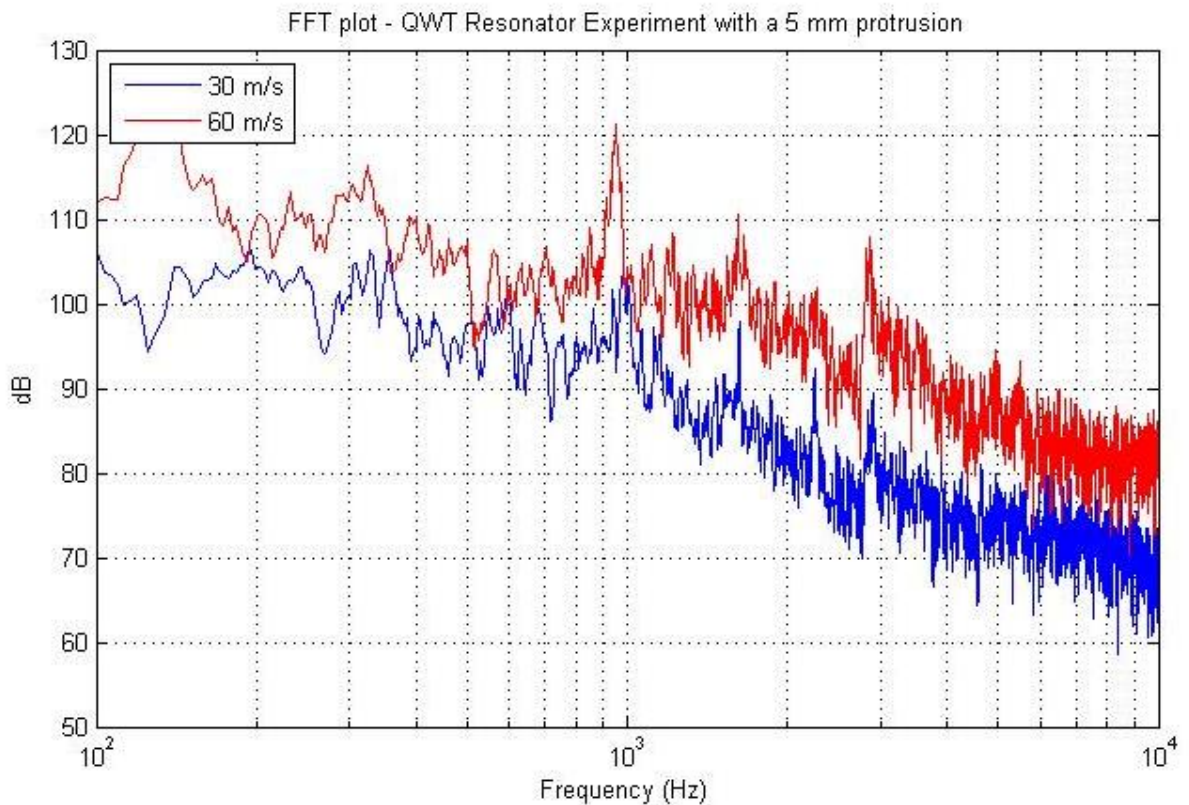


**Figure 43: FFT plot showing frequency distributions at the downstream monitor location for 5 mm protrusion at 30 m/s and 60 m/s**

What becomes increasingly clear from Figure 43 are the equally spaced frequency tones or frequency multiples, possibly related to the fundamental QWT resonant frequency tone. Coupling is likely to occur between the first two Rossiter modes and the acoustic standing waves. Using the Rossiter equation, Equation [16], the 2nd and 4th frequency modes are calculated to be 1450 Hz, 2900 Hz which are within 7% of the higher harmonic tones. The Rossiter mode appears to couple with an acoustic mode (or the quarter-wavelength mode) which is a multiple of the QWT fundamental tuned frequency. The tone around 950 Hz is the most pronounced with the largest protrusion length and highest flow velocity tested. However, the lower velocity tested does not exhibit such a pronounced tone at this frequency. Both tested velocities produce higher frequency tones at this protrusion length.

Overall, for the neck protrusion experiments, it can be said a higher air flow rate and a larger neck protrusion length does increase the amplitude of certain high frequency tones. The frequencies of the tonal peaks tend to increase slightly as flow rate increases.

Marsden (Marsden, et al., 2012) who observed the simultaneous presence of two large structures of different wavelengths in the shear layer. The presence of two coherent structures coexist associated with the second shear layer mode is confirmed. Meissner (Meissner, 2002) also presented similar findings and stated, since a sound generation is a result of resonance in a whole pipe system, the oscillation frequency for the lowest and the highest excited mode considerably differs from resonant frequency of the side-branch. Using the characteristic length as the diameter of the QWT opening, the vortex shedding occurs between  $St = 0.5$  to  $1.3$ . This is also in a similar region to comparable studies considered in Chapter 1. It is possible vortex shedding does not occur either side of this range as it is thought the diameter of the QWT is mainly responsible for the frequency of the high amplitude tones. More experiments would need to be carried out to investigate this.

These findings now need to be compared with simulation results. The aim and expectation is the frequency distributions for experiments and simulations will follow closely. This validates simulation work and further simulations can be utilised as a tool to find more patterns and relationships between Strouhal number, frequencies, velocities, shape and size.

## 2.5 Charge Air Cooler Experiments

A Charge Air Cooler resonator pipe configuration used within the premium automotive company which is known to whistle under certain conditions is tested. This real-world application of a resonating section helps to further validate the CFD simulations via experimental comparisons. The CAC (Charge Air Cooler) resonator section has produced a high frequency whistle during vehicle testing under normal running conditions. This is undesirable for the end user. The internal sleeve of the CAC resonator section was fitted in the reverse direction as a cure for the high frequency noise. It is currently unclear as to why the high frequency tone is present with this geometry and why flowing the reversed geometry removes or reduces this high frequency tone. For this thesis, the CAC Resonator which has been understood to reduce/eliminate the audible tone is called the Production CAC Resonator. The CAC Resonator which produced a high amplitude tone is called the Pre-Production CAC Resonator. The experimental analysis aims to re-create this phenomenon. It will also provide results to compare to simulations. The simulations are expected to give more information on the underlying flow processes which create this high frequency tone.

The geometry of the section is provided in Figure 44 and Figure 45. The CAC Resonator has two equal volumes separated by a plate to produce two resonating sections. The volumes wrap 360 degrees around the central sleeve which is a hollow thin-walled tube. Each volume has two openings which are rectangular slits through the central tube. These openings are facing one another (approximately 180 degrees apart). One section of the CAC Resonator has an opening width of 10 mm, whereas the other section has an opening width of 3 mm. Using Equation [6], the resonant frequencies of CAC resonator sections are calculated to be 9038 Hz with 10 mm width opening and 4950 Hz with 3 mm width opening.

Using Figure 44 as a reference, the volume section closest to the inlet (right) is referred to as CAC Resonator Section 1 and the volume section nearest the outlet (left) is CAC Resonator Section 2 for the subsequent chapters in this thesis.

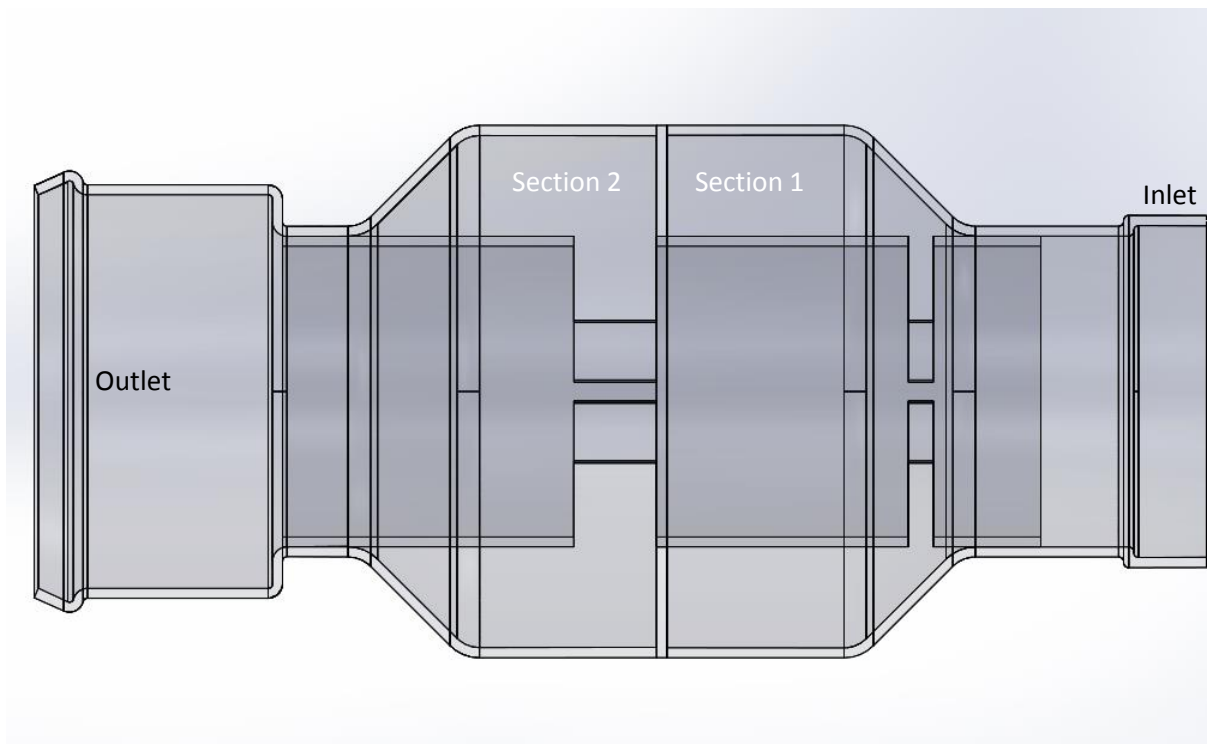


Figure 44: CAC Resonator in the Pre-Production (whistle) layout. Flow from right to left.

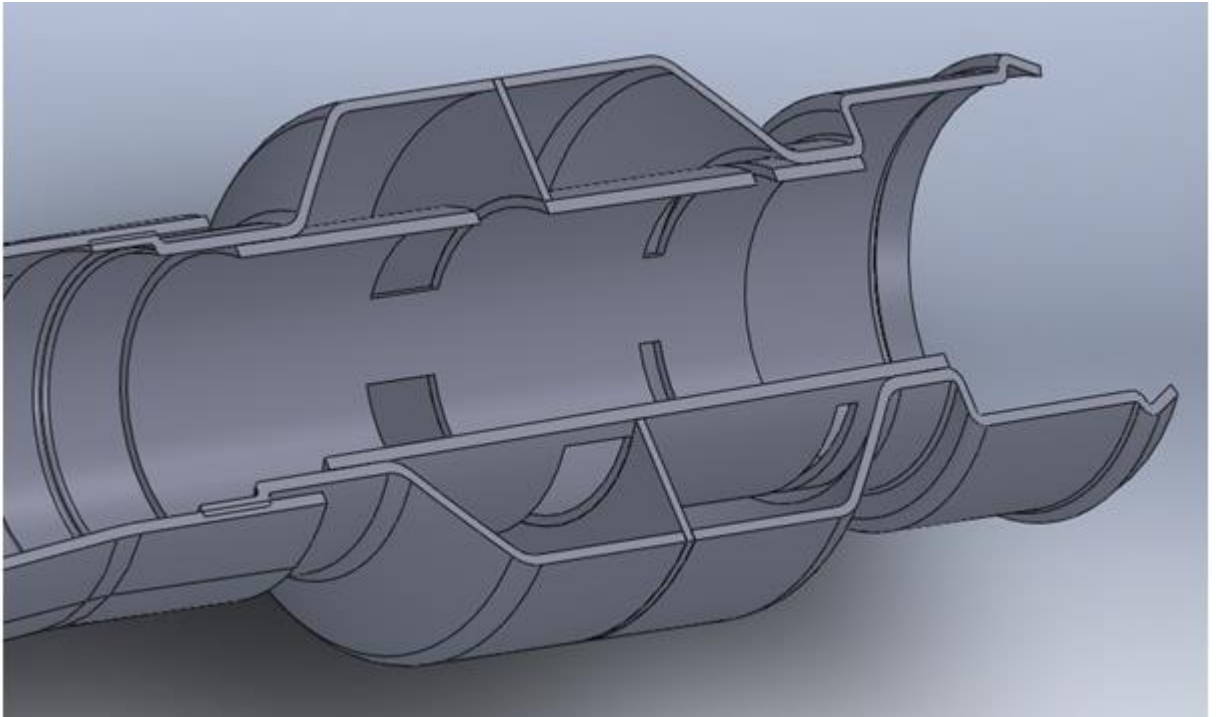


Figure 45: Isometric cut-away view of the CAC Resonator in the Production layout. Flow from left to right.

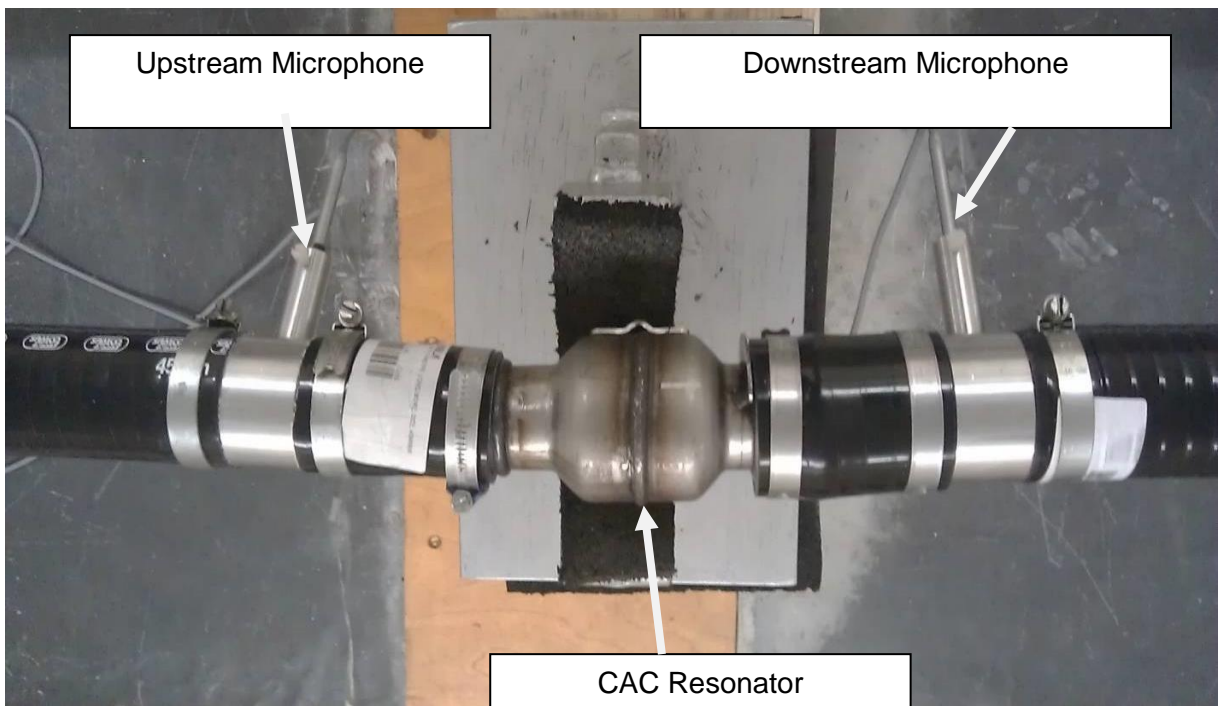
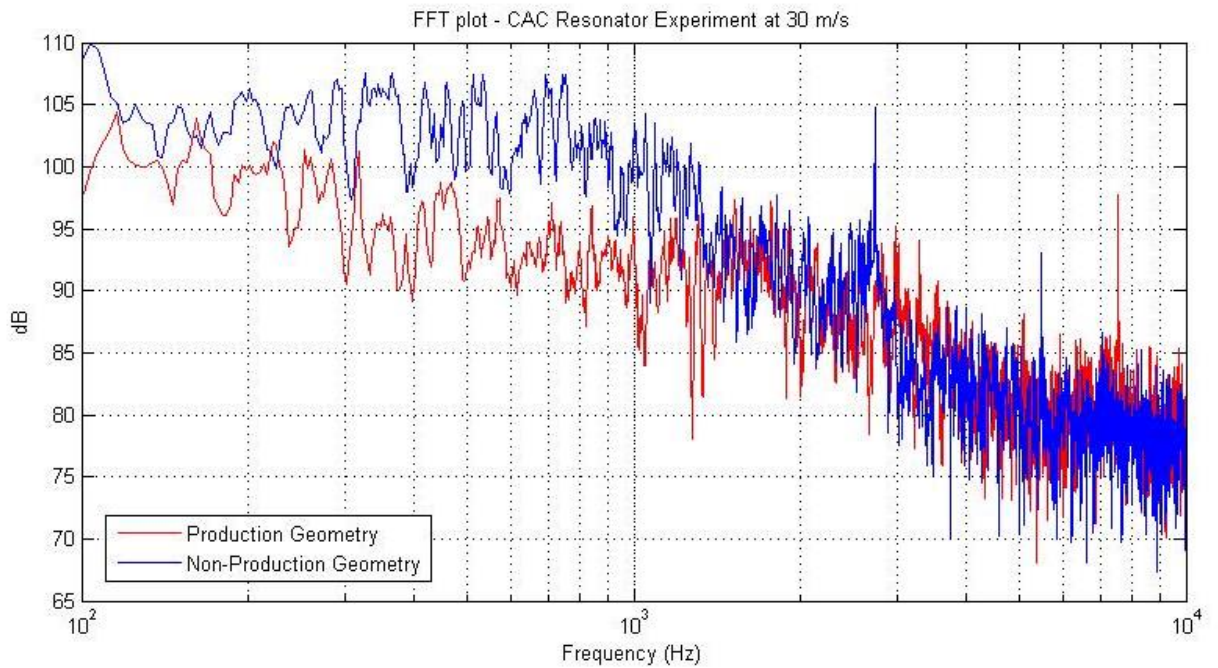


Figure 46: CAC Resonator microphone and pipework set-up

As in previous experiments, microphones are located flush against the sidewall of the main pipe either side of the test piece, immediately upstream and downstream of the CAC resonator section. Figure 46 is an image of the experiment set-up with a fan, for flow at the inlet and an anechoic termination at the outlet. The experimental apparatus is the same as described in Section 2.3. The 74 mm diameter pipe (wind tunnel duct) is reduced to the working cross section of the CAC resonator by one metre long smooth silicone hoses and aluminium reducers.

The CAC resonator section is first tested in the Pre-Production geometry which Figure 44 shows. This geometry was found to produce a loud tone during Pre-Production testing at the automotive manufacturer's facility, particularly at low speed running. The following sets of results aim to replicate this tone generation. The results will be compared with simulations which replicate the geometry. See Section 4.2.4. The production CAC resonator is then tested (geometry shown in Figure 45) and this set of results aim to replicate this reduction in tone generation. The results will again be compared with simulations which replicate the geometry.

Five flow velocities are tested with three to mirror the simulation work - 30 m/s, 45 m/s and 60 m/s. Results for flow velocities are given to correspond with flow rates given for low RPM running in the vehicle set up, which is said to be a problem area for the premium automotive company. Results for 30 m/s, 40 m/s, 45 m/s, 50 m/s and 60 m/s flow velocities are given below as a series of FFT plots which provide a direct comparison of the noise frequency distributions between Production and Pre-Production CAC resonator geometries at the downstream microphone point. Upstream microphone data is not plotted for clarity purposes. For the following set of figures, the red line represents the frequency distribution data for the Production CAC resonator. The blue line represents the frequency distribution data for the Pre-Production CAC resonator.



**Figure 47: FFT plot - CAC Resonator experiment comparison between production and Pre-Production geometries with a 30 m/s flow velocity**

For the 30 m/s case shown in Figure 47, it is clear there is a noise reduction between 100 – 1000 Hz for the production CAC resonator compared with the Pre-Production geometry. A tone signified by a large peak in the frequency distribution at around 2800 Hz with amplitude of approximately 25 dB is apparent with the Pre-Production CAC resonator. This tone has been eliminated with the production geometry. The same can be said of the lower amplitude peak around 5600 Hz. This is thought to be the 2<sup>nd</sup> harmonic tone of the 2800 Hz peak. A high amplitude tone is shown to exist around 8700 Hz with the production geometry. This is unexpected but it is thought to be a coupling of the fundamental resonant frequency of the volume with the 10 mm opening.

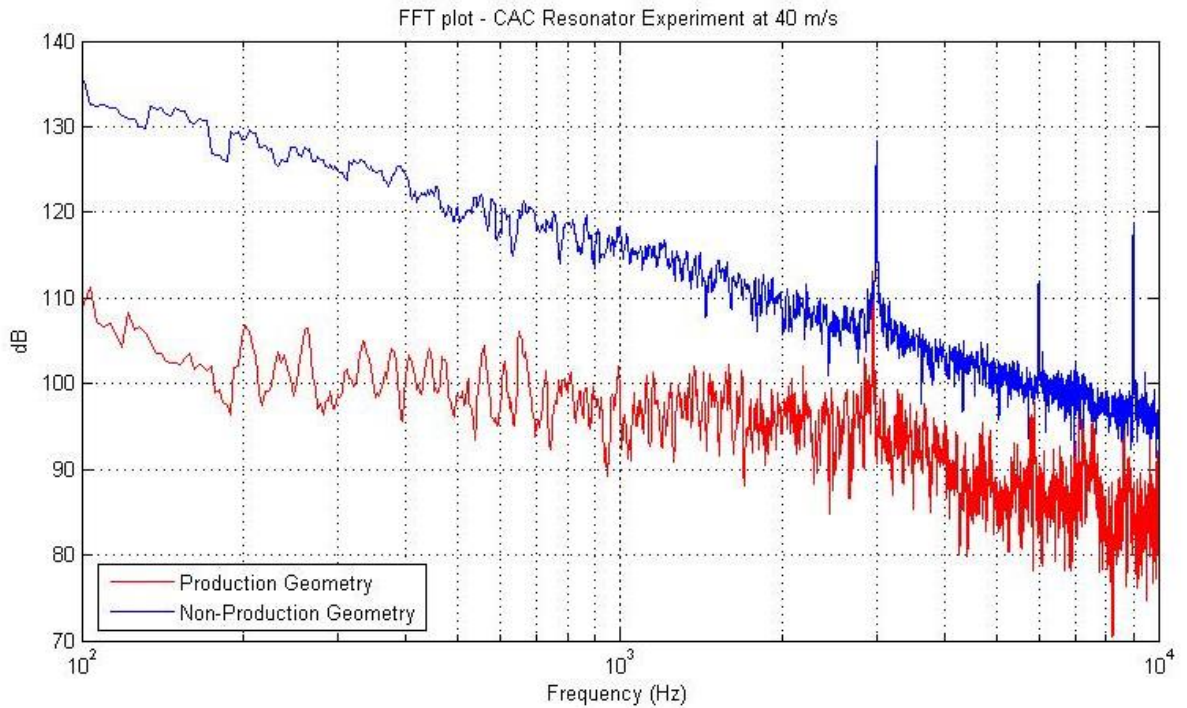


**Figure 48: FFT plot - CAC Resonator experiment comparison between production and Pre-Production geometries with a 40 m/s flow velocity**

For the 40 m/s case shown in Figure 48, there is a noise reduction at all frequencies for the production CAC resonator compared with the Pre-Production geometry. There is a tone present with both geometries with a frequency of 3000 Hz. However the production geometry has reduced the amplitude of the tone by half. The Pre-Production geometry produces clear harmonic tones of the 1<sup>st</sup> 3000 Hz tone. The 3<sup>rd</sup> harmonic at 9000 Hz is approximately twice the amplitude of the 2<sup>nd</sup> at 6000 Hz. These higher harmonics have been reduced to negligible amplitudes with the production CAC resonator.

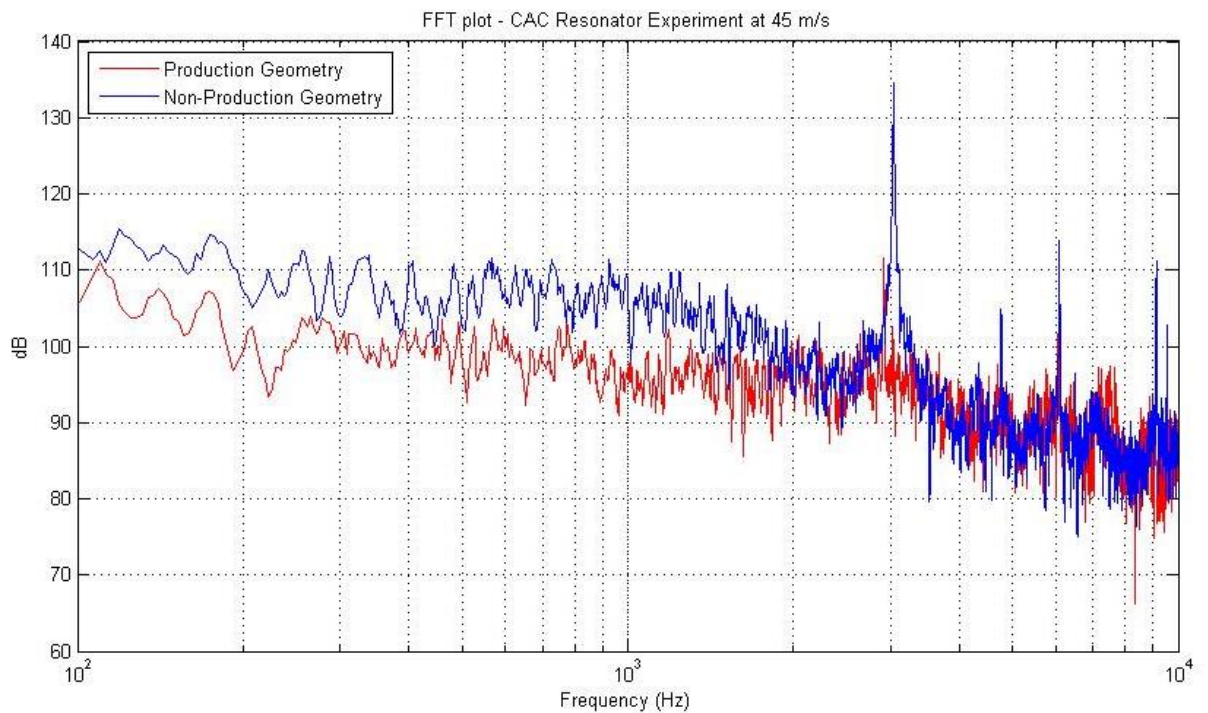


**Figure 49: FFT plot - CAC Resonator experiment comparison between production and Pre-Production geometries with a 45 m/s flow velocity**

For the 45 m/s case shown in Figure 49, again, there is a noise reduction between 100 – 2000 Hz for the production CAC resonator compared with the Pre-Production geometry. The Pre-Production geometry still creates a tone around 3000 Hz. However, the tone has increased slightly in frequency and has increased dramatically in amplitude. The tone now has increased to 40 dB. As with the 40 m/s case, the Pre-Production geometry produces clear harmonic tones of the 1<sup>st</sup> tone. The 2<sup>nd</sup> and 3<sup>rd</sup> harmonics are approximately the same amplitude at 25 dB. These higher harmonics have been reduced to negligible amplitudes with the production CAC resonator.

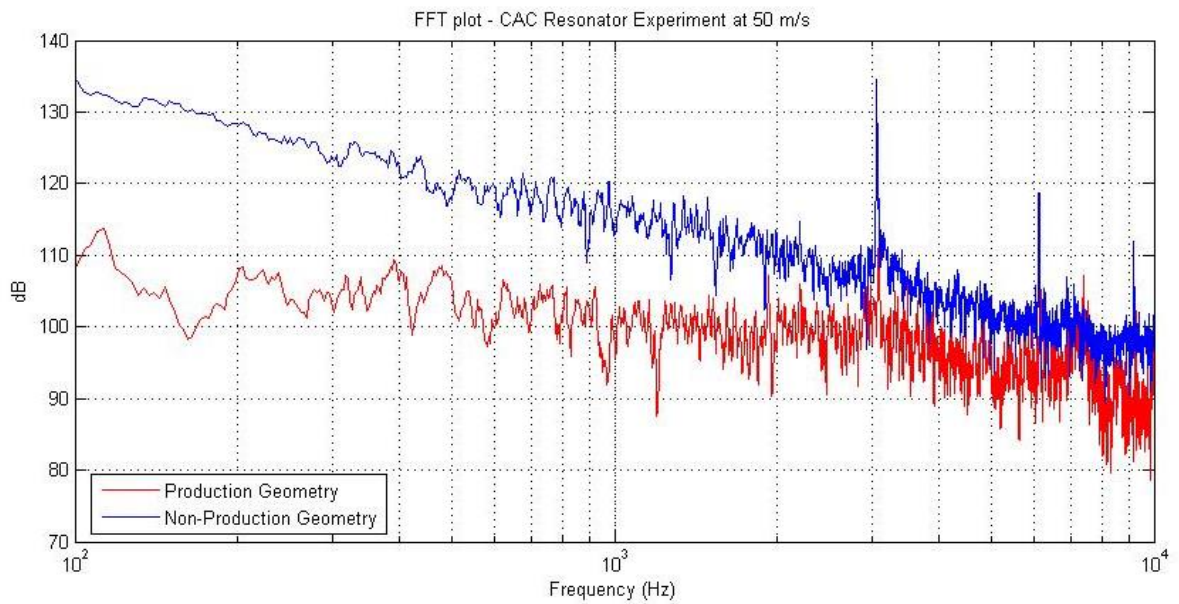


**Figure 50: FFT plot - CAC Resonator experiment comparison between production and Pre-Production geometries with a 50 m/s flow velocity**

For the 50 m/s case shown in Figure 50, there is a noise reduction at all frequencies for the production CAC resonator compared with the Pre-Production geometry. There is a tone present with both geometries with a frequency of 3000 Hz. However the production geometry has reduced the amplitude of the tone by approximately 60%. The Pre-Production geometry produces clear harmonic tones of the 1<sup>st</sup> 3000 Hz tone. The subsequent harmonic tones show a reduction in amplitude of approximately 5 dB. These higher harmonics have been reduced to negligible amplitudes with the production CAC resonator. The exception to this is a small but noticeable peak in the production geometry frequency distribution at around 7500 Hz. This is thought to be a coupling mode of a harmonic of one resonator section.

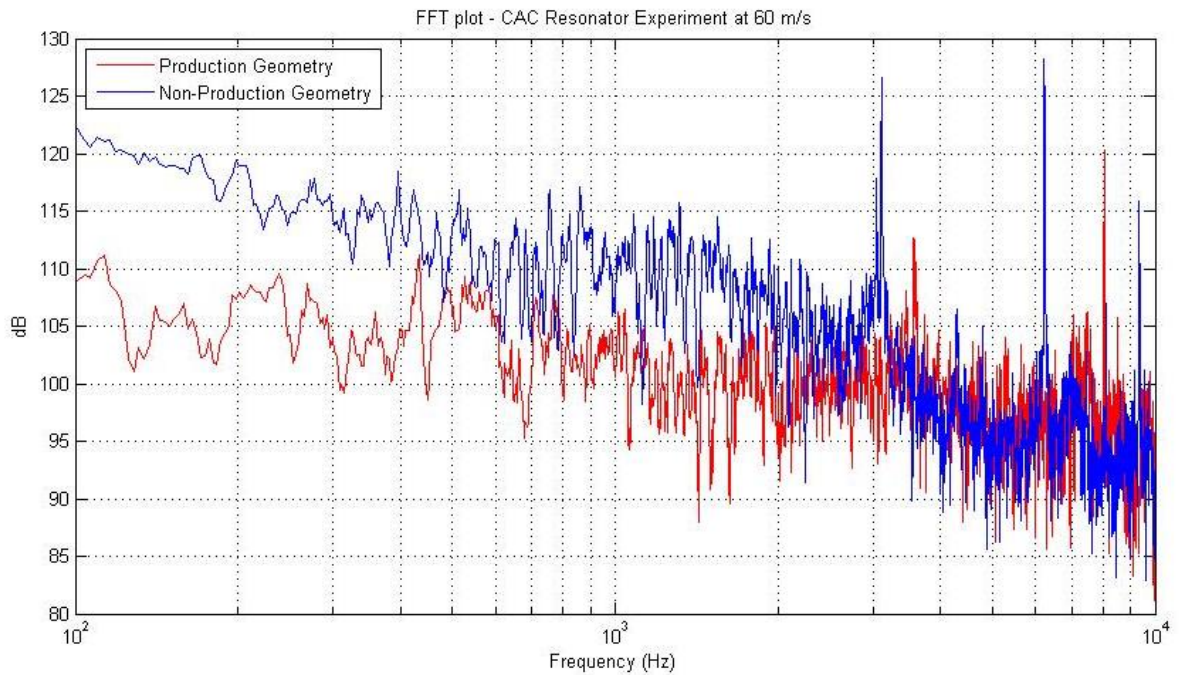


**Figure 51: FFT plot - CAC Resonator experiment comparison between production and Pre-Production geometries with a 60 m/s flow velocity**

For the 60 m/s case shown in Figure 41, again, there is a noise reduction between 100 – 2000 Hz for the production CAC resonator compared with the Pre-Production geometry. The Pre-Production geometry still creates tones around 3000 Hz, 6000 Hz and 9000 Hz with a small frequency shift upwards by around 50-100 Hz as was the case at higher velocity flows with the QWT (see Section 2.4). The 2<sup>nd</sup> and 3<sup>rd</sup> harmonic tones have increased dramatically in amplitude with the increasing flow velocity and mass flow. The tone around 6000 Hz has increased to around 30 dB. The production CAC resonator frequency distribution shows no noticeable tones at these frequencies. However, a tone around 3500 Hz and a higher amplitude 120 dB tone around 8000 Hz appears to be produced in this case. These tones are of lower amplitude compared with the respective tones from the Pre-Production geometry. However, they are significant in terms of SPL.

The insertion loss between production and Pre-Production versions of the CAC Resonator experiments at each flow rate has been plotted in Figure 52 to Figure 56. A positive amplitude value indicates a reduction in noise at a given frequency for the production CAC resonator as opposed to the Pre-Production geometry. A negative value indicates an increase in noise for the production CAC resonator. The plots below clearly demonstrate the effect of rotating the internal sleeve of the CAC resonator 180 degrees.

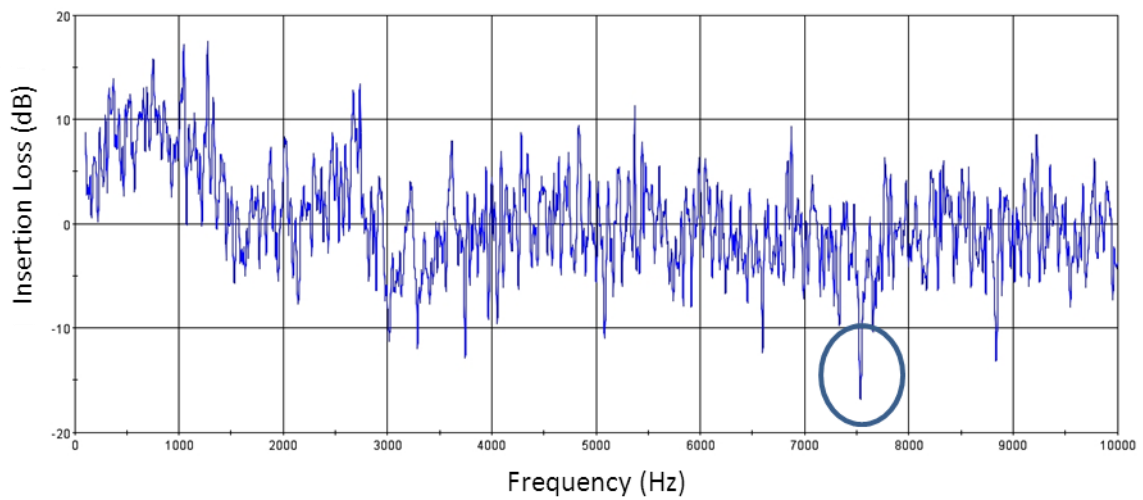


Figure 52: Experiment Insertion Loss at 30 m/s between Production and Pre-Production CAC Resonators

For the 30 m/s case (Figure 52), the production CAC resonator appears to generally reduce noise in the lower frequency range. The mean noise is generally unchanged. Narrow band higher frequency tones appear to be produced by the production CAC resonator such as the negative pulse shown at around 7500 Hz.

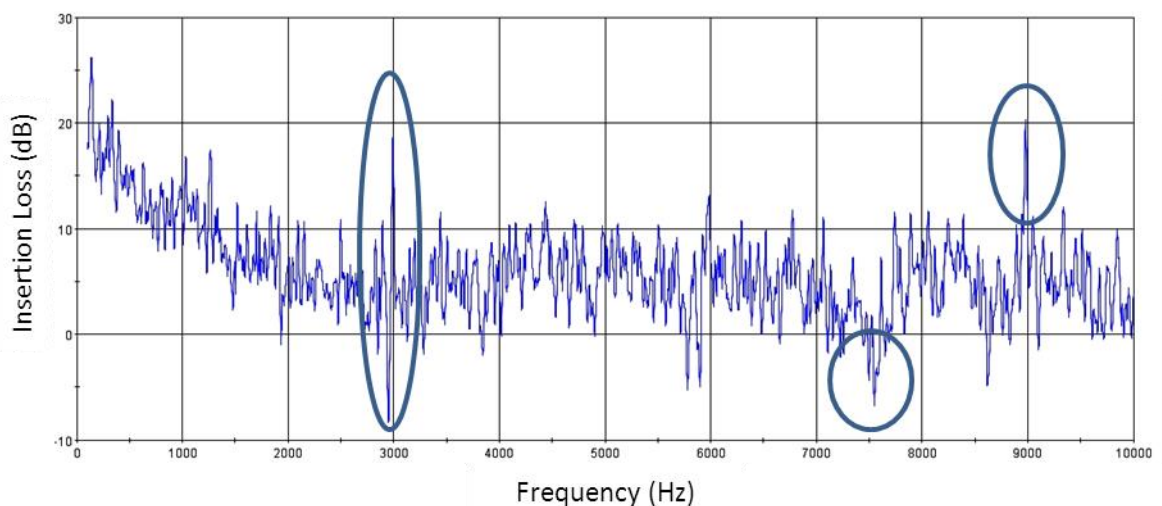


Figure 53: Experiment Insertion Loss at 40 m/s between Production and Pre-Production CAC Resonators

Figure 53 shows the insertion loss at 40 m/s in-flow velocity. The tone at around 3000 Hz appears to have been shifted to a slightly lower frequency but with no reduction in amplitude. The small tone around 7500 Hz is still shown to be created by the production CAC

resonator, similar to the 30 m/s case. A large noise reduction is present at a narrow frequency band around 9000 Hz.

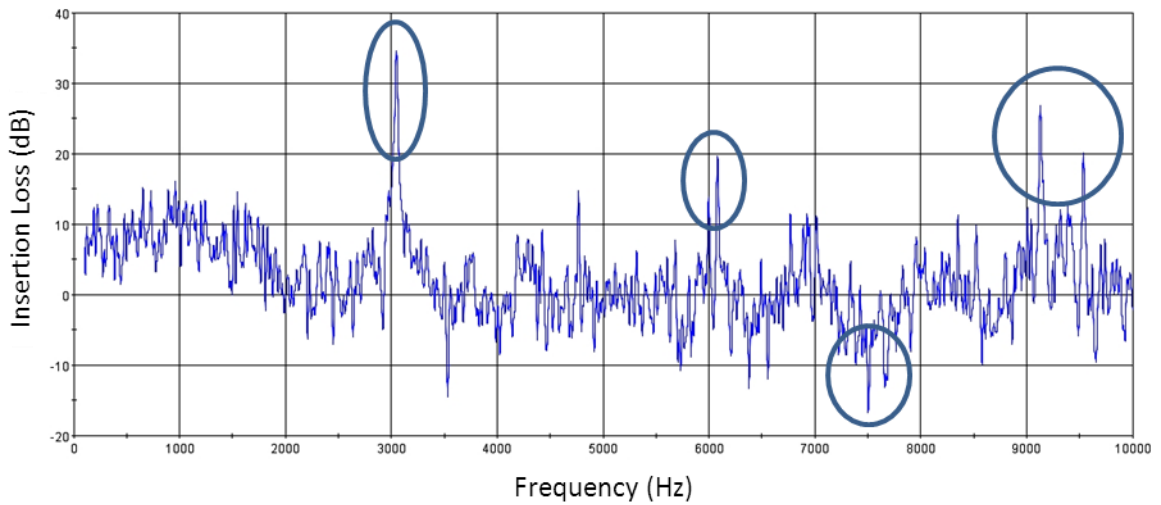


Figure 54: Experiment Insertion Loss at 45 m/s between Production and Pre-Production CAC Resonators

The insertion loss at 45 m/s is shown in Figure 54. A large 35 dB attenuation of a tone at 3100 Hz is given by the production CAC resonator over the Pre-Production version. A 20 dB attenuation of the tone is apparent at just over 6150 Hz. The peak around 9000 Hz at 40 m/s has increased in amplitude at 45 m/s with a secondary peak at approximately 9600 Hz. The peaks have all shifted up the frequency scale by 50-100 Hz at the higher flow rate.

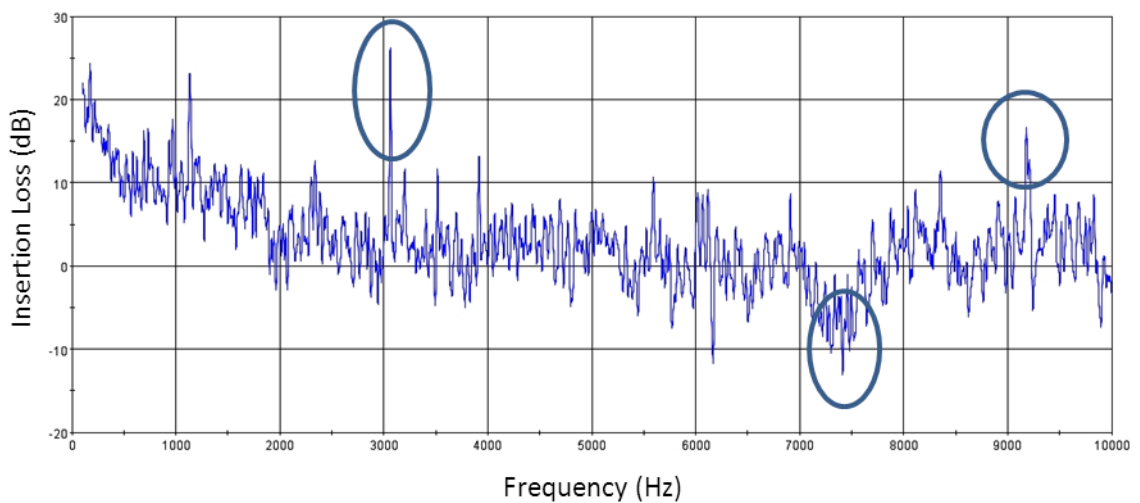
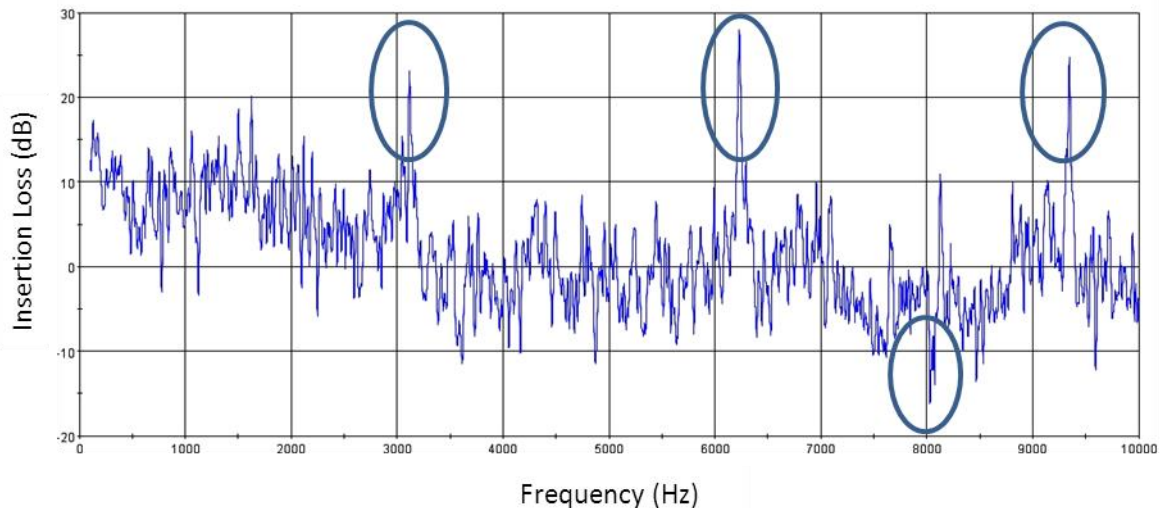


Figure 55: Experiment Insertion Loss at 50 m/s between Production and Pre-Production CAC Resonators

Figure 55 shows the insertion loss at 50 m/s. The peaks at 3100 Hz and 9200 Hz are still present. However the peak at around 6000 Hz is reduced to around 8 dB. A continuing theme across all inflow velocities is the relatively wide frequency band at around 7500 Hz which shows a negative pulse in amplitude. This is noise created by the production CAC resonator which is not created by the Pre-Production CAC resonator.



**Figure 56: Experiment Insertion Loss at 60 m/s between Production and Pre-Production CAC Resonators**

Figure 56 gives the insertion loss at 60 m/s. Although the insertion loss amplitude is beginning to fluctuate significantly more than with lower tested velocities, clear peaks in the insertion loss frequency plot are present. At this higher velocity, the amplitude of the 3000 Hz attenuation is lower, yet the attenuation further up the scale around 6000 and 9000 Hz as increased considerably. The negative pulse at around 7500 Hz shown at lower velocities is not as apparent here. There is also a negative pulse (noise created by the production CAC Resonator) at just over 8000 Hz, the exact cause of which is unknown but it is thought to be a resonant mode of one resonator section.

Overall, the insertion loss plots have reinforced the FFT plots showing the Pre-Production CAC resonator creates higher amplitude tones at specific frequencies which the production CAC resonator eradicates. The 45 m/s and upwards in-flow velocity cases show the production CAC resonator reduces the tone around 3000 Hz (believed to be the 1st harmonic) by up to 35 dB. Interestingly some high frequency (>4000 Hz) tones are still produced in certain circumstances with the production resonator. However, all experiments show a mean reduction in noise for the production CAC resonator at the lower frequencies

i.e. <1000 Hz. As flow rate increases, the insertion loss plots again show, the high amplitude tones tend to increase slightly in frequency.

From the CAC resonator experiments, it is clear to see high amplitude high frequency tones are produced in all cases tested with the Pre-Production CAC resonator geometry. This aligns with the findings in Pre-Production testing at Jaguar Land Rover. Rotating the internal sleeve appears to reduce or eliminate these high frequency tones in the majority of cases. This also aligns with the findings at Jaguar Land Rover. In summary, for the production CAC Resonator geometry, the experiments show;

- A general noise reduction, particularly at lower frequencies.
- Large 3000 Hz tone reduced or eliminated in all cases.
- Higher frequency tones reduced or eliminated in all cases with the exception of the 30 m/s and 60m/s cases.
- Overall, the experiments broadly follow expectations.

## 2.6 Experimental Work Summary

The experimental work has been carried out in an attempt to gain further understanding into how a resonator behaves under various flow conditions geometries and acoustic signals. Several validation experiments have been conducted to investigate the effect of acoustic signals and the air flow as it passes the opening of various side branch configurations. A side branch consisting of a VVH Helmholtz resonator and an adjustable Quarter Wave Tube (QWT) has been analysed in terms of the effect on the acoustic field in a straight section of pipe. Various parameters have been explored including; inlet signal, multiple resonators in series, flow rate, resonator geometry, resonator volume and side branch neck protrusion length. Later, the premium automotive manufacturer section of charge inlet tract was flowed with a change of internal geometry. The experiments have given an insight into the trends and geometries which can cause high frequency flow-generated noise. Several experiments produced high frequency (>1000 Hz) tones which were found to be semi-independent from the tuned fundamental resonant frequency. This phenomenon, thought to be related to the shedding of vortices from the resonator opening will be investigated further throughout the following chapters of this thesis. Each experiment has been designed to mirror the CFD models which allow direct comparisons to the simulation work carried out in the follow section, Chapter 4.

The following chapter will explain the fundamental basis of three-dimensional CFD codes and the solvers available. Turbulence and aero-acoustic modelling will be discussed in reasonable detail as it is the fundamental basis for flow phenomena discussed in this thesis. It is also a very challenging area to simulate accurately.

### 3 Computational Fluid Dynamics

Traditionally, engine, intake and exhaust simulations are based on one-dimensional solvers such as WAVE to calculate predicted noise. The Transfer Matrix Method, Finite Element Method (FEM), Boundary Element Method (BEM) or Computational Fluid Dynamics (CFD) methods are widely employed to predict the exhaust pipe noise. The most common calculation method was the transfer matrix method (or four-pole theory) as discussed by Munjal (Munjal, 1987). This method is based on the linear one dimensional wave propagation in ducts and the transfer matrix formulation of the individual elements such as ducts and branches. Noise attenuation of simple mufflers can be calculated by this method in the frequency domain. (Yasuda, et al., 2010). However, this method has several disadvantages:

- It can only be used under the assumption of linear wave propagation
- It is impossible to calculate the back pressure of the duct using this method
- It cannot predict the transient acoustic characteristics of a geometry
- Poor at capturing higher frequencies, i.e. above 1-2 kHz
- Cannot capture 3D effects such as turbulence and vortex shedding. Therefore cannot capture noise generation from resonators, sharp edges and obstructions.
- Impossible to model complex resonator shapes, bends, etc.

Modern three dimensional codes have overcome these problems and have also improved on the one dimensional methods. Several CFD three-dimensional codes at the present time, including Star CCM+, utilises the finite volume method which is, in general, 2nd order accurate in space (Haren, 2011) (Versteeg & Malalasekera, 2007). The numerical algorithm, within the CFD solver utilised in this thesis, consists of the following steps:

1. Integration of the governing equations of fluid flow over all the finite control volumes of the domain
2. Discretisation - conversion of the resulting integral equations into a system of algebraic equations
3. Solution of the algebraic equations by an iterative method.

These complex three dimensional solvers provide very detailed flow solutions as they include discretisation techniques for convection and diffusion as well as other non-linear phenomena which change in time for real fluid flows. Automotive applications generally imply high-Reynolds number, low Mach number flows in very complex geometries. That is why industrial codes solving the U-RANS/LES equations, which are explained in the

following section, in the incompressible regime are retained by the manufacturers (Gloerfelt, 2009 (1)). However, as turbulent flow generated acoustics is the primary concern here, both the acoustic and flow fields need to be solved directly. Using the low-Mach number incompressible formulation of the Navier-Stokes equations, the acoustic waves propagate at an infinite speed. When the acoustic wave speed plays an important role, as in the formation of instabilities, the compressible Navier-Stokes equations must be solved (Moureau, et al., 2005) to accurately predict the generation and propagation of these acoustic wavelengths.

The development of numerical methods to capture the important effects due to turbulence has undergone a vast amount of research. Detailed reviews have been written by Durbin et al (Durbin & Medic, 2007), Davidson (Davidson, 2013) amongst many others. Turbulence modelling methods can be grouped into the following three computation techniques:

- Direct Numerical Simulation (DNS) requires no modelling, but it requires resolution of scales all the way to dissipation scales.
- Large Eddy Simulation (LES) requires modelling of part of the inertial sub-range and into beginning of dissipation scales.
- Reynolds averaged Navier-Stokes (RANS) requires modelling of everything from the integral scales into the dissipation range.

Direct Numerical Simulation (DNS) fully resolves all energy scales and as can be expected, is the most accurate solver, especially when the boundary layers are of great interest. Such is the requirement for computational resource, it is rarely used in practical forms at the time of writing. Typically, LES requires only 1% of the computational resource compared to fully resolved DNS (Schlatter, 2005). The ratio of modelled/resolved turbulence for the three techniques is shown in Figure 57.

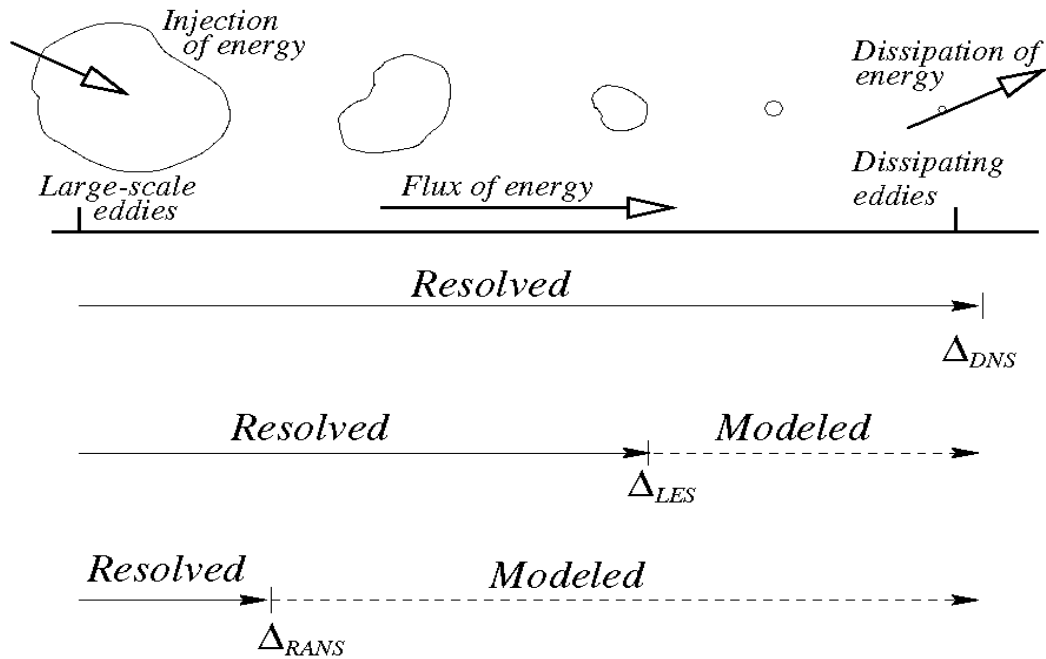


Figure 57: A diagram to show how turbulence is calculated in Direct Numerical Simulation (DNS), Large Eddy Simulation (LES) and Reynolds averaged Navier-Stokes (RANS) solvers.

The vortices produced by Helmholtz resonators are a type of turbulent structure which cause eddies in the flow. These eddies contain a wide range of length and time scales that interact in a dynamically complex way (Versteeg & Malalasekera, 2007). Modelling these phenomena in CFD requires unsteady RANS, DES or LES flow solvers with acoustic modelling. RANS solutions, although modest in computing resource, are inherently an averaged solution. Therefore, it is difficult to directly capture the random turbulent eddies contained in these types of flows. Detached Eddy Simulation (DES) is a hybrid approach which consists of RANS solutions calculated for attached boundary layers in the near wall region and LES in the rest of the computational domain. Although DES is useful to simulate large eddy structures in the bulk flow, it is not suitable to accurately predict acoustic fluctuations originating from the boundary layer area as the RANS region is highly dissipative. Therefore, to directly predict acoustic phenomena in these types of flow, LES is the best practical solution. This is discussed in more detail with published studies in Section 3.2. The automotive and aerospace manufacturers are among the first to use Large Eddy Simulations (LES) in an industrial context.

Selecting an appropriate CFD solver which has the capabilities to handle complex meshes and possesses efficient numerical solvers to obtain accurate results is of primary importance. The present work has been carried out using STAR-CCM+ (STAR-CCM+, 2009). STAR-CCM+ is a finite volume multi-physics solver with capabilities of creating good quality arbitrary hexahedral and polyhedral meshes for complex geometries. The CFD solver provides a vast array of simulation settings which can vary the end solution in terms of accuracy and complexity substantially. It is possible to solve for steady state and transient analysis, with a range of solvers using an advanced and flexible meshing engine. The software also allows for transient and static post processing whether tabular, graphical, or animated. It should be noted though despite the software flexibility, modifying the underlying code within the software is not possible.

Creating a high quality wall resolved mesh which meets the LES requirements (Piomelli, 1997) is far from simple, especially when the computational domain involves sharp 90 degree joints. In the present T-junction case, such a sharp angle exists in the junction between two pipes. STAR-CCM+ meshing tool is equipped with advanced methodologies to treat such complexities. In terms of the numerical solver, STAR-CCM+ uses advanced cell-based discretisation techniques and sophisticated Algebraic-Multi-Grid (AMG) strategies for convergence acceleration. STAR-CCM+ utilises the bounded-central scheme which is useful when performing simulations using polyhedral cells (Jayaraju, et al., 2010). Some alternative commercial CFD codes such as OpenFOAM use the pressure-implicit split-operator (PISO) algorithm for iteratively solving the equations. STAR-CCM+ utilises a version of the Semi-Implicit Method for Pressure Linked Equations (SIMPLE) algorithm developed by Karki et al (Karki & Patankar, 1989) which is suitable for low mach number compressible flows, such as the scenarios under study in this thesis. The algorithm performs several steps as detailed by Ferziger et al (Ferziger & Peric., 2002):

- Predictor Step - the pressure field at  $t^{n-1}$  is used to solve the momentum equation, resulting in an intermediate velocity field. This velocity field will in general not satisfy the continuity equation.
- Corrector step - In the corrector step, a pressure correction equation is solved to obtain a correction for the pressure field. The pressure field is updated using this correction and using under-relaxation.
- The velocity field is updated using the correction for the pressure field. This procedure is then iterated until the fields do not change within a certain tolerance (see Section 3.2.5).

Star CCM+ has proven to perform very strongly with low Mach number flows against comparable CFD solvers and experimental results as demonstrated by Haren (Haren, 2011) and (Jayaraju, et al., 2010) amongst many others. Similar resonator studies using this software, including compressible flows have also been undertaken by Caro et al (Caro, et al., 2005), Mendonca et al (Mendonca, 2005) and more. Further information about the algorithms used by these commercial codes can be found in the paper by Haren (Haren, 2011). STAR-CCM+ has been chosen by the premium automotive company and thus used in this paper to be one of the most efficient solvers for the present work.

### **3.1 Turbulence Modelling**

Turbulence is one of the least understood topics in fluid dynamics and can be loosely described as irregular motion in rotational flow obeying probabilistic constraints. These flows are characterised by velocity fluctuations in all directions with infinite number of scales. It has been shown several times in the past that turbulence can only develop and persist in rotational flow or in the presence of shear. The velocity gradient developed due to the presence of shear provides the energy differential that converts the small initial perturbations into large scale coherent structures (Lesieur 1997). A visual example of turbulence is provided in Figure 59 which is a smoke jet visualisation. Flows at very low Mach numbers tend to produce no lateral mixing due to the action of the fluid viscosity. This is known as laminar flow. However, the vast majority of real flows are above a Reynolds number value of 3000. This is the typical transition from laminar to turbulent flow although the exact value can vary significantly in certain extreme conditions. Turbulent flow is only possible at high Reynolds number as this is when inertial forces can overcome the influence of viscous forces which are used to damp down the small initial perturbations.

Although there is no strict definition of turbulence present in the literature, turbulence is generally described by the following characteristics:

*Three-Dimensional:* Real turbulent flows are always three dimensional and unsteady.

*Irregularity:* Turbulent flow is random, irregular and chaotic. It consists of a spectrum of different scales known as turbulent eddies. As described by Davidson (Davidson, 2013), these turbulent eddies have their characteristic velocity and length scales and exist somewhere in space for a certain time and are subsequently destroyed. Although turbulence is chaotic, it is deterministic and can be described by the compressible Navier-Stokes equations.

*Diffusivity:* Diffusivity is stronger in turbulent flow than laminar flow. This can be useful as this increases the exchange of momentum due to the diffusion of turbulent eddies. This strongly enhances the heat transfer, mixing and friction.

*Continuum:* Turbulence is also a continuum phenomenon. Although the smallest scales of turbulence are extremely small, they are still many orders of magnitude bigger than the molecular length scale. This is followed by the fact that time dependent, three dimensional continuity and compressible Navier-Stokes equations contain all of the physics of a given turbulent flow.

*Dissipation:* Vorticity is connected to the rotational nature of the fluid and its three-dimensionality. The larger eddies in the flow interact most strongly with the mean flow. In turn, vortex elements that comprise most of the smaller eddies are stretched and compressed by the larger eddies, transferring their energy to smaller eddies. There is an energy cascade which allows the transfer of kinetic energy from larger eddies to the smaller eddies. The smallest eddies receive energy from slightly larger eddies and the larger eddies receive energy from even larger eddies and so on. The largest eddy receives its energy from the mean flow. This process of energy transfer is called the cascade process. This process is summarised in Figure 58. The energy is dissipated in the shortest wavelengths by viscous forces. Since the kinetic energies of small eddies are transformed into thermal energy, the flow is dissipative.

These properties lead to the inference that turbulence is definitely not isotropic, except at the smallest scales, where it is non-directional. The larger eddies strongly depend on the mean flow direction.

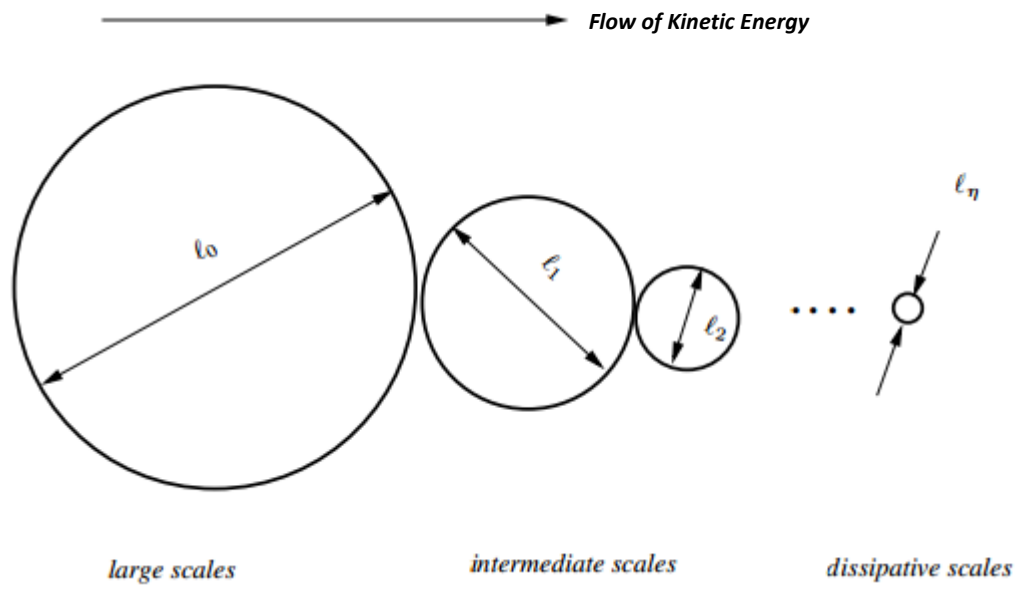


Figure 58: Energy cascade process where  $l$  denotes the size of eddies in the inertial sub-range. (Davidson, 2013)



Figure 59: Example of turbulent flow (Dyke, 1982)

The energy cascade process eventually creates structures that are small enough where molecular diffusion becomes important and viscous dissipation of energy finally takes place. The scale at which this happens is the Kolmogorov length scale. As turbulence is essentially random, it is difficult to find solutions of the compressible Navier-Stokes equations governing fluid motion. All such solutions are unstable to finite perturbations at large Reynolds numbers. Sensitive dependence on the initial and boundary conditions makes fluid flow irregular both in time and in space so that a statistical description is needed. Kolmogorov proposed the first statistical theory of turbulence, based on the notion of the energy cascade. This energy cascade means turbulent flow can be understood as a superposition of a spectrum of velocity fluctuations and eddies upon a mean flow. Turbulent eddies can be thought of as coherent patterns of velocity, vorticity and pressure.

The average magnitude of velocity fluctuations, often expressed as  $\overline{u'^2}$ ,  $\overline{v'^2}$  and  $\overline{w'^2}$ , are proportional to the momentum fluxes induced by turbulent eddies, which cause additional normal stresses experienced by fluid elements in a turbulent flow. These stresses are called Reynolds Stresses. The correlation of fluctuating velocity and pressure appears in the transport equation of turbulence properties such as the turbulence kinetic energy and the Reynolds stress. For homogeneous flows, the flow velocities can be considered in terms of mean and fluctuating terms as given in Equation [23].

$$u_i = \overline{u_i} + u'_i \quad [23]$$

The total turbulence kinetic energy per unit mass can be calculated at a given location using these stress components as given in Equation [24] below (Versteeg & Malalasekera, 2007).

$$k = \frac{1}{2} (\overline{u'^2} + \overline{v'^2} + \overline{w'^2}) \quad [24]$$

The turbulence intensity,  $T_i$ , is the average R.M.S. velocity divided by a reference mean flow velocity,  $U_{ref}$ .  $T_i$  is linked to the turbulence kinetic energy,  $k$  by Equation [25]

(Versteeg & Malalasekera, 2007). Both Equations [24] and [25] are useful to evaluate the turbulence conditions in a flow field.

$$T_i = \frac{\left(\frac{2}{3k}\right)^{1/2}}{U_{ref}} \quad [25]$$

Kolmogorov's analysis deduced that the energy density per unit wave number should depend only upon the wave number and the rate of energy dissipation per unit volume,  $k$  and  $\varepsilon$  respectively. The upper limit of the inertial range,  $k$  should depend only upon the molecular viscosity  $\nu$  and  $\varepsilon$ . An assumption is made in Kolmogorov's theory that the large scale influence of anisotropy is gradually lost when energy is transferred from larger scale to smaller scales. Kolmogorov's law is graphically represented by the dotted line in Figure 60 which gives the turbulent energy spectrum for typical real turbulent flows. Kolmogorov's law is derived from dimensional analysis and expressed as in Equation [26]:

$$E(k, \varepsilon) = Ck^{-5/3}\varepsilon^{2/3} \quad [26]$$

where  $C$  is a universal constant and experimentally found to be of the order of 1.5.

Kolmogorov's law states that, if the flow is fully turbulent then the energy spectrum should exhibit a -5/3 law in the inertial region. The energy spectrum, shown in Figure 60 can be broadly divided into three parts from left to right, generally known as the large eddy region, inertial range and dissipative range respectively.

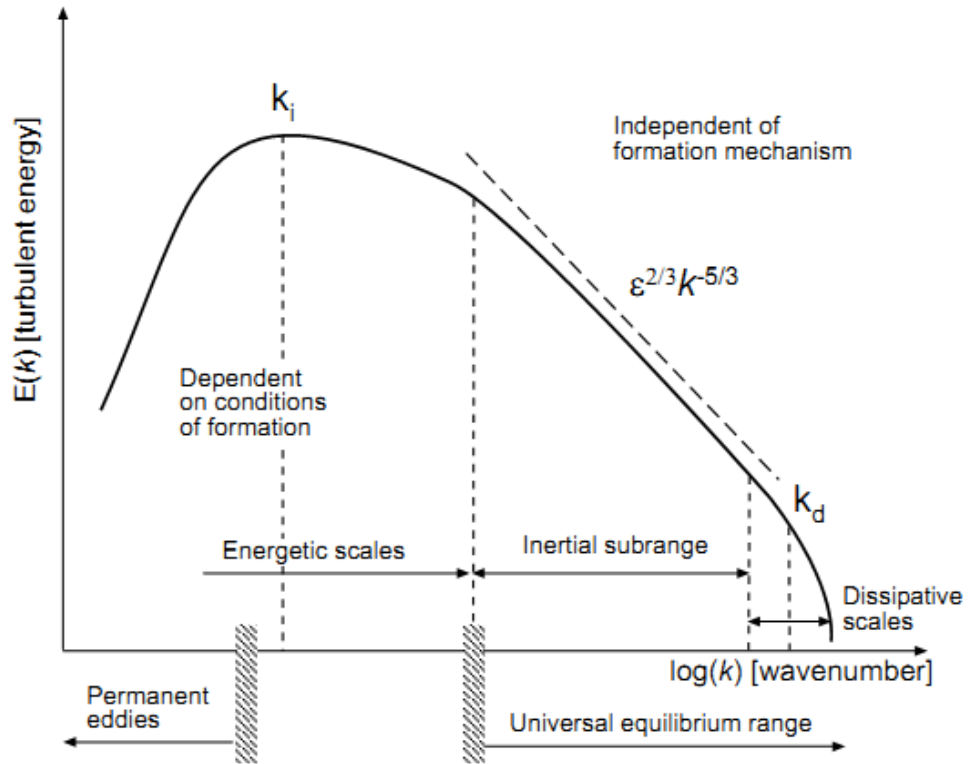


Figure 60: Turbulent Energy Spectrum (Hinze, 1975)

Most of the kinetic energy within the turbulent motion is contained in the large-scale structures. The Integral length scales are the largest scales in the energy spectrum. These eddies take energy from the mean flow and also from each other. They have large pressure fluctuations and are low in frequency. The integral scales are highly anisotropic and are defined in terms of the normalized two-point velocity correlations. The maximum length of these scales is constrained by the characteristic length of the apparatus. For example, the largest integral length scale of pipe flow is equal to the pipe diameter. The intermediate scales which make up the inertial sub-range are called the Taylor micro-scales. Taylor micro-scales are not dissipative, thus they play a dominant role in energy and momentum transfer in wave-number space. The highest frequency scales in the spectrum form the viscous sub-layer range. In this range, the energy input from nonlinear interactions and the energy drain from viscous dissipation are balanced. These smallest, so-called Kolmogorov scales need to be resolved in numerical simulations based on the compressible Navier-Stokes equations. The simulation accuracy strongly depends on the spatial and temporal resolution employed. (Schlatter, 2005)

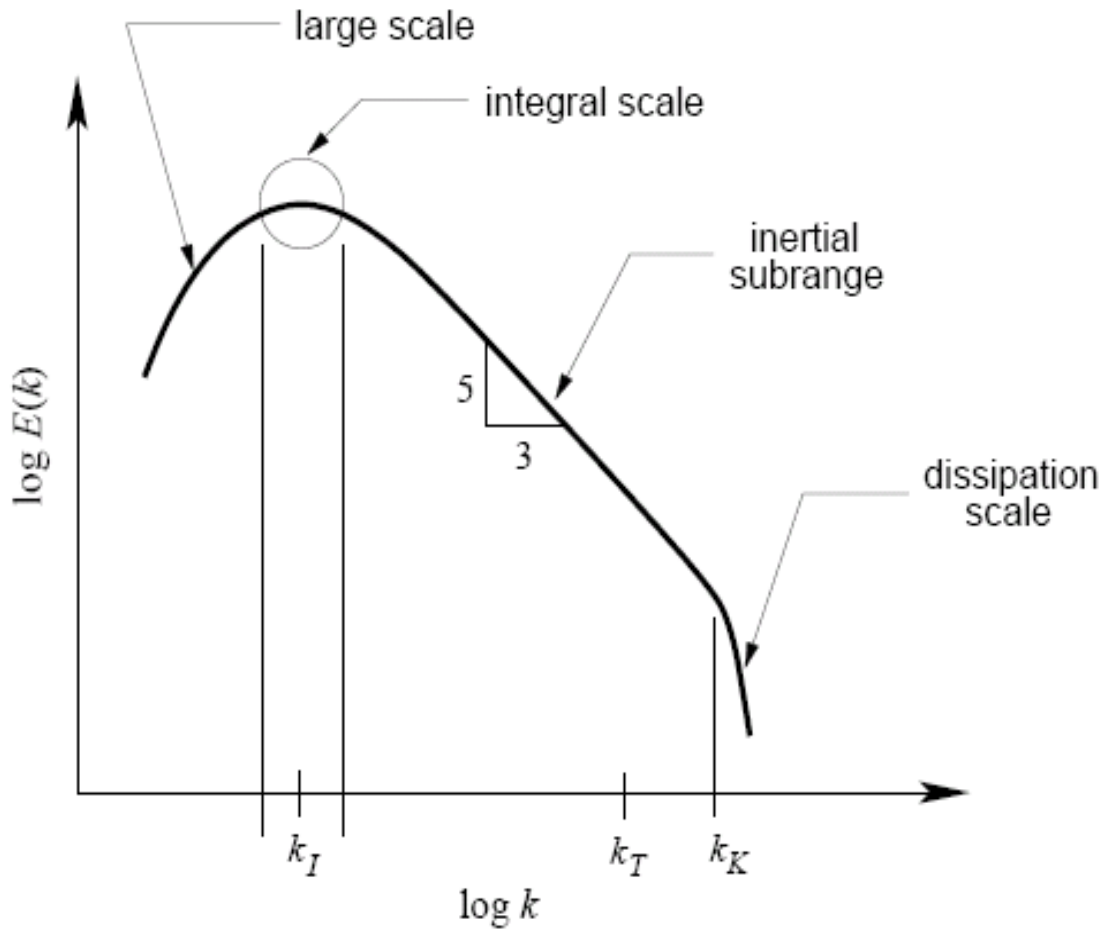


Figure 61: Turbulence energy wavenumber spectrum

Flow in the presence of walls, i.e. pipe flows is considerably different from free turbulent flows. Velocity fluctuations or turbulent stresses are generated and maintained by the shear in the flow. An early book by Schlichting (Schlichting, 1979) and Versteeg et al (Versteeg & Malalasekera, 2007) provides great detail into the characteristics of the turbulent boundary layer laws and will be summarised here. In practical pipe flows such as the ones in this thesis, the Reynolds number  $Re_L$  based on the flow direction tends to be large,  $> 10^5$ . This means the inertia forces are much larger than the viscous forces at these scales. However, close to the wall as the value of velocity approaches 0 and thus so does  $Re_L$ , viscous forces become dominant. Therefore, a point located in the bulk flow will be mainly affected by the no slip condition on the wall which manifests itself as the wall shear stress ( $\tau$ ), not viscosity itself, on the bulk flow. The flow away from the wall is inertia-dominated, whereas the thin layer close to the wall is controlled by viscous effects.

The viscous sub-layer, closest to the wall, is extremely thin, typically  $Y^+ < 5$ . As the name suggests, this near-wall region is dominated by viscous effects with a linear mean

velocity profile and is responsible for a large amount of dissipation. The dimensionless wall distance,  $y^+$  is defined in Equation [27] as:

$$y^+ = \frac{U^* d}{\nu}$$

[27]

Outside of this sub-layer is a turbulent region where both viscous and turbulent effects are important.  $U^+$  is a dimensionless number defining the mean flow velocity,  $U$  divided by the friction velocity,  $u^*$ . This inertial region where the  $y^+$  value ranges from 30 to 500 is often called the log-law layer because of the logarithmic relationship between  $u^+$  and  $y^+$ . The shear stress is deemed to be constant and equal to the wall shear stress. This layer is where the turbulent (Reynolds) stresses dominate. The relationship between  $u^+$  and  $y^+$  is graphically represented in Figure 62.

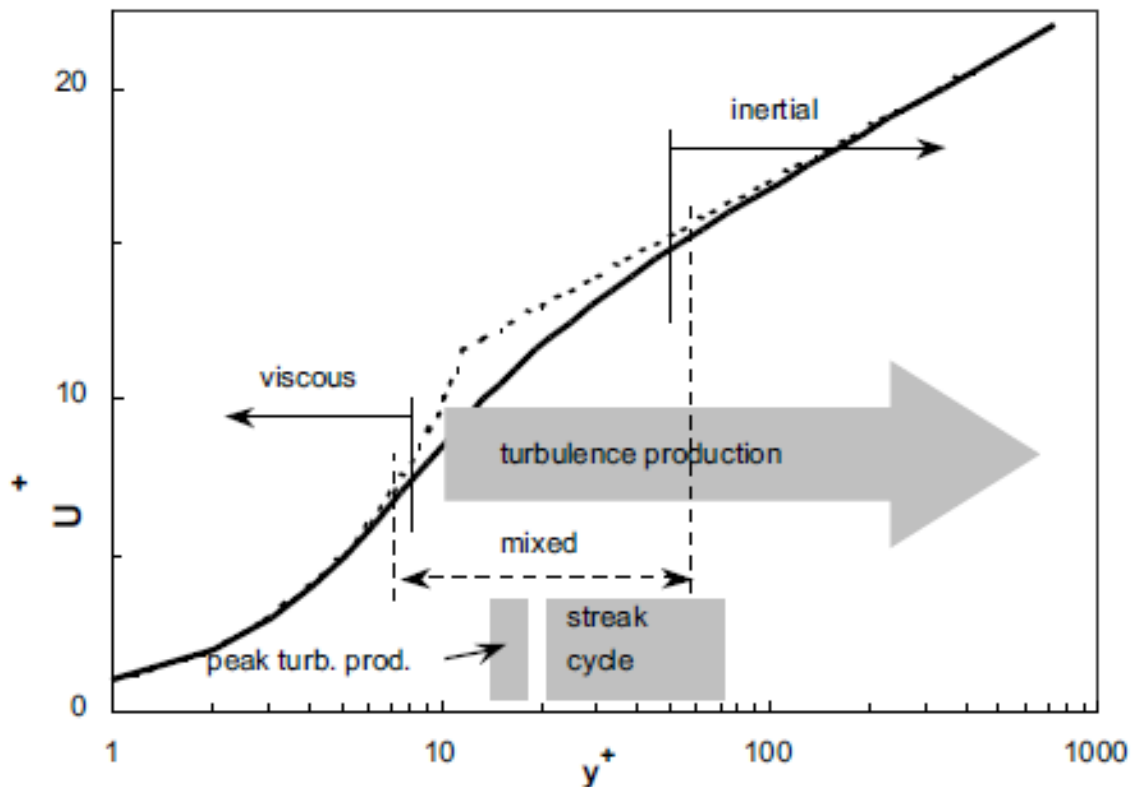


Figure 62: Velocity profile for a fully developed wall-bounded flow (Villiers, 2006)

The outer layer follows the velocity-defect law. The wall shear stress, when viewed as the cause of the velocity retardation effect reduces as the pipe centreline is approached. Thus, the effect of viscosity is negligible. The velocity deficit law is given in Equation [28] (Versteeg & Malalasekera, 2007):

$$\frac{U_{max} - u}{u^*} = g \left( \frac{y}{\delta} \right) \tag{28}$$

Overall, these characteristics of turbulent flows create a velocity profile as shown Figure 9 and in Figure 63 below.

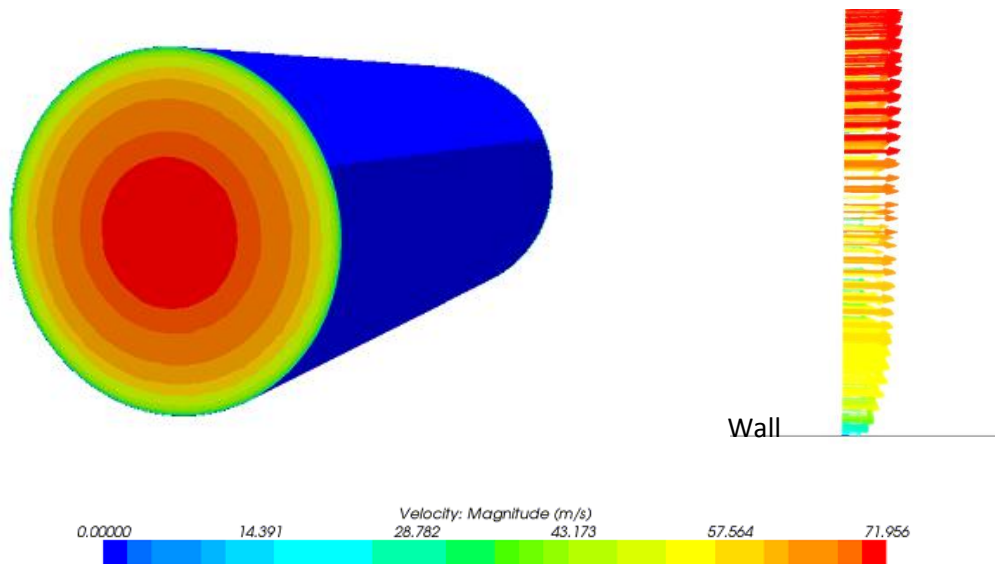


Figure 63: Steady state fully developed profile

The velocity distribution (profile) of fully turbulent flow in a pipe can be generally described by the 1/7-th power law as derived by Shlichting (Schlichting, 1979). The relation between the mean flow velocity  $U$  and  $U_{max}$  is given by Equation [29].

$$\frac{u}{U_{max}} = \left( \frac{y}{\delta} \right)^{1/7} \tag{29}$$

This chapter section has described how turbulence can be a very complex problem to accurately solve in fluid dynamics computations. Turbulence is maintained, as well as generated, by shear stresses in the main flow and viscous effects close to walls due to wall friction. This results in a very complex flow structure with many length scales of fluctuating velocities. All of the above effects and interactions must be sufficiently captured to accurately determine the flow behaviour in complex geometries. Ideally, the whole spectrum of the turbulent scales would be solved completely. However, at the current time of writing, this is impractical for even the most basic cases. Therefore, some, or the entire spectrum of turbulence needs to be modelled in some form. The statistical analysis calculations briefly described above are some of the ways turbulence can be modelled and monitored. The turbulence characteristics can be compared with detailed experimental turbulence statistics as detailed by Kim et al (Kim, et al., 1986). In the paper by Kim et al, direct numerical simulation of turbulent channel flow is performed where all essential scales of motion are resolved. The database generated by such a simulation is essential to validate turbulence in wall-bounded flows and for the design and testing of turbulence closure models. For reference, turbulent statistics are presented in the conference paper and Journal article by Piomelli (Piomelli, 2001) and (Piomelli, 2008) respectively.

### 3.1.1 RANS Solvers

The basic equations that govern fluid flow are generally known as the Navier-Stokes equations of motion. The Navier-Stokes equations can also be used for turbulent flows with appropriate modifications – the Reynolds averaged Navier-Stokes equations (RANS). Turbulence modelling using RANS equations are based on averaging the flow properties. RANS are time-averaged modification of the compressible Navier-Stokes equations and turbulence models are semi-empirical mathematical relations that are used to predict the general effect of turbulence. The derivation of the RANS equations can be found in fluid mechanics literature, such as Schlichting (Schlichting, 1979). Except for a number of simple laminar flow cases, no closed analytical solutions to these non-linear equations are known. Therefore, one needs to resort to numerical simulation techniques in order to get at least an approximate solution of a given fluid dynamics problem (Schlatter, 2005). As stated by Georgiadis et al (Georgiadis & DeBonis, 2007), RANS models can only provide a simple statistical representation of the turbulence in the form of the turbulence kinetic energy and

a local length scale. Because of the interactions between the turbulent fluctuations, extra terms appear in the flow equations. The process of finding a closure to the extra terms is called turbulence modelling. Two approaches are commonly used in CFD – the second moment closure and the eddy-viscosity approach (CD-Adapco, 2011).

In the second moment closure approach, transport equations are derived for each of the Reynolds stresses. The resulting equations are similar to the Navier-Stokes equations as they have a time derivative term, convective terms and source terms. These differential equations are derived by manipulations of the Navier-Stokes equations and introducing approximate models for complex terms of the flow gradients. A further term usually appears in the equation called the dissipation term which requires another differential equation to describe its transport. In three dimensional incompressible flows, the system results in seven additional differential equations for the six Reynolds-Stress terms and the dissipation term. These need to be solved together with the four flow equations to get a complete solution for the flow field. This requires a very large computational effort to solve (Sayma, 2009).

The eddy-viscosity approach is, in theory, less accurate but far more practical in terms of computational resource required (Sayma, 2009). In this approach, the Reynolds stress terms act like the viscous terms and a new quantity called the turbulent viscosity is introduced. This takes a similar form to the original momentum equation. However, the viscosity is replaced by the sum of the viscosity and the turbulent viscosity. Thus, the problem becomes finding the distribution of the turbulent viscosity within the domain.

Several models have been developed to find this unknown distribution. The most basic forms are called the zero-equation models. Simple algebraic relations are used to obtain eddy viscosity. The next order of complexity (and accuracy) are the so-called one-equation models. In these models, a transport equation which contains time derivative, convection, diffusion, source and sink terms is derived for the transport of the eddy viscosity.

A further level of complexity and accuracy can be obtained from solving the two transport equation models – one representing the generation and transport of turbulence and the other representing dissipation (Wilcox, 2004). These extra terms are generally accounted for with classical steady state turbulence models, the most popular being the K- $\epsilon$ , K- $\omega$  and the Reynolds stress model (Versteeg & Malalasekera, 2007). The K- $\epsilon$  model which is utilised in this thesis is explained along with a summary of other common two-equation RANS solvers.

The K-Epsilon model solves two separate transport equations which allows the turbulent velocity and length scales to be independently determined. It has become the workhorse of practical engineering flow calculations since it was proposed by Launder & Spalding (Launder & Spalding, 1972). The model is a good compromise between robustness, computational cost and accuracy. It is based on the presumption that an analogy exists between the action of viscous stresses and Reynolds stresses on the mean flow. In two-dimensional thin shear layers the changes in the flow direction are always so slow that the turbulence can adjust itself to local conditions. In flows where convection and diffusion cause significant differences between production and destruction of turbulence e.g. in recirculating flows, a compact algebraic prescription for the mixing length is no longer feasible. The way forward is to consider statements regarding the dynamics of turbulence. The K- $\epsilon$  model focuses on the mechanisms that affect turbulent kinetic energy (Versteeg & Malalasekera, 2007). The two variables,  $k$ , turbulence kinetic energy and  $\epsilon$ , viscous dissipation rate are introduced when using this model.  $K$  and  $\epsilon$  are used to define velocity scale,  $u_l$  and the length scale,  $\Delta$  representative of the large-scale turbulence as given in Equation [30].

$$u_l = K^{1/2} \quad \Delta = \frac{K^{3/2}}{\epsilon} \quad [30]$$

By applying dimensional analysis, the eddy viscosity ( $\mu$ ) is given by Equation [31].

$$\mu = C\rho u_l \Delta \quad [31]$$

Production and destruction of turbulent kinetic energy are closely linked. Adoption of this theory within the model ensures that  $\epsilon$  increases rapidly if  $K$  increases rapidly and vice versa. The specific models within K-Epsilon enable a custom solver for specific conditions. They concentrate on specifying the type of wall treatment necessary with a choice of wall  $Y^+$  groups, and single or two layer approaches. Typically, small cells on the wall are necessary to result in a low wall  $Y^+$ , in order to model the viscous sub-layer correctly. The two layer model divides the domain into two layers, whereby in the lower layer the turbulent viscosity and dissipation rates are calculated as a function of wall distance. The dissipation rate values are

then blended with the values obtained for the upper layer, and then the turbulence kinetic energy is solved for the whole of the flow.

There are many examples of U-RANS-K- $\epsilon$  based aero-acoustic studies. Several automotive examples, including the side window buffeting study by Yang et al (Yang, et al., 2014 (Accepted)), exhaust gas after treatment by Haynes et al (Hayes, et al., 2012) external aerodynamics, heat transfer and HVAC flows detailed by Tu et al. (Tu, et al., 2012).

The K-Omega model provides a very similar model to K-Epsilon, whereby two equations for turbulence are used alongside the introduction of turbulence kinetic energy and dissipation rate terms,  $k$  and  $\omega$ . A disadvantage of the  $k$ - $\omega$  model is that it creates sensitive free-stream/inlet conditions.

Robustness, economy, and reasonable accuracy for a wide range of turbulent flows explain RANS-based solver popularity in industrial flow and heat transfer simulations. Many variances of these RANS-based solvers are available including unsteady solvers in an attempt to model specific flow regimes more effectively. They are semi-empirical models, and the derivation of the model equations relies on phenomenological considerations and empiricism. Thus, as the effects of turbulence are replaced by a turbulence model, these models inherently have limitations with significant 3-dimensional compressibility, unsteady eddy capture and acoustic analysis due to only being able to provide time-averaged turbulent information. Smaller eddies are close to isotropic and produce a universal behaviour at sufficiently high Reynolds numbers. Conversely, the larger eddies tend to be more anisotropic and their behaviour tends to be more dictated by the geometry of the domain (Versteeg & Malalasekera, 2007). An Unsteady RANS (U-RANS) based solver must be described by a single turbulence model. Thus, the U-RANS simulations are compromised and are moreover often ill-posed for separated flows as studied by Villiers (Villiers, 2006), Garnier et al (Garnier, et al., 2012) and (Breuer, et al., 2003) amongst others. An LES solver is often more suitable for these conditions as the large eddies are directly computed. LES solvers are described in more detail in the following section.

### 3.1.2 LES Solvers

Unlike RANS solvers, with Large Eddy Simulation (LES), only part of the turbulence is modelled. The large scale turbulence is solved directly and the smaller scale eddies are space filtered by the unsteady RANS equations. Sub-grid scale kinetic energy is a physical by-product of the flow. It is a sub-grid model as the LES solvers use it as a function of grid spacing. The grid spacing,  $\Delta$ , is treated as a mixing length from which an effective viscosity is formed. (Durbin & Medic, 2007) This means large grid scales (LGS) are resolved and the small sub-grid scales (SGS) are modelled. (Davidson, 2010). LES always uses a sub-grid scale model such as Smagorinsky or WALE—which in turn directly computes sub-grid viscosity. Within this computation is an implicit level of sub-grid kinetic energy.

With a significantly lower proportion of the flow modelled compared to Unsteady Reynolds-Averaged Navier-Stokes (U-RANS) methods, LES solutions are more useful in providing a greater insight into processes involved inside the cavity. Whilst the LES equations are similar to U-RANS equations, they are very different in application. LES solvers fully resolve the large eddies in a time accurate manner and significant unsteady motion should be present. U-RANS uses ensemble averaging (i.e. realisations of the mean flow over many instances) and resolve the transient behaviour of the flow variables, which are shown to vary significantly over time (Salim, et al., 2011). LES gives a much greater detailed solution as large turbulent scales are directly resolved at instantaneous fluctuations in time, unlike U-RANS solvers which model the complete range of turbulent eddy scales. However, this also means LES is much more computationally expensive. The  $Y^+$  value for Large Eddy Simulations should be less or equal to 1 for adequate resolution of the near wall flow (see Chapter 3.1 for details). For reference, when using a U-RANS K-E solver, a  $Y^+$  value of between 30 and 100 is acceptable depending on Reynolds number (Versteeg & Malalasekera, 2007).

Large eddy simulation (LES) directly computes only into the inertial sub-range of the turbulent energy spectrum, provided in Figure 61. By explicitly solving for more of the turbulence and modelling less of it, the error in the turbulence modelling assumptions is not as consequential. It is hypothesized that the smaller eddies are self-similar and thus lend themselves to simpler and more universal models. The smaller eddies are more isotropic and homogeneous than the larger scale eddies and they also tend to be less affected by particular flow conditions, i.e. geometry, inflow, etc. (CD-Adapco, 2011)

As previously stated, the governing equations for fluid dynamics are the compressible Navier-Stokes equations for velocity components,  $u$  ( $i = 1,2,3$ ). In this

decomposition,  $\bar{u}$  is termed the filtered or resolved scale part of the solution.  $u'$  is termed as sub-grid scale or unresolved part. It is important to note that both resolved and unresolved scales depend on both space and time.

The x-component of unsteady Navier-Stokes equations for a fluid with constant viscosity  $\mu$  is as shown in Equation [32]:

$$\frac{\partial(\rho u)}{\partial t} + \text{div}(\rho u u) = -\frac{\partial p}{\partial x} + \mu \text{div}(\text{grad}(u)) + S_u$$

[32]

When the flow is incompressible, the viscous momentum source term becomes zero. Spatial filtering by a low pass filter of above equation and  $u' = 0$  yields Equation [33]:

$$\frac{\partial(\rho \bar{u})}{\partial t} + \text{div}(\rho \bar{u} \bar{u}) = -\frac{\partial \bar{p}}{\partial x} + \mu \text{div}(\text{grad}(\bar{u}))$$

[33]

To compute the convective non-linear term on the left hand side, it can be expanded as in Equation [34].

$$\text{div}(\rho \bar{u} \bar{u}) = \text{div}(\bar{u} \bar{u}) + (\text{div}(\rho \bar{u} \bar{u}) - \text{div}(\bar{u} \bar{u}))$$

[34]

The first term on the right hand side can be calculated from the filtered  $u$  solution and the second term is replaced by a model. Substitution of Equation [34] into the filtered compressible Navier-Stokes equations and some re-arrangement yields the LES momentum equation, Equation [35].

$$\frac{\partial(\rho\bar{u})}{\partial t} + \text{div}(\rho\bar{u}\bar{u}) = -\frac{\partial p}{\partial x} + \mu \text{div}(\text{grad}(\bar{u})) - (\text{div}(\rho\bar{u}\bar{u}) - \text{div}(\bar{u}\bar{u}))$$



Momentum



Convection



Pressure



Viscous forces



Sub-grid Stresses

[35]

One component of the tensor,  $\text{div}(\rho\bar{u}\bar{u})$  can be examined in detail to deduce the structure induced by decomposition and filtering:

$$\overline{(\bar{u} + u')(\bar{u} + u')} = \overline{\bar{u}\bar{u}} + \overline{\bar{u}u'} + \overline{u'\bar{u}} + \overline{u'u'}$$

[36]

The first term in Equation [36], called Leonard stresses are due to effects at resolved scales. The second term is the cross-stresses. They are due to interactions between the sub-grid scale (SGS) eddies and resolved flow. Finally, the LES Reynolds stresses are caused by convective momentum transfer due to interaction of SGS eddies. A more complete definition and derivation of the fundamental LES governing equations and filtering operators is provided by E. Garnier et al, (Garnier, et al., 2009).

Just like Reynolds stresses in RANS equations, SGS stresses must be modelled. The filtered equations which appear similar to the U-RANS equations include the turbulent stress tensor,  $T_t$  which represents the sub-grid scale (SGS) stresses. With this approximation, the SGS stress can be written analogously to the turbulent Reynolds stress of the RANS equations. Within the CFD solver, the eddy-viscosity/diffusivity is modelled using the Boussinesq approximation (Boussinesq, 1877) which parameterizes the SGS stresses as follows in Equation [37]:

$$T_t = 2\mu_t S_r - \frac{2}{3}(\mu_t \omega + \rho k)$$

[37]

The main role of the SGS model is to determine the correct eddy viscosity by extracting energy from the resolved scales. The accuracy of an LES simulation is essentially dependent on the SGS model in mimicking the drain associated with the energy cascade. Substantial work has been carried out in the last few decades surrounding this topic to create a robust and widely usable SGS model. This is accomplished by using two filters, the usual LES filter and a “test filter”.

The Smagorinsky Sub-grid Scale model, first published by Smagorinsky, (Smagorinsky, 1963) provides the following mixing-length type formula for the SGS viscosity (Equation [38]). The Smagorinsky model is the oldest and most widely used SGS model. The Smagorinsky Sub-grid Scale model uses a mixing length hypothesis to model the sub-grid scale stresses. It assumes a local equilibrium between production and dissipation of SGS kinetic energy (Lu, 2014). It is the original and most basic sub-grid scale model, upon which many more advanced models are based.

$$\mu_t = C_s \Delta^2 S_t$$

[38]

The sub-grid stresses are represented by evaluating the Smagorinsky SGS coefficient,  $C_s$  from the resolved test filter band. This is not a universal value. Different types of flow problems require varying values and this has to be determined empirically. As the SGS can give inaccurate scaling at walls, a Van Driest damping function which modifies the length scale closer to the wall is required for the accurate simulation of wall bounded calculations. The length scale is directly related to the cell volume,  $v$  and the wall distance,  $d$  as given in Equation [39]:

$$\Delta = \begin{cases} f_v C_s V^{1/3} & \text{If length scale limit not applied} \\ f_v \min(\kappa d, C_s V^{1/3}) & \text{If length scale limit is applied} \end{cases} \quad [39]$$

The Van Driest damping function,  $f_v$  is computed as shown in Equation [40]:

$$f_v = \begin{cases} 1 & \text{No damping} \\ 1 - \exp\left(-\frac{y^+}{A}\right) & \text{Standard} \\ \sqrt{1 - \exp\left(-\frac{y^+}{A}\right)^3} & \end{cases}$$

[40]

The standard Van Driest damping function was formulated by Van Driest in 1956, (Driest, 1956). The modified version of the Van Driest damping function which is utilised in the CFD solver is attributed to Piomelli et al, (Piomelli, et al., 1996). The damping coefficient,  $A$  has a default value of 25 (CD-Adapco, 2011). The damping function is used to correct the Smagorinsky SGS model's erroneous near wall behaviour. The cut-off wave number needs to lie within the constant gradient region of the energy spectrum, i.e.  $k^{-5/3}$  of the Kolmogorov energy cascade region. The damping of the turbulence increases as the value of the SGS coefficient increases. Typical values of  $C_s$  reported in the literature range from 0.1 to 0.2 depending on the flow (Garnier, et al., 2009). Lilly (Lilly, 1967) suggested values of  $C_s$  between 0.17 and 0.21 in the inertial sub-range of energy spectrum. Rogallo and Moin (Rogallo & Moin, 1984) suggested values of  $C_s$  between 0.19 and 0.24 for results across a range of grids and filter functions. However, with the modified damping function, the coefficient  $C_s$  is found to lie in the reduced value range of 0.165 for homogeneous isotropic decaying turbulence to 0.07 for channel flows to sustain turbulence. Therefore  $C_s$  has a default value of 0.1 in Star CCM+ as this value was found to be a good compromise between these extremes.

The Smagorinsky SGS model is useful for reference simulations, since it is the original algebraic sub-grid scale model formulation. In its basic form, it is simplistic and is not computationally expensive. However, eddy-viscosity/diffusivity models, such as the Smagorinsky model are completely dissipative and it is due to this that it has inherent robustness limitations for wall-bounded flows. It is now known that for wall-bounded flows, 1/3 of turbulence kinetic energy is backscattered i.e. small eddies pass energy back to large scales. Mixed models consist of some linear combination of a dissipative model such as Smagorinsky model and scale-similarity model. Piomelli (Piomelli, 1999) and Lu (Lu, 2014) note the scale-similarity models produce too much backscatter themselves and consequently are numerically unstable. Mixed models have not been as effective at least in part because the weighting to be employed for two parts is not easily estimated.

The production of dynamic models has caused significant progress in the SGS modelling of turbulent flows and has removed many of the shortcomings encountered with static models (Villiers, 2006). Dynamic models such as proposed by Germano (Germano, et al., 1991) are constructed as to permit determination of Smagorinsky “constant” as a function of both space and time. The coefficient is dynamically adjusted to the local flow conditions such as in the vicinity of walls and transitional flow regions, a function which is normally performed by the van Driest damping function. The SGS stresses obtained using this model vanish in laminar flow and at solid boundaries and is said to maintain good asymptotic behaviour in the near-wall region of a turbulent boundary layer. The WALE (Wall-Adapting Local-Eddy Viscosity) SGS model is another more modern sub-grid scale model that uses a novel form of the velocity gradient tensor in its formulation. The main advantage of the WALE model is that it does not require any form of near-wall damping. This is an alternative model to the standard Smagorinsky model. The major drawback of this approach is that additional averaging, either in homogeneous directions, along streamlines or in local regions of the flow, is necessary to avoid excessive fluctuations in the model coefficients (Villiers, 2006). More information on dynamic SGS models is provided in the article by Nicoud and Ducros (Nicoud & Ducros, 1999). There are still some drawbacks to these more recent approaches, which includes the requirement of additional averaging, either in homogeneous direction, along the streamline or in local region of the flow which is necessary to avoid excessive fluctuations in model coefficients. In addition to this, unless the scheme is additionally bounded, the dynamic procedure occasionally produces negative dissipation, which if left unchecked, could violate the conservation of energy law and leads

to unphysical results. A detailed study of current SGS models is covered by Schlatter (Schlatter, 2005), in particular, Section 2.2.

The Smagorinsky SGS model is used in this project as it has substantial published literature and validations with theory/experiments such as the work carried out by Moin and Kim (Moin & Kim, 1982) where analysis of fully developed turbulent channel flow was simulated numerically. Rizzetta and Visbal (Rizzetta & Visbal, 2003) carried out Large-eddy simulations of supersonic cavity flow fields using a high-order numerical method with a Smagorinsky derived SGS model. No wall functions were used at the solid boundaries with a 20 million point grid. It has proven to create extremely good results with the majority of geometry configurations. Salvador et al (Salvador, et al., 2011) modelled cavitation in a diesel injector nozzle using the Smagorinsky model as the sub-grid scale turbulent model and the Van Driest model for the wall damping. The model is able to predict with a high level of confidence the behaviour of the internal flow at cavitation conditions (Salvador, et al., 2011).

### **3.2 Numerical Investigations into Cavity Flows**

More recent studies of aero-acoustic cavity flows tend to include the use of numerical computational codes as a useful comparison tool such as Caro, et al (Caro, et al., 2005), Tam, et al (Tam, et al., 2005), Marsden, et al (Marsden, et al., 2012), Rizzetta & Visbal (Rizzetta & Visbal, 2003) and Vikramaditya & Kurian (Vikramaditya & Kurian, 2013), as also used in the present study. This is mainly due to the rapid increase of affordable computational resource within the last two decades. The use of CFD enables visualisation of the flow in a much more detailed way to the options available in purely experimental papers discussed in the above section. Other important and useful tools are available from CFD for the study of resonant devices. It is possible to assess very complex geometries, analyse many variables quickly and perform post-processing of the data in several visual and numerical forms. The use of CFD as a design tool has the potential to vastly reduce time and cost constraints for industrial design and manufacture. The following section aims to discuss previous studies carried out with the use of CFD for the field of aero-acoustic resonant cavities. The various CFD solvers of current times are summarised along with best practices and discussions for mesh, time-step and boundary condition settings.

Schlichting's book (Schlichting, 1955) is very important for the field of Computational Fluid Dynamics (CFD) in general. It is a very well recognised and respected source of

information on boundary layer theory. Shlichting explains the fundamental behaviour of flow close to no-slip walls, such as used in this paper and in most practical scenarios. The shape and the primary functions of the universal boundary layer laws are described. This enables the reader to assess, with greater understanding, the suitability and quality of a CFD model with respect to real turbulent flows.

Radavich et al (Radavich, et al., 2001) investigated the flow-acoustic coupling of QWT's as side-branches. Two-dimensional CFD simulations are compared against the experiments of Ziada (Ziada, 1994) and the acoustic power theory of Howe (Howe, 1984). Radavich et al reported good agreements between the CFD simulations and experiments/theory and showed CFD can be used to visualise flow in a resonant cavity.

The paper by Peters, et al (Peters & Riezebos, 2001) has similarities to the one here as it aims to assess the validity of a simulation tool for flow induced pulsations. In this paper, Peters, et al applies the one-dimensional (1D) PULSIM code to cases which have occurred in two real life gas control stations. Strong flow-induced pulsations were observed at these stations. These resonances were found to occur when the gas flow was passing closed side branches in the system at a sufficiently high velocity. Peters et al (Peters & Riezebos, 2001) states, flow separation does not only occur when the mean flow is flowing along a closed side branch, but also when the mean flow is bending into the side branch or coming out of the side branch. In particular the local geometry of the edges of the T-joint where the shear layer is generated appears to be critical. This does suggest the neck area, particularly the joint between the side branch and main flow is significant for unwanted noise generation. Since the frequencies of interest were below the cut off frequency for plane acoustic waves in the pipe, a one-dimensional simulation of the piping network was sufficient. This is not the case here as detailed vortex shedding is not captured in a 1 dimensional solver. The maximum frequency in (Peters & Riezebos, 2001) is 500 Hz. This is well below the frequency of interest, which in this case is up to 5-10 kHz.

At the current time of writing, the majority of studies in industry are RANS based simulations, primarily due to the costs associated with LES. Many of the assumptions and limitations of these models can be overcome by specialised modifications, such as those available for in-cylinder studies. However, for aero-acoustic studies, by solving the full compressible Navier–Stokes equations, the nonlinearities in the acoustic waves can be solved, thereby circumventing the constraint of linear wave amplitude treatments. Also, for vortex modelling, which is of great importance throughout this thesis, rather than approximating the vortex strength, location and path as they travel across the mouth of a

side-branch, as is done in many of the vortex methods, LES solvers allow the vortex to develop naturally and interact with both the acoustic and flow field as it travels over the side-branch. Many of the analytical 1D and RANS models also use the assumption of incompressible flow for low Mach numbers. This requires that the acoustic waves be introduced externally from experimental measurements. Such approaches do not allow for a true interaction between the vortices and the acoustic field. As the vortices are unable to affect the fixed acoustic amplitude. Thus, this simplification makes prediction of variations of the acoustic pressure amplitude impossible. By solving for compressible flow, the acoustic element of the flow is solved in parallel. As acoustics is an inherent fluid dynamics problem, this is essential for the prediction of flow generated noise.

Following on from an earlier study by Kannan (Kannan, et al., 2004) – see Chapter 1.5, Kannan et al (Kannan, et al., 2005) studied tonal noise produced by an automotive intake manifold with a side-branch cavity. The intake manifold in this case was found to produce a whistle noise in high torque conditions. The whistling geometry was tested using 2D CFD to understand the mechanism of the flow-generated noise. The results were compared to a modified geometry which was found to suppress the whistle. The CFD clearly demonstrates some flow phenomena present, particularly at the leading and trailing edges of the cavity. The direction and amplitude of the shed vortices can be estimated. However, the limitations of the 2D CFD are well documented. Kannan et al states the shear layer development is inherently complex 3D in nature and it's coupled response to the acoustic field cannot be simplified to 2D. This is also mirrored by the noticeable difference between the frequency and SPL of the tones when compared to the experimental results. Overall, this study has shown how CFD is able to predict aero-acoustic noise from a cavity. Although the absolute results are not robust with a 2D simulation, the study shows a high level of optimism for 3D CFD to be utilised as a precise design optimisation tool.

The paper by Cattafesta (Cattafesta III, et al., 2008) is a recent review of flow induced cavity oscillations, particularly active control of these oscillations. The review focuses on experimental implementation of open and closed-loop control approaches to flow control, yet has a very good bibliography of work in the research area of cavity flows. The review article is based around aircraft store openings so supersonic speeds are more relevant, unlike the research carried out in this thesis. The review article states, "Some factors to be considered include; A reduction in the flow unsteadiness provides the store with more repeatable and stable initial conditions compared to the uncontrolled case and reduces disturbances that affect the store trajectory after it is released. Secondly, a change

in the mean profile of the shear layer can alter the forces and moments encountered by the store, especially as it traverses a finite-thickness shear layer.” (Cattafesta III, et al., 2008). Clearly, the influence of changes in the mean flow field is still not completely clear. A more complete assessment of cavity dynamics needs to be carried out to provide high resolution time dependant tests. Cattafesta echoes this comment and suggests such data would enable the incorporation of more relevant physics into cavity flow dynamics and would also serve as a benchmark for validation of CFD simulations (Cattafesta III, et al., 2008).

Xu (Xu, et al., 2007) performed an interesting study of Simulations of the Separated Flow Around a cylinder using DES and LES. Xu found the trends for the mean quantities for the Large Eddy Simulation (LES) were in good agreement with measured data. A decline in accuracy was shown in the results for Detached Eddy Simulation (DES) with the same mesh. However, the far-field radiated sound from the DES agreed significantly better with the measured results compared to the LES results which over-predicted the sound levels. This is explained in the paper by Xu by the coarse grid used for the LES which yields too coherent structures, whereas the high dissipation in the DES reduces the turbulent motions. The wall-pressure spectra was also better predicted by the LES along with exhibiting a greater cut-off frequency. The authors concluded that the LES is a better candidate compared to DES even if the mesh resolution does not fulfil the traditional restrictions in LES. The simulations described by this paper reveal the dependence of the results on the mesh resolution and on the SGS model. The radiated field induced by the cavity flow is greatly sensitive to small variations in flow such as the concentration of the coherent structures. Thus, the computation of the correct acoustic levels in the far field is challenging problem. It requires subsequent investigations on the role of the SGS models and on the effects of the numerical resolution. This thesis does not focus on the far-field noise. Instead, the area of interest surrounds the generation of acoustic pulsations in the immediate geometry of the noise source, to investigate the detailed interactions present.

Gloerfelt, (Gloerfelt, 2009 (1)) gives a concise overview of the current progress in automotive cavity noise design and control. The first section is a review article of automotive component noise. The second section by Gloerfelt (Gloerfelt, 2009 (2)) is a more detailed investigation of cavity noise and the substantial amount of theory surrounding this research area. Gloerfelt agrees with other authors in that LES solvers are required and RANS is not suitable. Experimental data is obtained for comparison with numerical results. Several works were compared using 2D simulations based on U-RANS which predicted the main resonance frequency. Two-dimensional behaviour of the recirculation zone was visible but a 3D

approach is required to describe the turbulent mixing inside the cavity, and if necessary the turbulent character of the incoming flow. Gloefelt also echoed that a Direct Numerical Simulation (DNS) solving all the scales down to the Kolmogorov scale would be impractical. To achieve reasonable computational cost, and given the dominance of coherent structures in the shear layer for cavity flows, LES is an ideal candidate.

The paper by Tam et al (Tam, et al., 2010) reports the results of a study extending the author's previous work to three dimensions of local-reacting acoustic liners used to suppress fan noise from jet engines. In a previous works by the present authors (Tam, et al., 2005), a computational and experimental investigation of the acoustic properties of two-dimensional slit resonators was carried out. For the later paper, the authors compared Direct Numerical Simulation (DNS) results with experimental measurements in a normal incidence impedance tube with zero mean flow. The second objective was to study the flow physics of resonant liners responsible for sound wave dissipation. Both discrete frequency and broadband sound sources were tested with reasonable agreements found over a wide range of frequencies and sound pressure levels. Direct numerical simulation confirmed the findings in the earlier paper suggesting vortex shedding is the dominant dissipation mechanism at high sound pressure intensity. It was found, in three dimensions, the shed vortices tend to evolve into ring (circular in plan form) vortices, even though the slit resonator opening from which the vortices are shed has an aspect ratio of 2.5. Under the excitation of discrete frequency sound, the vortices are shed periodically. The paper provides images of the vortices being shed from each sharp corner of the slit. Tam, et al also found that the resonator impedance during broadband sound is found to not necessarily be the same as the resonator impedance during discrete frequency input. In other words,  $Z(o)$  does not equal  $Z$  if  $Z(o)$  is the impedance of the resonator under broadband input noise and  $Z$  is the impedance of the resonator under single frequency input noise. It was found, in general, the simulation results track the trends of the measured impedances quite well, but do not match to an acceptable tolerance to support the exclusive usage of direct numerical simulation for liner evaluation.

A comprehensive review of numerical simulations for cavity flows, mainly surround aircraft weapon bay problems is given by Lawson & Barakos (Lawson & Barakos, 2011). The authors state clearly that computational results quickly revealed that detailed simulation of transonic cavity flows with Rossiter tones present is not possible with RANS and U-RANS models. LES and DES simulation methods, however, ensured convergence of the results and useful comparisons against experiments. Lawson & Barakos also reviewed papers containing

passive flow control devices (spoilers, rods, wall modifications) and noted LES and DNS simulations are useful to analyse the effectiveness of these techniques and their influence in the cavity flow configuration. Limited studies associated with cavities of more realistic geometries suggest that the fundamental conclusions from the idealised cases are still valid. One further piece of useful information gathered from the paper suggests that energy is actually exchanged between the Rossiter modes so the dominant Rossiter mode shifts in time. At the current stage of cavity flow research, as suggested by Lawson & Barakos, experiments are required to compare unsteady pressure measurements with flow-field data from the simulations. The paper also gives an idea of the future direction of cavity flow research citing more complex cavity geometries could be analysed. The effect of the exterior cavities on the overall aerodynamics of the vehicle could be studied as well as the influence of the near-field of the cavity on stores during their release phase. Lawson & Barakos state, dynamic and static tests of the vehicles with the cavity exposed would be necessary over a range of speeds and altitudes. CFD work in this direction is perhaps easier than experimentation (Lawson & Barakos, 2011). This idea is exactly what the paper here is investigating – using CFD as a tool in the design phase to reduce the use of experimentation.

It is expected LES will become ever more prelevant in industry and research as computational power increases. However, for large complete geometries such as aircraft/vehicles at practical Reynolds numbers, LES is not a viable solution due to the large computational effort compared with the widely used steady state RANS equations such as the K- $\epsilon$  model. The future of LES and DNS to a lesser extent, has a future in the prediction and analysis of complex turbulent flows in which the representation of the unsteady turbulent fluctuations are important, such as large-scale flow separation in aerodynamics, aeroacoustics, heat transfer problems, transitional flows and turbulent combustion.

The remaining section of this chapter will describe the fundamental solver settings used throughout this study which are found to give the most optimal solution in terms of accuracy and computational solve time.

### 3.2.1 Aero-acoustic models

As the acoustic phenomena discussed in this thesis are predominantly a fluid dynamics problem, capturing the small pressure fluctuations accurately is essential to capture the acoustic wavelengths. Therefore, the computational aero-acoustic conditions need to simulate real life conditions to allow direct comparisons to be made between the simulation and real world experiment.

There are two main methods of Computational Aero acoustics (CAA). The first one option called Direct Noise Computation (DNC) in which the flow field and acoustic field is solved directly. It is essentially the method used for the full unsteady simulation to record the time-varying static pressure on points (probes) or surfaces. This method has strong similarities with experimental procedures using microphones to record the pressure fluctuations. There are large disparities between the small scales of turbulence and the relatively large scale of acoustic radiation wavelengths in turbulent flows. Therefore, a large range of energy scales need to be adequately captured. Preliminary basic simulations with steady state models and a relatively coarse mesh must be carried out, followed by transient runs in a refined mesh. Therefore, a compressible unsteady solver is needed using either Direct Numerical Simulation (DNS), Large Eddy Simulation (LES), Detached Eddy Simulation (DES), or Unsteady Reynolds Averaged Navier-Stokes simulation (U-RANS). Accurate aero-acoustic modelling is computationally expensive even with the use of U-RANS solvers. Very fine meshes and preservation of the weak acoustic waves are required because the small amplitudes and the propagative nature of acoustic waves. The use of low dissipation and low dispersion numerical methods to preserve the weak acoustics waves is essential, together with non-reflecting boundary conditions to allow the sound waves to exit the geometry freely. This means, although DNC is a powerful tool to investigate the noise generation mechanisms, it is computationally expensive to be used as an engineering tool. Hence it is often restricted to the more simplistic geometries. See for example the paper by Colonius (T Colonius, 2004). As the acoustic sources are directly computed, this is the most suitable method to accurately capture the wavelengths close to the source, thus this is the method used in this thesis.

It is worth noting the second approach, where the turbulent noise source field is computed and/or modelled separately from the far-field noise calculation. This class of methods are referred to as hybrid methods, or two-step methods. They are commonly used in CAA because the existing CFD solvers can be used to compute the aerodynamic field

(Gloerfelt, 2009 (1)). This can be advantageous as the required solver can be selected at the required time. Therefore, this approach is very affordable in terms of computational power although care must be taken to ensure adequate source terms are provided in the flow, i.e, adequate mesh density, to account for the sound radiation produced, comparable to real life situations. The various types of hybrid acoustic modelling available in Star CCM+ are detailed below.

Synthesized Fluctuations SNGR and Lilley noise source models use the modelled turbulence kinetic energy and length scales to create synthetic fluctuations in pressure and velocity. These fluctuations may subsequently be output directly for use in acoustics propagation codes. Broadband Noise Source models are based on the assumptions implicit to RANS turbulence modelling, these provide aero-acoustic source information through correlations. The acoustic modelling part is constructed from the acoustic source created from the RANS flow solution. They are strictly applied to flow-noise generated by turbulence. The Broadband Noise Source models are intended to be used as tools for qualifying a volume mesh before a transient acoustic analysis. They are applied in the post-processing stage of a preliminary steady analysis. The Broadband Noise Source models are applied in the post-processing stage of a simulation. There are two types available within the CFD solver - the Curle and Proudman models. The Curle acoustic power model, which assumes an isotropic turbulent flow field, computes the sound generated by dipole sources. This represents the fluctuating surface pressure with which the solid boundary acts on the flow. The noise level emitted by the turbulent boundary layer over a surface at low Mach number can be shown. The Proudman acoustic power (in dB) estimates the local contribution of the quadrupole sources as generated by isotropic turbulence. It displays the acoustic power per unit volume as emitted by the turbulence structures. The Ffowcs Williams-Hawkings (FW-H) acoustics simulation model is able to calculate the mid- to far-field sound signal radiated from near-field flow data provided by a CFD solution. The goal is to predict small amplitude acoustic pressure fluctuations at the receiver locations. In the FW-H approach, propagation of sound into the far field is not explicitly calculated, but computed using an analytical integral solution to the generalized wave equation. Therefore, numerical accuracy is an issue of much less concern than in the full DNC aero-acoustics approach, which explicitly resolves propagation of sound waves all the way to the far field. The FW-H model is ideal for wind tunnel simulations or stationary sources such as landing gear (CD-Adapco, 2011). The FW-H model is used only to predict the propagation of sound in free space. It does not include effects such as sound reflections, refraction, or material

property change. A FW-H simulation computes the time-accurate data on the emission surfaces (sources of noise), which are the integration surfaces for the FW-H solver, corresponding to a very fine mesh on the near field. Time-accurate solutions can be obtained from an unsteady turbulent or laminar simulation. Time variation of the sound pressure at user receiver locations is computed based on the FW-H solver.

### 3.2.2 Mesh

Large Eddy Simulations are very sensitive to mesh density. A mesh independence study is carried out in Chapter 4.2.1. The Mesh Frequency Cut-off scalar is a useful qualification of the suitability of the mesh before a transient calculation. A Mesh Frequency cut-off analysis makes it possible to assess whether the chosen mesh has adequate density to capture turbulent flow structures in the frequency range of interest. Thus, it gives a reasonable approximation of the maximum frequency the mesh is locally able to resolve. Given a cell dimension  $\Delta$  and local turbulence kinetic energy  $k$ , the smallest length scale of a turbulent eddy structure captured by the mesh is  $2\Delta$ ; its associated isotropic fluctuation velocity is  $\sqrt{2/3k}$ . Therefore the maximum frequency,  $f$  reasonable resolved by the local grid spacing  $\Delta$  is given by Equation [41];

$$f_{mc} = \frac{\sqrt{2/3k}}{2\Delta}$$

[41]

The transport-equation for  $k$  is derived directly from the unsteady compressible Navier-Stokes equations, therefore contains contributions from all the important mechanisms: convection, diffusion, production and dissipation. So long as the mean flow features are well captured in the modelling, the  $k$  solution tends also to be reasonably grid independent (Wagner, et al., 2007). Since this measure is derived from a steady-state solution, some limitations are inherent. The frequencies associated with time varying large-scale motions such as vortex shedding, which convect through the mesh, will not be accounted for. Instead, its usefulness is to approximate the frequencies of the turbulence scales which are modelled with U-RANS, and which become resolved in Large Eddy

Simulation. As Mendonca (Mendonca, 2005) states in other words, this measure is more valid for the broadband and less so for narrowband excitations. The mesh frequency cut-off measure has been applied to typical industrial applications at low Mach number flow. Wagner et al (Wagner, et al., 2007) demonstrated how the time-step and mesh density can affect the frequency distribution predicted by CFD simulations. If the frequency distribution tends to level out before the comparable experiment frequency, the time-step is likely to be too large. If the inverse is true, the maximum cell size is too large.

For the acoustic simulations in this thesis, the frequency range of interest is from 100 Hz to around 10,000 Hz. The maximum cell size can be calculated based on this requirement. One acoustical wavelength ( $\lambda$ ) needs to be resolved with at least 10 points. To allow the propagation of a 10,000 Hz noise source through the mesh, the maximum cell size is calculated in Equation [42].

$$\lambda = \frac{c}{f}$$

[42]

where  $C = 343$  m/s and  $f = 10000$  Hz. Therefore, maximum cell size =  $\frac{\lambda}{10} = \frac{0.0343}{10} = 0.00343$  m = 3.43 mm.

Thus, the maximum cell size which can resolve frequencies of up to 10,000 Hz, in this case, is found to be 3.4 mm. To accurately model the geometry and to reduce the numerical error as much as practically possible, it was decided to use a core mesh size of 2 mm with refinement in areas of interest/complex geometrical areas. There are two main mesh types available within the CFD solver for the core flow region. Visual representations of these meshes are provided in Figure 64. The Polyhedral mesh is, as the name suggests, a polyhedral cell shaped mesh which is created from an underlying tetrahedral mesh. This cell structure makes it ideal for highly complex geometries. The trimmed cell mesh provides a robust and efficient method of producing a high-quality grid for more regular geometries. The hexahedral mesh is constructed from cells from which it cuts or trims the core mesh using the starting input surface. The Hexahedral mesh tends to form a more uniform and less memory intensive mesh for the same base settings. Both are investigated in Chapter 4.1.

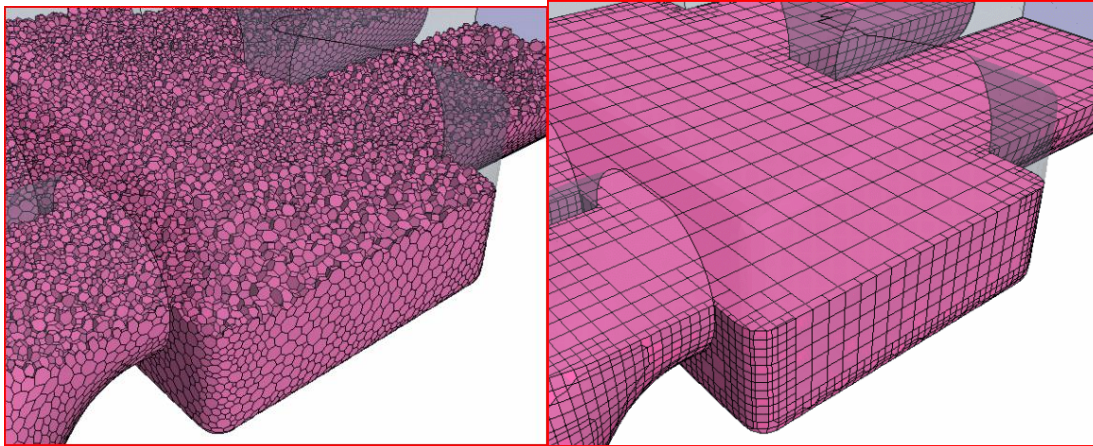


Figure 64: Volume mesh example. Left – Polyhedral, right – Hexahedral (CD-Adapco, 2011)

The Star CCM+ user guide (CD-Adapco, 2011) suggests some general guidelines as summarised below:

Memory requirements for meshing:

Trimmed mesh: ~ 0.5 GB / million cells.

Polyhedral mesh: ~ 1GB / million cells.

Memory requirements for solving (serial, two-equation turbulence model, assumed no multiphase flow, no energy equation, no chemical reaction etc...):

Polyhedral mesh:

Segregated: ~1GB / million cells

Coupled explicit: ~ 2GB / million cells

Coupled implicit: ~ 4GB / million cells

Trimmed mesh:

Segregated: ~0.5GB / million cells

Coupled explicit: ~ 1GB / million cells

Coupled implicit: ~ 2GB / million cells

Thus, the most efficient mesh and solver in terms of computational resource, as a generalisation, is a trimmed mesh with segregated solver. The polyhedral mesh can prove to be more effective, especially when the flow is not aligned to the mesh lines.

Prism layers allow the solver to resolve near wall flow accurately, which is critical in determining the flow features close to the wall such as separation. Accurate prediction of these flow features depends on resolving the velocity and temperature gradients normal to the wall. Depending on the Reynolds number, a turbulent shear layer requires in excess of 10-20 cells in the wall-normal direction for accurate resolution of the turbulent flow profile.

If only the main flow features such as large scale vortex shedding are required, coarser prism layer meshes including a wall-function can yield acceptable results. An example of a volume mesh including prism layers is provided in Figure 65. Prism layers do not only provide near wall mesh density, they also allow high-aspect-ratio cells to be used, thus providing better wall-normal resolution without incurring an excessive stream-wise resolution.

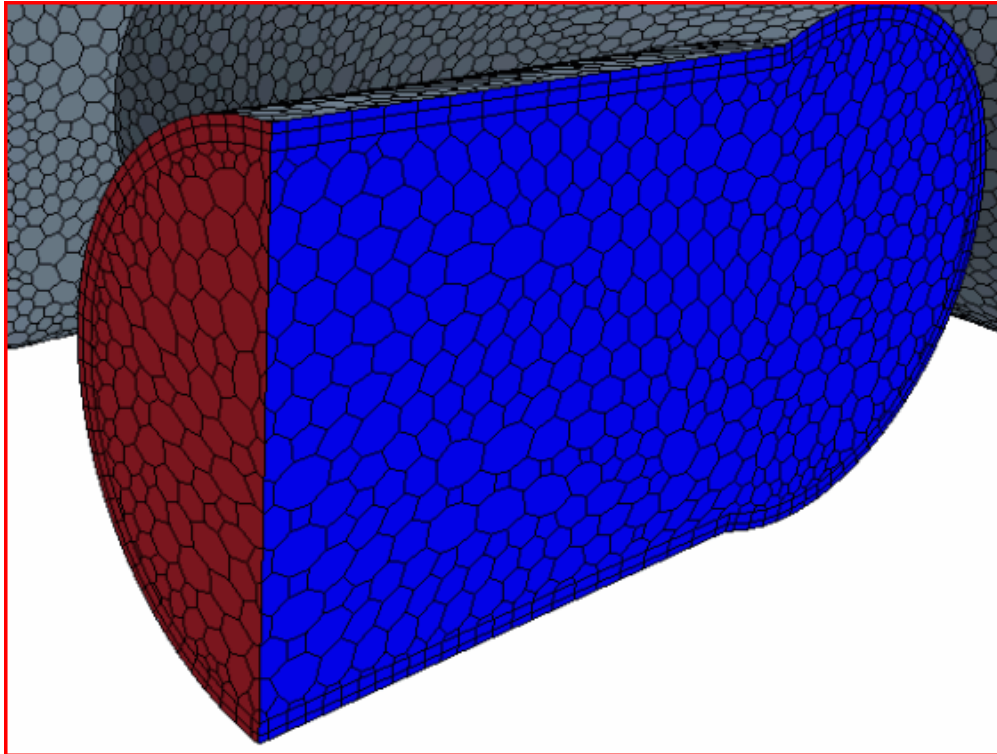


Figure 65: Prism layer example (CD-Adapco, 2011)

Prism layers also reduce numerical diffusion near the wall which is discretization error. Numerical diffusion is minimized when the flow is aligned with the mesh. The use of prism layers greatly enhances accuracy as a result. Typically, in this thesis, 5 – 10 prism layers with a wall function is specified. Using the best practices (CD-Adapco, 2011), the total prism layer thickness is 100% of the base size (typically 2 mm) with a prism layer stretch between each consecutive layer of 1.5.

### 3.2.3 Time Step

Time step size is very important in aero-acoustic simulations as it can often decide the maximum resolvable frequency. Time step size based on the required maximum frequency, i.e. 10,000 Hz can be calculated due to allowing for at least 10 points in a wave form. This is specified as a recommendation by Wagner et al (Wagner, et al., 2007) as well as Mendonca (Mendonca, 2005) amongst others. Therefore, these figures support the assertion that the CFD time-step size should be at least one tenth of the inverse of the maximum frequency required to be resolved. In this case, that is  $10 \times 10,000 \text{ Hz} = 10,000 \text{ Hz}$ . The inverse of this gives a required maximum time step of  $1\text{E-}5$  seconds (s). Time step size based on convective Courant number should aim for no more than a mean Courant value of 1. This is due to Courant-Freidrichs-Lewy (CFL) stability condition which states that in an unsteady flow, disturbances should move less than one grid spacing per time step (Durbin & Medic, 2007). The CFL is defined using the characteristic velocity at the cell face ( $U_f$ ), the grid spacing ( $\Delta x$ ) and the time step ( $\Delta t$ ) shown in Equation [43] (Haren, 2011):

$$CFL = \frac{U_f \Delta t}{\Delta x} \quad [43]$$

Using a grid spacing of 2 mm and the maximum velocity tested, the maximum time step calculated from Equation [43] is calculated to be  $3.33\text{E-}5$  s. Therefore, as fully resolving the acoustic wavelengths appear to be the limiting factor in defining the maximum time step size, a  $1\text{E-}5$  s time step is chosen as a default value for the simulations in this study using the one tenth rule. This is validated in Chapter 4.1.

### 3.2.4 Boundary Conditions

RANS solvers tend to reach universal asymptotic behaviour irrespective of initial boundary conditions (Davidson & Davidson, 2004). By their definition, both LES and DNS solve the large scale turbulence and the full scale turbulence respectively, thus LES and DNS approaches are found to require a turbulence representation at the inlet for an accurate turbulence representation. The inlet and outlet boundaries must be sufficiently far away to allow the correct level of random turbulence to form. Although an upstream flow condition should provide as much useful inflow data as possible, the computational boundary cannot be extended upstream indefinitely. The inlet condition should also be consistent with the turbulence model chosen for simulation.

From Versteeg et al (Versteeg & Malalasekera, 2007), it is clear that for compressible viscous flows, due to the requirement of acoustic results, Density ( $\rho$ ), Velocity ( $u$ ) and Temperature ( $T_0$ ) must be known at time,  $t = 0$  everywhere in the solution domain. Solid walls require a no slip condition ( $u = u_w$ ) and fixed temperature ( $T = T_w$ ). On fluid boundaries,  $\rho$ ,  $u$  and  $T$  must be known as a function of position at the inlet and the outlet must satisfy the stress continuity equation to achieve realistic surface stresses.

Rai and Moin (Rai & Moin, 1993) found in some cases, random fluctuations are superimposed on uniform inlet velocity to achieve turbulent behaviour at the inlet. It has also been found that the various flow types have different requirements of in-flow condition. For instance, in simulating free shear flow, the random perturbation could amplify the disturbances exponentially and inflow condition is believed to be of less importance. Whereas, in the wall-bounded flow, these random fluctuating in-flows are found to be of importance. The generation of random velocity profile for inflow data to match actual turbulent flow field is a difficult and computationally challenging process. It is therefore more preferred to use a lower order description provided by different related turbulent quantities than to use enormous amount of information to describe turbulence.

A variety of turbulence methods have been developed in an attempt to accurately represent turbulence in in-flow data such as the models proposed by Klein et al (Klein, et al., 2003), Billson et al (Billson, et al., 2003), Banamadouche et al (Benamadouche, et al., 2006) and Jarrin (Jarrin, 2008). Methods described in these papers mostly use the superposition of spinning eddies, whose spin (clockwise or counter-clockwise) and position are drawn from a normalized uniform distribution. The eddy size is the characteristic scale of turbulence. For

acoustic simulations, these synthetic fluctuations generated by the boundary condition turbulence models can start repeating over time due to the nature of how the size of the vortices are determined and projected. Therefore, it is inappropriate at this time of writing to use the Synthetic Eddy Method (SEM) boundary condition which is accessible within the CFD solver. A practical demonstration of this is discussed in Chapter 4.2.

The dependency of accurate acoustic results also poses a further constraint on the boundary conditions. Both the inlet and outlet boundaries must be non-reflective and allow acoustic waves to travel out of the simulation with no effect on the solution. Any reflected waves could interact with the generated noise in a destructive or constructive way, blurring or even destroying the acoustic results. Acoustic reflections can be terminated either by using highly dissipative terminations or by using long ducts between the geometry to be studied and the duct ends. The latter would require an impractically large domain unless non-reflective boundary conditions could be used. Therefore non-reflective boundary conditions have been utilised in this thesis for both the inlet and outlet faces. This, in effect simulates an infinite duct whilst considerably reducing the computational time as opposed to modelling a long duct to dissipate the pressure waves.

For the non-reflective (free-stream) boundary, the inlet and outlet is modelled as an anechoic termination through a 'transient-wave transmissive boundary' condition that allows pressure waves to escape without reflection (CD-Adapco, 2011). This transient-wave transmissive boundary or 'free stream' follows an approach similar to that for stationary shocks. For given boundary conditions, wave theory is used to calculate the magnitude and direction of the flow at the transmissive boundary (CD-Adapco, 2011). The free-stream boundary condition is based on extrapolation of Riemann invariants under the assumption of non-rotational, quasi-1D flow in the boundary-normal direction. The boundary face velocity, temperature and pressure are extrapolated from the adjacent cell value using reconstruction gradients. This condition generally applies to external flows when the boundary is placed sufficiently far from the body (Torregrosa, et al., 2012). Internal flows often have walls, possibly of irregular shape, immediately next to the flow boundary. These walls can produce boundary layers, vortices, or other multi-dimensional flow structures such that the non-rotational, quasi-1D isentropic flow assumption breaks down. Therefore, care must be taken to place boundaries far from the region under study. Torregrosa et al (Torregrosa, et al., 2012) evaluated the non-reflective boundary conditions available in ANSYS-FLUENT. The method used by ANSYS is that also used by CD-Adapco in Star CCM+. Torregrosa et al found good correlations with published experimental studies.

### 3.2.5 Convergence Criteria

For CFD results to be valid, the solution must be converged. This is essential in any CFD simulation. After ensuring the solution is grid-independent through a mesh independence study, to monitor convergence the solution should be evaluated by using available data coupled with knowledge of the expected physical values.

The overall temporal convergence is monitored for the unsteady CFD residuals using energy and momentum Root-Mean-Squared (RMS) residuals. Residuals are the differences in the value of a quantity (for example x-velocity or kinetic energy) between two iterations. All discrete conservation equations (momentum, energy, etc.) are monitored until there is negligible difference between two iterations. From initialisation, the scaled energy residuals are expected to decrease by at least five orders of magnitude and the solution in the bulk flow no longer changes dramatically with subsequent iterations (ANSYS, 2011).

Overall, monitoring convergence using residual history helps to ensure mass, momentum, energy, and scalar balances are achieved. Generally, a decrease in residuals by three orders of magnitude indicates at least qualitative convergence. At this point, the major flow features should be established. To monitor quantitative convergence, the key variables/physical quantities are monitored as an absolute confirmation. Physical scalar values such as pressure and velocity are monitored for each simulation to ensure the absolute values are within range (10%) of what would be expected in real world pipe flows. Scalar point monitors also provide evidence on iterative convergence for all presented unsteady computational methods. The monitor point should be placed in an area of complex flow and of importance. Figure 66 gives an example of iterative convergence for a pressure point probe placed centrally in the geometry of interest. During one time-step, the pressure is shown to stabilise to within 2% of the previous iteration before the next time-step is solved.

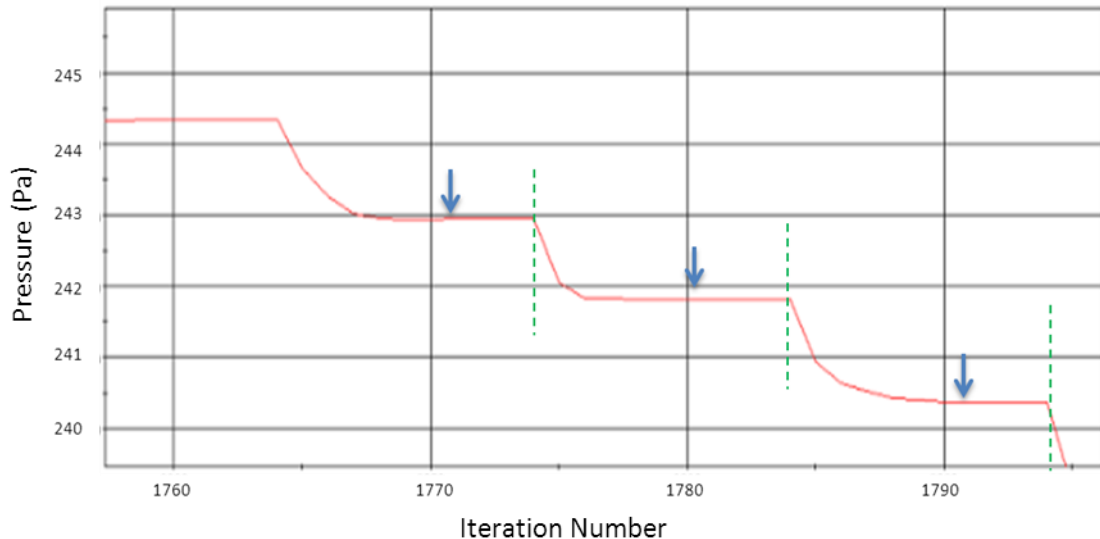


**Figure 66:** Pressure monitor probe located centrally in the region of interest against inner iteration number. The blue arrows give an indication of when convergence within tolerance has occurred for each timestep – marked with green dashed line.

Under Relaxation Factors govern the extent to which the new iteration solution supplants the old solution. It is included to stabilize the iterative process. Increasing the under-relaxation factor decreases the number of inner iterations required for time-step convergence. Decreasing under-relaxation factors often aids overall convergence and accuracy of the solution. For transient simulations, it is possible to increase under-relaxation factors, typically up to 0.9. Values can be higher than for steady state cases since the contribution of the transient term has the same effect as under-relaxation. Reducing the number of inner iterations enables a faster solver time. Care must be taken to ensure the time-step has converged to within the specified tolerance before the time-step is completed. For this study, for convergence within the specified tolerances coupled with acceptable solve-times, the under-relaxation factors are 0.9 for velocity and 0.7 for pressure with 7 inner iterations per time-step.

### 3.3 Computational Fluid Dynamics Summary

This chapter section has characterised the use of CFD codes and the solvers available for automotive applications. The vast area of turbulence and aero-acoustic modelling has been summarised in reasonable detail, as it is the fundamental basis for flow phenomena discussed in this thesis. It is also a very challenging area to simulate accurately. The history

and state-of-the-art in CFD solvers such as RANS and LES has been analysed to enhance the understanding of the advantages as well as the limitations of these schemes.

The current state-of-the-art of aero-acoustic cavity flows using CFD has been understood. Previous studies carried out with the use of CFD for the field of aero-acoustic resonant geometries are discussed, which is the main focus of this thesis. It is possible to assess very complex geometries, analyse many variables quickly and perform post-processing of the data in several visual and numerical forms. The use of CFD as a design tool has the potential to vastly reduce time and cost constraints for industrial design and manufacture. This chapter section has also described the fundamental simulation settings used throughout this study which are found to give the most optimal solution in terms of accuracy and computational solve time. The various CFD solvers of current times are summarised along with best practices and discussions for mesh, time-step and boundary condition settings.

## 4 Modelling and Simulation Work

The experiments carried out in the previous chapter are re-created as numerical simulations using a commercial Computational Fluid Dynamics (CFD) code. The results are analysed and compared with the experiments to deduce whether the CFD code is suitable for use as a design tool, and thus could be utilised early on in the product design phase.

The simulations allow further understanding into how a resonator behaves under various flow conditions and geometries. Several validation simulations will be conducted to investigate the effect on the acoustic frequency distribution for various side branch configurations as mesh, solver and boundary settings are varied. A side branch consisting of a VVH Helmholtz resonator and an adjustable Quarter Wave Tube (QWT) will be analysed in terms of the effect on the acoustic field in a straight section of pipe. Various parameters will be explored to replicate the experiments, along with further geometry changes and variations. The premium automotive section of charge inlet tract is simulated in an aim to replicate the experiments as well as being able to visualise the complex flow phenomenon responsible for the high frequency tones which are shown in Chapter 2.

### 4.1 RANS Simulations

Initially, simple pipe flows are simulated, whereby mesh, solver and turbulence settings are tested for robustness. U-RANS simulations with the K- $\epsilon$  solver are carried out for initial validation purposes before moving on to LES due to its robustness in terms of solve time and reliability for uncomplicated flows as discussed in Chapter 3.1.

Initially, a straight pipe is modelled with a pipe diameter which corresponds to the dimensions of the experimental configuration. A controlled negative pulse pressure (in time) is created at the inlet and monitored downstream as a basic validation test. Only one half of the pipe is modelled with a symmetry plane applied, to lower solution time. A fairly coarse Polyhedral mesh is created including 2 prism layers. A 5 mm core mesh size is specified to produce approximately 400,000 cells which is found to be a reasonable initial mesh density.

A monitor point approximately 1.5 m down the length of the pipe is placed centrally to record pressure and velocity values downstream. Flow is from left to right for all plots given in this chapter. The compressible flow equations are solved using an implicit segregated solver and a second-order upwind scheme is used to model artificial viscosity. The chosen physics models are listed below. The initial solver values are given in Table 3.

- Compressible Ideal gas (Air)
- U-RANS Realizable K-Epsilon Two- Layer
- 2nd order Implicit Unsteady
- Segregated Flow (Fluid Temperature)
- Turbulent, Three Dimensional
- All  $y^+$  Wall Treatment

Mass flow rate	0.0294 kg/s
Flow velocity	10 m/s
Time-step	0.1 s
K	1.0
$\epsilon$	1.2
$C_u$	0.09
$C_{1\epsilon}$	1.44
$C_{2\epsilon}$	1.9
Pressure	101325 Pa
Temperature	25 °C
Density	1.184 kg/m <sup>3</sup>

**Table 3: U-RANS solver initial values**

A 0.1 s time-step is used, as the inlet pressure fluctuation does not require a high resolution to resolve with a simple pressure ramp and a low Mach number flow. A ten second maximum physical time to allow ample time for convergence of this problem and 2<sup>nd</sup> order Temporal Discretization is chosen. 2<sup>nd</sup> order Temporal Discretization is routinely used in standard CFD applications as explained by Wagner (Wagner, et al., 2007). 2<sup>nd</sup> order time schemes are attractive because of their built in de-aliasing property (A.G Kravchenko, 1997).

A stagnation gauge pressure inlet with the following values which vary with time, as shown to create a large pressure pulse (for testing purposes) is shown in Table 4. The pressure values are interpolated linearly. A free-stream outlet is selected and set to atmospheric pressure (0 Pa gauge). The no-slip boundary condition,  $v = 0$ , is used at the walls to simulate unsteady wall boundary flow.

Time (s)	Gauge Pressure (Pa)
0.0	100
5.0	100
5.5	80
6.0	100
10.0	100

Table 4: Inlet pressure in relation to time

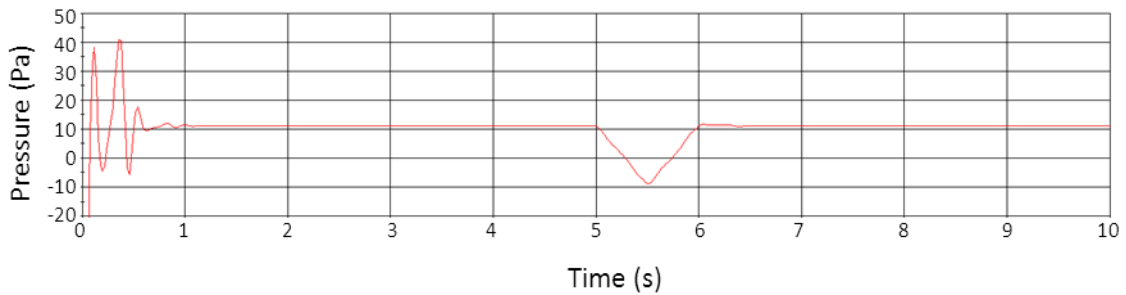


Figure 67: Pressure (Pa) in relation to time (s) at 1.5 m along the length of the pipe

Figure 67 shows the gauge pressure, in Pascals, from the monitor point 1.5 m along the length of the pipe which is plotted against time in seconds. The graph appears to show the simulation is converged around 1 second (~200 iterations). The graph shows a clear negative pulse in pressure of 20 Pa at 5.5 seconds, plus the time delay of 0.0044 seconds which accounts for the wave propagation speed. This is as expected from the inlet values shown in Table 1. Pressure is constant at around 11 Pa (gauge). It is also interesting to note the inlet pressure is around 35 Pa (gauge) so there is a drop of around 24 Pa down the length of the pipe. This is a realistic pressure drop for the flow Reynolds number here, as verified with the Darcy-Weisbach equation given in Equation [44] (Rouse, 1946).

$$\Delta p = f_D \frac{L}{D} \frac{\rho V^2}{2}$$

[44]

This model has provided satisfactory results and validation of the solvers used. The forced negative pulse pressure does not appear to dampen out or diffuse along the pipe which indicates an acceptable mesh quality and solver. The simulation is an ideal benchmark on which to build on for future pipe simulations.

#### 4.1.1 VVH Resonator Pipe Simulation

The pipe simulated in the previous section now includes a Helmholtz resonator. This represents the geometry of the VVH Resonator experiments, see Chapter 2.3. The pipe and resonator layout is shown below in Figure 68. The model is solved with steady state RANS and a negative pulse pressure is applied at the inlet which matches the straight pipe simulation in the previous section with the same boundary conditions and U-RANS solver configuration.

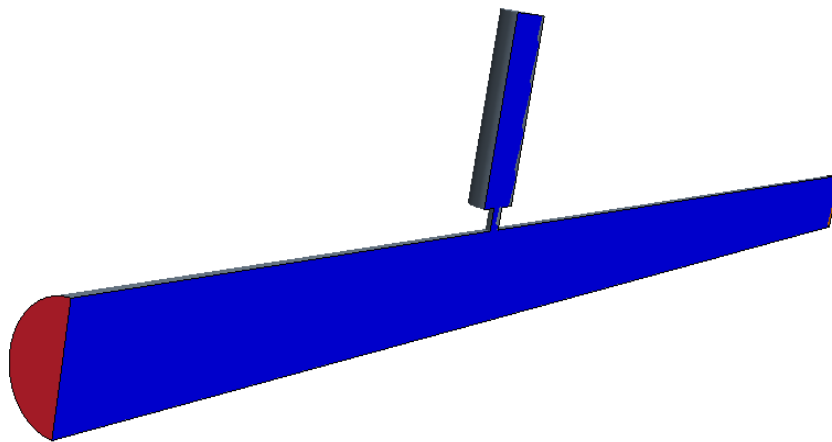


Figure 68: Resonator and Pipe Layout

The Helmholtz resonator has a set volume height of 150 mm with other feature dimensions being identical to the experiment test piece. The resonator is situated 500 mm down the length of the pipe. Figure 69 shows the initial volume mesh. The density of the mesh is increased particularly around the resonator neck to capture the flow around this area in more detail.

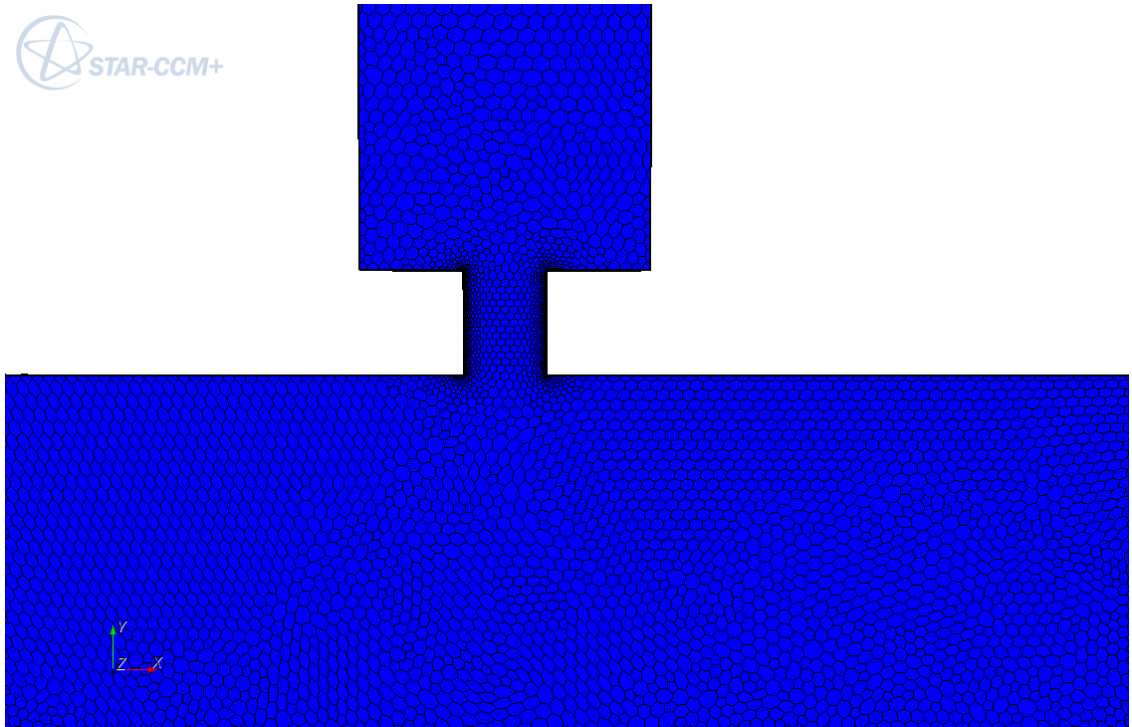


Figure 69: Resonator pipe initial volume mesh - neck close-up

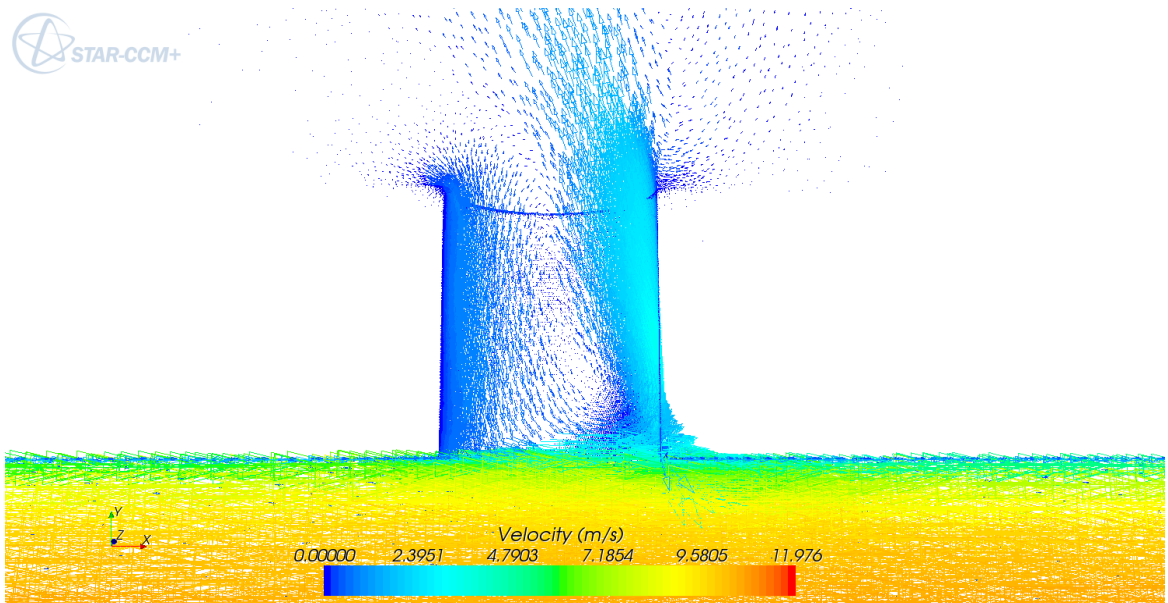


Figure 70: Velocity magnitude vectors around the neck

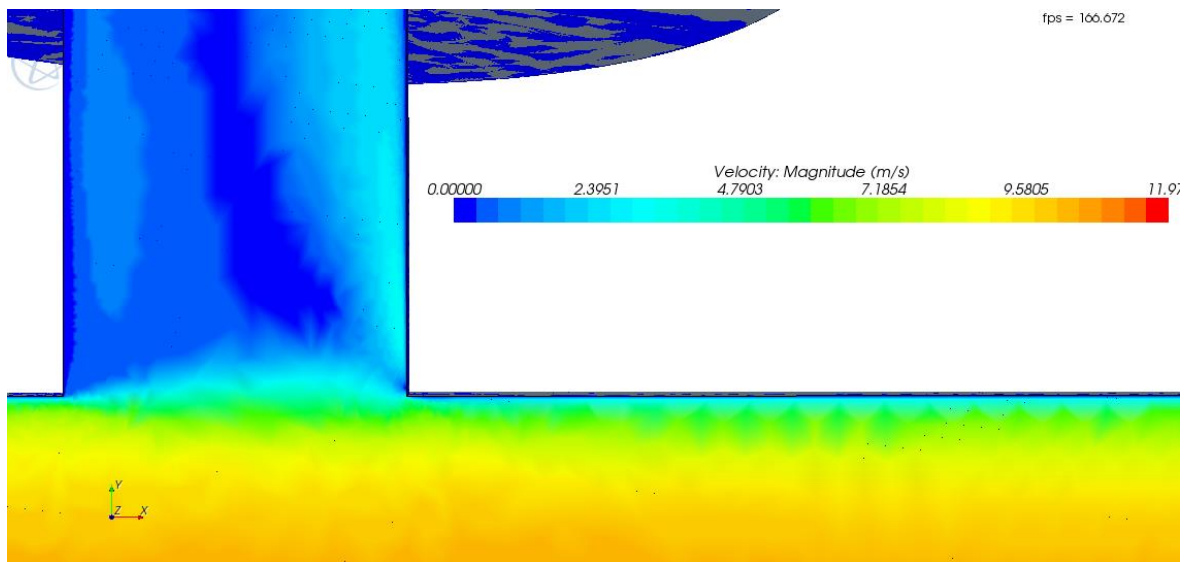


Figure 71: Velocity magnitude around the VVH resonator neck

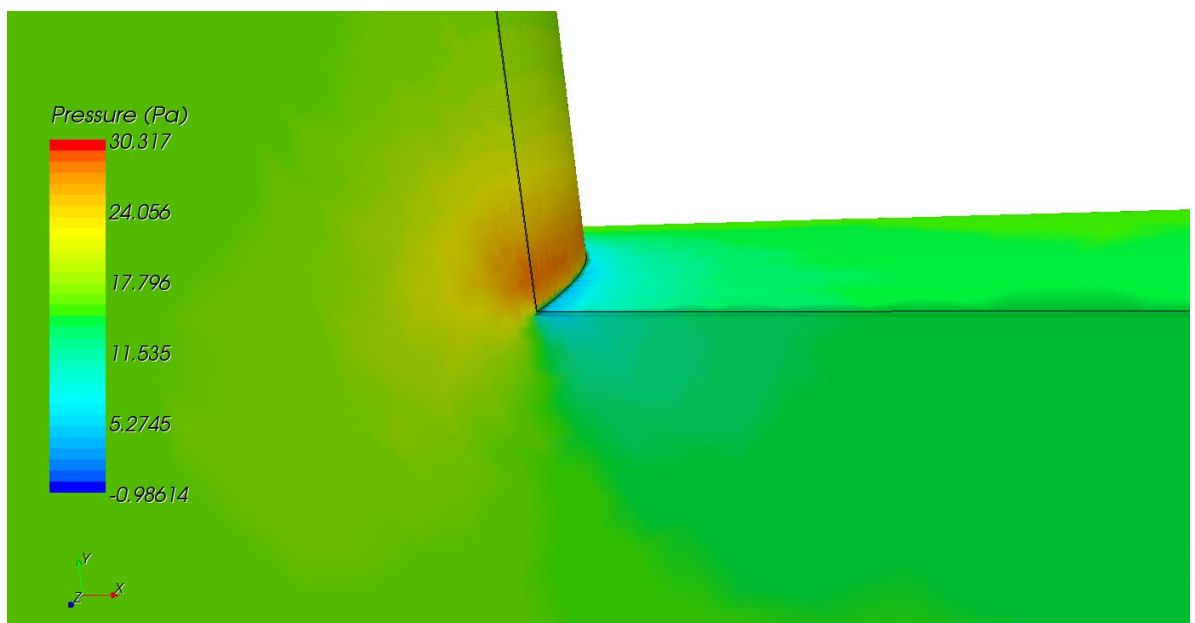


Figure 72: Pressure (gauge) around the VVH resonator neck

The model is initially solved with a constant mean 10 m/s velocity imposed at the inlet to ensure the model is behaving correctly. Figure 70 shows the velocity vector plot after convergence at 1000 iterations, with the flow clearly being drawn into and circulated out of the resonator. The pressure and velocity plots given in Figure 70, Figure 71 and Figure 72 show the flow velocity and pressure magnitudes around the neck. This is where flow is of most interest and should hopefully capture more of the pressure fluctuation after the negative pulse pressure, which is expected due to instabilities caused by the resonator neck.

It is expected the unsteady simulations along with a more refined mesh will capture much more detail around this area. Figure 72 in particular, shows the high pressure on the trailing edge of the entrance to the resonator and the low pressure created below it. This sudden change in pressure is expected to be the cause of noise due to distinct turbulent eddies and vortex shedding around these areas.

The pressure values given in Table 1 are applied at the inlet. The solver is changed to Implicit Unsteady with a time step of 0.1 seconds and a maximum time of 10 seconds. The monitor point is placed in roughly the same place as the plain pipe (1.5 m along the length). The gauge pressure is, again, measured at this point and is shown on a graph against time in Figure 73.

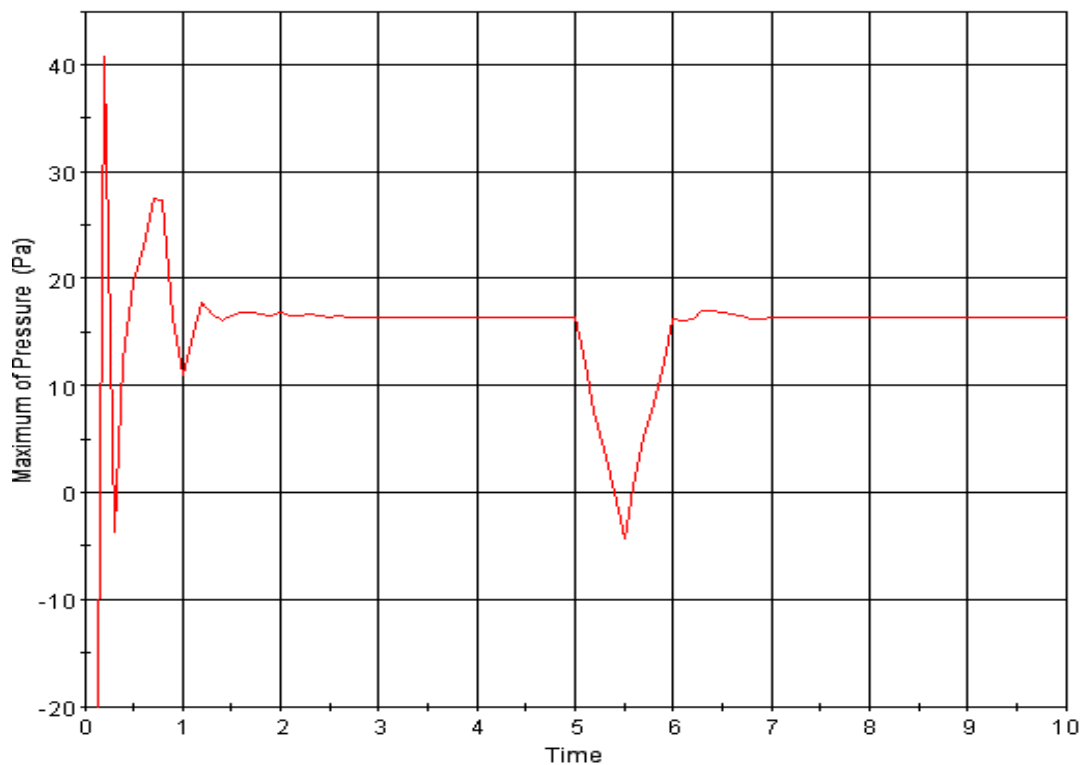


Figure 73: VVH resonator and pipe simulation - pressure (Pa) against time (s)

The pressure at the monitor point (Figure 73) initially appears to be very similar to the plain pipe pressure plots shown in Figure 67. However, there appears to be an area of instability after the negative pulse pressure which is not so apparent with the straight pipe only. This could be caused by either, the resonator creating fluctuations after the pulse, or the model is not being simulated accurately enough. The first option is as predicted. This is

due to the pulse passing the resonator causing pressure fluctuations in the resonator which pass down the pipe later on in time. If it is found to be the second option, a finer mesh and a smaller time step should reduce this.

As the solution becomes steady, the Frequency Mesh cut-off plot can be utilised. This is shown in Figure 74.

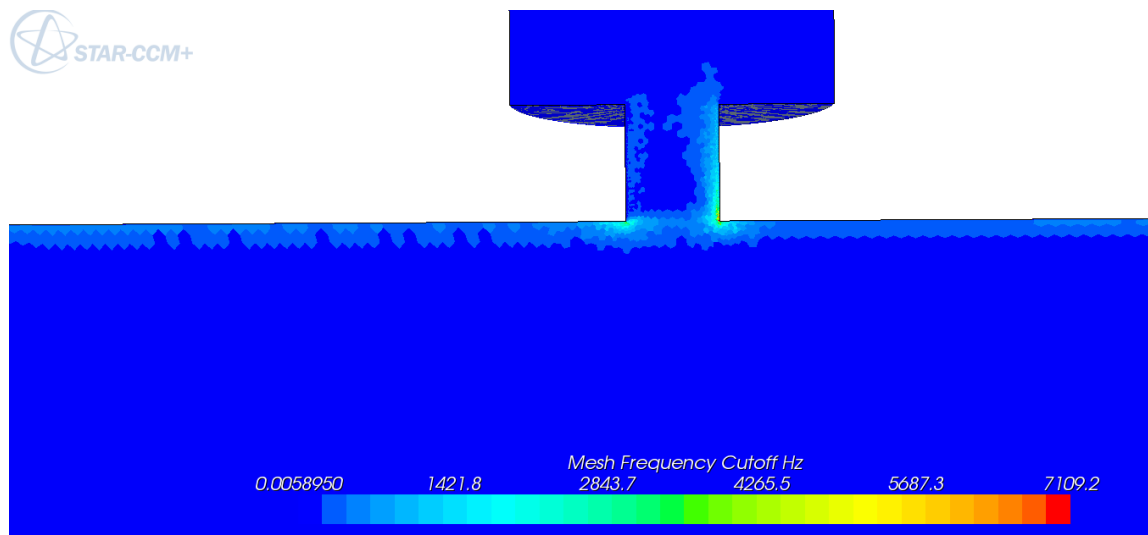


Figure 74: Mesh Frequency cut-off contour

The Mesh Frequency cut-off given Figure 74 indicates that around the neck walls, the maximum frequency resolvable is around 3-4 kHz which is adequate for future simulations. However, the majority of the neck and the trailing edge of the neck has a very low mesh frequency cut-off. Clearly, a finer mesh will increase the resolvable frequencies around this crucial area.

The mesh is refined to around 900,000 cells and the time step is halved to 0.05 seconds with the maximum time set at 10 seconds as before. Figure 75 shows the refined mesh around the trailing edge of the neck. The base size of the mesh is approximately 5 mm. The mesh around the neck is approximately 5 times smaller to capture the expected turbulence and turbulent frequencies created by the resonator. Figure 76 is a close-up representation of this region.

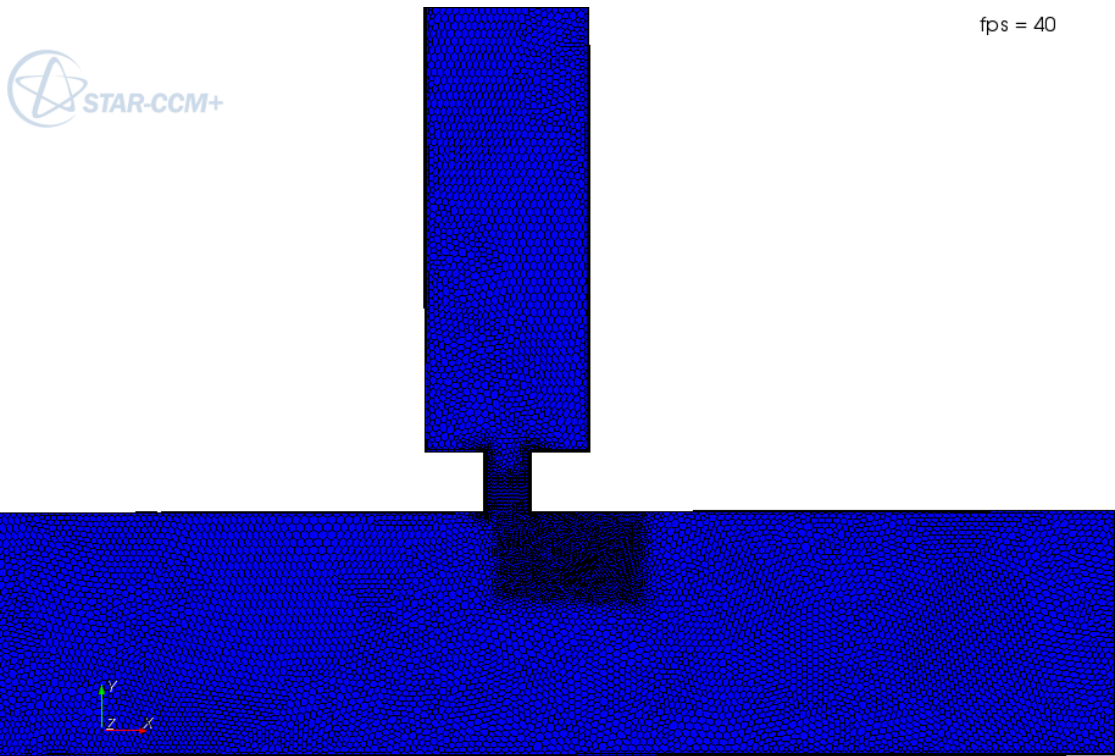


Figure 75: VVH resonator refined mesh

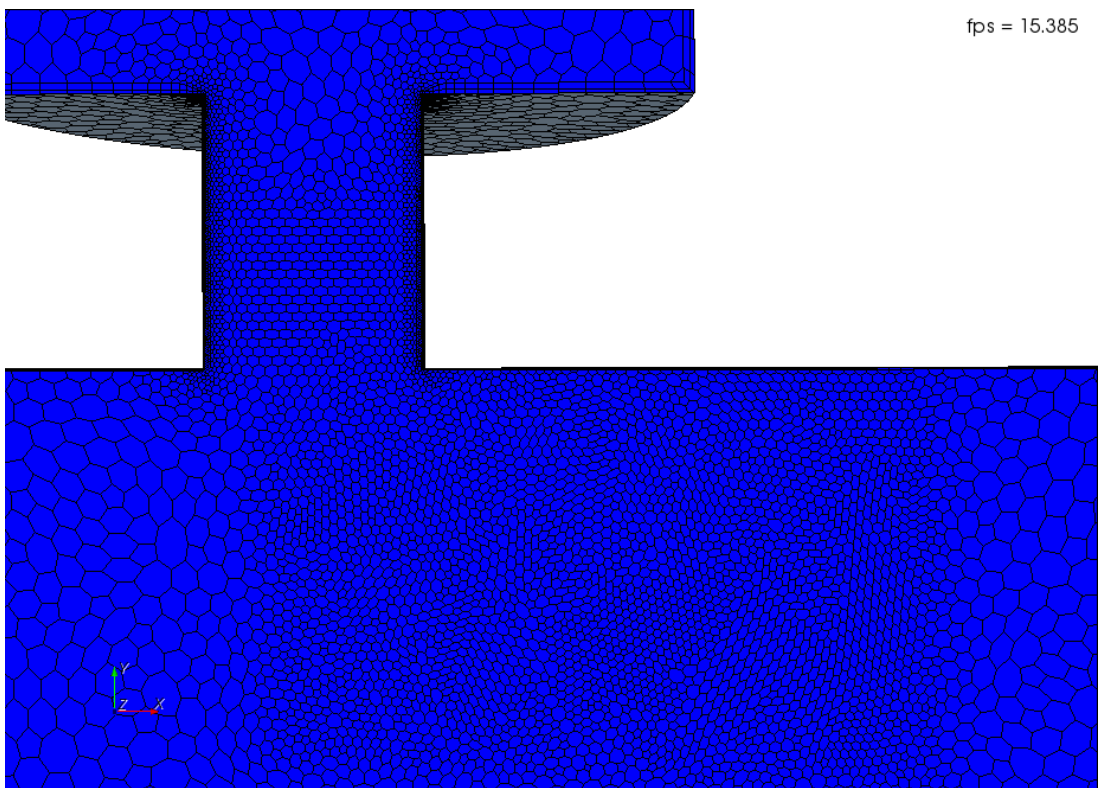


Figure 76: Refined mesh around neck close-up

Figure 77 shows the mesh frequency cut-off contour for the re-meshed case. The contour plot indicates that the dense mesh around the neck has slightly improved the turbulence resolving capability of the mesh, although not much as expected.

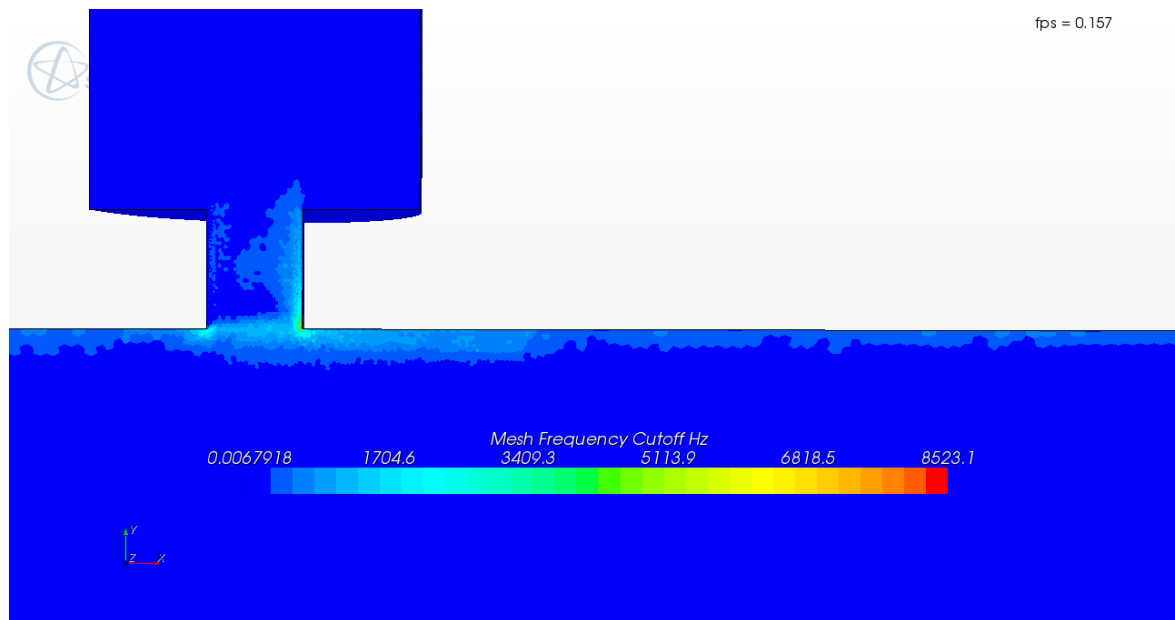


Figure 77: Re-mesh - Mesh Frequency cut-off contour

The simulation is re-solved and Figure 78 shows the results as presented with the previous mesh. The results appear very similar to the previous simulation. However, the line appears to fluctuate slightly more around the mean value. This may be due to the smaller time step capturing more unsteadiness in the flow. Interestingly, the small fluctuation after the negative pulse pressure (6-7 seconds) is still evident, as in Figure 73. This appears to suggest the fluctuation is indeed caused by the resonator and not by the lack of mesh density/large time step.

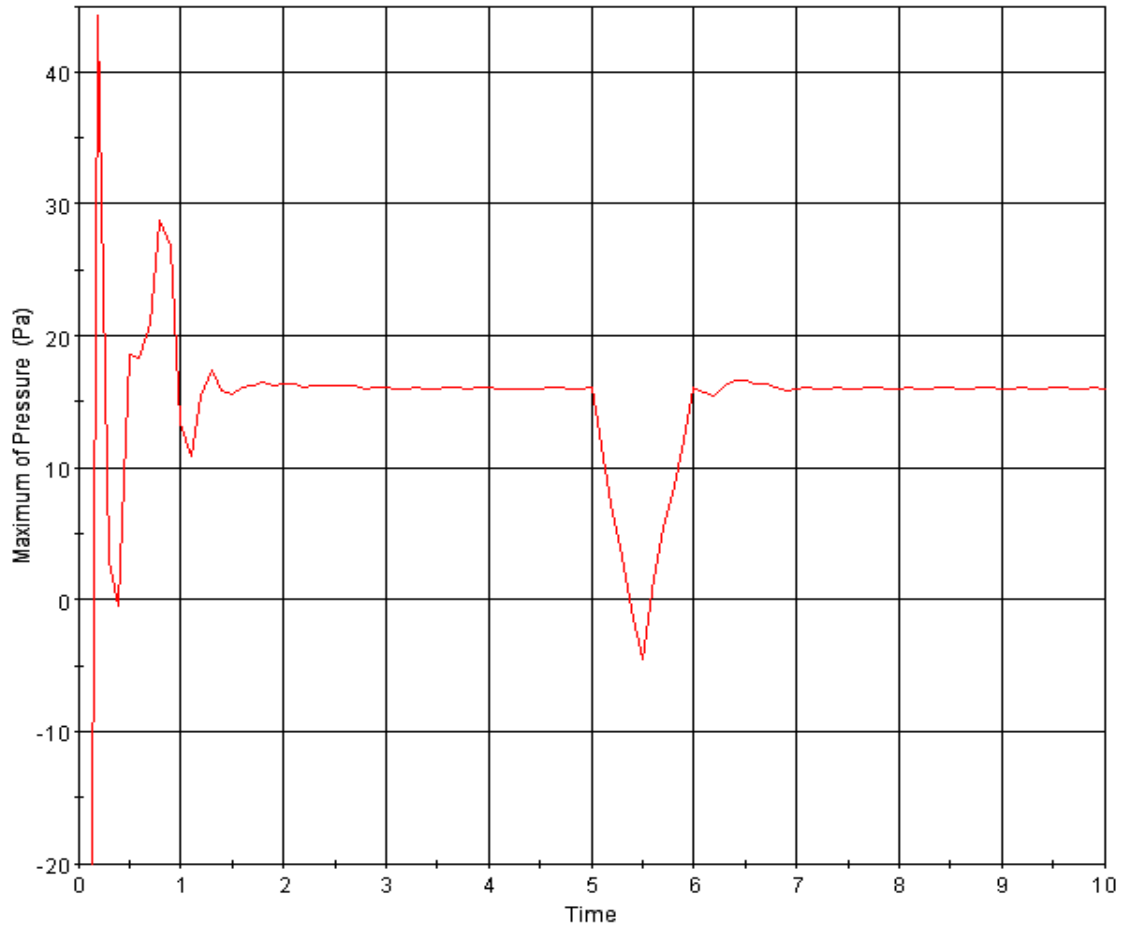


Figure 78: VVH resonator and pipe re-mesh simulation - pressure (Pa) against time (s)

Overall, the re-mesh has raised several points. Firstly, the finer mesh has not decreased the time for the solution to become steady or had any significant effect on the pressure results. The finer mesh has had a slight effect on the maximum resolvable frequency. However, a vastly finer mesh would need to be used to resolve the full human hearing range (up to 20 kHz). The mesh density will almost certainly have an effect on the accuracy of the simulation as smaller amplitude fluctuations are introduced into the pipe in future simulations. The shorter time step produced very small fluctuations in the pressure plot shown in Figure 78. This may be due to smaller time step capturing the slight unsteadiness of the flow.

What is clear from the negative pulse pressure validations is there appears to be some extra fluctuations due to the resonator after the negative pulse pressure, as expected. These validation simulations have identified some interesting flow results along with some mesh and solver characteristics. However, further simulations need to be carried out to

establish how the flow is behaving around the resonator. This needs to be compared with the experimental results to validate these findings.

#### 4.1.2 VVH Resonator with a 1000 Hz Sine Wave Pulse

A sinusoidal pulse is created at the inlet of the geometry given in the previous chapter section. The wave is tracked as it travels down the pipe, noting any effects the VVH resonator has upon the pulse. This is compared with an idealised sine wave pulse. Any discrepancies such as excessive dissipation of the wave amplitude could signify an error within the solution and/or simulation set-up.

The resonator is tuned to 200 Hz. One period of a 1000 Hz sinusoidal waveform is created at the inlet and propagated downstream. As the pulse has a frequency of 1000 Hz, little to no effect is predicted to occur on the pulse due to the resonator. Firstly, the time the pulse will require to travel down the pipe is calculated and the time step size and number is calculated from this.

##### 1 time period, T:

$$T = 1/f$$

Where:  $f = 1000 \text{ Hz}$

$$T = 1/1000 = 1\text{E-}3 \text{ seconds}$$

As stated in Chapter 3.2, at least 10 points need to be solved in a waveform. Therefore, the time step size needs to be at least 1 tenth of the waveform period:

$$\text{Time step size} = 1\text{E-}3/10 = 1\text{E-}4 \text{ seconds}$$

##### Time to travel down pipe:

Velocity  $\sim 343 \text{ m/s}$  at ground level and room temperature.

$$\text{Time to travel } 1 \text{ m} = 1/343 = 2.94\text{E-}3 \text{ seconds}$$

$$\text{So, for } 1.66 \text{ m, } 2.94\text{E-}3 * 1.66 = 4.88\text{E-}3 \text{ seconds}$$

##### Number of time steps required for modelling of complete pulse through pipe:

$$4.88\text{E-}3/1\text{E-}4 \sim \underline{49 \text{ time steps}}$$

Figure 79 below shows the sine wave pulse moving through the pipe from left to right. The yellow/orange area to the right is the pressure peak and the blue area in the negative pulse pressure. This is followed by a small pressure rise shown by the yellow area. Figure 80 shows the sine wave pulse leaving the pipe. The blue area at the exit is the

negative pulse pressure and the red area in the extra fluctuation which needs to be investigated further.

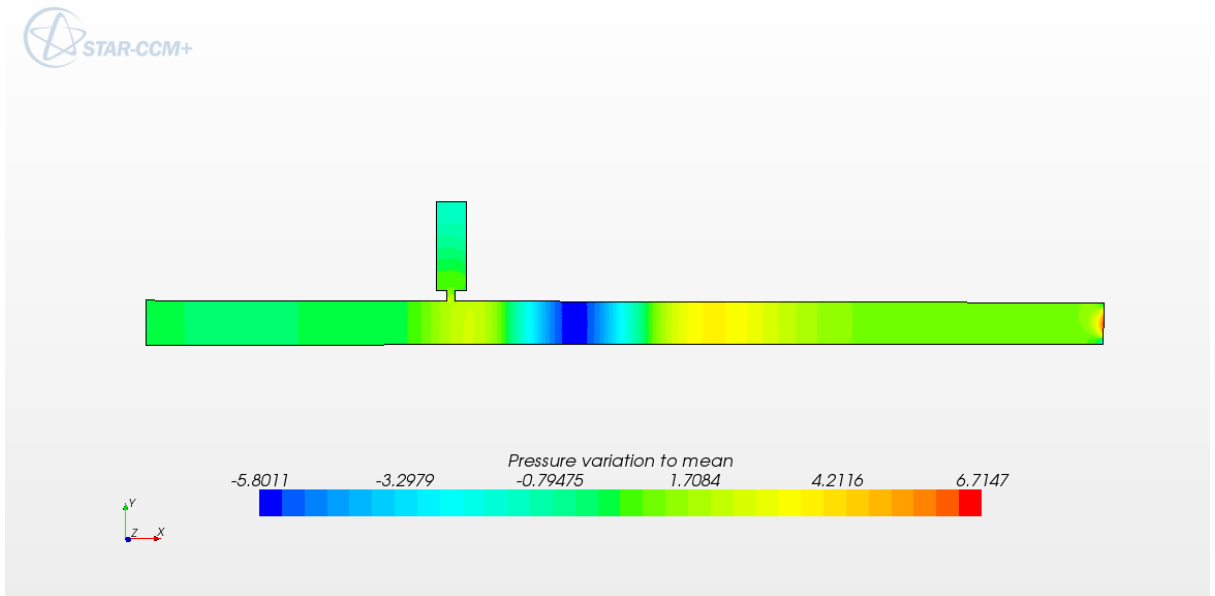


Figure 79: A pressure scene to show the sine wave pulse moving along the pipe

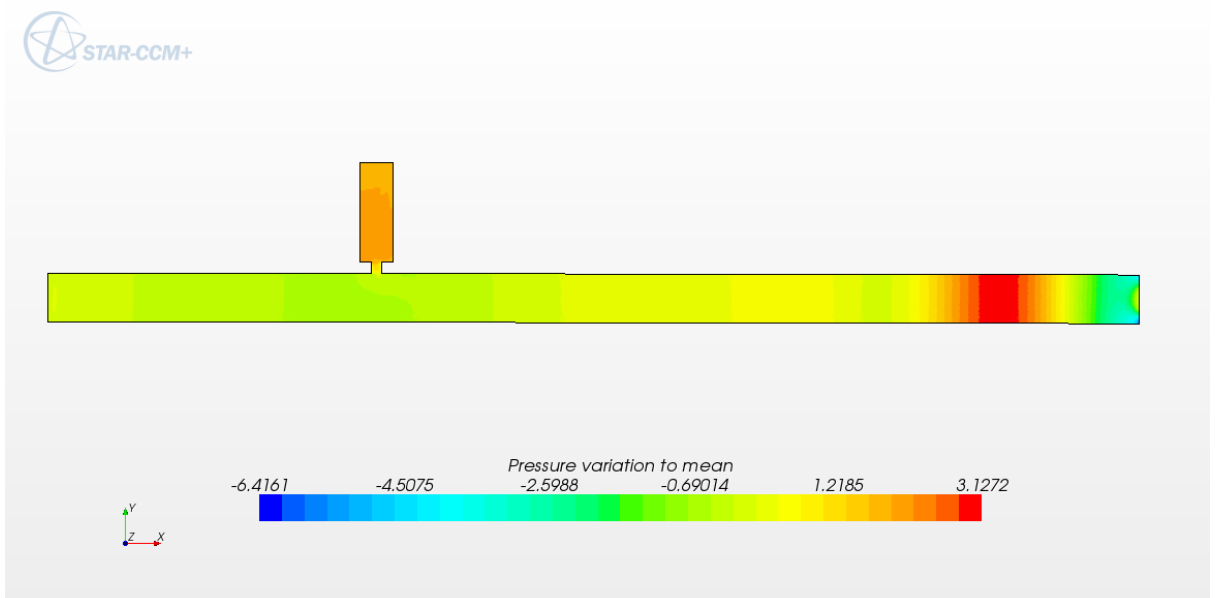
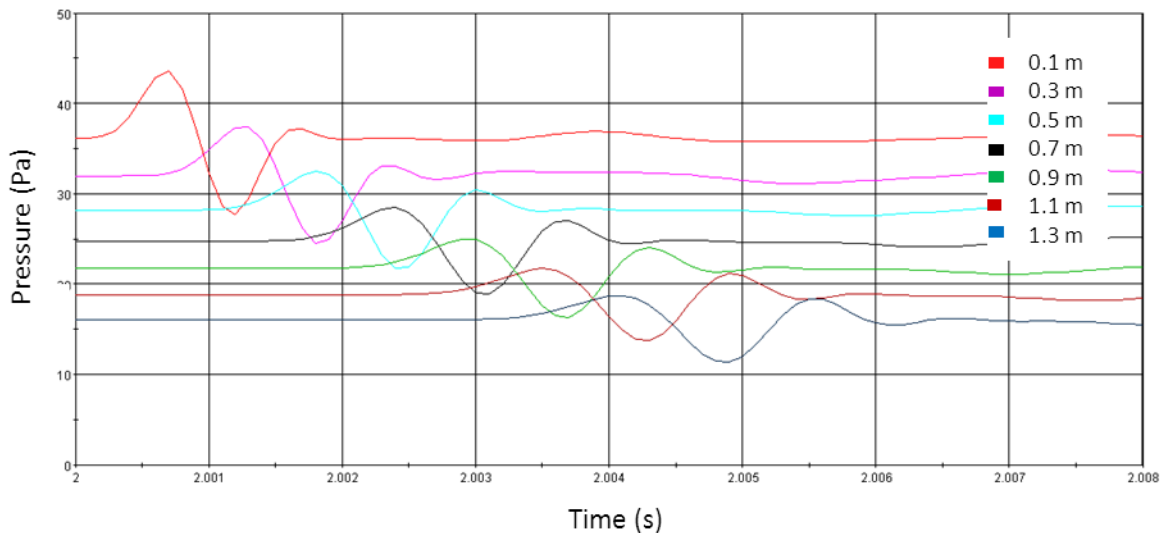


Figure 80: A pressure scene to show the sine wave pulse leaving the pipe



**Figure 81: Simulation of a sinusoidal wave - A plot to show Pressure (Pa) at points along the pipe against time (s).**

Figure 81 shows a plot of the pressure wave propagating down the pipe. Each line represents the pressure at a point. The points are equally spaced down the pipe and are placed in the centre of the cross-section. General trends are apparent from the results. Firstly, the amplitude of the pulse appears to decay to around half at the end of the pipe compared with the initial pulse. Secondly, the pulse appears to elongate slightly towards the end of the pipe (decreases in frequency). The artificial dissipation present in the U-RANS 2-layer model is possibly the main reason for the decrease in amplitude and elongation of the pulse. Care must be taken not to decrease this artificial dissipation too much as it can cause dispersive errors. This causes extra oscillations in the solution. These errors are hoped to be avoided in later simulations using LES.

The first two monitor points are located before the resonator with the rest being located after the resonator. There appears to be no clear difference between the pressure fluctuations before and after the resonator although an extra fluctuation is present as the pulse moves down the pipe as shown in Figure 79 and Figure 80. This extra fluctuation needs to be investigated to examine the source. A likely cause is a numerical error due to the time step being too large and/or the mesh not being fine enough.

The simulation is re-run after some changes. Firstly the pipe length is halved to make the pipe length after the resonator much shorter. This is done to lower computational time and to allow a finer mesh around crucial areas. The time step is shortened by a factor of 10 to create 100 points per wave pulse. This is done to solve the waveform more accurately to reduce dissipation errors. Using the information detailed in Chapter 3.2, the pipe is re-

meshed with a base size of 2 mm and a total cell count of around 1.7 million cells. The geometry was re-meshed to a hexahedral mesh as this was found to create a more uniform mesh in the pipe. These changes are predicted to be more than adequate for initial Large Eddy Simulations as a mesh this size should be able to capture up to 17 kHz frequency.

The refined mesh is shown in Figure 82. The mesh is more dense and uniform in all areas. The region around the neck is 10 times finer than the base size. This means this area has a mesh size of 0.2 mm to capture vortex shedding expected in this area due sharp edges at the resonator neck.

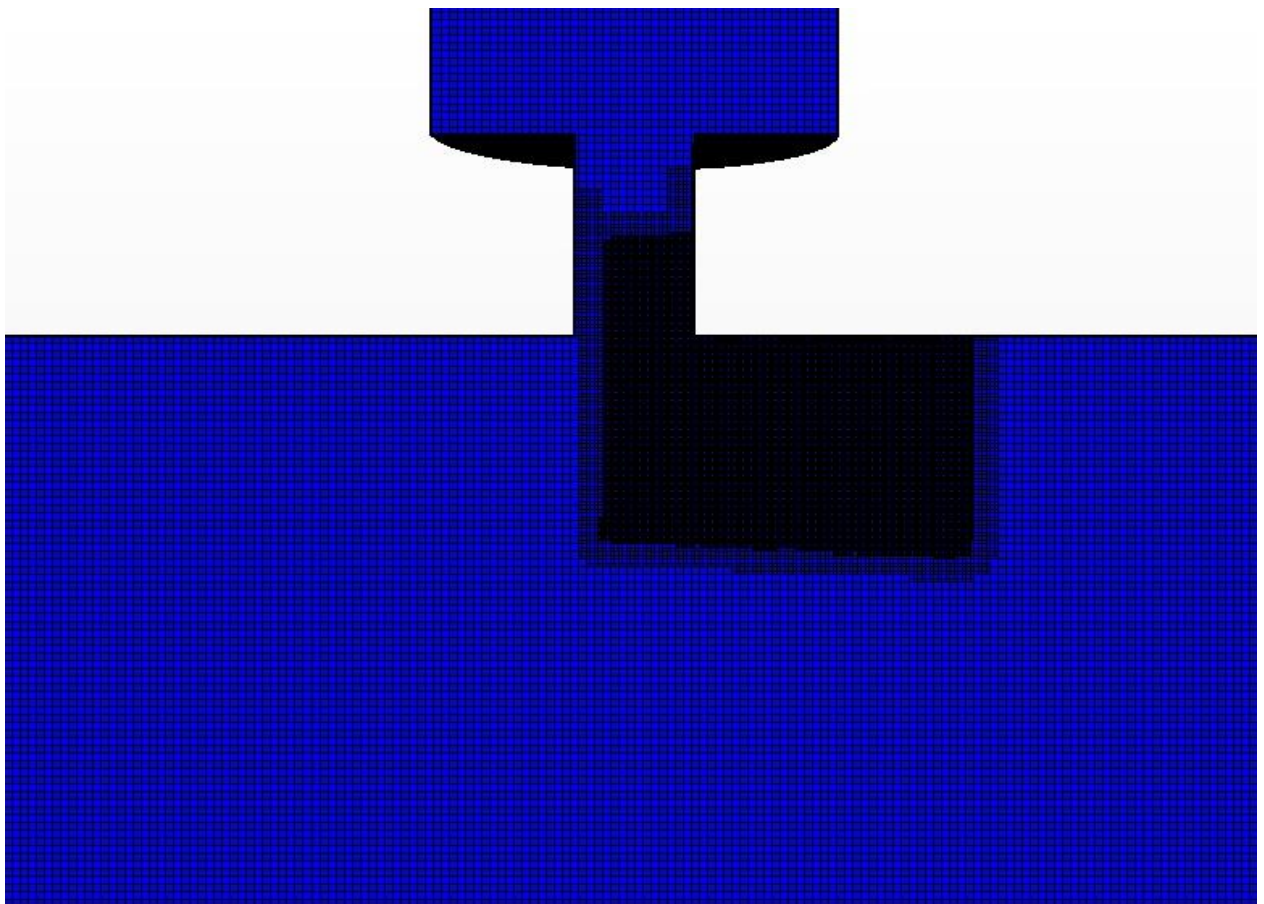
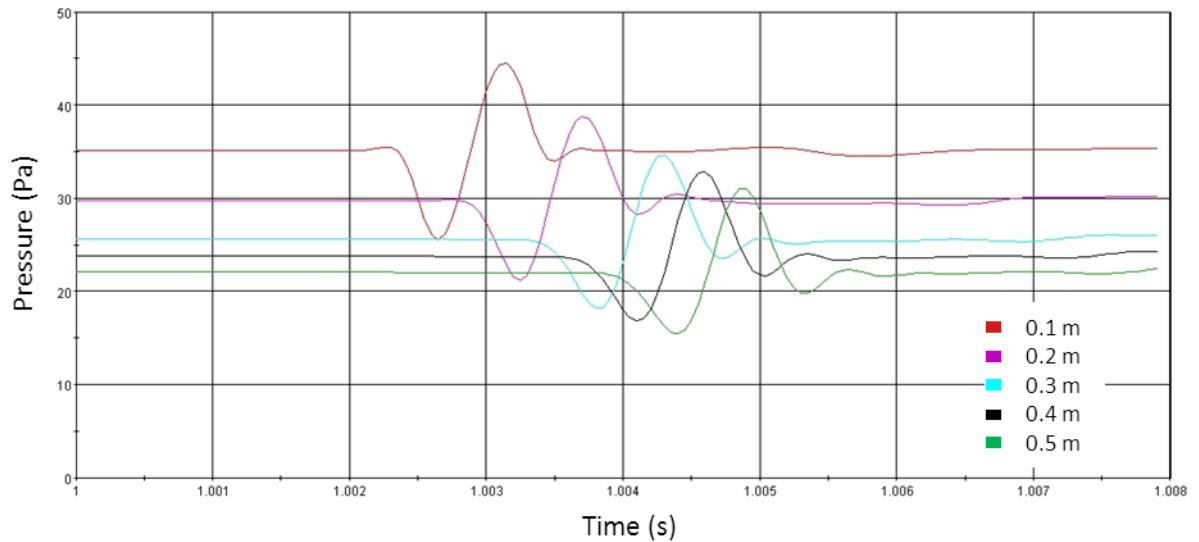


Figure 82: Refined trimmer mesh



**Figure 83: 1000 Hz pulse simulation re-run - A plot to show Gauge Pressure (Pa) at points along the pipe against Time (s).**

Figure 83 shows the results of the re-run 1000 Hz pulse pressure wave propagating down the pipe. Only 5 monitor points are present now as the pipe is shortened, the first two are still located before the resonator and the rest afterwards. The plot is very similar to Figure 80 with an extra fluctuation present as the pulse moves through the pipe. However, the fluctuation is much smaller, possibly due to the smaller time step and/or the finer mesh. Hence, the extra fluctuation could be a small error due to inaccuracies in the calculation known as numerical error, time domain errors known as temporal discretization errors during the period of the pulse or mesh error, commonly known as ordered discretization errors which disappear as the mesh size approaches zero. This can be combined to be called a dispersive error. The slight dispersion of the pulse wave is most likely caused by a dissipation error which causes a smoothing effect on the pulse. Overall, an even smaller time step and a finer mesh will help reducing the errors. However, the errors are negligible in this context and the pulse is clearly simulated well. Again, there does not appear to be any differences between the pressure fluctuations before and after the resonator. This suggests the resonator is having very little/no effect on the pulse as expected.

The time-step is shortened further to  $1E-5$  seconds, which is theoretically acceptable for forthcoming Large Eddy Simulations. The simulation is re-run once more. The pressure results are provided in Figure 84. The smaller time step of the simulation shown in Figure 84 has created some dissimilarity when compared to the previous simulation (Figure 83). Firstly, the pulse is more unsteady, particularly as it travels down the pipe. Secondly, the pulse tends to lose the sine wave shape as it travels down the pipe. The most likely cause of this is

dispersive errors which are inherent in the U-RANS eddy-viscosity model. The underlying turbulent viscosity cannot disappear, unlike in LES. Therefore, with a highly resolved mesh/time-step, URANS is expected to be more dispersive than LES. However, the extra fluctuation error has been almost completely removed by shortening the time step. This proves the extra fluctuation in earlier simulations was caused by a time step error. For future simulations, a time step size of  $1E-5$  s is chosen to reduce any dispersive errors.

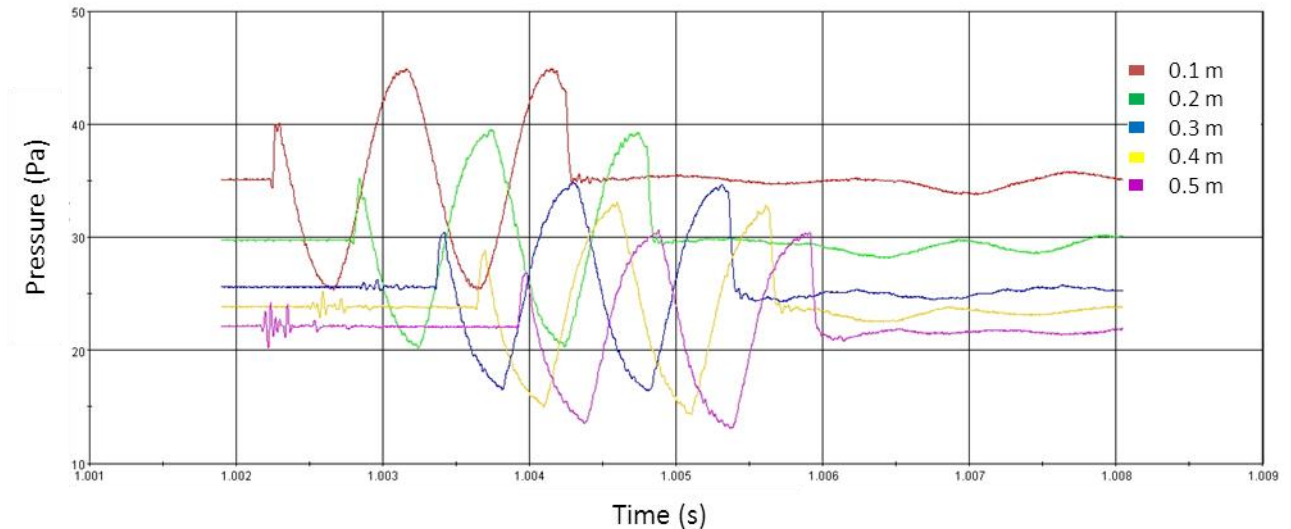


**Figure 84: 1000 Hz pulse, time step:  $1E-5$  s, 2 periods - A plot to show pressure (Pa) at points along the pipe against time (s)**

Overall, the simulations with a 1000 Hz sine wave pulse have behaved as expected. With a resonator tuned to 200 Hz, there is negligible attenuation of the signal due to the resonator. This set of simulations has shown adequate mesh density and a small time step are essential to reduce dispersive errors to acceptable levels. For these types of simulations, a time step size of  $1E-5$  seconds and a mesh base size of 2 mm are found to be more than adequate to capture waveforms accurately up to the required frequency.

#### 4.1.3 VVH Resonator with a 200 Hz Sine Wave Pulse

To validate the simulation further, resonator attenuation is expected to be captured by sending a 200 Hz sine wave pulse through the resonator pipe. The resonator is tuned to 200 Hz. Therefore, the signal is expected to be attenuated as it passes the resonator by at

least 50% around 200 Hz which would agree with experimental results detailed in Chapter 2.2.

The 200 Hz pulse is entered into a pipe with no resonator for comparison. The initial conditions and mesh is the same as the 1000 Hz pulse simulation. A plot of this simulation of pressure against time for two periods of the 200 Hz pulse simulation is shown in Figure 85.

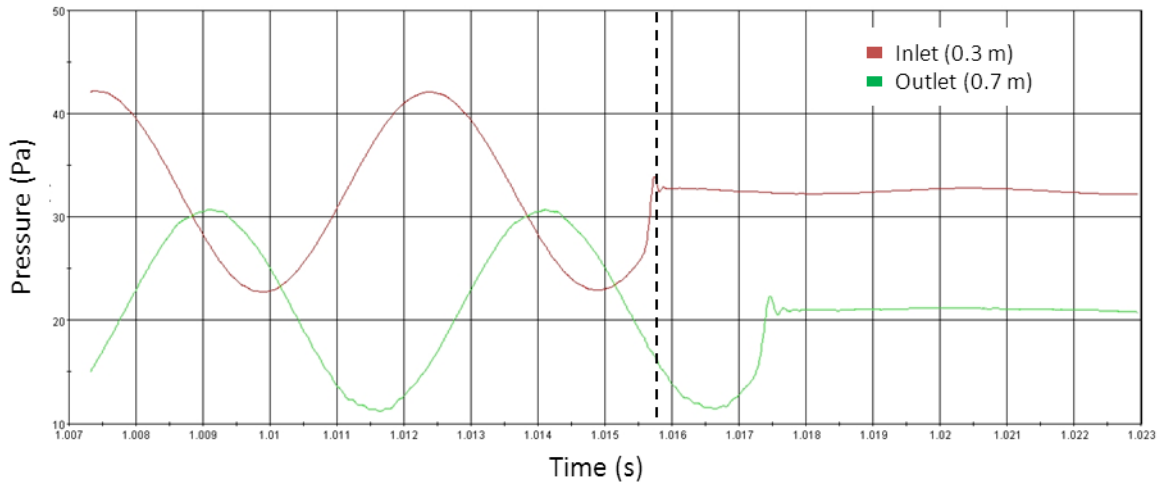
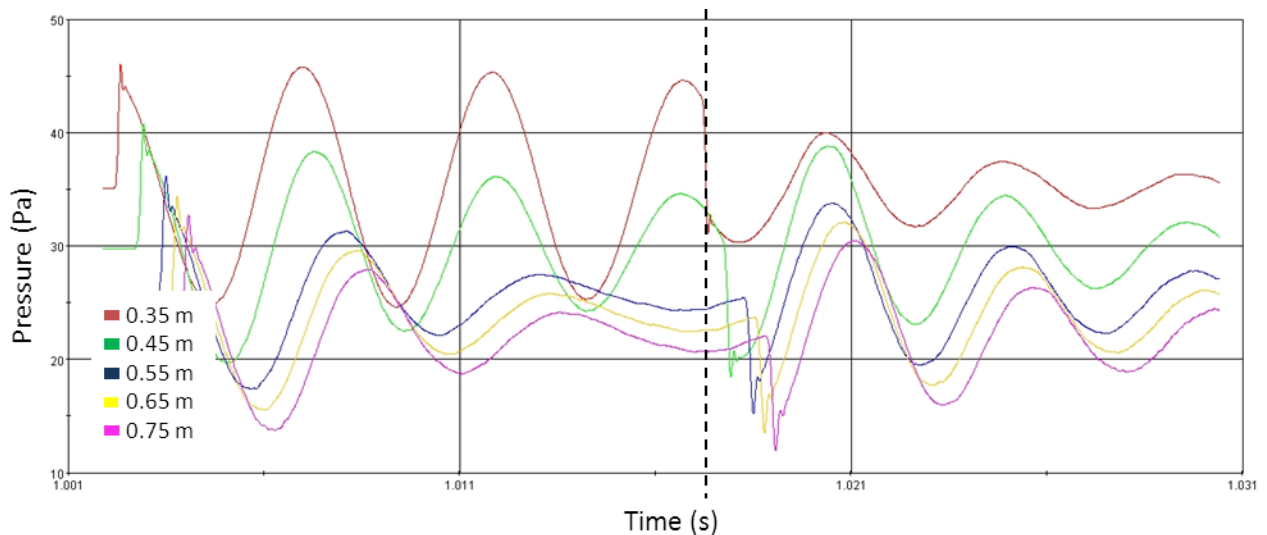


Figure 85: Pressure monitor points plot - 200 Hz pulse simulation, no resonator. Pressure (Pa) against Time (s)

Clearly, there is negligible difference between the pulse towards the inlet (red line) and outlet (green line) located after the resonator, as expected. Of course, there is a mean pressure difference between the two points due to the pressure drop through the pipe. There also appears to be negligible fluctuations after the pulse, signified by the black dotted line, which suggests there is very little numerical error.

A resonator with the same dimensions as before, only smaller in volume (h variation) - tuned to 200 Hz, is now included as a side branch on the pipe. All initial conditions for this simulation are kept the same as the previous simulation. The simulation is converged, then two periods of a 200 Hz sine wave is transmitted through the pipe. The pressure plot for the 200 Hz wave simulation is shown in Figure 86.



**Figure 86: Monitor points plot - 200 Hz pulse simulation with resonator tuned to 200 Hz. Pressure (Pa) against Time (s)**

The centralised monitor points at 0.35 m and 0.45 m from the inlet - red and green lines respectively, shown in Figure 86 are located before the VVH resonator and following points are located afterward. The inlet pulse terminates at the dashed line and a constant pressure inlet condition replaces the wave. Comparing points located upstream of the resonator with the points located downstream, it is clear from the plot, there is a distinct dampening of the pulse after the resonator. This is confirmed by the significant difference in pressure fluctuation amplitude comparing the downstream monitor with no resonator (Figure 85) and the three downstream monitors with the resonator. The acoustic wave reduces significantly in amplitude towards the end of the pipe, shown by the three monitors after the resonator, whereas the first two monitors are fairly constant in amplitude. However, several traits are unexpected, the first being the dissipation on the pulse before the resonator, shown well by the second monitor. This is much more apparent compared to the 1000 Hz pulse simulation shown in the previous section. After the dashed line (constant pressure region), it takes some time for the pressure to settle down to near constant, unlike the 1000 Hz simulation, see Figure 84. This is thought to be due to the longer wavelength of the 200 Hz signal. Each wavelength contains more energy. Thus, a lower frequency will take a longer length of time to dissipate or attenuate. Interestingly, as the input signal is removed, the resonator stops attenuating the signal immediately. This indicates the attenuation is driven by the input signal.

In this section, a simulated 200 Hz signal is shown to be attenuated by a VVH resonator. The simulation has behaved as expected with a high wavelength resolution of over 20 points-per-wavelength and low levels of dispersive errors.

#### 4.1.4 VVH Resonator U-RANS Noise Generation Simulation

The VVH Resonator experiment which created a loud 460 Hz tone, shown in Chapter 2.3, is re-created in the CFD solver. The mesh and solvers are the same as the simulations reported in the previous section to this chapter. The initial conditions are set the same as the experiment – resonator tuned to 460 Hz and the inlet velocity at a constant 20 m/s. Monitor points are created in the centre of the cross section as shown in Figure 87. The neck and resonator monitors are provided to show the pressure fluctuations inside the resonator and the downstream edge monitor is to capture the vortex shedding predicted to occur in this area. The resonator, inlet and outlet monitor points aim to replicate the microphone locations used in the corresponding experiments. This is to reduce any distance-related effects when a comparison to the corresponding experiment is carried out.

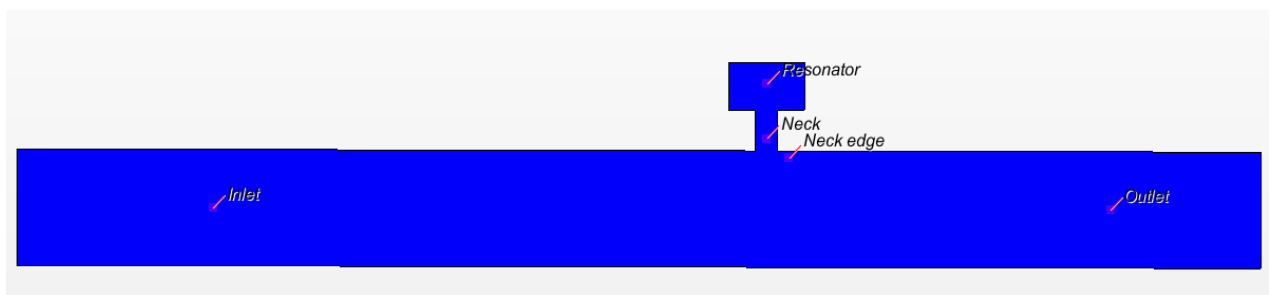


Figure 87: Monitor point locations

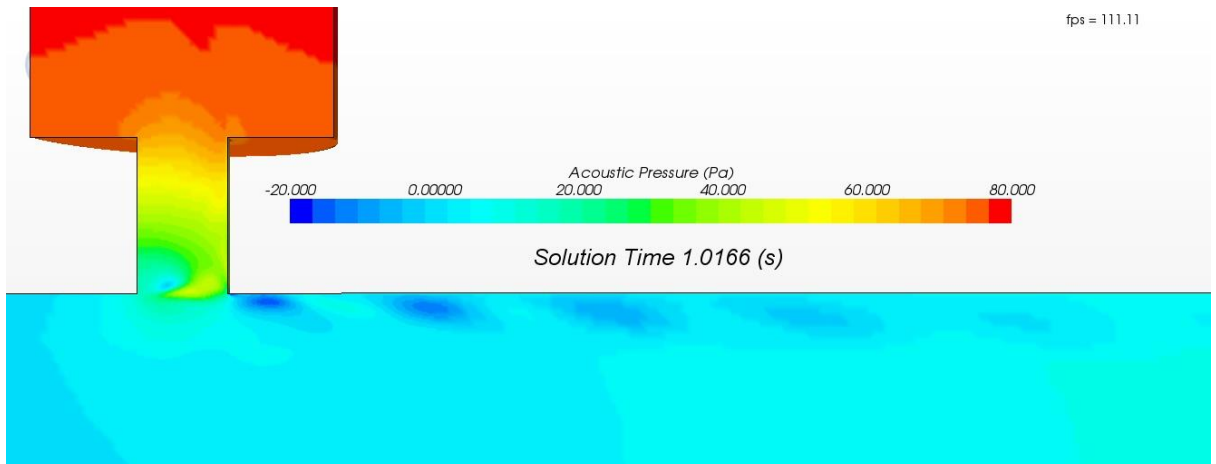


Figure 88: Scalar acoustic pressure scene showing vortex shedding on the trailing edge of the resonator neck.

Figure 88 is a scalar scene showing acoustic pressure (or pressure relative to mean pressure). There appears to be some periodic vortex shedding captured on the trailing edge of the neck, as indicated by the darker blue areas, issuing from the trailing edge. The darker blue areas appear to lighten in colour and grow in size as they move further away from the resonator. This indicates a significant level of dissipation present. The 460 Hz tone experienced in the corresponding experiment could be due to this vortex formation process and the resonant response becoming coupled, forming a flow induced cavity resonance. Therefore, vortex shedding is creating large sound pressure levels inside the resonator. This agrees with the background and literature review in Section 1.4.1.

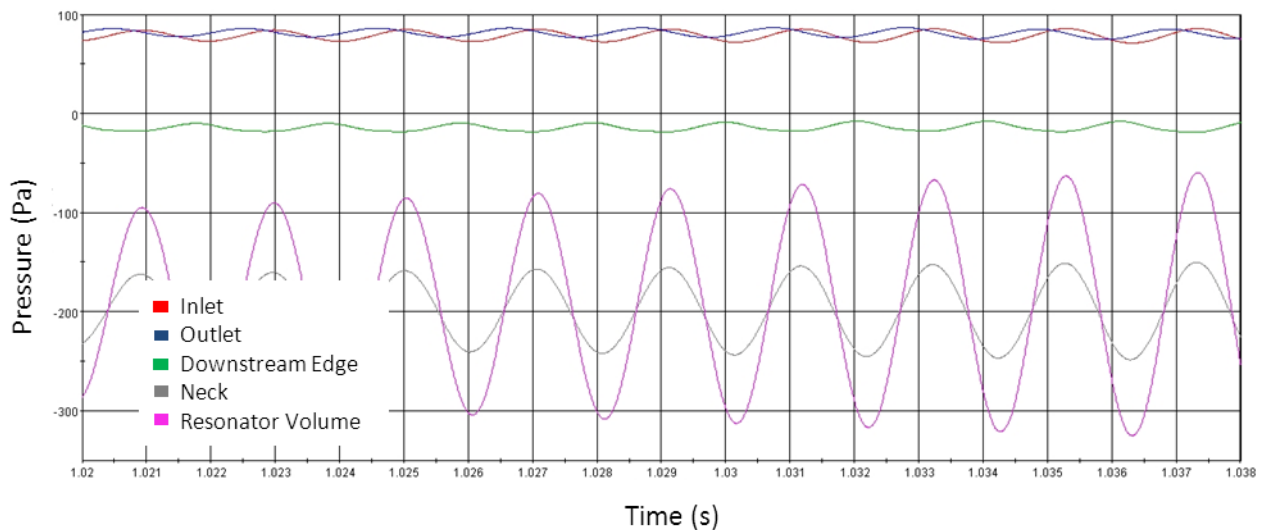
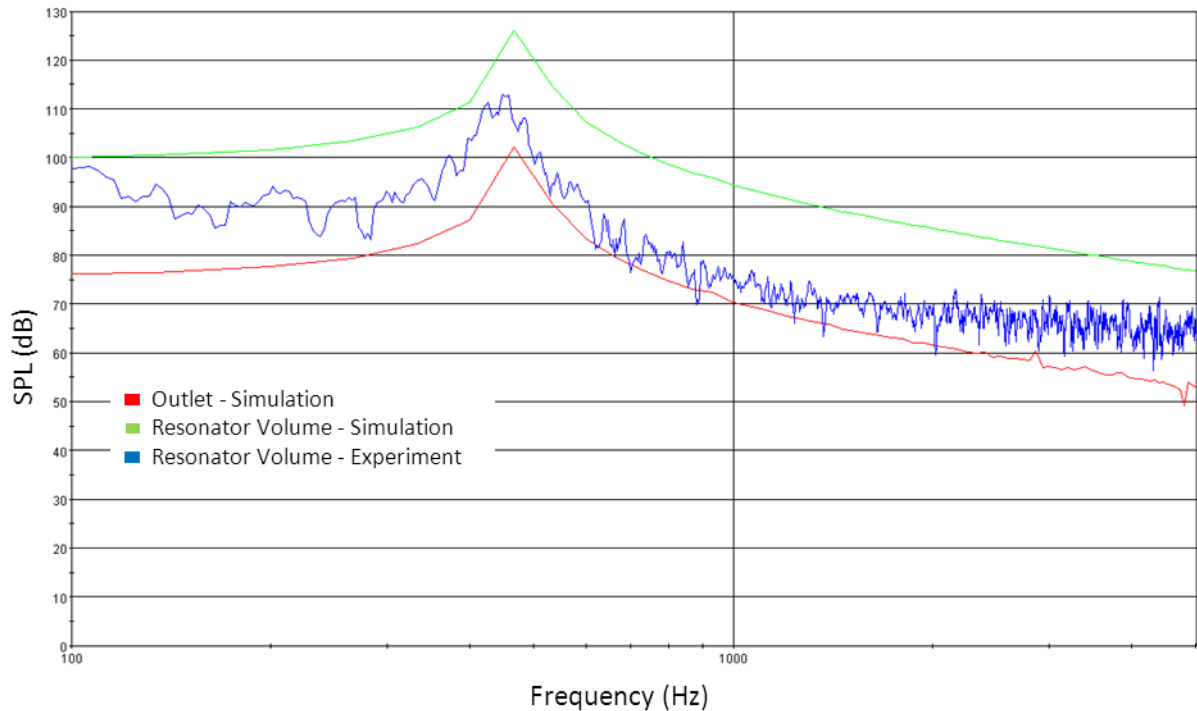


Figure 89: Monitor points plot - Simulation whistle with inlet, outlet, downstream edge, neck and resonator monitor points

A pressure against time plot for each monitor point is shown in Figure 89. The results correspond well with what was shown in Figure 88 and during the experiment. Clearly, the flow pressure is oscillating. Large oscillations are present in the neck and resonator shown by the monitor points. Smaller oscillations are present at the downstream edge which appear to be out of phase to the resonator oscillations but they appear to be similar wavelengths. Oscillations are also present towards the outlet and the inlet. Therefore, assuming the oscillations are caused by the resonator, the oscillations must be travelling back towards the inlet.

An FFT plot for the Outlet and Resonator Volume monitors are shown in Figure 90 along with the Resonator Volume experiment frequency distribution. Star CCM+ uses the Mixed Radix -2-4 method for FFT plots. The solver parameters used throughout the simulation work aim to mirror those utilised for the experiments in Chapter 2. The plot shows a reasonable correlation between experiment and CFD at this relatively low frequency of interest. The experiment produces a 460 Hz tone inside the resonator volume with an approximate Sound Pressure Level (SPL) of 115 dB. The simulation predicts a ~480 Hz tone, around an SPL of 125 dB within the resonator volume. This offset in frequency is also mirrored by the frequency distribution at the Outlet. There is an offset in SPL magnitude throughout the range of frequencies between the experiment and simulation results. Therefore, although the simulation does predict a tone as given by experiments, it can be said, the frequency and SPL of the frequency distribution is not precise and robust enough for this type of flow phenomena.



**Figure 90: FFT plot – U-RANS Simulation of VVH resonator tuned to 460 Hz. Experimental and simulation results shown for inlet and outlet points.**

CFD with a U-RANS solver has been used to predict flow acoustic coupling in a resonant cavity. Overall, the VVH Resonator simulation has produced interesting results. Pressure fluctuations appear to be produced by the resonator which corresponds well with experiment studies. However, what is also clear is the lack of detail, visually and numerically, around the flow phenomena present. The frequency and SPL of the tone predicted has approximately a 10% error when compared with experiment. Although some vortex shedding from the trailing edge is apparent - both visually and in the acoustic frequency spectrum, it is difficult to understand and analyse any flow generated noise processes, such as the onset of shear layer vortex shedding. These phenomena are expected to surround the side-branch entrance to produce the flow-generated noise. This begins to show the limitations of U-RANS. The amplitude and frequency error of the dominant tone is expected to dramatically reduce with the use of an LES solver due to the ability to resolve the larger scales of turbulence directly without averaging the properties of the flow.

#### 4.1.5 Summary

The experiments carried out in the previous chapter have been re-created as numerical simulations using a commercial Computational Fluid Dynamics (CFD) with a U-RANS solver. The results have been analysed and compared with the experiments to deduce the limitations of the U-RANS solver with respect to aero-acoustic investigations. This section helped to understand the role Large Eddy Simulations can play within an industrial design setting.

Several initial validation simulations have been carried out to ensure robust and accurate results are obtained. Robust simulation results are essential to compare to the respective experimental results. Several validation simulations have been conducted using a U-RANS solver to investigate the effect on the acoustic frequency distribution for various side branch configurations as mesh, solver and boundary settings are varied. A side branch consisting of a VVH Helmholtz resonator and an adjustable Quarter Wave Tube (QWT) has been analysed in terms of the effect on the acoustic field in a straight section of pipe. The VVH noise generation simulations began to show the limitations of U-RANS to predict high frequency flow-generated noise. The lack of detail, visually and numerically, around the flow phenomena hampers understanding of the flow-acoustic noise generation present. The frequency and SPL of the tone predicted has approximately a 10% error when compared with experiment. Thus, the limitations for U-RANS have been revealed from an aero-acoustics perspective. It is believed LES can provide substantial improvements in accuracy as well as to enable detailed visual flow patterns and correlations.

## 4.2 Large Eddy Simulations

The LES capability of commercial CFD is assessed by undertaking equivalent simulations of the flow rig experiments to model how the acoustic spectrum of turbulent fluid flows can be affected by a resonator inserted in a pipe or attached as a side-branch. LES solutions are more useful in providing a greater insight into the processes involved inside and around the resonator. LES solvers are used to investigate the phenomenon involved in noise generation due to resonating geometries. It is expected, the LES solver will enable the opportunity to visually inspect the process(es) which are the cause of the noise generated in many of the experimental studies carried out in Chapter 2.

A primary aim of this study is to gain understanding into the advantages and concerns surrounding simulations using an LES solver. In turn, the flow processes, such as shear layer vortex shedding, which are thought to be responsible for the unwanted high frequency noise can be analysed, visually and analytically, in greater detail than is possible through experimental studies alone.

The following LES investigations will firstly validate the simulation set-up, taking into account the extra requirements the LES solver demands for an accurate solution. The inlet flow profile will be discussed along with further validation of the mesh. Furthermore, a RANS vs. LES comparison will be carried out. The advantages of LES will be reinforced. LES is much more accurate as large turbulent scales are directly resolved at instantaneous fluctuations in time, unlike U-RANS solvers which only model the time-averaged turbulent information. Following on from the RANS simulations which are detailed in the previous chapter section, the aim is to further these simulations by simulating the QWT and the automotive CAC resonator geometries using LES. These geometries are shown by the experiments (detailed in Chapter 2) to create high frequency noise, which is the primary concern of this thesis. The Large Eddy Simulations will predict the noise-generating phenomena caused by turbulent flows coupling with certain resonating geometries. The acoustic results will be analysed and compared with the experiments to deduce whether the CFD code is suitable for use as a design tool, and thus could be utilised early on in the product design phase.

#### 4.2.1 LES Validation Simulations

Several validation simulations are carried out to ensure robust and accurate results are obtained. This will ensure confidence when the simulation results are compared to their respective experimental results. A direct comparison between RANS and LES solvers is demonstrated to highlight the benefits of Large Eddy Simulations. The importance of inflow conditions are demonstrated along with a further mesh independence study.

CFD LES physics models for all simulations, unless otherwise stated, are listed below.

- Compressible Ideal gas (Air)
- Large Eddy Simulation
- Standard Smagorinsky SGS
- 2nd order Implicit Unsteady
- Segregated Flow (Fluid Temperature)

- Turbulent, Three Dimensional
- All  $y^+$  Wall Treatment
- Momentum - second order upwind
- Algebraic Multigrid (AMG) method

#### **4.2.1.1 Turbulent flow profile using LES**

Producing an accurate level of turbulence is very important when aero-acoustics is the primary concern. As the range of Reynolds number dealt with here is firmly in the turbulent region, ideally a fully developed transient pressure, temperature and velocity profile needs to be imposed at the inlet. This would help to create an accurate level of turbulence and therefore obtain correct broadband noise towards the outlet or monitoring region of interest. The acoustic pressure scene, provided in Figure 91, shows the importance of inflow boundary conditions. Using a mean 'single value' inlet condition forces the turbulent flow to be developed over a long distance. A fully developed turbulent flow takes 10-20 diameters to form (Tu, et al., 2012). Therefore, a substantial amount of extra CPU resource is required for this purpose. What is also interesting, from Figure 91, is the contribution to the acoustic noise the turbulence has towards the end of the pipe. This must be captured in simulations to predict an accurate mean SPL.

The turbulent boundary layer brings into question how the boundary layer thickness will affect noise generation in the area of interest. A very high level of background turbulence could 'hide' the vortices created by the resonator, both visually and numerically. If CFD with LES is to be used as a design aid, the areas of high turbulent pressure fluctuations and vortex generation must be known. According to G. Kooijman (G. Kooijman, 2008), for boundary layers with similar shape, the amplitude of the oscillations increases with decreasing boundary layer thickness. This suggests only the SPL will be affected by the thickness of the boundary layer. Thus, the difference between fully turbulent flow and partial turbulent flow is not expected to have a great effect on the initialisation of noise generation and the frequency spectrum. However, to validate the Large Eddy Simulations to experiment, the incoming flow must be modelled as realistically as possible. The flow field at the upstream boundary condition is investigated with a view to replicating the experimental rig flow.

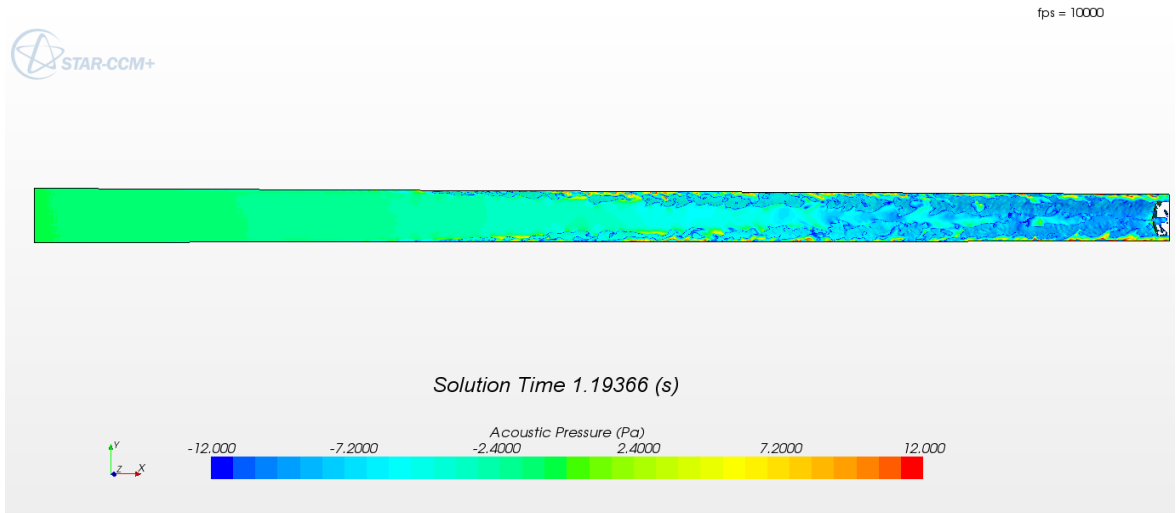


**Figure 91: Straight pipe showing a developing turbulent flow using LES**

The recommended procedure to run efficient simulations using LES is to initialise Large Eddy Simulations with a steady RANS solution. This flow field is then used as an initial guess for the fully compressible transient LES simulation. This is a useful technique for optimizing the computational time of the transient simulation by providing a representative initial field. Inlet validation tests are carried out between a fully developed inlet, a time dependant fully developed inlet and using the Synthetic Eddy Turbulence Model (SEM), see Chapter 3.2, to assess the effects on acoustic results.

A steady state fully developed inlet is formed as follows. A pipe geometry is created that represents a short 0.2 m section of the experimental duct. Periodic boundary conditions are imposed on this geometry, linking the upstream and downstream boundaries – essentially creating an infinitely long pipe. The RANS Reynolds stress turbulence model is used to solve in steady state. The resulting case is used to extract the upstream boundary conditions to a table (Reynolds stresses, turbulent length scale, and velocity magnitude, as a function of XYZ position) ready to import as inlet conditions for the geometry of interest. The case of interest is carried out in steady state with the K- $\epsilon$  turbulence model, to establish an initial flow field and large flow structures. The continuum is then changed to transient, with an LES solver. The inlet boundary conditions are imported as a table and the shear boundary shear layer and the instabilities are allowed to become random and fully turbulent over time and a short inlet distance.

A transient fully developed inlet is the most accurate and realistic in terms of turbulence propagation. Random vortices can be created and fed in directly at the inlet, eliminating the need for a length upstream of the test section. The procedure is similar to

the steady state inlet. However, the LES solver with transient conditions is used for the short section of the experimental duct with periodic boundary conditions. An example of turbulent fully developed flow is shown as a velocity scalar scene in Figure 92. Pressure, velocity and temperature profiles are extracted from the boundary every time-step and imported into the simulation of interest at the inlet boundary using a macro.

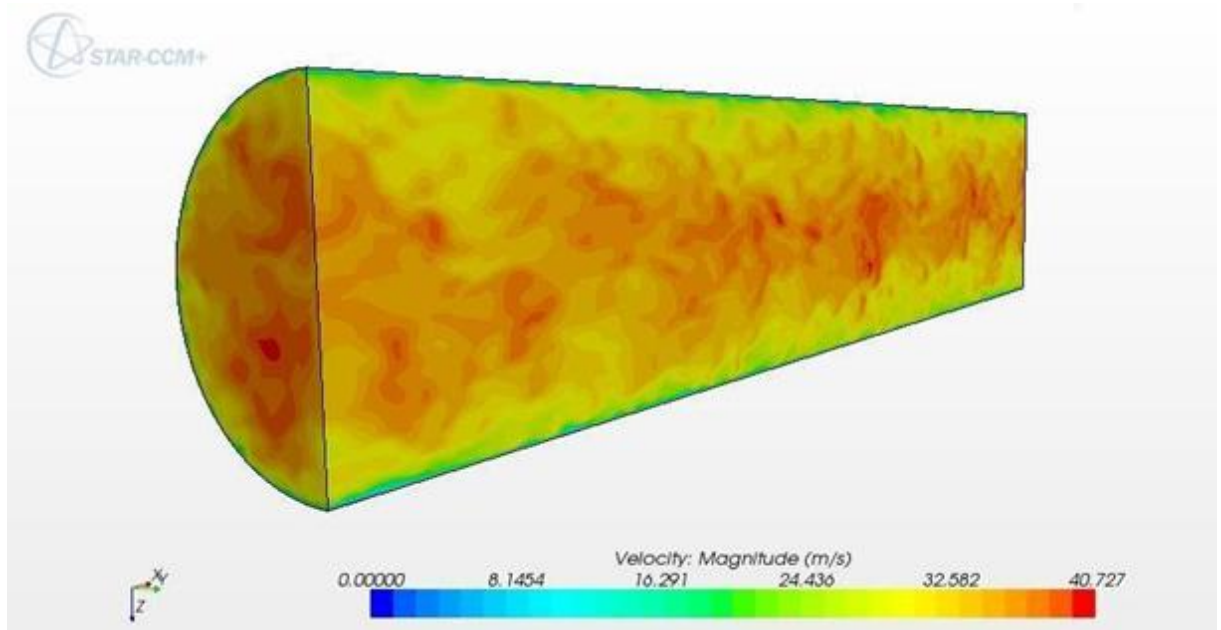


Figure 92: Turbulent fully developed flow

The SEM imposes, as the name suggests, synthetic turbulent structures as perturbations on top of the inlet profile. The size of these perturbations is related to the turbulence conditions specified. When computing the SEM velocities, the number of eddies that are used in the calculation is inversely proportional to the length scale cubed. Reynolds stress data is necessary as a precursor. Therefore it is ideal to utilise the SEM with a steady state fully developed profile. The formulation for the SEM is summarised here. More detailed information can be found in the Star CCM+ user guide (CD-Adapco, 2011). The fluctuating velocity signal is generated on an interval  $[L_{x,\min}, L_{x,\max}] * [L_{y,\min}, L_{y,\max}] * [L_{z,\min}, L_{z,\max}]$  using a shape function defined in  $[-\sigma_x, +\sigma_x] * [-\sigma_y, +\sigma_y] * [-\sigma_z, +\sigma_z]$ . The interval limits are based on the geometric limits of the inlet section, as shown in Figure 93 where  $\sigma$  is the mean eddy length scale in each coordinate direction.

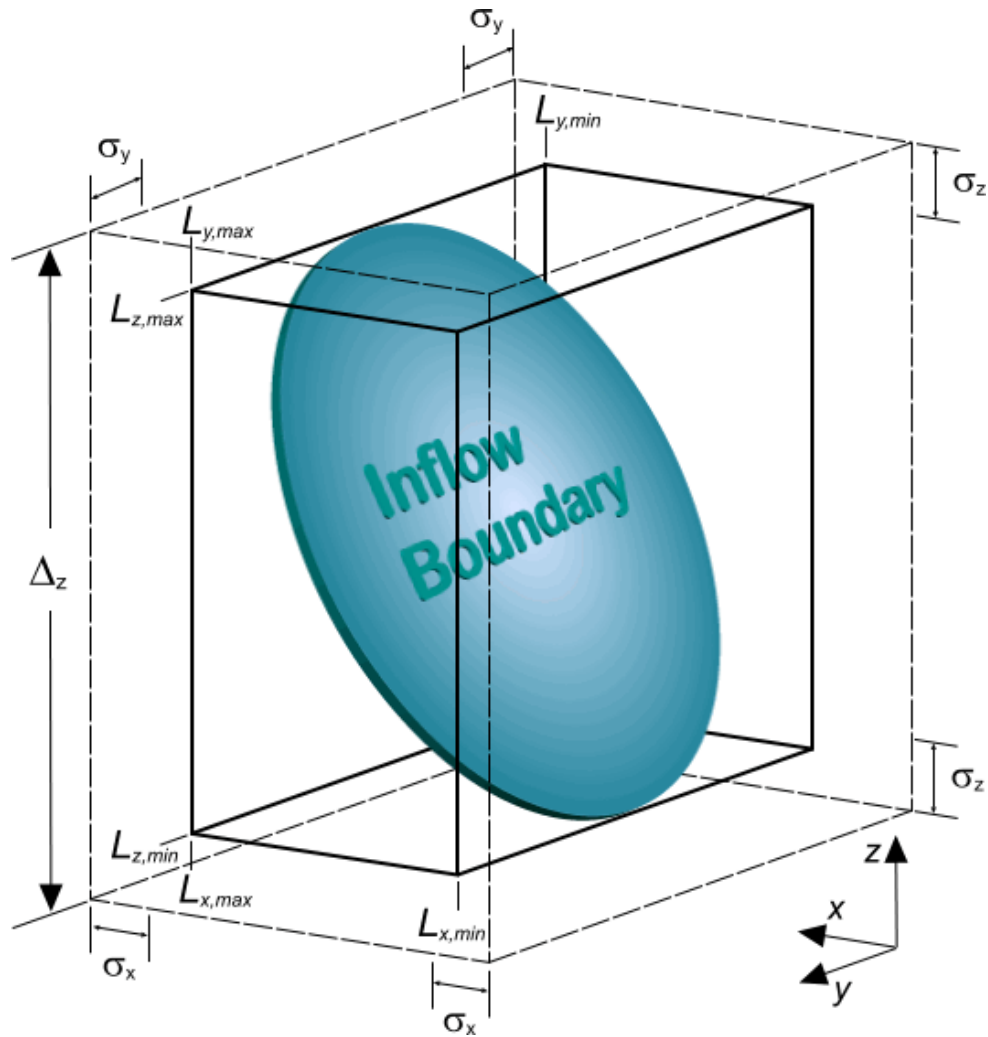


Figure 93: Geometric inlet section limits (CD-Adapco, 2011)

A tent function is used to represent the influence exerted by the  $k$ -th eddy at position  $x_k$  on a point  $x$  on the inlet surface. The scale,  $\sigma_k$  and a rotation direction is given as shown in Equation [45] (CD-Adapco, 2011):

$$\epsilon_{k,i} = \pm 1 \tag{45}$$

The direction of rotation is chosen randomly from a uniform distribution. The eddy turbulent length scale,  $\sigma_k$ , is assumed to be isotropic, so while it may vary according to position in space, it must have the same value in each coordinate direction at any one point. The Star CCM+ documentation (CD-Adapco, 2011) states the reason for this is preliminary studies have shown that for increasing values of anisotropy in the turbulent length scale,

there is a progressively larger departure from the analytical normalization properties of the shape function. This results in distortion of the instantaneous velocity signal, which fails to recover the prescribed moments. This area is currently the subject of on-going research. The coordinates of the centre of each eddy is chosen randomly in a volume. The number of eddies, is obtained from the ratio of this volume to the average eddy volume. The position of each eddy,  $k$  is advanced in each coordinate direction according to Equation [46] (CD-Adapco, 2011):

$$x_{i,k}^{new} = x_{i,k}^{old} + \Delta t V_i \quad [46]$$

The convective speed,  $V$  is obtained as an average over the inlet area of the mean flow velocity profile. From this inherent isotropic eddy scaling, the SEM solver is expected to create some non-random turbulence which will manifest itself as maxima and minima if the acoustic frequency distribution is analysed. The SEM solver also requires  $\sim 10$  pipe diameters upstream for the turbulence to fully develop. An upstream length is also required for a mean velocity profile imposed at the inlet. However, the transient fully developed profile does not need such a length upstream and should in theory yield a quicker simulation run time. In reality, this is not the case as the cumulative time required for the macro to import the profile each time step is considerable, along with solving the initial periodic LES simulation.

The FFT plot comparing each of these options is provided below in Figure 94 and a close-up of the region of interest is given in Figure 95.

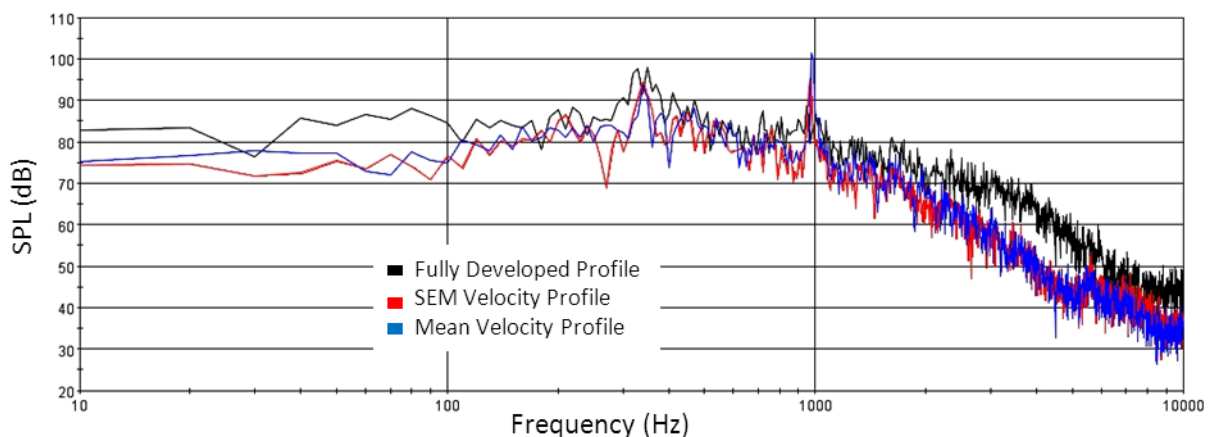
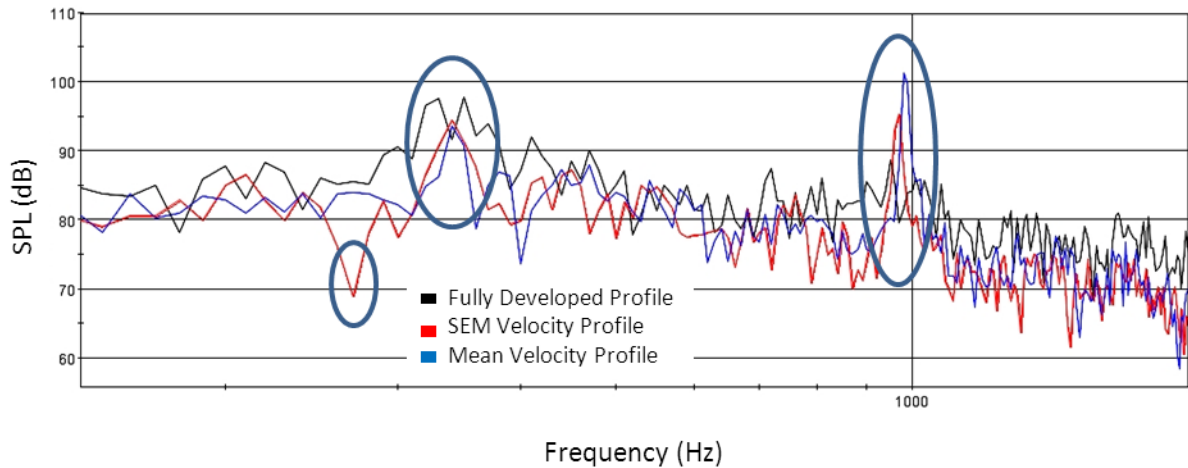


Figure 94: FFT plot of simulations showing SPL (dB) against logarithmic frequency for three inlet conditions on a straight pipe with a side-branch QWT and a flow velocity of 30 m/s



**Figure 95: A close-up region of an FFT plot showing simulations three inlet conditions on a straight pipe with a side-branch QWT and a flow velocity of 30 m/s**

Each line represents the frequency distribution at a downstream point of the QWT monitoring location in the centre of the main pipe. The simulation is of a 40 mm diameter QWT, the same geometry used in the experimental work, with no neck protrusion and a flow velocity of 30 m/s. The black line represents the transient fully developed inlet profile simulation. The red line represents the simulation using a mean velocity profile with the SEM solver turned on and the blue line represents the simulation with a mean fully developed profile. A peak or tone is present for the SEM and mean velocity simulations at  $\sim 1000$  Hz and a small peak is present at 350 Hz. The peaks are not visible with the transient fully developed inlet profile. This is possibly due to the shedding frequencies being 'lost' in the background turbulence noise. A negative pulse is also present at just under 300 Hz with the SEM model turned on, which is not present in the other two cases. This suggests the SEM model could have some unwanted effects on the frequency distribution downstream. This is thought to be caused by the inherent nature of the model where by the synthetic vortices created will tend to repeat over time causing the frequency distribution of the flow to be somewhat characterised by these repeating frequencies. The transient velocity profile condition tends to produce a higher mean SPL, which although possibly more realistic in terms of turbulence flow properties, the increase in mean noise may reduce the ability to locate high frequency shedding. The transient fully developed option becomes even less attractive when considering the extra run time required, firstly extracting the data and then to re import the data every time step.

Overall, from a practical point of view, this validation exercise has shown a mean velocity profile with an adequate length upstream of the test section appears to be the most ideal solution for the simulations which are detailed in this thesis.

#### **4.2.1.2 Turbulence Levels for Large Eddy Simulations**

Although a mean velocity profile with an adequate length upstream of the test section is chosen as an inlet flow condition for reasons of practicality whilst not reducing accuracy of the results under study, it is interesting to investigate the level of turbulence generated by a fully developed transient LES flow within the CFD solver

The energy spectrum of a simple straight pipe with the LES solver is analysed and compared to theory such as the Kolmogorov  $-5/3$  power law (Kolmogorov, 1941) for turbulence kinetic energy. This is to assess the level of turbulence and dissipation in the flow and to ensure it is analogous to real fully developed turbulent flow. However, the turbulence kinetic energy spectrum is unavailable directly, with the LES solver enabled in Star CCM+. Mean-flow quantities must be obtained by gathering statistics either over a long physical time, and/or from a homogeneous spatial coordinate. Therefore, as detailed in Chapter 3.1, calculation of the Reynolds stress from time averaged velocity values is necessary to construct the complete turbulence kinetic energy spectrum.

To provide a baseline for the Reynolds Stress values, a simple straight pipe, 74 mm in diameter and 0.5 m in length is solved with a 1.25 million cell mesh (1 mm core, 10 prism layers) and a steady RANS  $K-\epsilon$  solver. A periodic interface is imposed on the boundaries to create the effect of an infinitely long pipe. The Reynolds stresses in the 'uu' direction for evenly spaced line monitors along the pipe is shown in Figure 96. The line probe monitors are placed centrally through the geometry at 0.1, 0.2, 0.3 and 0.4 m in the longitudinal direction. The flow is time averaged when the mean turbulent stresses have the same profile along the pipe i.e. when the lines overlay such as the plot shown in Figure 97. The line plot the stress distribution normal to the wall. The lines show the averaging period is acceptable. The initial Reynolds stress distributions across the pipe look promising and as expected when compared to published data, such as Mathieu and Scott (Mathieu & Scott, 2000).

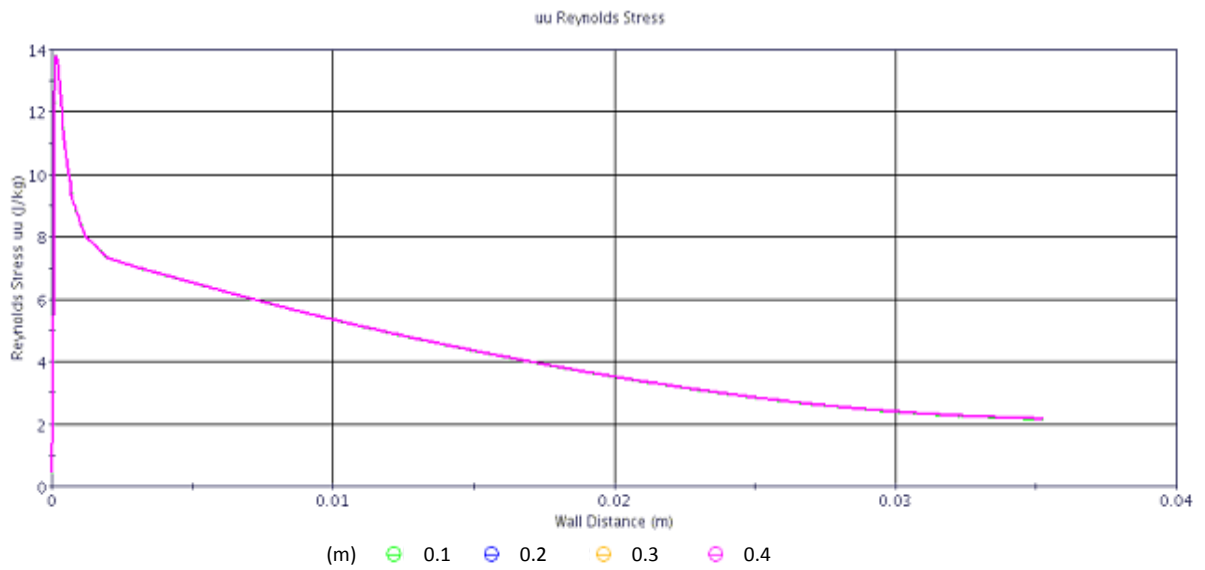


Figure 96: Steady State RANS 'uu' Reynolds Stress distribution in a radial direction at four points, evenly spaced, along the pipe.

An identical simulation with the LES solver is carried out to provide a Reynolds stress and kinetic energy comparison with theory/published results and the RANS data. The 'uu' Reynolds stress for evenly spaced line monitors along the pipe with the LES solver is shown in Figure 97.

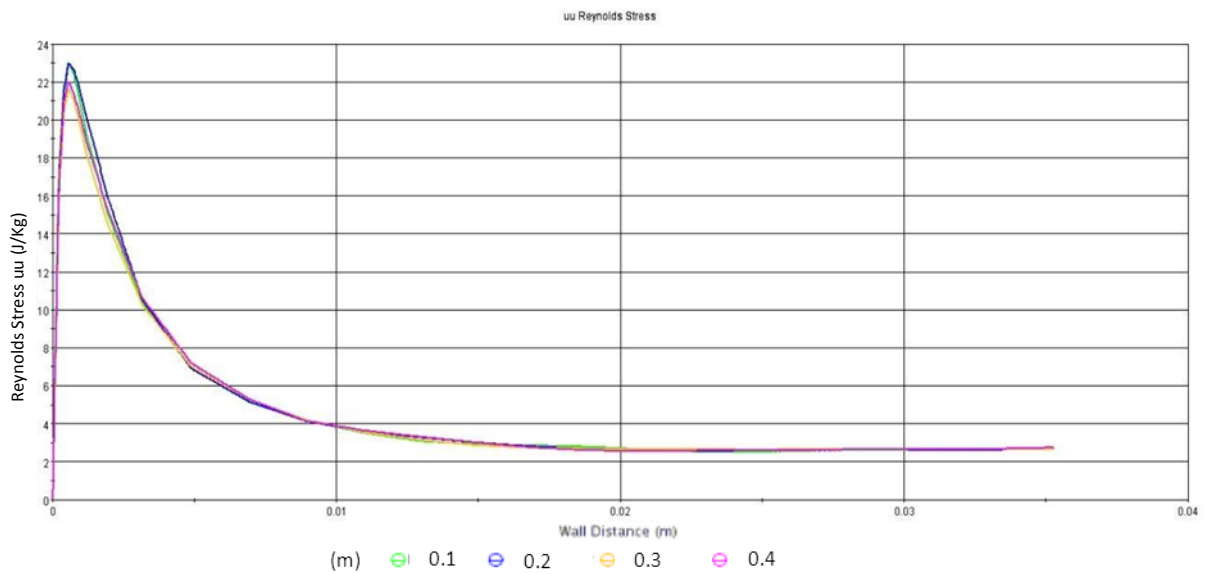


Figure 97: LES 'uu' Reynolds Stress distribution in a radial direction at four points, evenly spaced, along the pipe.

Figure 97 reveals the peak values are much higher than the RANS results with the same mesh. This indicates the overall turbulent energy values are higher than anticipated, particularly in the region close to the wall.

As the region close to the wall appears to produce incorrect turbulent energy values, the effect of the wall function is analysed. The wall-function available in the CFD solver is an empirically derived correlation based on the log-law, as given in Figure 98, which is in turn derived from the boundary layer equations under steady state conditions. As Jayaraju et al (Jayaraju, et al., 2010) states; applying wall-functions to predict unsteady effects contradicts the very physical assumption behind the derivation of wall-functions. Hence, it is conceivable that the wall-function based approaches may not yield satisfactory results for the prediction of near-wall fluctuations. On the other hand, performing wall-resolved simulations for the Reynolds numbers occurring in industrial applications is simply not feasible due to large computational costs. Therefore, wall-functions are still most widely used in practical studies to capture the boundary layers. It is recognised that near-wall modelling is a very important and critical aspect that influences the accuracy of a CFD prediction.

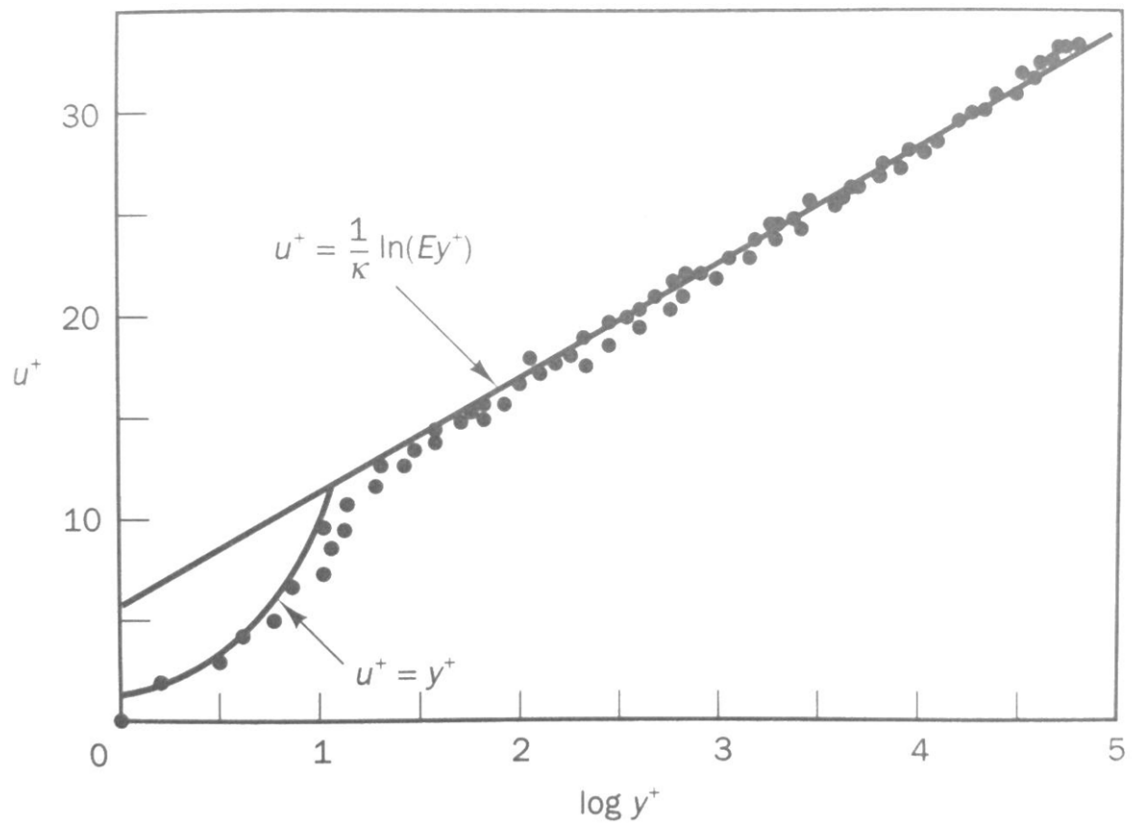


Figure 98: Boundary layer velocity distribution near a solid wall (Schlichting, 1979)

The effect of the wall function is analysed by running back-to-back simulations with and without the wall function applied. Both ANSYS-FLUENT (ANSYS, 2011) and CD Adapco (CD-Adapco, 2011) advise at least 10 cells in the viscous sub-layer - below a  $Y^+$  value of 10, to ensure the boundary layer is fully resolved. The mesh quality for various numbers of prism layers is analysed and recorded in Table 5. To resolve below a  $Y^+$  value of 10, 10 cells must be located within a thickness from the wall of 0.16 mm. The mesh utilised in the simulations in this section only has approximately 4 cells in the viscous sub-layer (shown in blue in Table 5). This mesh density is not fine enough to resolve the boundary layer.

Number of Prism Layers	Y+	1 <sup>st</sup> prism layer height (mm)
1 (2 mm base size)	120	2
2 (2 mm b/s)	55	0.80
4 (2 mm b/s)	20	0.30
6 (2 mm b/s)	10	0.16
8 (2 mm b/s)	5	0.08
10 (2 mm b/s)	3	0.041
10 (1 mm b/s)	1.2	0.022
20 (1 mm b/s)	<1	<<0.02

**Table 5: A table to shown how the number of prism layers affect the Y+ value and 1st prism layer height in mm with a constant stretch factor of 1.5**

To fully resolve the boundary layer with no wall function, the number of prism layers needs to be as stated highlighted red. This equates to an overall cell count of 8.6 million cells which is not practical to solve in general industry when scaled to real world geometries. This agrees with Jayaraju et al (Jayaraju, et al., 2010) who suggests a wall function must be utilised. However, as a validation study and as the Reynolds stresses and turbulent energy has been shown to be higher than theory and the RANS base line values would suggest being correct, the test case geometry is re-meshed with the red highlighted settings in Table 5. An LES simulation of this re-meshed case is carried out with wall functions disabled. The effects of the SGS model is also analysed as this parameter can have a considerable effect on the near-wall turbulence levels and thus affects the core turbulence energy level. SGS models are briefly discussed in Chapter 3.1. As stated in the aforementioned chapter, the ‘Standard’ Smagorinsky SGS model is utilised in this thesis. The Standard SGS model is compared to the Dynamic Smagorinsky SGS model and the Kolmogorov  $-5/3$ 's law. The Turbulent Energy Spectrum is plotted for both SGS models and compared to Kolmogorov’s law in Figure 99. The Turbulent Energy Spectrum is also plotted for the fully resolved boundary layer case which can be compared to the ‘Standard’ Smagorinsky SGS simulation results.

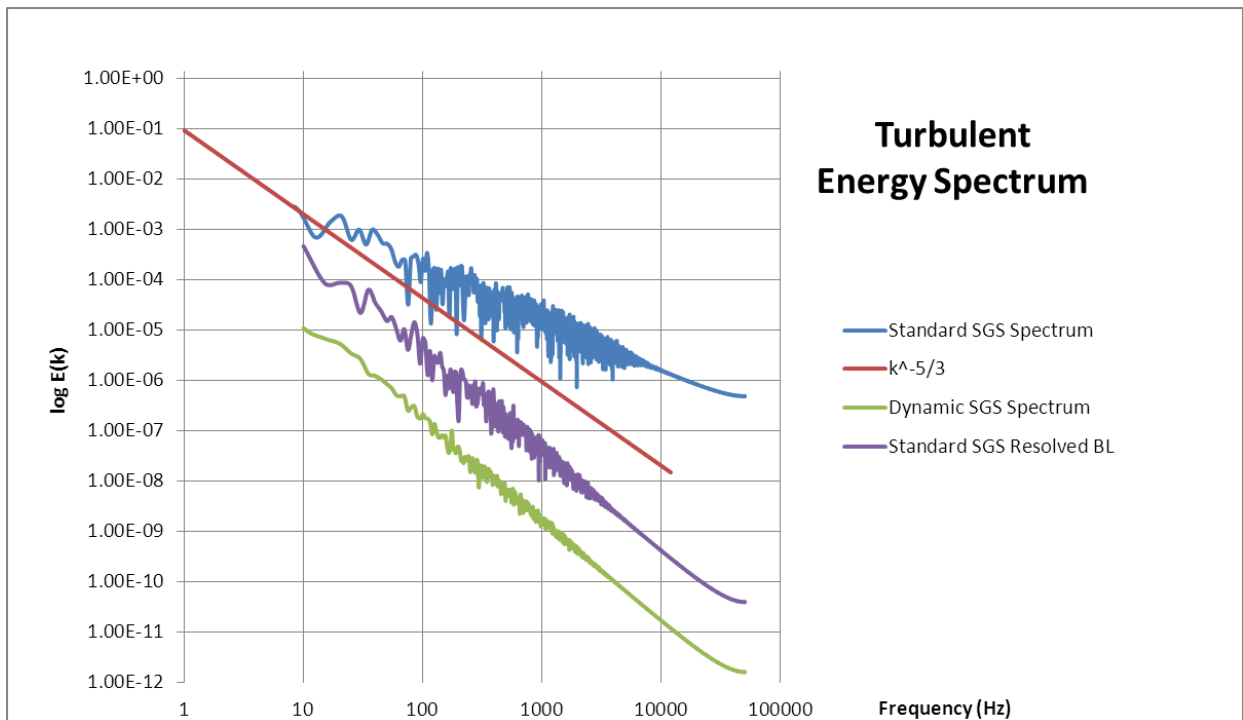


**Figure 99: Turbulent Energy Spectrum for Standard and Dynamic SGS models along with the Kolmogorov 5/3's law.**

The SGS model is shown to have a dramatic effect on the mean energy content across all wavelengths as well as the gradient of the energy cascade across the eddy scales. The turbulence intensity, calculated using Equation [25], coupled with the energy spectrum given in Figure 99 provides a robust set of data to compare the various SGS methods and boundary layer construction under consideration. The Standard SGS model provides an overall energy spectrum which is of the same order as theory (Kolmogorov's law) would suggest being accurate. However, at higher wavelength numbers, the turbulent energy is much higher than the published data. This reinforces the results given by the Reynolds stress plot. The Dynamic SGS solver produces a vastly different energy spectrum. The mean energy across the wavelengths is around two orders of amplitude lower when compared with the  $-5/3$ 's law. However the gradient, i.e. the energy distribution across the scales follows the  $-5/3$ 's gradient very closely. The resolved boundary layer case produces differing results again. The energy spectrum follows the Kolmogorov law closely in gradient when compared with the coarse mesh (with the All  $Y^+$  wall function applied). The mean amplitude of the energy spectrum is one order lower compared with the  $-5/3$ 's law. This appears to show the resolved boundary layer case with the Standard SGS model produces more accurate results than the dynamic SGS case with the wall function applied. Overall, the dynamic SGS model is not found to be suitable in combination with a wall function and periodic boundary

conditions – around 2-3 orders of magnitude away from the theoretical energy distribution. Therefore, the standard SGS model is utilised in this thesis. With the default coefficient applied, the energy spectrum is less than one order of magnitude away from the theoretical energy distribution. Tuning the SGS coefficient is proposed to increase accuracy of the energy cascade process within the simulations. However, for the purpose of this thesis – proving LES as a tool to be utilised in predicting the production of high frequency tones, the SGS model with default settings provides adequate accuracy of the turbulence energy spectrum.

This chapter section has examined the level of turbulence generated by a fully developed transient LES flow in the CFD solver. This is to assess the level of turbulence and dissipation in the flow and to ensure it is analogous to real fully developed turbulent flow. Although a fully developed transient turbulent inlet flow profile was not used throughout this thesis for reasons discussed in the previous chapter section, it is deemed to be worthwhile investigating the high level of turbulence found in the previous flow profile analysis simulations.

The Reynolds stresses and turbulent energy using the LES solver and the standard SGS model has been shown to be higher than theory and RANS base line values would suggest being correct. The mean and peak values with the U-RANS simulations are much lower than the LES results with the same mesh. This is also found to be the case when the mesh is refined. The wall function has been shown to have a dramatic effect on the level and distribution scales of turbulence. When the wall function is disabled, with a mesh fine enough to adequately resolve the boundary layer, the gradient of the energy scales follow theory closely. The mean amplitude of turbulence decreases below the theoretical values. Results for the resolved boundary layer case are expected to become very accurate if the SGS coefficient is reduced, which will decrease the damping. This will increase the mean energy amplitude to the correct levels.

The difference in turbulent energy levels between the dynamic and standard SGS models is dramatic. The standard SGS model is found to over predict the level of turbulence, whereas the dynamic model is found to under predict the turbulence level by several factors of magnitude. Therefore, this is further evidence to suggest wall functions, coupled with periodic boundary conditions are incapable of providing accurate and realistic fully developed turbulent flow with settings that are practical from an engineering perspective. The level of turbulence is found to be very sensitive to the SGS dissipation rate. Therefore, iterative steps must be taken to determine the correct SGS coefficient for the specific

problem under study. The dynamic SGS model is not found to be suitable in combination with a wall function and periodic boundary conditions. It is suggested the dynamic SGS model provide more realistic turbulence levels if it is used without periodic boundary conditions and a wall function applied.

#### 4.2.1.3 Mesh Independence

A series of mesh independence simulations is carried out using the QWT geometry with a 5 mm protrusion and a mean flow inlet velocity of 30 m/s. As this is an acoustically based study, the mesh validation is primarily based on the ability to accurately capture acoustic wavelengths.

The standard mesh which is used for previous simulations – 2 mm base with 1 mm refinement in the area of interest, as shown in Figure 100, is compared with a 1 mm base mesh with no refinement area and a 2 mm base mesh with no refinement area. The total number of Hexahedral mesh cells is 1.5 million cells, 6.5 million cells and 1.3 million cells respectively. The 1 mm base mesh is shown in Figure 101. A representation of the 2 mm base mesh is provided in Figure 102.

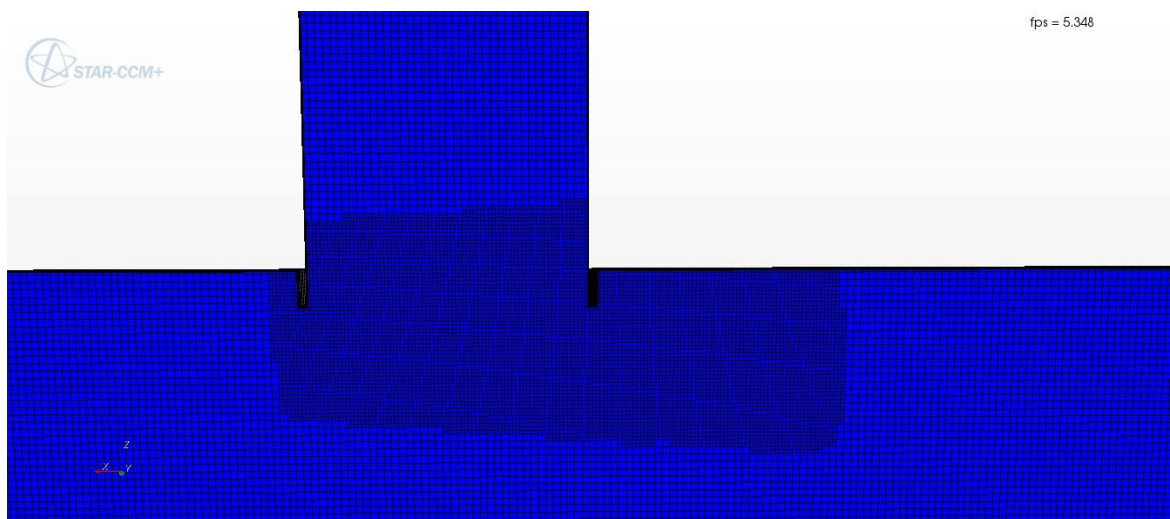


Figure 100: Volume mesh - 2 mm base size, with 50 % further refinement around area of interest

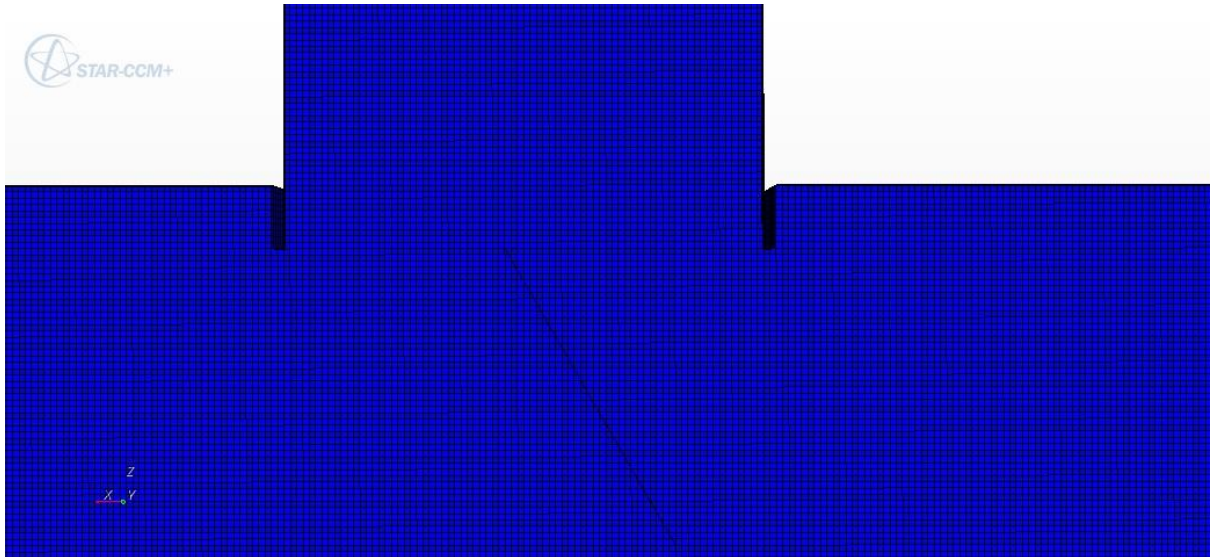


Figure 101: Volume mesh - 1 mm base size, no refined areas

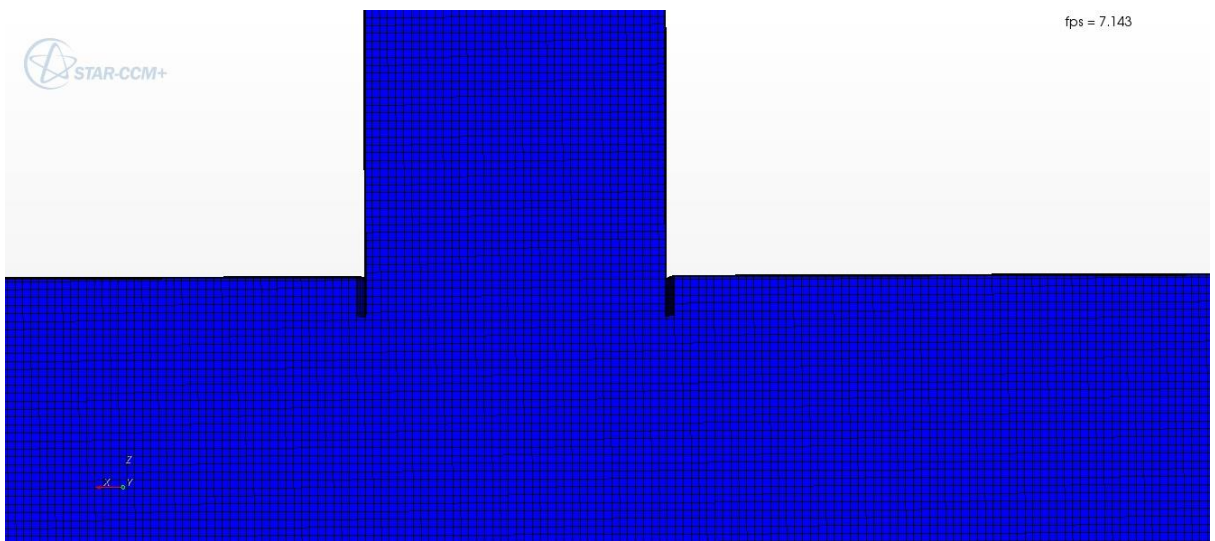


Figure 102: Volume mesh - 2 mm base size, no refined areas

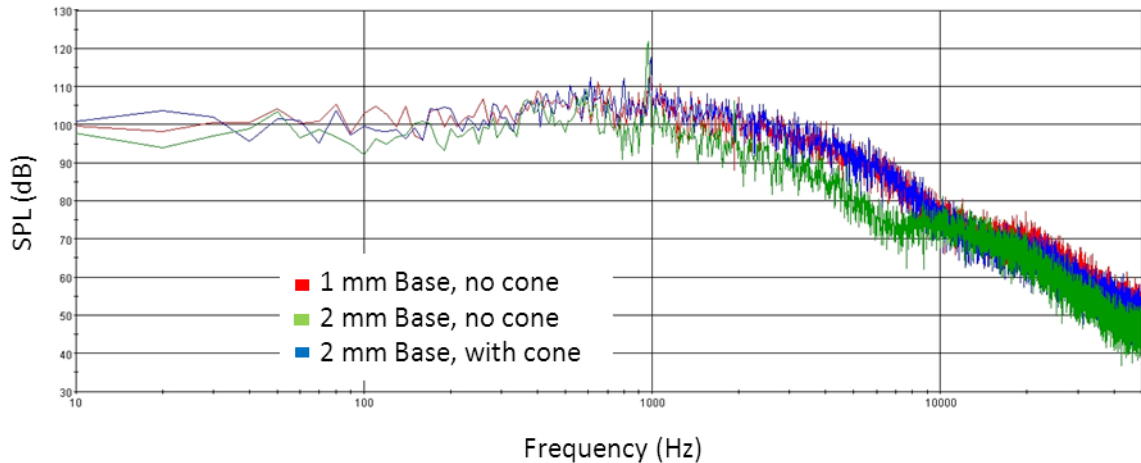


Figure 103: FFT plot - Simulation downstream edge monitoring point of a QWT with three different meshes

Figure 103 shows the noise frequency distribution around the downstream edge of the QWT. The three meshes produce similar FFT's. The 1 mm mesh and the 2 mm mesh with refinement create almost identical results in this area, whereas the more coarse 2 mm mesh doesn't appear to be as robust in the higher frequency region. The refinement around the neck gives an increase in the mesh frequency cut-off, very similar to the fine mesh. The more coarse mesh (green line) does capture the 1000 Hz peak accurately, although this mesh does not capture the higher frequencies as effectively as the finer meshes. The original 2 mm mesh with 1 mm refinement is found to capture the turbulence adequately whilst utilising a fairly modest cell count. The refinement around the neck gives an increase in the mesh frequency cut-off, yet only increases the mesh count by 0.2-0.3 million cells.

#### 4.2.1.4 RANS/LES QWT Comparison

A simulation of an accurate representation of the experimental geometry with the QWT, flush to the main pipe is carried out with the U-RANS K- $\epsilon$  solver to compare the results to an identical LES simulation. This study allows a direct comparison between RANS and LES to be demonstrated to highlight the advantages of the LES solver. Figure 104 below shows an acoustic pressure scene from the LES simulation. Clearly pressure fluctuations due to vortex shedding are apparent around the QWT with the pressure against time plot showing noise at all monitoring points in the geometry. Conversely, the same geometry using the U-RANS solver, Figure 105, shows little noise in the geometry. The pressure plot confirms this with the pressure fluctuations becoming negligible in all point monitored areas.

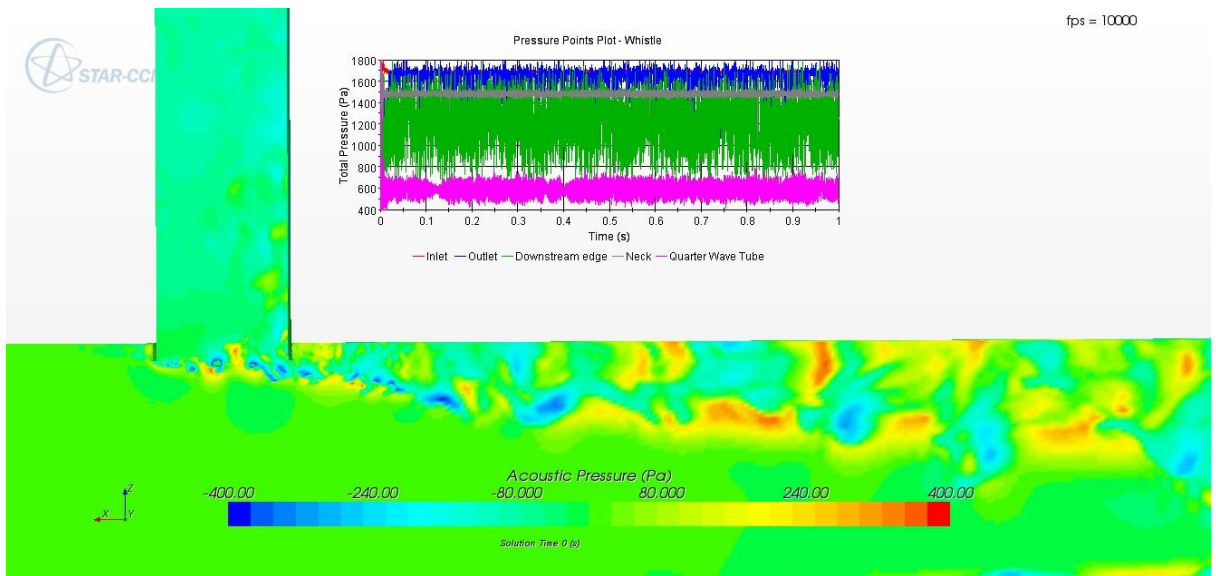


Figure 104: LES simulation of the QWT geometry at 30 m/s mean flow velocity

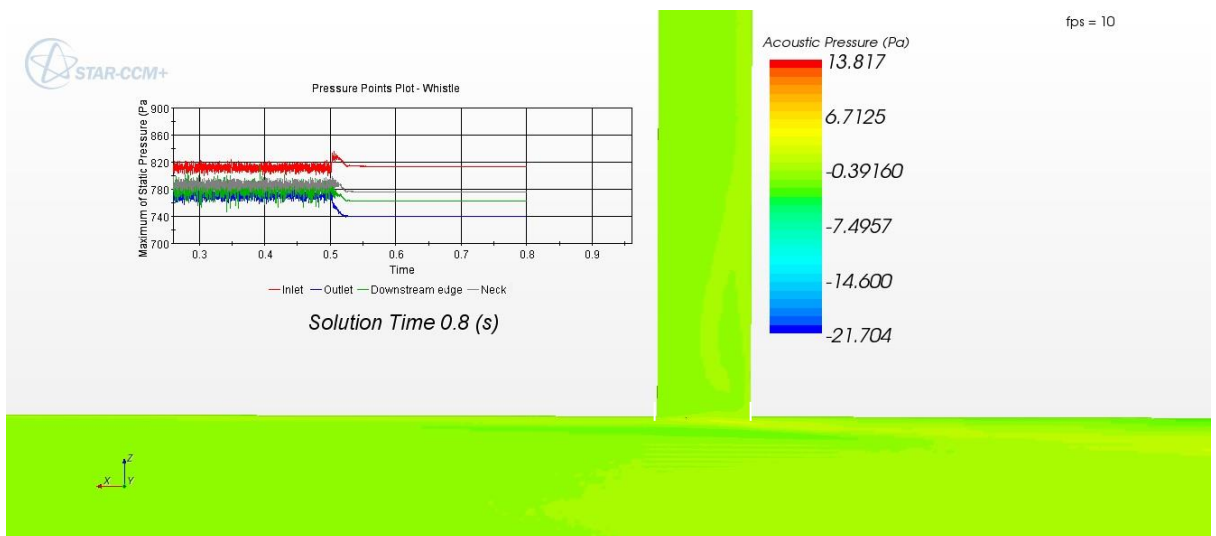


Figure 105: U-RANS simulation of the QWT geometry at 30 m/s mean flow velocity

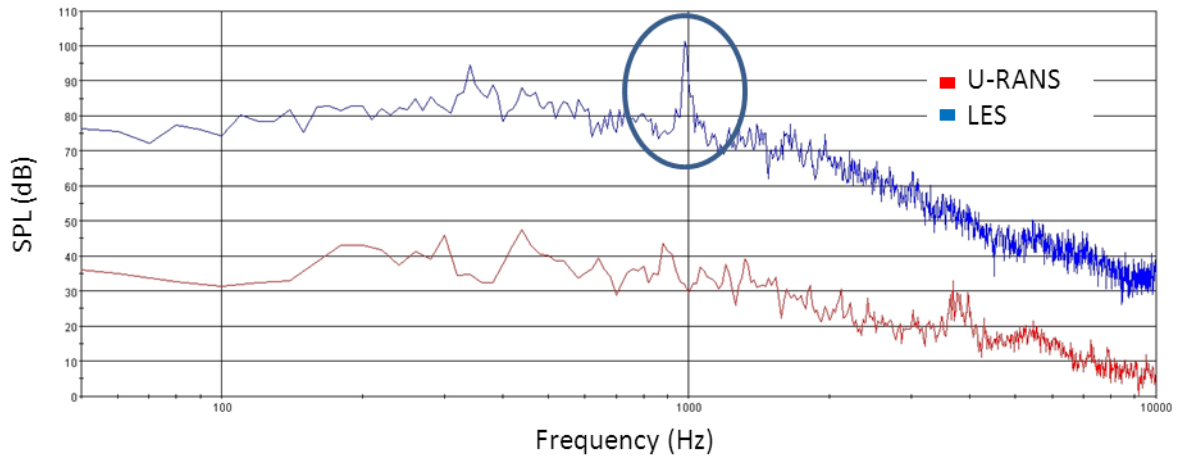


Figure 106: FFT plot - Outlet monitor point comparison between LES and U-RANS

The eddies which are shed off the edges of the QWT have a large effect on the noise generation which is not picked up with U-RANS. As a visual exercise, Large Eddy Simulations can provide clear and detailed information regarding the location and amplitude of the vortices and thus, the pressure fluctuations transmitted further downstream. This is highlighted by the FFT plot provided in Figure 106 which compares the frequency distribution for both U-RANS and LES at a point towards the outlet. The SPL of the broadband noise content for the U-RANS simulation is typically half of that shown for the LES simulation. The large peak at around 1000 Hz and the smaller peak around 350 Hz which are clear in the LES simulation do not appear to be present in the U-RANS simulation. This analysis has shown the advantages of an LES simulation as opposed to U-RANS. The U-RANS solver does not appear to be able to predict vortices being shed off the sharp edges around the resonator neck. This lack of fidelity manifests itself as an inability to capture high frequency noise issuing from these geometries which are central to this thesis. Therefore, LES is essential to enable the prediction of high frequency noise.

#### 4.2.2 VVH Resonator LES Noise Generation

The VVH Resonator experiment which created a loud 460 Hz tone, as shown in Chapter 2.3, is re-created in Star CCM+. An identical simulation using a RANS solver has been carried out in Chapter 4.1.4. Thus, this LES VVH resonator simulation can be validated against experiment and can also be compared against the RANS simulation. The mesh and

solvers are the same as the RANS simulation – resonator tuned to 460 Hz and the inlet velocity at a constant 20 m/s. Monitor points are created in the centre of the cross section as shown in Figure 87. Further detail is expected to be shown of the flow induced cavity resonance. The resonating tone is expected to be captured more accurately, both in terms of frequency and amplitude. The vortex formation process, shown to issue from the trailing edge (see Chapter 4.1.4), is anticipated to form from the leading edge fluctuations. These fluctuations should be modelled in the LES simulation with greater detail than the RANS solver can allow.

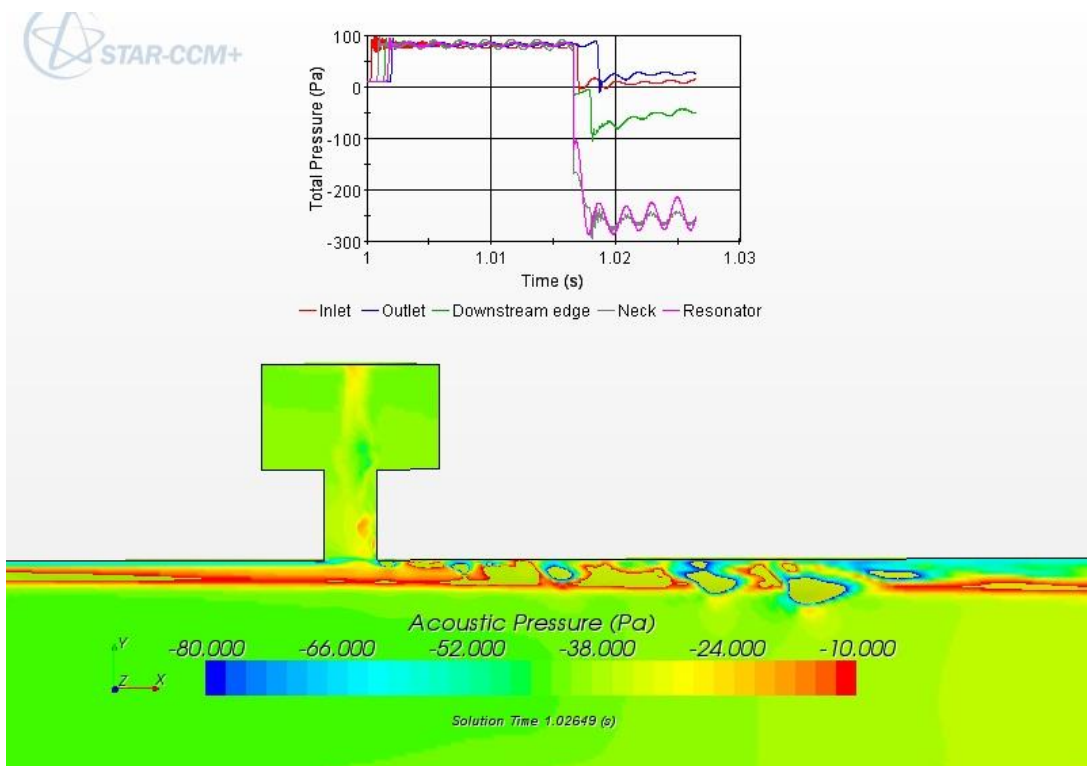


Figure 107: Acoustic pressure plot 1 - Shear layer about to roll up and enter the resonator

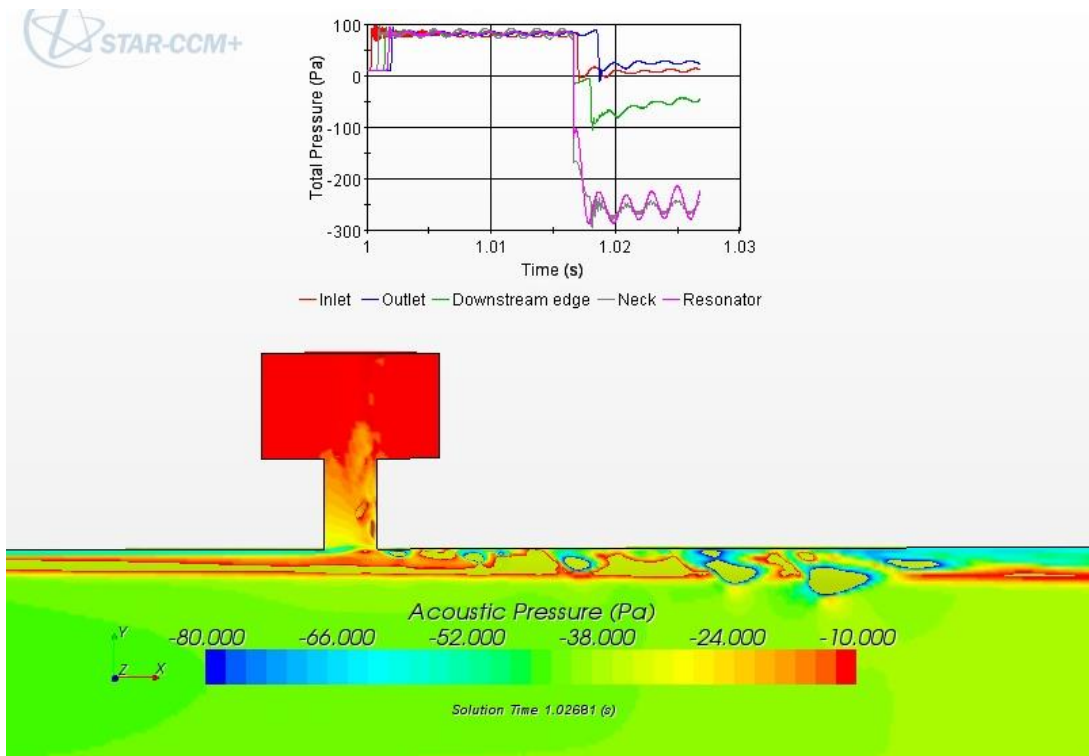


Figure 108: Acoustic pressure plot 2 - Vortex entering resonator and creating high pressure internally

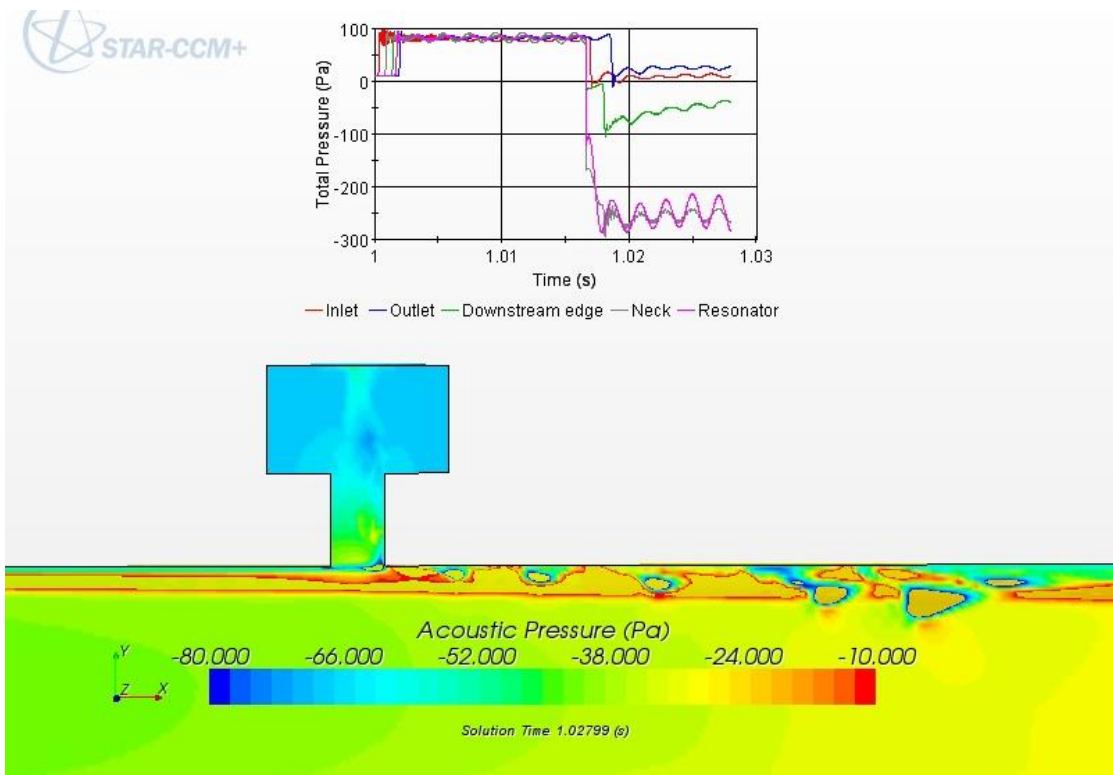
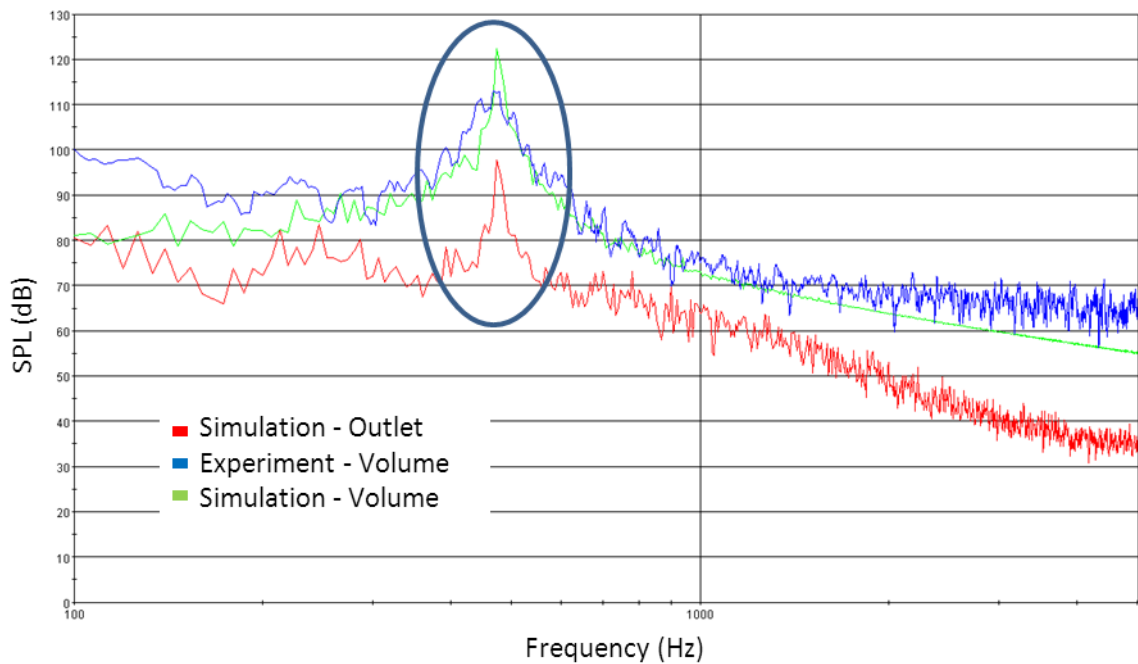


Figure 109: Acoustic pressure plot 3 - Vortex exiting resonator, about to be entrained downstream

Figure 107, Figure 108 and Figure 109 are acoustic pressure plots of the LES VVH resonator simulation at differing snap-shots in time. The plots show the shear layer resonance coupling phenomenon which has been revealed to be the cause of the high SPL tonal noise. The shear layer is created between the moving fluid in the main duct and the stationary fluid in the side branch. The instability in the shear layer creates oscillations, which can then go on to excite acoustic resonances in the side branch. The acoustic resonances then amplify the oscillations in the shear layer, and the whole process continues to amplify until large-amplitude vortices are formed. The process is repeated continuously to create the 460 Hz tone. This visualisation study has exhibited the description of resonator noise generation given by several authors in Chapter 1.5.



**Figure 110: LES Simulation of VVH resonator tuned to 460 Hz. Experimental and simulation results shown for inlet and outlet points.**

An FFT plot for the Outlet and Resonator Volume monitors are shown in Figure 90 along with the Resonator Volume frequency distribution from the experiment. The plot shows a very good correlation between experiment and CFD. The amplitude and frequency prediction of the tone has improved noticeably over the corresponding RANS simulation. The mean SPL of noise also follows much more closely to the results given by the experiment in the region of interest – within 2-4 dB of experiment between 500 and 1000 Hz. The tone

(blue circled region) amplitude is predicted by the simulation to within 7% and the frequency is predicted by the simulation within 4% of the experiment. Rather than modelling the vortex strength, location and path as it travels across the mouth of the side-branch as with a RANS-based solver, LES fully resolves the vortex formation process and allows the vortex to develop naturally and interact with both the acoustic waves and the flow field as it travels over the side-branch.

To summarise, the LES simulation has demonstrated a clear increase in accuracy and detail in comparison to the equivalent RANS simulation. Both solvers predict a tone to match the experiment. However, the 10% error of SPL and frequency prediction experienced with the RANS is eliminated with the use of the LES solver. This increase in fidelity does predict a tone as given by experiments, it can be said, the frequency and amplitude of the frequency distribution is not precise and robust enough for this type of flow phenomena.

### 4.2.3 QWT Simulations

Simulations with a Quarter Wave Tube (QWT) test section are carried out. The experiments with the QWT found the instabilities in the air flow over the mouth of the cavity appeared to excite the acoustic modes of the resonator which then coupled with its resonant modes and resulted in self-sustained oscillations which transmitted downstream through vortex shedding, thus producing the acute tones. The experiments are compared with simulation results. The aim and expectation is the frequency distributions for experiments and simulations will follow closely. This will validate the simulation work and further simulations can be utilised as a tool to find more patterns and relationships between Strouhal number, frequencies, velocities, shape and size in real geometries.

Simulations with the QWT comprise of the flow velocity being varied, the diameter of the QWT as well as the neck protrusion length into the flow being adjusted. It is expected high frequency noise will be predicted by the simulations as found in the experiments given in Chapter 2.4.

#### 4.2.3.1 Neck Protrusion Length

Neck protrusion lengths of 0 mm (flush to the main pipe), 2.5 mm and 5 mm at flow velocities of 30 m/s, and 60 m/s are chosen to be simulated and compared to experiments. The effect of the protrusion can also be analysed in more detail.

The geometry of the test section matches the QWT geometry used in the experiments. The mesh and solver settings are as defined in Chapter 3.2 and the LES validation studies to provide accurate results with reasonable solve times. An example of the simulated QWT geometry (half) with a 5 mm neck protrusion is given in Figure 111.

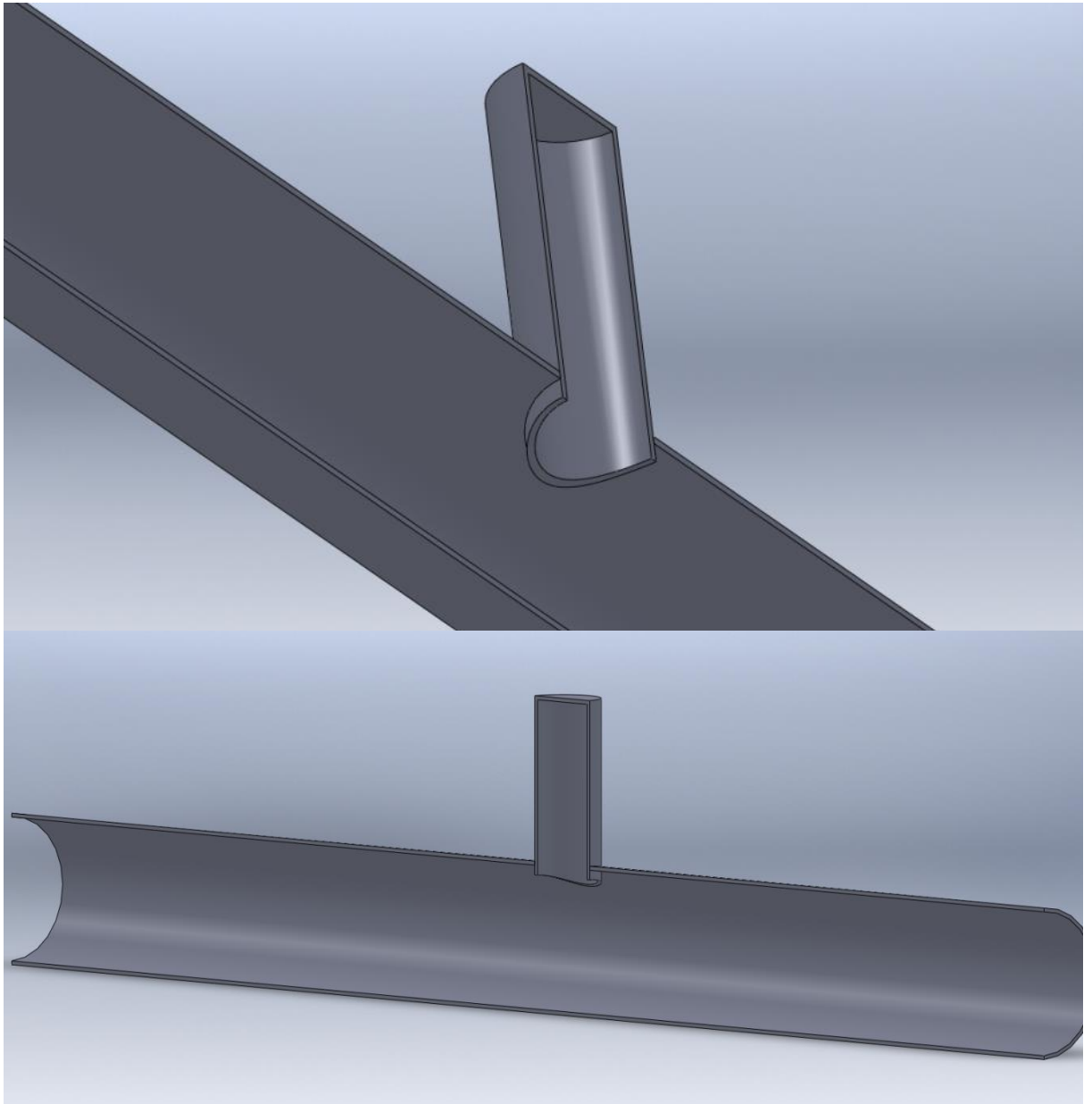


Figure 111: QWT geometry with a 5 mm neck protrusion

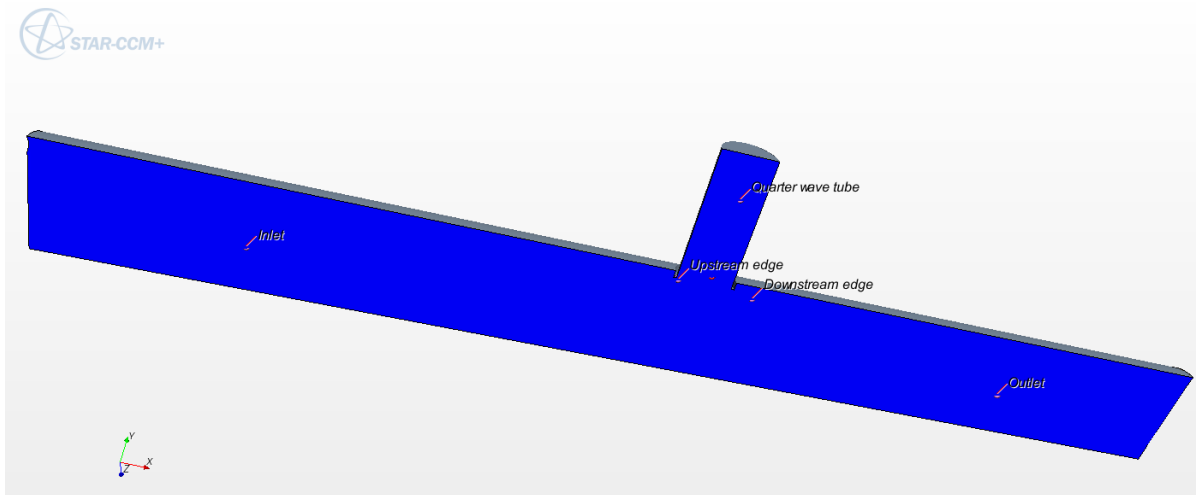


Figure 112: QWT also showing monitor point locations. The inlet and outlet monitor locations approximately five QWT diameters upstream and downstream of the QWT resonator

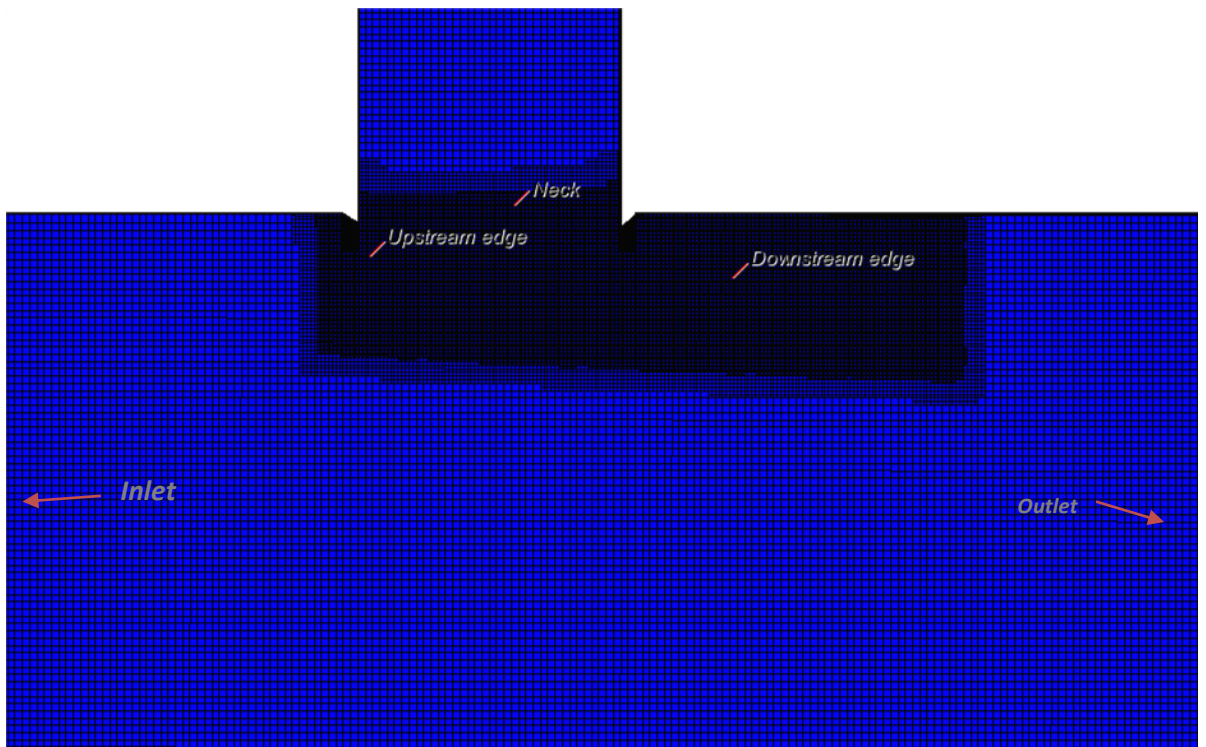


Figure 113: QWT mesh also showing monitor point locations.

The pressure monitor points are situated as shown in Figure 112 and Figure 113 for all simulations given in this chapter section. They are placed to mirror the microphones in the experiment as closely as possible, along with several more monitor points for further information in the area of interest. The mesh around the area of interest is also given in Figure 113.

Velocity scalar plots for the QWT simulations with no protrusion and a 2.5 mm protrusion at 60 m/s are given in Figure 114 and Figure 115. It can be seen from Figure 114, even without a protrusion into the bulk flow, the QWT creates disturbances in the shear layer which transmit downstream in the form of regularly spaced vortices. The QWT with a small protrusion (Figure 116) creates noticeable differences within the flow field. It can be seen that a significant amount of disturbance is created by the leading edge protrusion which 'trips' the flow. The eddies which are produced in the wake of this region flow into the cavity and are re-circulated. The turbulent flow then passes over the trailing edge protrusion. The vortices which are trailed downstream are of much higher amplitude and this is expected to be apparent in the forthcoming FFT plots. The scalar results, although not shown here, are very similar for the lower velocity tested (30 m/s).

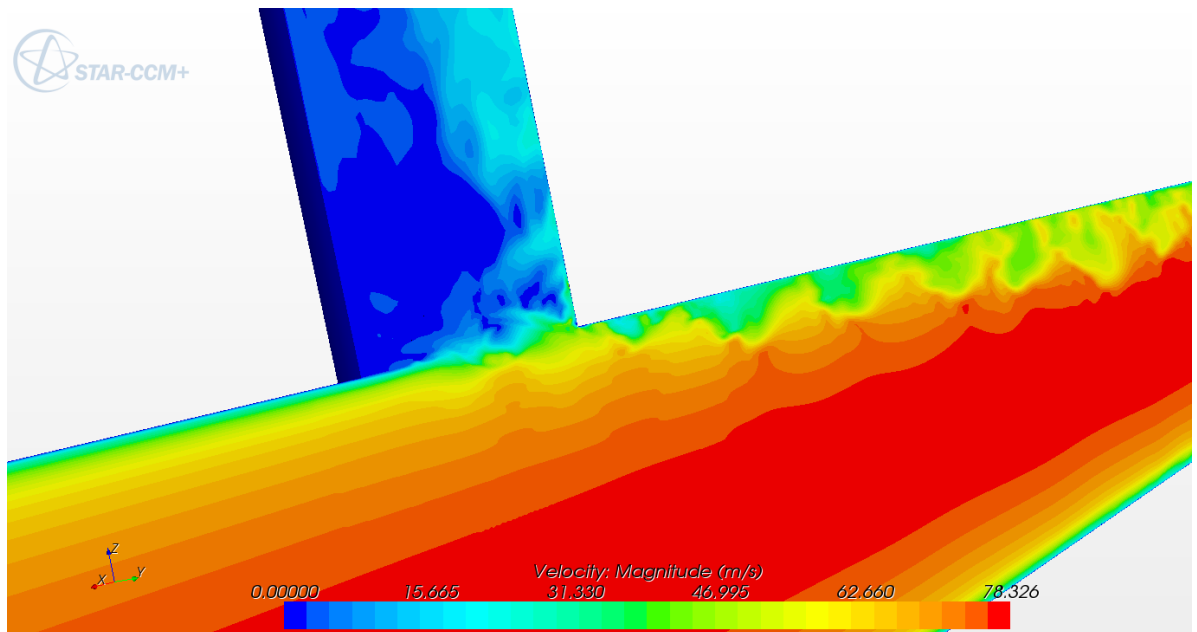


Figure 114: Velocity scalar - QWT with no neck protrusion. 60m/s flow.

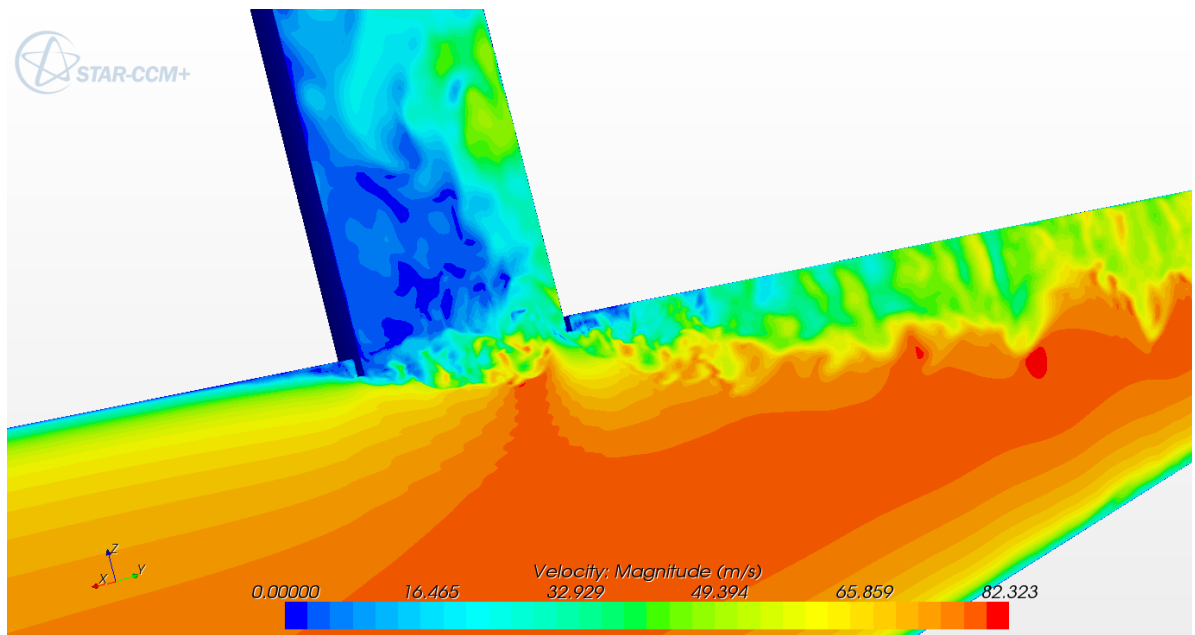


Figure 115: Velocity scalar - QWT with 2.5 mm neck protrusion. 60m/s flow.

For the QWT simulations, large amplitude discrete frequencies are present in the results, in the region of 120 dB close to the QWT opening. A baseline simulation is undertaken with no QWT present (a simple straight pipe) to provide relative dB values for the frequency distribution. This more clearly defines the high amplitude peaks in the results created by the QWT. Figure 116 compares the baseline frequency distribution with the frequency distribution of a QWT set up with no neck protrusion at 30 m/s. The inlet and outlet monitor point frequency distributions are given for both simulations. The inclusion of the full spectrum results show the mesh frequency cut-off is 5-5.5 kHz as highlighted by the dashed green line. Figure 116 clearly shows the high SPL tone at the outlet point monitor with the QWT in place. A small peak is present around 340 Hz with the QWT in place. This corresponds to the fundamental resonant tone of the QWT which correlates with experiment.

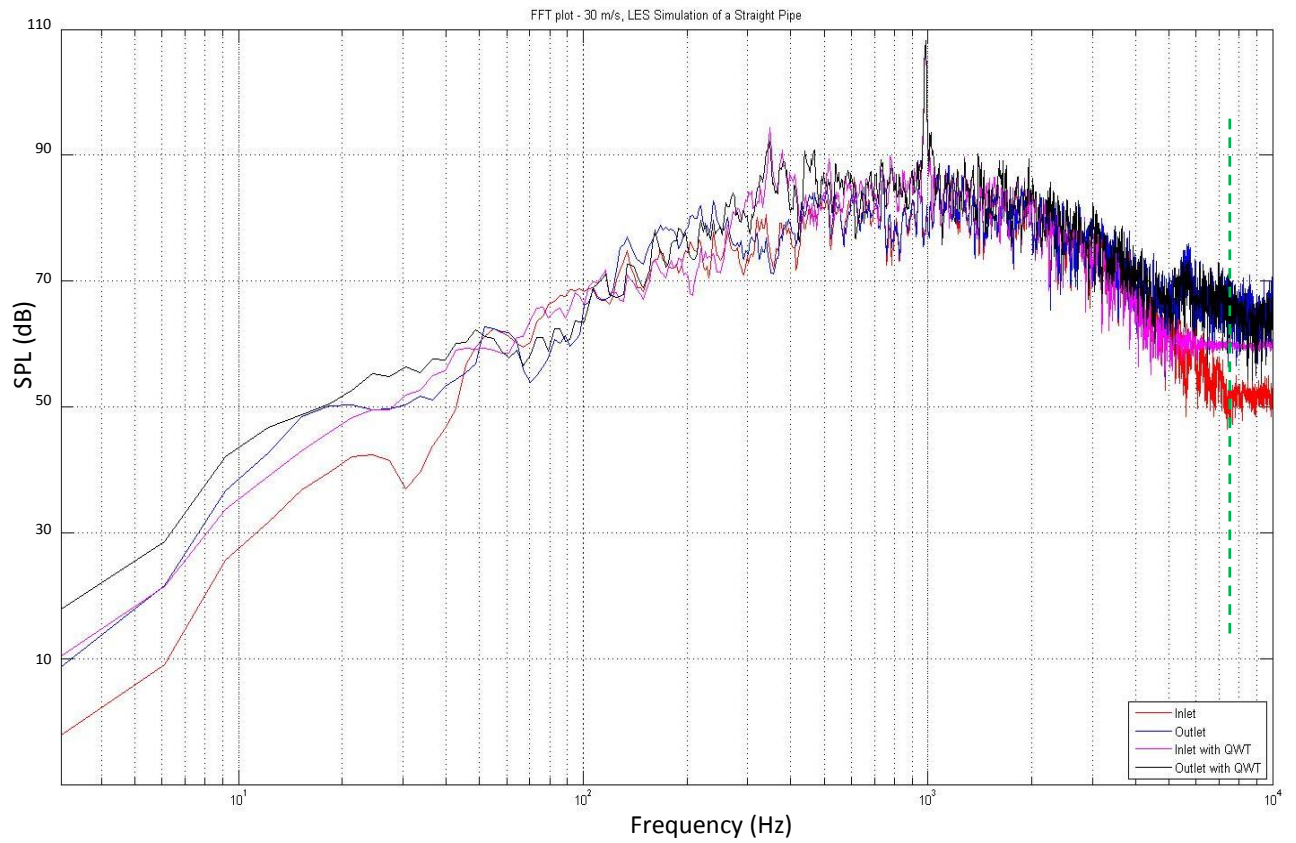
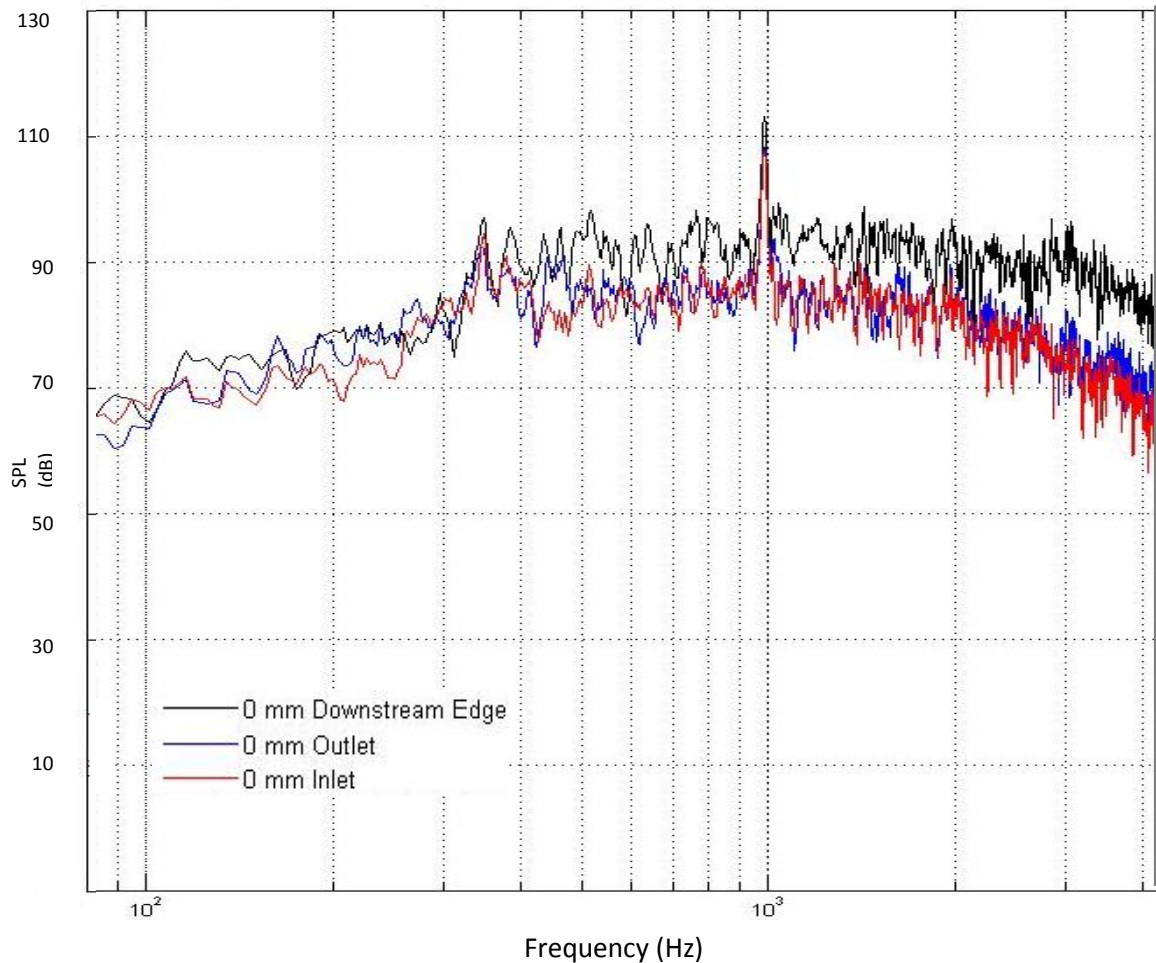


Figure 116: FFT plot CFD simulation frequency distribution comparison at 30 m/s flow velocity showing straight pipe against QWT with no neck protrusion



**Figure 117: FFT plot showing CFD simulation results of QWT protruding into the main pipe by 0 mm with a flow velocity of 30 m/s.**

Figure 117 shows the results of the QWT with no protrusion in more detail. The inlet, outlet and downstream monitor points all indicate a high SPL tone around 1000 Hz. This is likely to be a harmonic of the fundamental resonant frequency of the QWT. A tone of this amplitude is unclear from the corresponding experiment which mirrors this geometry. The experiments only begin to give a tone of this frequency as the neck protrusion length increased. The sharp edges around the neck which are produced by the CAD geometry may be the cause of the premature prediction of a high frequency tone. Conversely, the manufacture of the experiment geometry has inherent limitations which may create a small radius on the sharp edges around the QWT joint, reducing or eliminating this high frequency tones at low protrusion lengths. A further limiting factor which could have reduced the visibility of this high frequency tone during experimental testing could be the higher levels of background noise due to the fan. The fan which provides the incoming flow could raise the mean noise level above the amplitude of the discrete 1000 Hz tone. A low SPL tone around

the fundamental QWT frequency (343 Hz) is present as predicted by the experiments of this geometry, but no further tones are apparent with this configuration.

A scalar velocity scene of the simulation with a 5 mm neck protrusion with an inlet flow velocity of 30 m/s is shown in Figure 118. A significant number of turbulent structures are created within the flow around the QWT entrance. These structures are shown to exist within the QWT itself and are clearly transmitted downstream. When compared to the higher flow velocity cases which are visually expressed in Figure 114 and Figure 115, the flow disturbances in this case appear to be as significant.

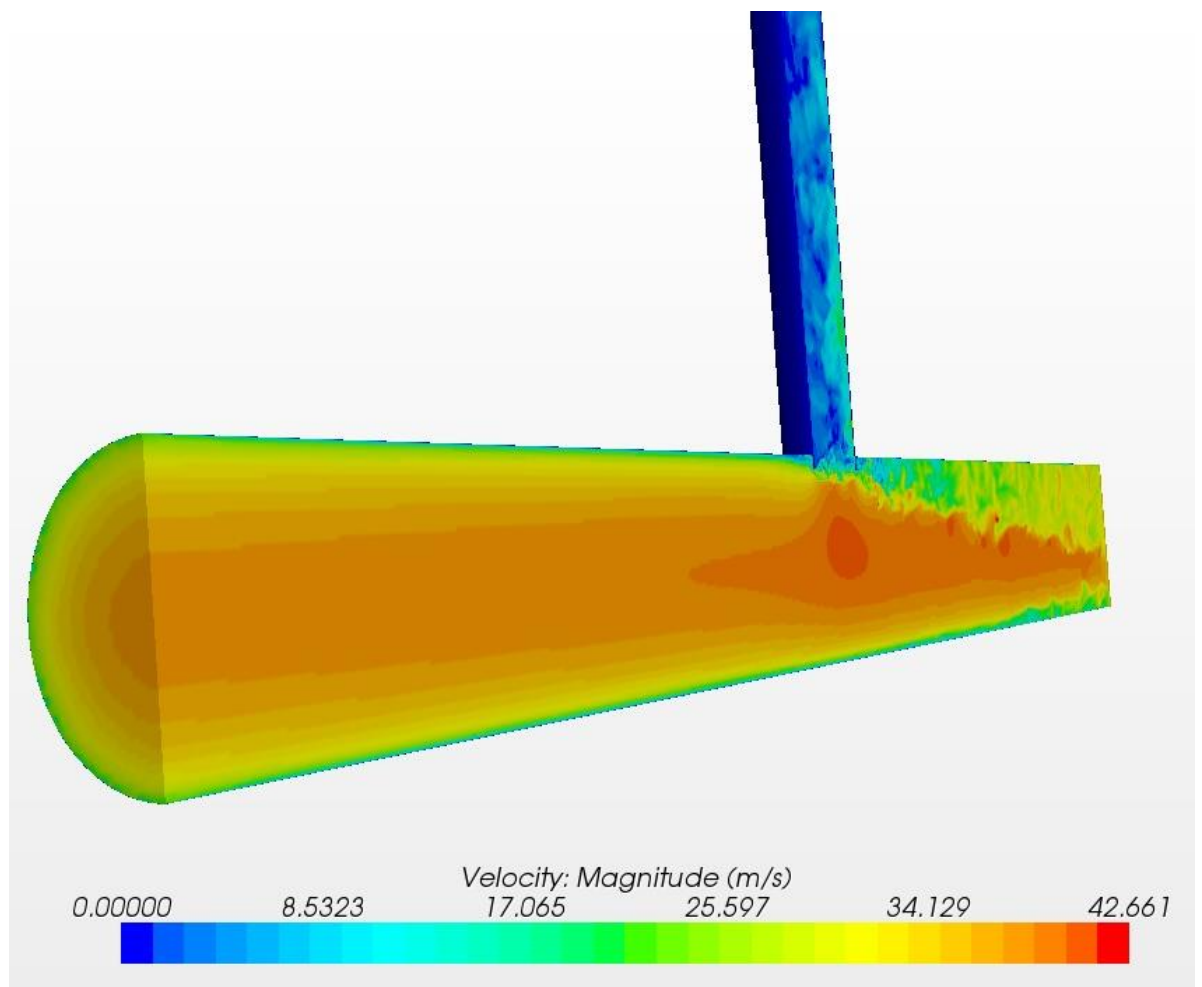


Figure 118: QWT scalar velocity (m/s) scene - 30 m/s in-flow velocity, 5 mm neck protrusion

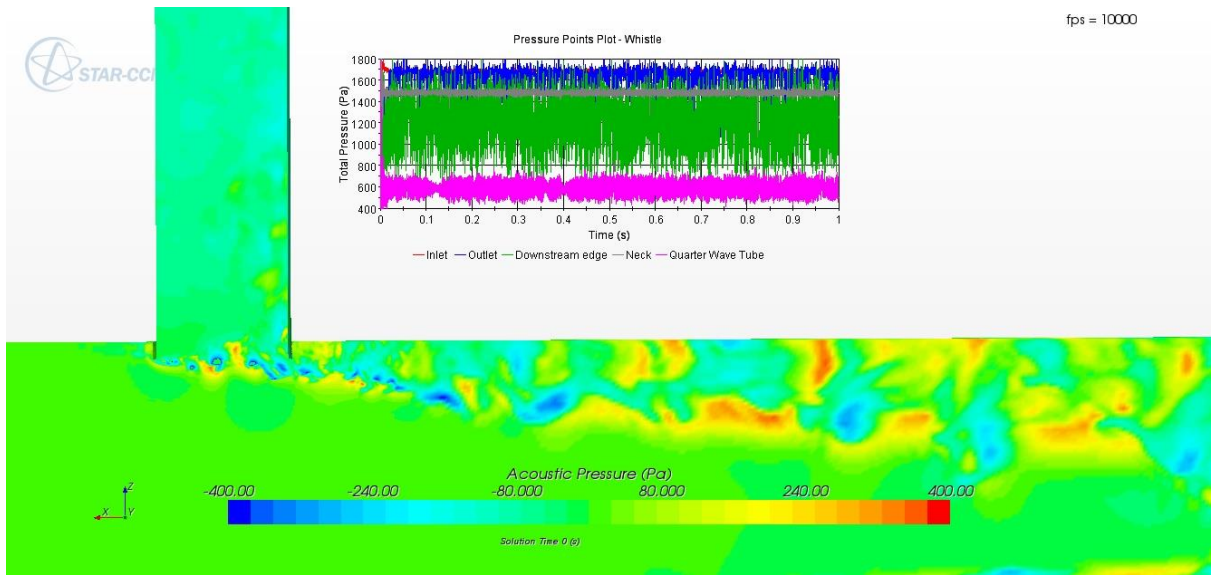


Figure 119: QWT acoustic pressure (Pa) scalar scene - 30 m/s in-flow velocity, 5 mm neck protrusion

The number and magnitude of the turbulent structures present is expected to create significant noise around the trailing edge and further downstream. Figure 119 shows, quite clearly, how the acoustic field is affected by turbulent structures issuing from the QWT area. The flow oscillations convect downstream resulting in large acoustic waves. The QWT simulations at 30 m/s are compared at the various protrusion lengths using an FFT plot of the monitor locations at the downstream edge, provided in Figure 120.

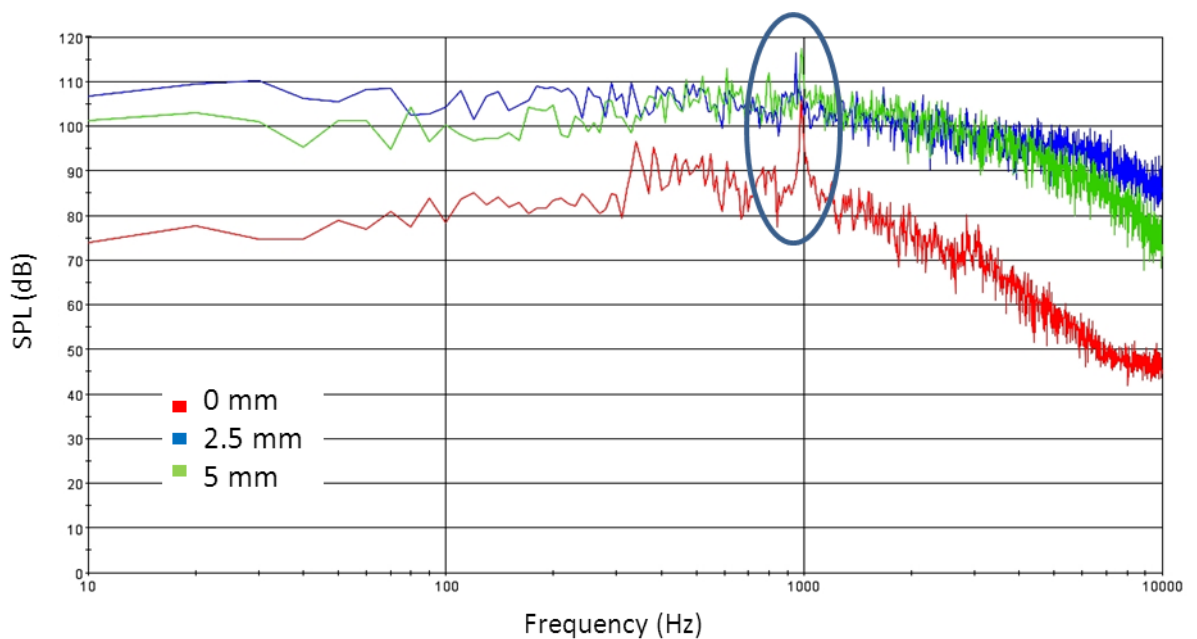
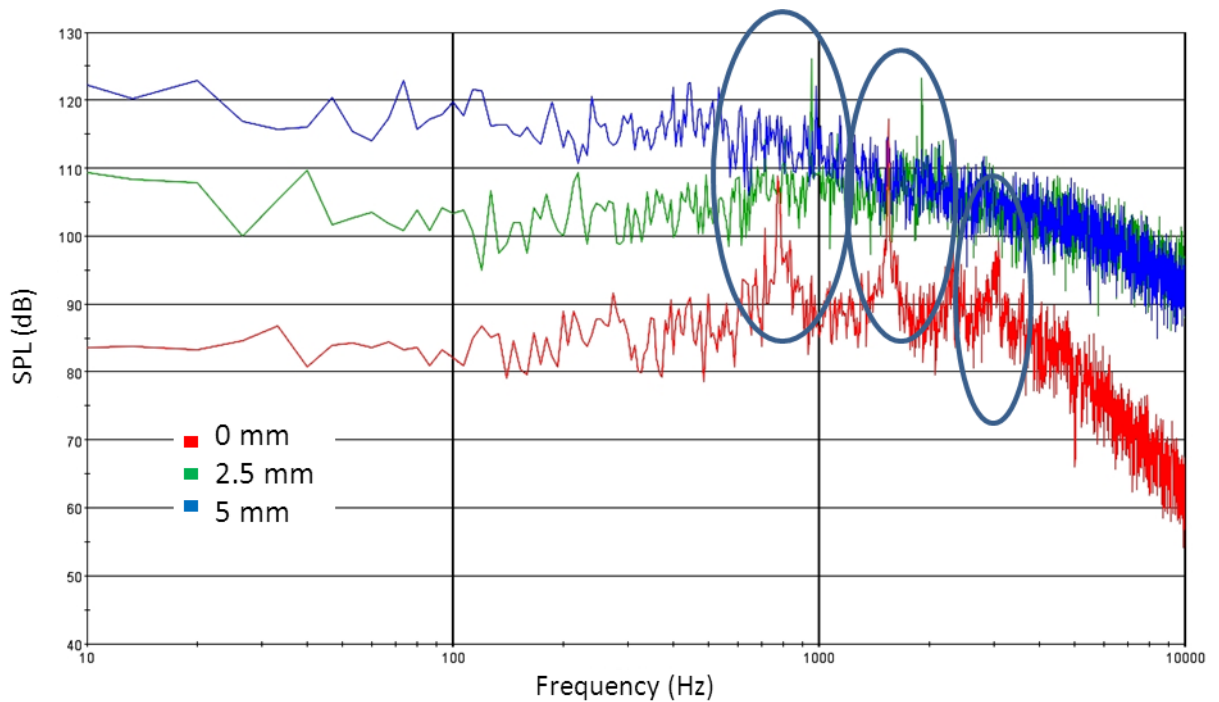


Figure 120: Simulation comparisons at the downstream edge point of the QWT protruding into the main pipe by 0 mm, 2.5 mm and 5 mm with a flow velocity of 30 m/s.

There are several trends apparent from the QWT protrusions at 30 m/s. Figure 120 shows a noticeable tonal peak for all three protrusion lengths. The frequency of the tone varies by 50-100 Hz around 1000 Hz. This 1000 Hz tone is suggested to be a product of sharp edges of the neck disturbing the flow which then couples with a certain harmonic of the fundamental resonating frequency. A clear tone at this frequency is found to exist in the experiments which replicated the 2.5 and 5 mm protrusion lengths. No further harmonic tones are predicted by the simulations which differs from the comparative experiments. The SPL of the 5 mm QWT protrusion is 1-2 dB higher than the 2.5 mm QWT protrusion as expected. The SPL of the 0 mm QWT protrusion simulation is considerably lower (15-20 dB) than the larger protrusions. This suggests the protruding edges have a considerable impact on the flow generated noise. It is anticipated the protruding leading edge disturbs the incoming flow which creates an oscillating flow field around the opening of the QWT. The flow-acoustic coupling inside the QWT then passes over the trailing edge shown in Figure 119 which, in effect, amplifies these disturbances which eventually roll up to form periodic vortices. The flush mounted (0 mm protrusion) QWT does not cause large pressure fluctuations due to a protruding leading edge. This reduces the amplitude of the flow-acoustic coupling within the QWT and thus reduces the level of periodic vortices being shed from the trailing edge, thus reducing the mean and peak SPL downstream. This set of simulations clearly show the impact a sharp lip has on the acoustic flow field.

Simulations to investigate QWT protrusions at 60 m/s are analysed and the results are shown in an FFT plot for the downstream edge monitor point for each protrusion length. This is shown in Figure 121.



**Figure 121: Simulation comparisons at the downstream edge point of the QWT protruding into the main pipe by 0 mm, 2.5 mm and 5 mm with a flow velocity of 60 m/s.**

Firstly, it is noted the simulations at 60 m/s yield a higher mean SPL of around 10 dB when compared to the QWT protrusions at 30 m/s. There are several trends apparent in Figure 121 which displays noticeable tonal peaks for all three protrusion lengths. Harmonic tones are predicted by the simulations which differ from the identical simulations carried out at the lower flow velocity of 30 m/s. The 0 mm protrusion simulation is again, considerably lower in amplitude (15-20 dB) than the larger protrusions. Tonal peaks appear in the frequency distribution at around 800, 1600, 2400 and 2800 Hz with a steady drop off in amplitude, the tone at 1600 Hz being the exception to this rule. The 2.5 and 5 mm QWT protrusion simulations also contain harmonic tones, around 1000 and 2000 Hz. Clear tones at these frequencies were found to exist in the experiments which replicated the 2.5 and 5 mm protrusion lengths. No further harmonic tones are predicted by the simulations, which differs from the comparative experiments.

One such experiment/simulation comparison is given in Figure 122. This FFT plot in this figure shows the downstream monitor frequency distribution for the 5 mm protrusion test with a 60 m/s incoming flow.

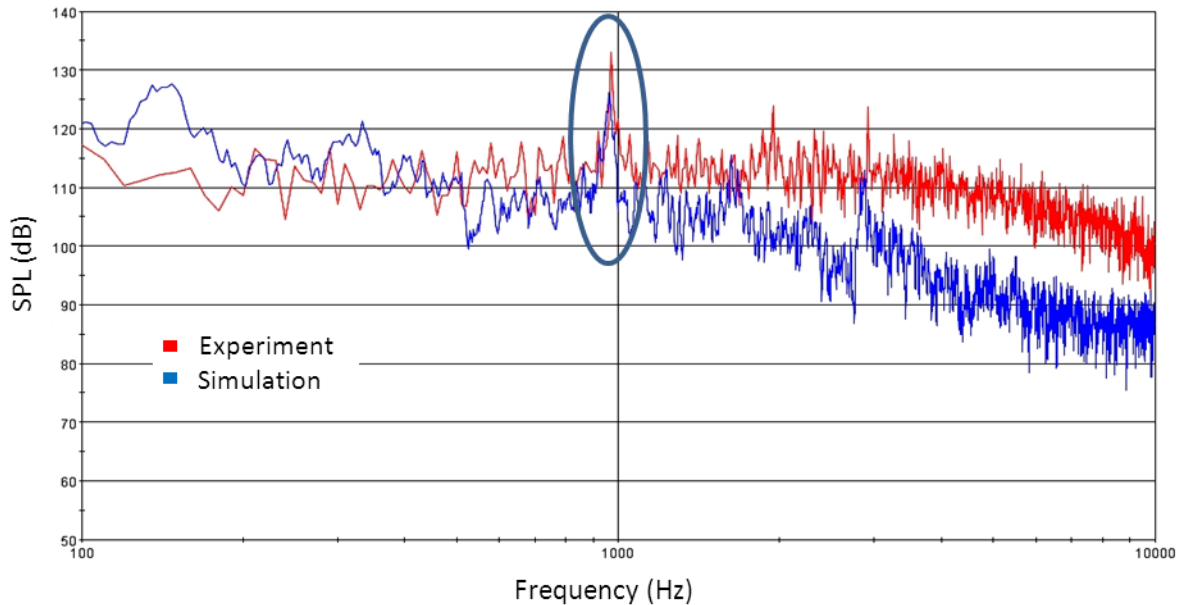


**Figure 122: QWT 5 mm protrusion at 60 m/s FFT plot – Downstream monitor point comparison between simulation and experiment.**

The blue line showing the simulation results follow closely to the red line (experiment) in the lower half of frequencies shown. The mean SPL of the simulation tends to drop away at the higher frequencies more than the experiment would suggest being correct. This indicates a high level of dissipation present within the simulations. This may affect the accuracy of predicting absolute SPL values at monitoring points far from the noise generation region. The concern of SPL correlation also highlights the importance of the monitoring location. To produce accurate SPL levels in a simulation, the monitoring points must be situated as close as possible to the comparable microphone location within the experimental analysis as the acoustic wavelengths naturally transmit and dissipate varying amounts throughout the geometry. However, the tonal frequencies in this case are predicted very accurately. The resonating tone, around 950 Hz, is predicted almost perfectly. The 2nd and 3rd harmonics are also predicted well, with a small disparity in frequency for the 2nd harmonic tone. The amplitude of the tone, circled in blue, is predicted by the simulation within 6% of experiment. The frequency of this tone is predicted within 1% of experiment.

The experiments have been compared with simulation results. Overall, the findings compare well between experiments and simulations. The tonal frequencies are very comparable in the majority of cases. The mean/tonal amplitudes show some normalisation issues. An increase in robustness is necessary to effectively predict the SPL levels of flow

generated noise with this set up. The simulations clearly visually demonstrate the phenomena present in the corresponding experiments. The neck protrusion experiments with the QWT found the instabilities in the flow over the mouth of the cavity appears to excite the acoustic modes of the resonator which then coupled with its resonant modes and resulted in self-sustained oscillations. These oscillations transmit downstream through vortex shedding, thus producing the acute tones. As was demonstrated by the experiments and is present in the simulations, when the flow velocity is increased, the succeeding resonant modes are excited and the acoustic response of the system occurs at a specific range of a Strouhal number. A transfer from one to the next mode is gradual, so at various flow velocities two discrete frequency components appear in the sound spectrum. These phenomena are difficult to prove, understand and visualise through experiments alone. The simulations follow the trends found in the corresponding experiments, such as an increase in mean SPL as the protrusion length is increased. Both the simulations and experiments provide suitable evidence to suggest, as the length of the protrusion is increased, the amplitude of the tone increases with no dramatic effect on the tone frequency.

This set of simulations has validated simulation work further. In the following chapter section, the diameter of the QWT is varied to analyse the effect on tone frequency and amplitude of flow generated noise.

#### **4.2.3.2 QWT Diameter**

The investigations with the QWT acting as a side-branch resonator have provided some interesting flow generated noise results, particularly when the QWT is allowed to protrude into the main duct. To further investigate the effect of a side-branch QWT with grazing flow, the diameter of the QWT is varied to analyse how the diameter can affect the frequency distribution downstream of the side-branch. This study is difficult to reproduce experimentally due to the resources available at the time of writing. Varying the QWT diameter in CFD is a relatively simple process in contrast. This highlights one of the advantages this type of CFD holds as a potential design aid. A 20 mm, 30 mm and 40 mm diameter QWT is tested at two velocities of 30 m/s and 60 m/s. The diameter ratio ( $d/D$ ) of the QWT's and the main duct are 0.27, 0.41 and 0.54 respectively.

The results for these simulations are studied in the following FFT plots.

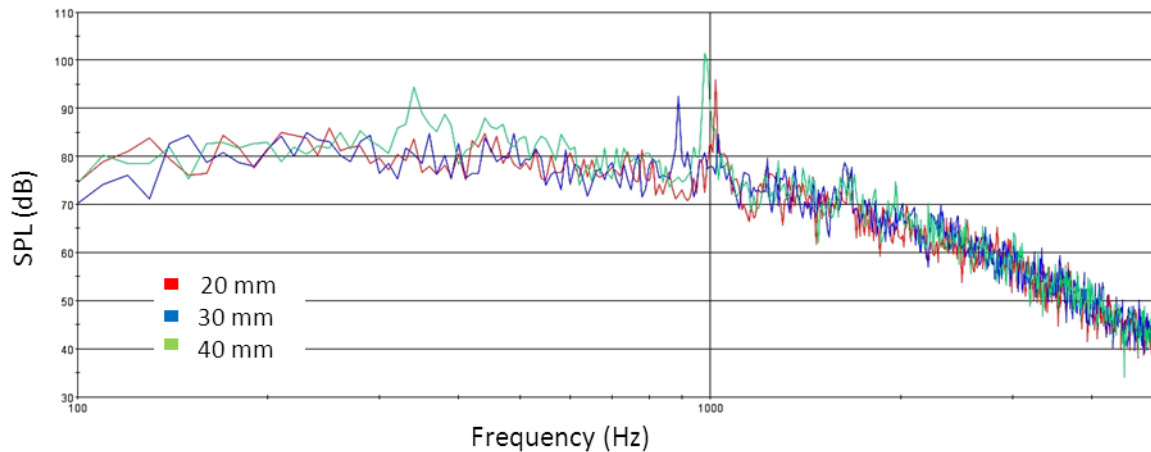


Figure 123: Simulation Outlet Monitor of 20, 30 and 40 mm diameter QWTs with a 30 m/s grazing flow

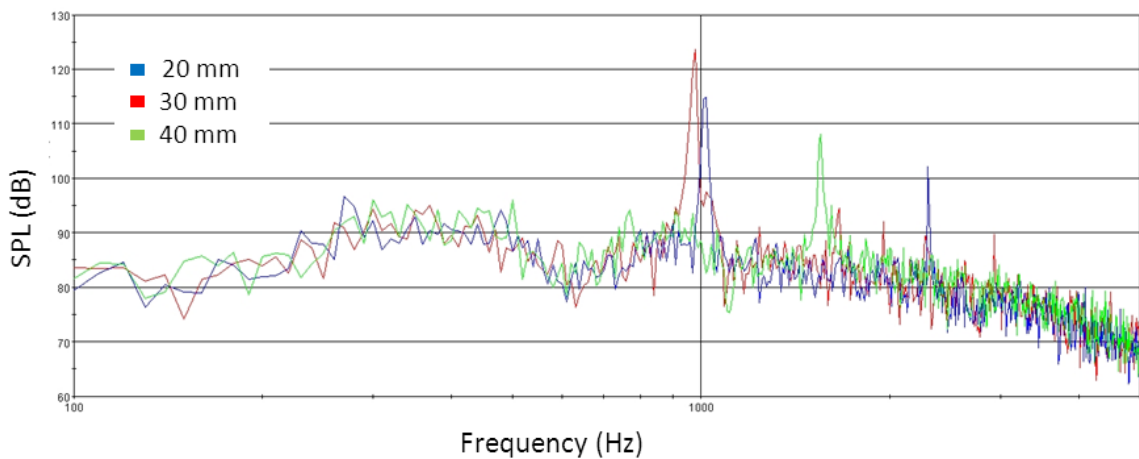


Figure 124: Simulation Outlet Monitor of 20, 30 and 40 mm diameter QWTs with a 60 m/s grazing flow

Figure 123 shows an FFT plot of the monitor point towards the outlet for each QWT diameter at 30 m/s. It can be seen from this plot, the peak around 1000 Hz tends to shift between 900 and 1050 Hz in the frequency spectrum as the diameter of the QWT is varied. The 0.41 diameter ratio test in fact produces two resonant tones in this region. The second, higher frequency peak sits between the peaks for the two alternative diameter ratio tests. This peak is 5 – 10 dB lower in SPL. The largest d/D ratio produces the highest SPL tone of the diameters tested. Another noticeable point is the small peak around 350 Hz - the resonant frequency of the 40 mm QWT. Interestingly, the other diameters tested do not exhibit any such tone at their respective resonant frequencies. Ziada & Shines (Ziada & Shine, 1999) investigations found the maximum SPL at resonance increases with the diameter ratio. Since the boundary layer thickness in the main pipe is independent of the side-branch diameter, a larger size vortex will experience a higher mean velocity and will be

swept faster along the branch mouth. The phase condition for the onset of oscillation, i.e., the favourable phasing between the vortex convection velocity and the acoustic oscillation, will therefore be achieved at a lower mean velocity when the diameter of the side-branch (and consequently the vortex size) is larger. The QWT diameter simulations broadly follow the trend found by Ziada & Shine. As flow generated noise is a very dynamic process, it is suggested the 0.41 diameter simulation at this in-flow velocity is transferring from one harmonic to the next. This explains the two peaks in the frequency distribution.

Figure 124 is an FFT plot of the monitor point towards the outlet for each QWT diameter at 60 m/s. Again, peaks in the frequency spectrum are present around 1000 Hz. The amplitudes of these peaks, as well as the mean amplitude is greater by 10 – 20 dB, as expected with double the grazing flow velocity. The 20 mm and 30 mm diameter QWT simulation results produce a similar tone frequency to the simulations carried out at 30 m/s. The larger  $d/D$  ratio produces a higher amplitude tone at this frequency as expected (see the discussion above). However, the results of the 40 mm QWT simulation are unexpected. There is no peak around 1000 Hz. Instead, a peak is present around 1500 Hz. Another peak is present with the 20 mm QWT at around 2200 Hz. These higher tone frequencies are demonstrated clearly in the corresponding experiments. When the flow velocity is increased, the succeeding resonant modes are excited and the acoustic response of the system occurs at a specific range of a Strouhal number. A transfer from one to the next mode is gradual, so at some flow velocities two discrete frequency components appear in the sound spectrum. In Ziada & Shine's study (Ziada & Shine, 1999), the resonance range, and in particular the onset of resonance was found to shift to lower Strouhal numbers (i.e. to higher velocities) as the diameter ratio is decreased. The relationship between Strouhal number and diameter ratio is recognised to be related to the convection velocity of the vortices forming at the branch mouth when the QWT diameter is varied. This is because the size of the formed vortices scales with the diameter of the side-branch (Ziada, 1994). Overall, the diameter of the QWT is found to have a significant effect on frequency and SPL of the flow-generated noise. As was found in the neck protrusion investigations, when the flow velocity is increased, the succeeding resonant modes are excited and the acoustic response of the system occurs at a specific range of a Strouhal number. Changing the diameter of the neck also has a similar effect. The SPL of the harmonic tones tend to increase as the diameter ratio is increased. The diameter change has been found to shift the fundamental resonant tone in frequency and in some cases, the dominant tone has moved to the next harmonic.

#### 4.2.3.3 Summary

The effect of a side-branch QWT on a grazing flow has been investigated to understand the important geometrical areas which help to facilitate the production of flow-generated noise. Several parameters have been studied to understand this phenomenon. Simulations of the QWT comprised of the flow velocity, the diameter of the QWT as well as the neck protrusion length into the flow being varied. The experiments with the QWT, in which the length of the neck protrusion was varied, found the instabilities in the air flow over the mouth of the cavity appeared to excite the acoustic modes of the resonator which then coupled with its resonant modes and resulted in self-sustained oscillations. The simulations clearly visually and numerically demonstrate this phenomena present in the corresponding experiments. The acoustic results are shown to give reasonable correlation between the experiments and LES CFD simulations. The CFD simulation analysis of QWT diameter has proved a useful further investigation to understand the important parameters which can affect resonator designs from an acoustic perspective. These phenomena, which rely on various geometrical and flow parameters are difficult to prove, understand and visualise through experiments only. This highlights one of the advantages this type of CFD holds as a potential design aid.

#### 4.2.4 Charge Air Cooler Resonator Simulations

A resonator section from the premium automotive derived charge air cooler pipe set-up which is known to whistle under certain conditions is tested using CFD. This real-world application of a resonating section helps to further validate the CFD simulations via experimental comparisons. The CAC Resonator which reduced/eliminated the high frequency noise found during vehicle testing and experiments, detailed in Chapter 2.5, is simulated along with the Pre-Production geometry. The CFD analysis aims to re-create this phenomenon. It will also provide results to compare directly to experiments. The simulations are expected to give more information on the underlying flow processes which create this high frequency tone and will further validate LES CFD simulations to be used as a tool to predict high frequency noise.

Figure 125 provides a CAD representation of the charge-air-cooler tract including the resonator approximately half way along the length of the tract. Figure 126 and Figure 127 are section views of the Pre-Production and production CAC resonators respectively. Using

Figure 126 as a reference, the volume section closest to the inlet (right) is referred to as CAC Resonator Section 1 and the volume section nearest the outlet (left) is CAC Resonator Section 2.

The CAC resonator simulations are defined with the LES solver conditions and mesh settings as in the QWT simulations in the previous chapter section. A visual representation of the volume mesh towards is given in Figure 128. A fully developed mean velocity profile is imported onto a free-stream inlet. The mass flow rate is equivalent to a mean flow velocity of 30 m/s, 45 m/s and 60 m/s for both resonator geometries.



**Figure 125: CAC tract geometry - CAD representation**

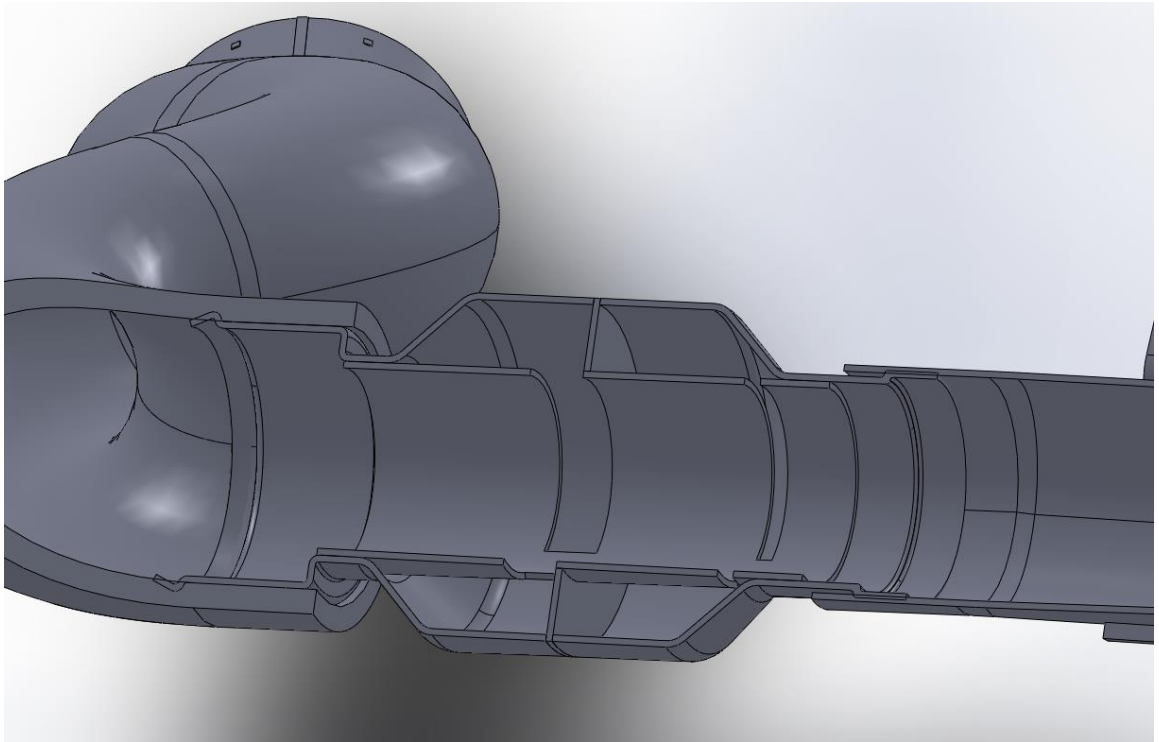


Figure 126: Pre-Production CAC resonator section view. Flow from right to left.

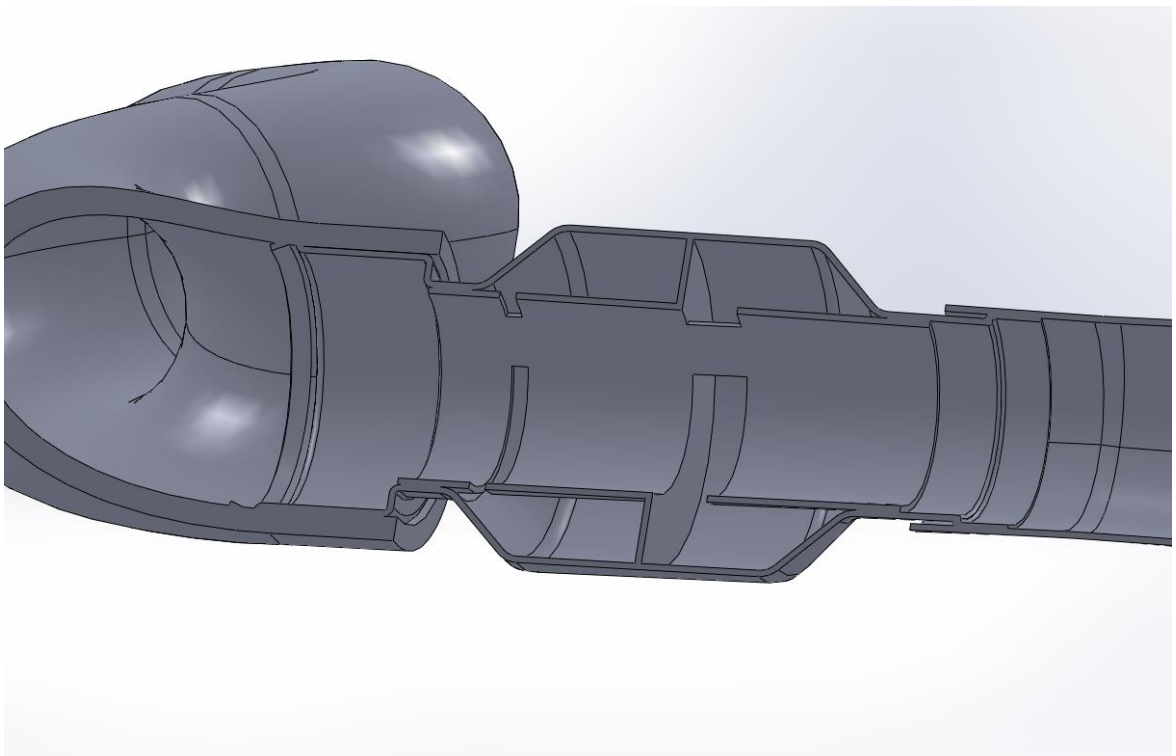


Figure 127: Production CAC resonator section view. Flow from right to left.



Figure 128: CAC resonator upstream pipe and inlet volume mesh

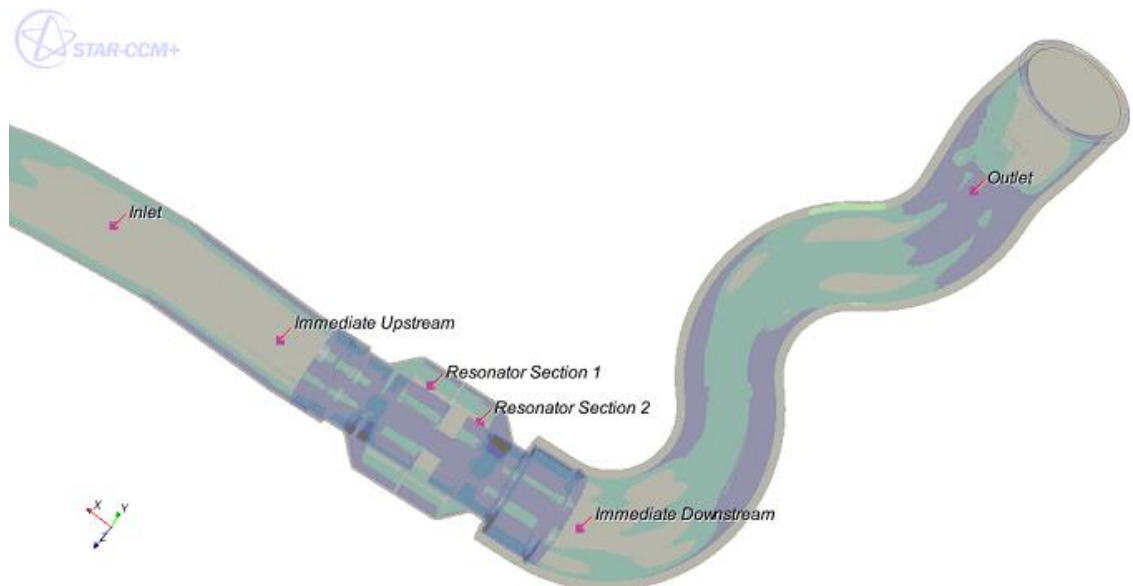


Figure 129: CAC Resonator geometry showing location of monitor points

Several points are set up at the locations highlighted in Figure 129 to monitor the simulations and to provide pressure data at these positions. Inlet, outlet, immediate upstream and immediate downstream monitoring points are located centrally, normal to the flow, to avoid any distortion the boundary layer may produce on the acoustic results. The monitoring points close to the CAC resonator inlet and outlet aim to replicate the location of the upstream and downstream microphones used in the corresponding experiments. An additional monitor point is positioned in each resonator volume section in order to produce detailed acoustic results within the resonator geometry itself. This highlights another advantage of LES CFD simulations as it is very difficult to monitor the pressure fluctuations

within this complex geometry. Detailed acoustic results along with pressure and velocity plots will be analysed for both CAC resonator geometries. They are then compared to one another and finally evaluated against the equivalent experiments which are given in Chapter 2.5.

#### 4.2.4.1 Pre-Production CAC Resonator Simulations

The Pre-Production CAC resonator LES simulation results with 30, 45 m/s and 60 m/s mean flow velocities are provided in this chapter section. Flow is from left to right for all scalar plots in this chapter. An acoustic pressure scene at a single point in time (Figure 130) for the 45 m/s case shows large amplitude oscillations within section 2 of the resonator. Interestingly, section 1 does not exhibit these high amplitude oscillations which appear to alternate between high and low pressures.

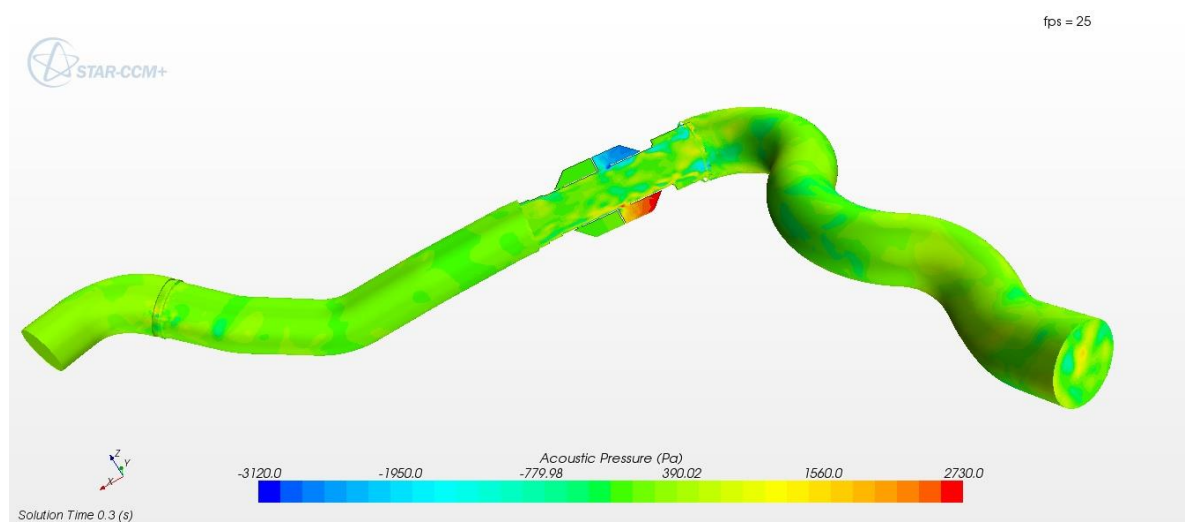
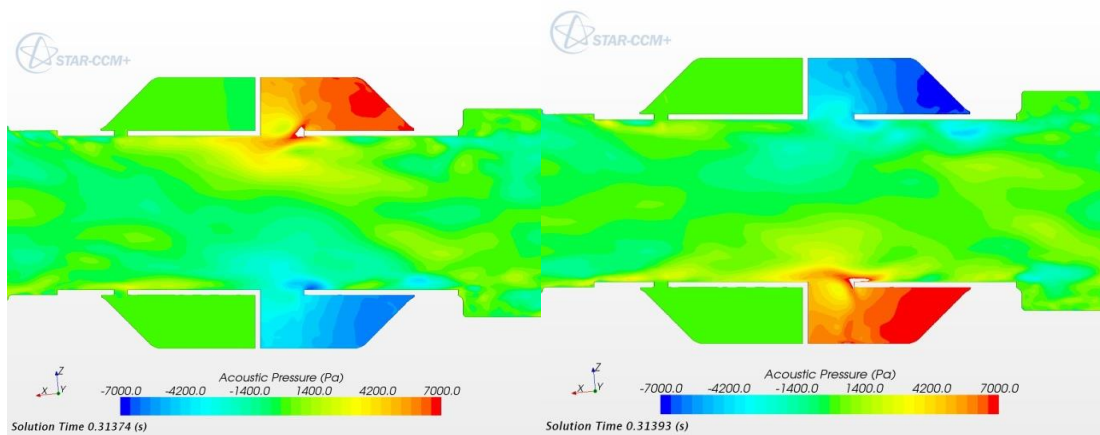


Figure 130: Pre-Production CAC Resonator – 45 m/s acoustic pressure scalar scene

Two static acoustic pressure plots for the simulation with a 45 m/s flow velocity, approximately 0.2 milliseconds apart, are presented in Figure 131. A section cut view of the resonator show the large acoustic pressure differences in the second half of the resonator. The high and low pressure appears to alternate between the upper and lower half of the volume. It must be noted, each section of the resonator is one complete volume with two long rectangular openings. Thus, the distance between the upper and lower openings is approximately a distance of half wavelength. It is suggested a waveform is created between

these two openings which causes significant oscillations of the flow around the openings. What is also apparent from Figure 131, is how the pressure fluctuations are being transmitted downstream. This is expected to produce significant noise within the CAC tract further downstream. Section 1 of the resonator does not appear to create significant pressure fluctuations within the volume. However, some flow-generated noise does appear to be produced by the sharp edges of the joints upstream of the resonator. As the sole difference between sections 1 and 2 of the resonator is the opening width and thus, the resonating frequency, the high pressure oscillations must be related in some way to the resonant frequency of the volume sections.



**Figure 131: Pre-Production CAC Resonator – Acoustic Pressure in the resonator at two points in time**

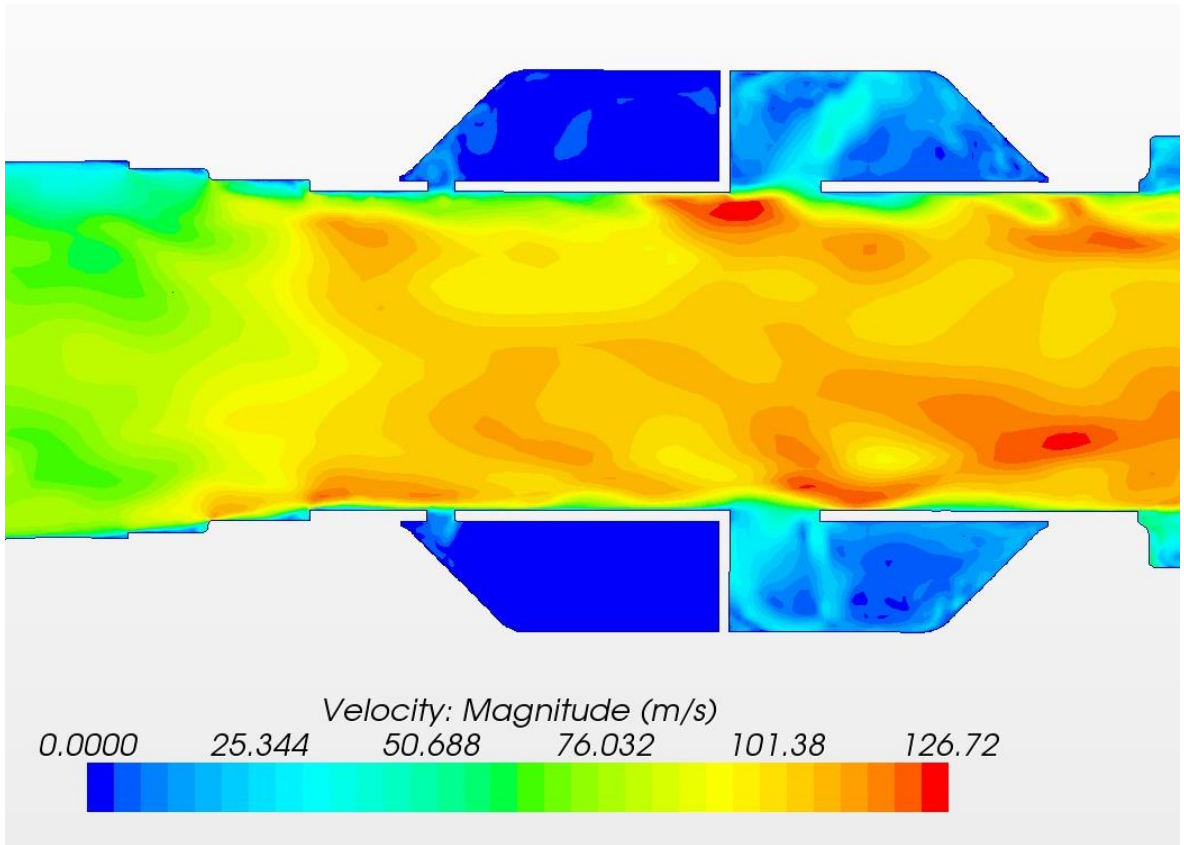


Figure 132: Pre-Production CAC Resonator - Velocity Magnitude scalar scene

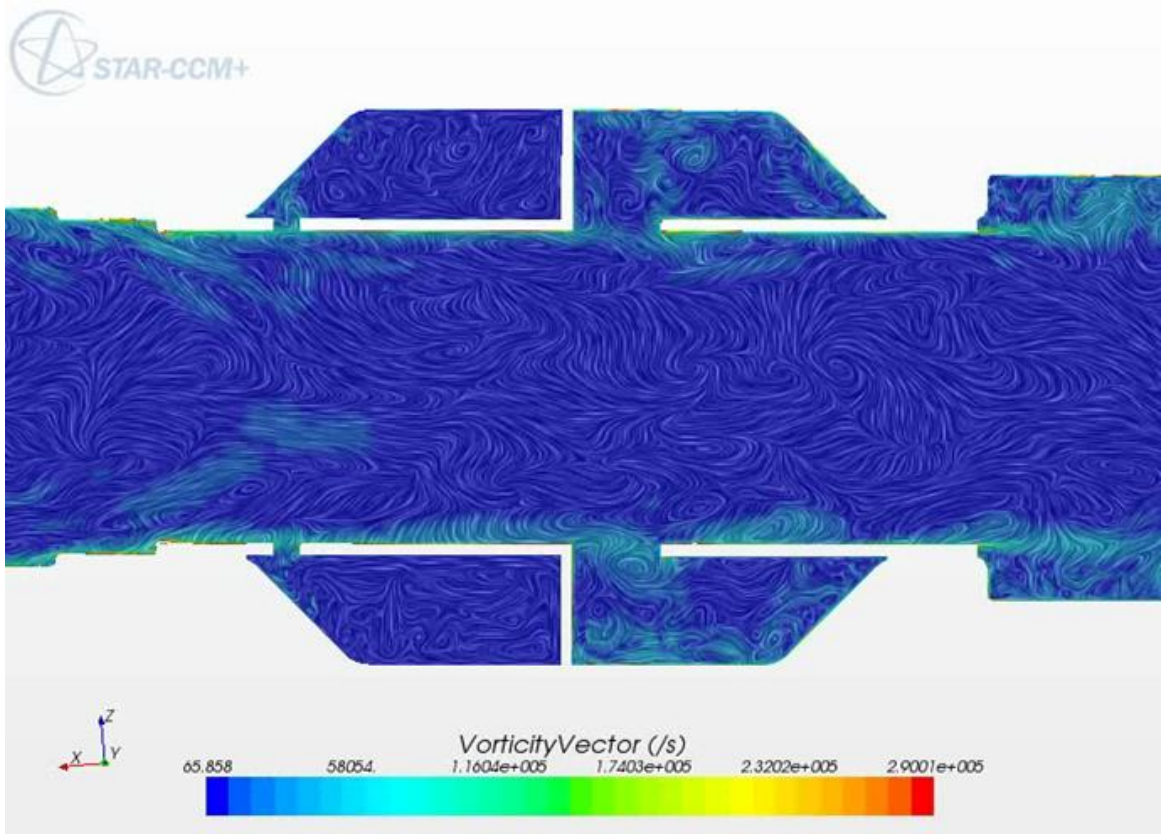


Figure 133: Pre-Production CAC Resonator - Vorticity Vector Scalar Scene

Figure 132 is a scalar velocity scene of a section view of the CAC resonator geometry at a single point in time. There is some circulation of the vortices which are created in the second section of the resonator within the volume itself. Figure 133 highlights the high level of turbulence within the geometry, particularly the formation of turbulent structures, i.e. vortices in and around Section 2 of the resonator. The turbulent eddies appear to initialise at the leading edge of the entrance of Section 2 of the resonator. The shear layer, which has been previously disturbed by the opening of Section 1 as well as the joints upstream enters the second volume due to the sharp trailing edge. The flow then appears to roll up into several vortices. A large vortex fills the cavity around the outer edge along with a smaller vortex – approximately the same width as the opening. The flow circulates and is then entrained back into the shear layer as vortices, which are transmitted downstream in regular intervals. The amplitude of this pressure fluctuation is so large, the bulk flow inside the resonator begins to oscillate. The pressure fluctuation between maxima and minima appears to create a large standing wave across the duct. The oscillation coupled with the geometry is such that 180 degrees of the resonator Section 2 volume is a pressure minima whilst the opposing 180 degree resonator section is a maxima. The pressure minima and maxima alternates due to the standing wave. It is noted there is a small vortex at the opening of Section 1 which, from a visual and an acoustic perspective does not appear to directly influence the acoustic distribution around this area.

The significance of the pressure fluctuations in Section 2 is clearly demonstrated by 0.2 s of pressure data for all monitor points which is plotted in Figure 134. Each monitor point is represented by a line. The monitor point inside Section 2 of the resonator predicts large periodic pressure fluctuations with at least two wavelengths with very short periods – a strong sign of discrete high frequency, high amplitude tones. Conversely, all other monitoring points are lower in amplitude by around a factor of 100, with the exception of the Immediate Downstream location. The pressure amplitude at the Immediate Downstream point is raised with a similar fluctuating wavelength. This suggests that high amplitude, high frequency noise is indeed produced within Section 2 of the resonator and is transmitted downstream but with a high level of dissipation.

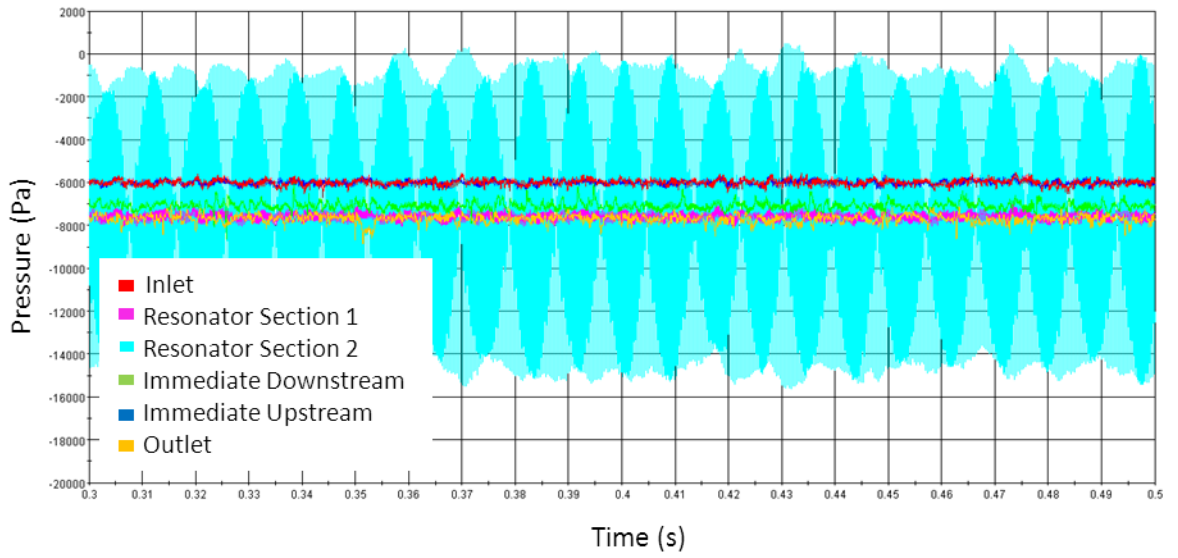


Figure 134: Pressure (Pa) against time (s) plot for Pre-Production CAC Resonator simulation monitor points - 45 m/s mean inlet velocity

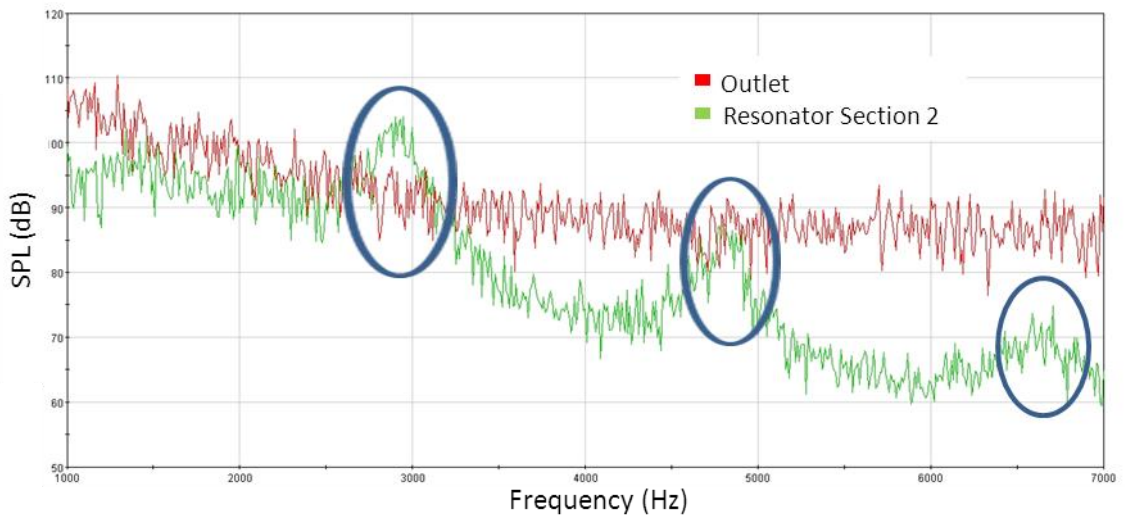


Figure 135: Pre-Production CAC Resonator FFT - Outlet and Resonator Section 2 Monitor points (30 m/s)

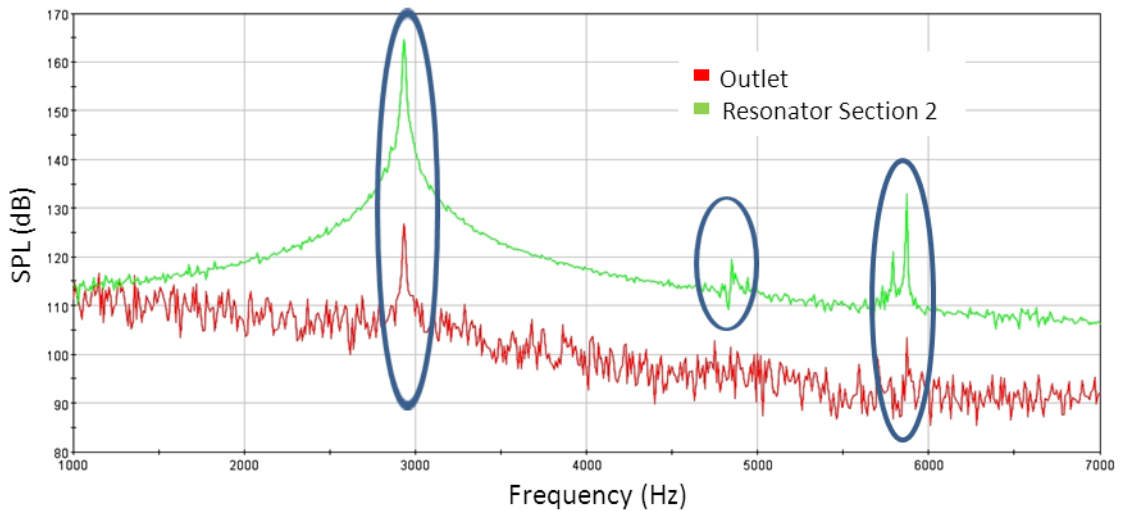


Figure 136: Pre-Production CAC Resonator Simulation - Outlet and Resonator Section 2 Monitor points (45 m/s)

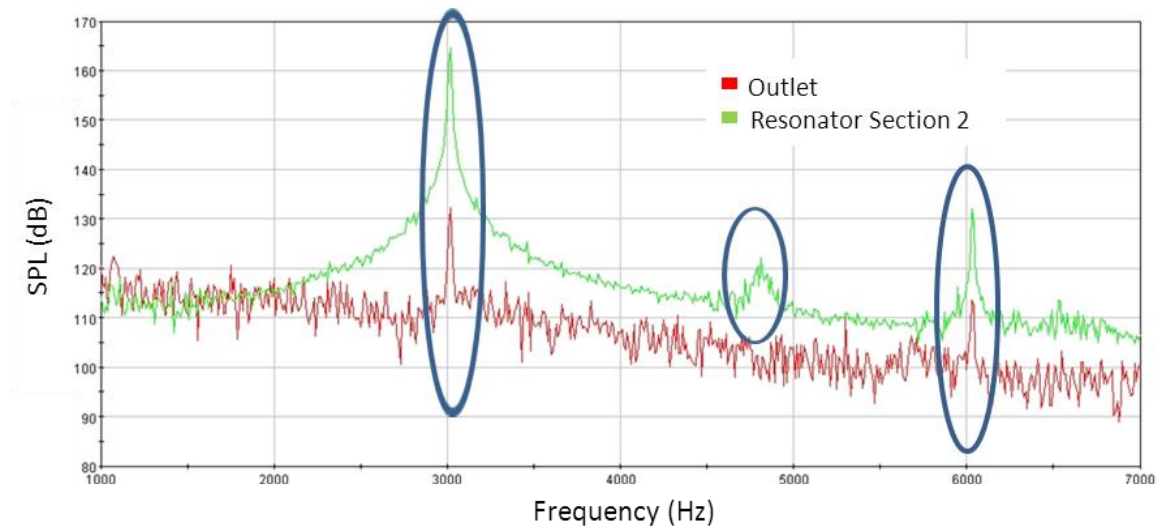
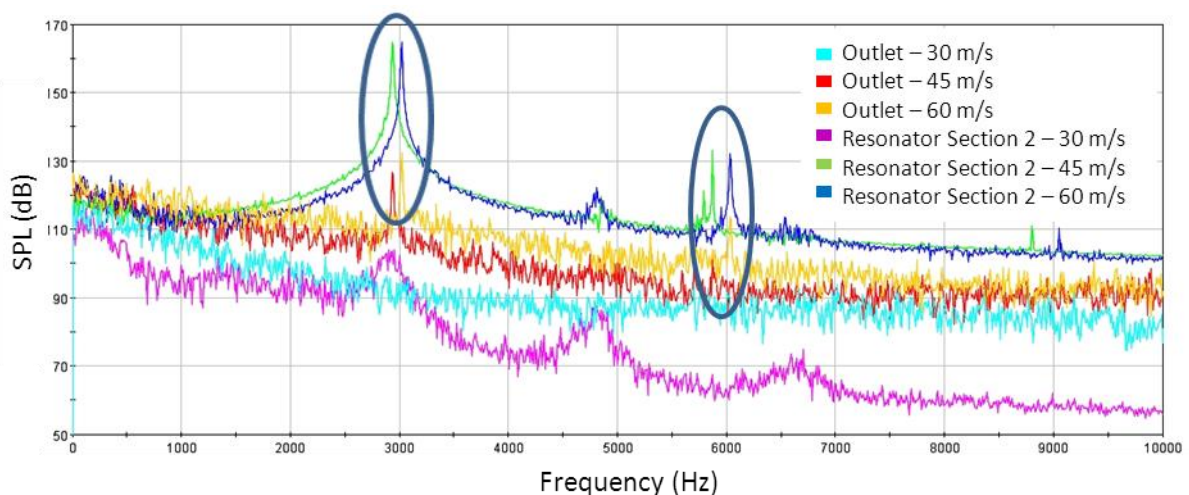


Figure 137: Pre-Production CAC Resonator Simulation - Outlet and Resonator Section 2 Monitor points (60 m/s)

Figure 135, Figure 136 and Figure 137 are FFT plots of the frequency spectrum at two locations – Resonator Section 2 and Outlet point monitors for the 30 m/s, 45 m/s and 60 m/s simulations respectively. For the 30 m/s case, small broad tonal peaks in the frequency distribution of the Section 2 monitor are apparent around 2900 Hz, 4800 Hz and 6600 Hz. These low amplitude tones do not appear to be transmitted downstream, as evidenced by the outlet monitor frequency distribution. Conversely, the 45 and 60 m/s cases exhibit a large peak at around 3000 Hz for the Section 2 monitor point. They also show a smaller peak at approximately 6000 Hz which is thought to be the 2<sup>nd</sup> harmonic of the larger peak. These very high amplitude tones are shown to be transmitted far downstream as matching

frequency peaks are evident in the frequency distribution of the Outlet monitors. There is also a small broader peak at around 4800 Hz. This is not transmitted upstream or downstream.

The FFT plot given in Figure 138 shows the combined results for Resonator Section 2 and Outlet point monitors for the 30 m/s, 45 m/s and 60 m/s simulations. This plot clarifies how, as the flow velocity is increased, the frequency and amplitude of the tones vary. The plot shows the large amplitude pressure waves created in the second section of the resonator which the higher flow rates. Focusing on the two simulations with the higher flow velocities, it can be seen the amplitude of the tones are very similar. Although the number of peaks is the same, there is a small offset in frequency as the flow rate changes. As the flow rate is increased, the frequency of each tone increased. The offset of the peaks also tends to increase as the frequency increases. The most prominent tone is predicted to be around 3000 Hz. The plot shows the amplitude of this tone to reach as high as 165 dB with the area of concern. This reduces to around 130 dB towards the outlet. Interestingly, the tone around 6000 Hz does not dissipate as rapidly from Section 2 of the resonator to the Outlet monitor point. Therefore, this tone, thought to be a harmonic of the 3000 Hz tone is shown to be significant from a flow-generated noise perspective. Because of the lower amplitude of the pressure fluctuations in the 30 m/s simulation, the fluctuations are not shown to propagate upstream or downstream as the disturbances are dissipated before the acoustic wavelengths have reached the downstream monitoring locations.



**Figure 138: Pre-Production CAC Resonator Simulation - Outlet and Resonator Section 2 Monitor point comparison: 30 m/s, 45 m/s and 60 m/s**

Overall, from this set of simulations, it has been shown several high frequency tones are produced in the Section 2 volume and two tones, approximately 3000 Hz and 6000 Hz in frequency are transmitted downstream. The tones become more discreet and grow dramatically in amplitude as the in-flow velocity is increased. Thus, it can be said the Large Eddy Simulations of the Pre-Production resonator does predict high amplitude tones, but only at the higher of the flow rates tested. The set of simulations using the Pre-Production geometry is now compared with the set of simulations using the production geometry in the following section.

#### **4.2.4.2 Production/Pre-Production CAC Resonator Comparison**

The Production CAC resonator simulations are solved at 30 m/s, 45 m/s and 60 m/s with identical mesh and solver settings to the previous Pre-Production CAC resonator simulations. The results are compared with the Pre-Production geometry simulations. This is to clearly identify how the geometrical differences of the Pre-Production and Production affects the flow and thus, the resonator's effect of the acoustic spectrum further downstream. The cause and location of the high frequency noise is expected to be identified with a great deal of detail from the use of LES CFD simulations.

Figure 139 shows a scalar velocity scene of a section view of the CAC resonator geometry at a single point in time. When compared to the matching scene shown in Figure 132, the rotation of the internal sleeve 180 degrees has had a considerable effect of the flow. The circulation of the vortices apparent within the volume of the second section of the resonator is almost eliminated. Only a low level appears to be entrained into this volume. However, the section 1 of the resonator now demonstrates a higher level of flow recirculation – similar to the Pre-Production Section 2 volume, but crucially without any clear vertical structures present inside and around the entrance to the volume. As Section 1 now has the same neck dimension as Section 2 of the Pre-Production resonator, it could be expected the same level of periodic pressure fluctuations would be created. Conversely, negligible levels of turbulent structures appear to be formed due to this opening. The bulk flow remains somewhat stable. Figure 140 shows a pressure-time plot for the simulation with 45 m/s flow velocity. Each monitor point shown in Figure 140 is represented by a line. Clearly the large pressure fluctuations, present for Section 2 monitor point with the Pre-Production geometry (see Figure 134) are no longer apparent, which is as expected. The pressure fluctuation at this point has dropped dramatically in amplitude. Conversely, the

pressure fluctuations in Section 1 of the resonator have become raised, suggesting Section 1 is now producing some noise. However, the amplitude of these fluctuations is around a factor of 8 lower than that found with the Pre-Production geometry. Thus, the fluctuations do not appear to propagate to the Immediate Downstream point in this case, indicating the amplitude of any noise transmitted from this area will be low.

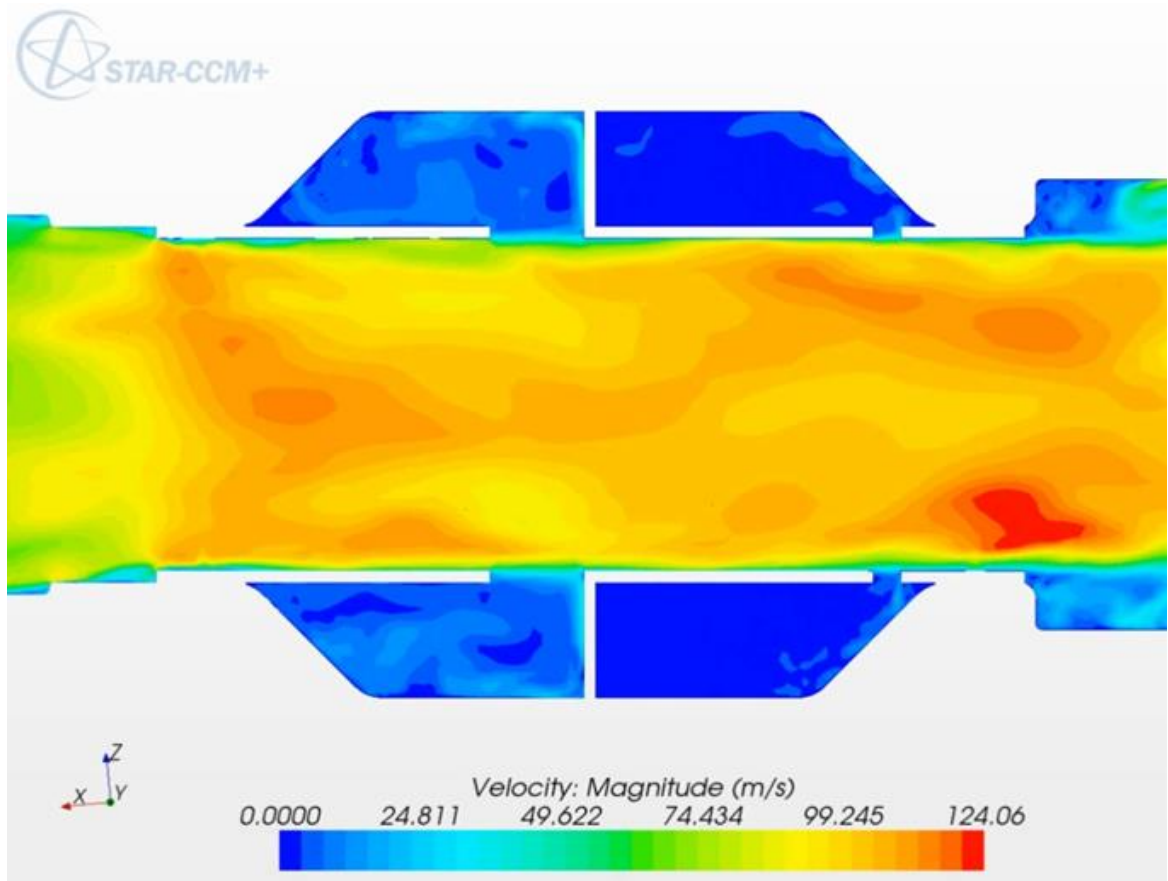
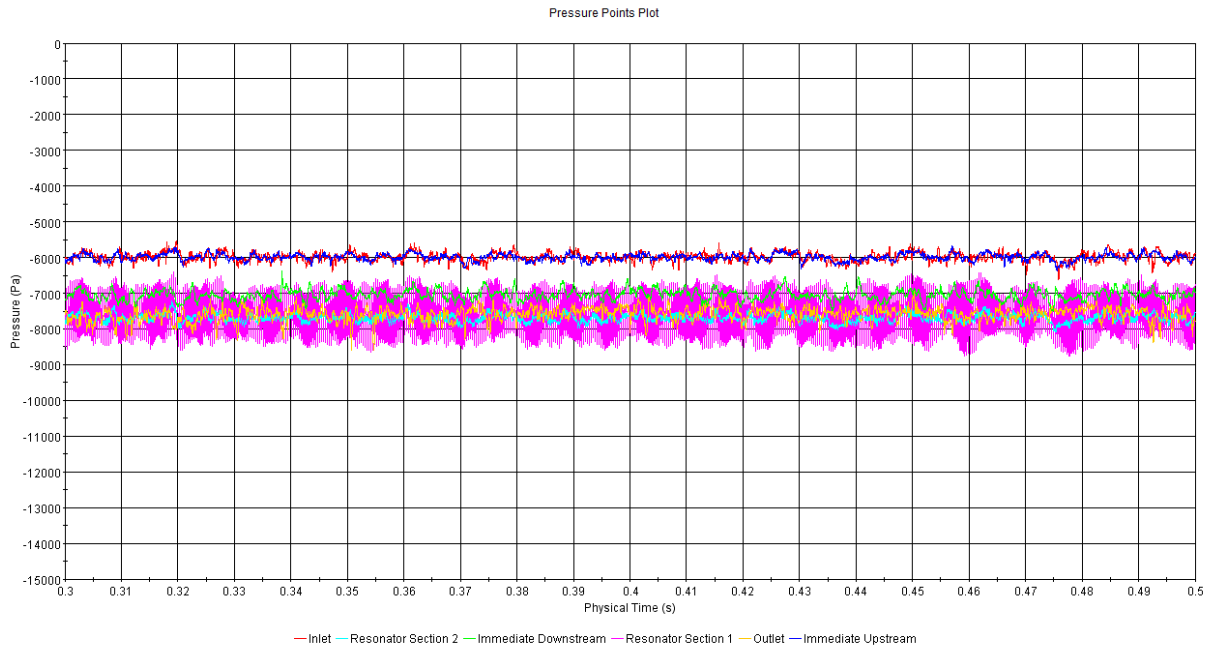


Figure 139: Production CAC Resonator - Velocity Magnitude scalar scene



**Figure 140: Pressure (Pa) against time (s) plot for Production CAC Resonator monitor points - 45 m/s mean inlet velocity**

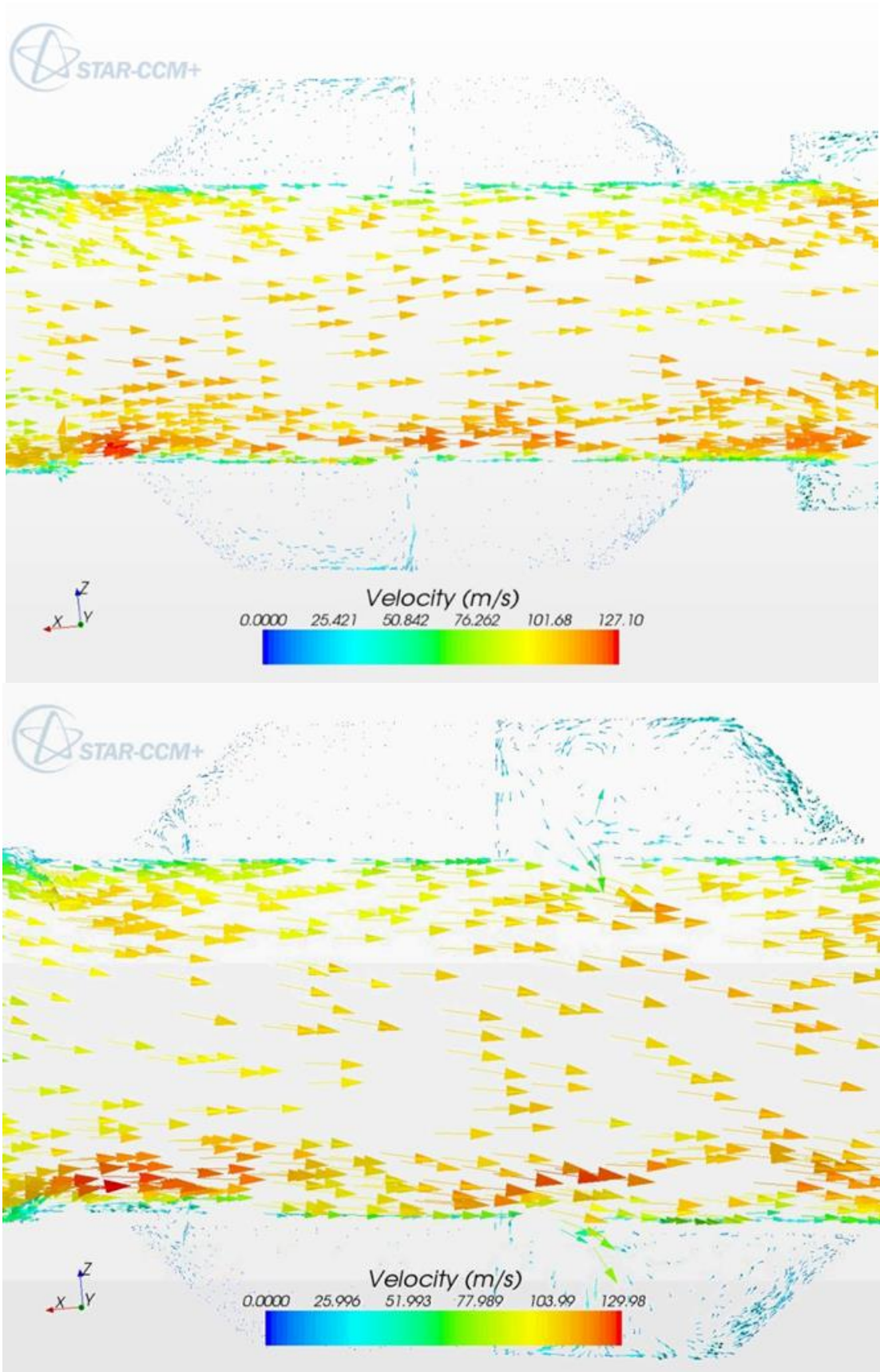


Figure 141: Production CAC Resonator - Velocity Vector scene for Production geometry (top) and Non-Production (bottom)

The dramatic change in the flow through the CAC resonator with the modified design is shown with further clarity in the velocity vector plots which are provided in Figure 141. The arrows inside the resonator volume sections for the top plot (production geometry) show little recirculation of the flow. This indicates a low level of turbulent structures being formed within the resonator. The net effect of this is an insignificant level of pressure fluctuations being transferred to the bulk flow further downstream, when compared to the lower plot. The Pre-Production velocity vector plot shows a considerable level of recirculation, given by the arrow size and direction, inside the volume of Section 2. The top half illustrates the flow re-entering the main shear layer towards the trailing edge and then goes on to affect the bulk flow direction. The lower half illustrates how the main shear layer is heavily disturbed, particularly around the trailing edge. The trailing edge appears to split the flow with a significant amount of fluid entering the volume. This flow re-circulates inside the volume and exits later in time to the main shear layer as before.

The flow within Section 2 of the Pre-Production has been shown to have a noticeable effect on the bulk flow. This indicates a significant level of turbulent fluctuations which are being formed by this process. These fluctuations are understood to give rise to the high amplitude, high frequency tones which are demonstrated in the previous chapter section. Conversely, the Production CAC resonator geometry is expected to reduce and possibly eliminate these high frequency tones as demonstrated by the testing carried out within the premium automotive company as well as the experimental studies conducted in Chapter 2.5.

The acoustic frequency spectrum for both Pre-Production and Production CAC resonators is analysed for all three flow rates tested. FFT plots for 30 m/s, 45 m/s and 60 m/s are provided in Figure 142, Figure 143 and Figure 144 respectively. For all cases, the red line is the acoustic spectrum at a location immediately downstream of the Production CAC resonator geometry and the green line is the acoustic spectrum a location immediately downstream for the Pre-Production CAC resonator geometry.

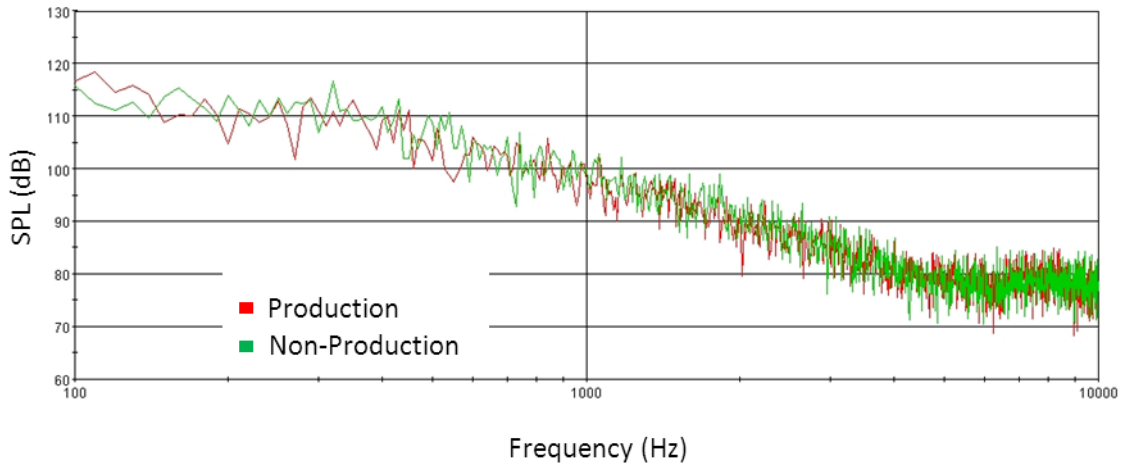


Figure 142: 30 m/s CAC Resonator Simulation Downstream Location - Production/Pre-Production Comparison

The 30 m/s case, Figure 142, both lines follow each other closely, therefore it is possible to say negligible noise is created or attenuated by the Pre-Production Resonator compared with the Production geometry.

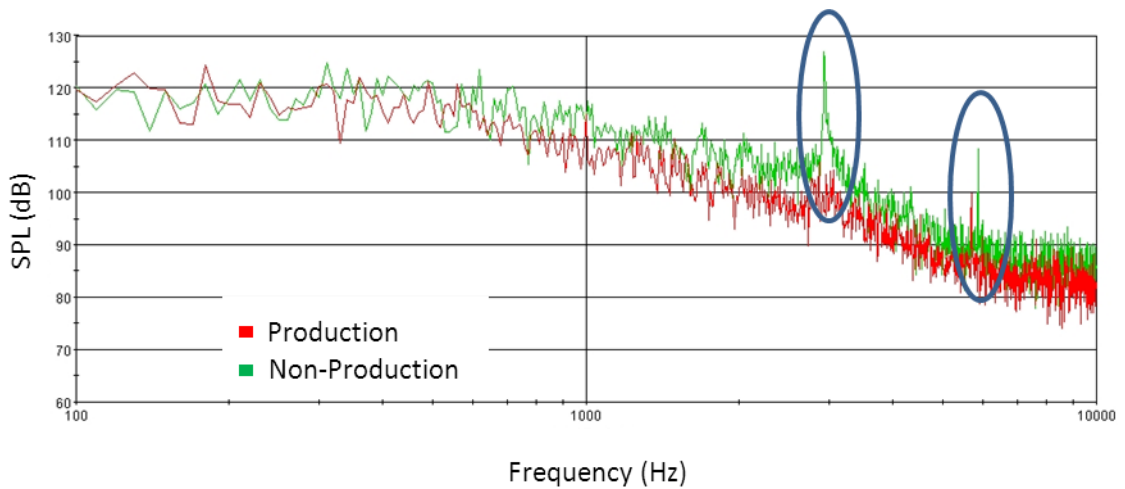
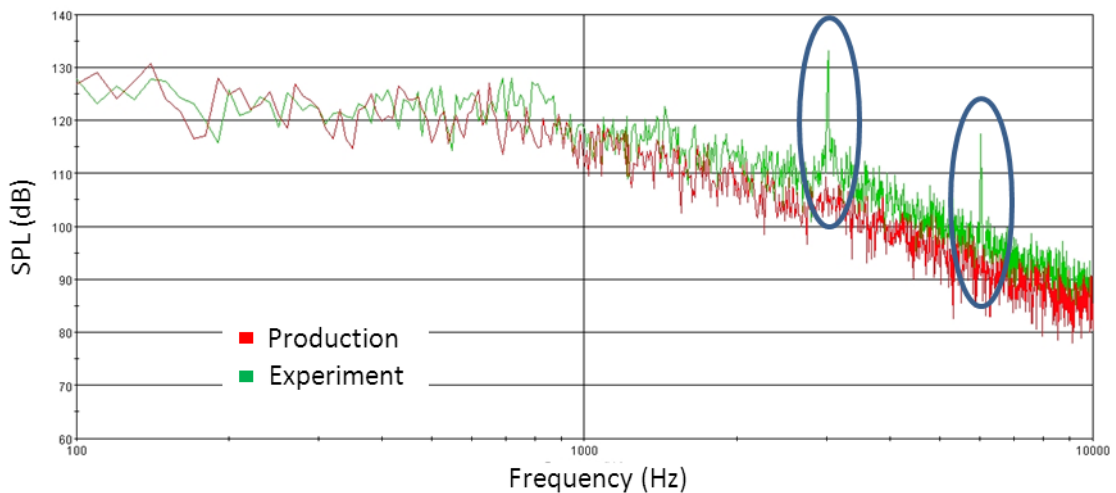


Figure 143: 45 m/s CAC Resonator Simulation Downstream Location - Production/Pre-Production Comparison

For the second case with a 45 m/s inflow velocity (Figure 143), differences can be seen between the two resonators tested. The Pre-Production version appears to create a raised mean amplitude from 500 Hz upwards. There is also a large 20 dB tone present at 3000 Hz which is not as noticeable in the production version. A tone around 6000 Hz is clear for both geometries. The Pre-Production section is shown to create a higher amplitude, thought to be a 2<sup>nd</sup> harmonic tone, of approximately 16-17 dB. The Production section

creates a tone of lower amplitude (10-11 dB) and a slightly lower frequency. This tone for the Production CAC resonator indicates the low-amplitude disturbances found in Section 1 (see Figure 140) are propagated downstream, although at a significantly lower amplitude when compared with the tones predicted from the Pre-Production geometry.



**Figure 144: 60 m/s CAC Resonator Simulation Downstream Location - Production/Pre-Production comparison**

The 60 m/s case shows broadly the same results as the 45 m/s case, however, no clear tone is produced by the production geometry around 6000 Hz. The amplitude of both tonal peaks issued from the Pre-Production geometry, assumed to be 1<sup>st</sup> and 2<sup>nd</sup> harmonics, have increased by approximately 5 dB with the higher flow rate.

This set of simulations has clearly shown that the Pre-Production CAC Resonator creates high amplitude tones, high frequency discrete tones, particularly at the higher flow velocities. The production CAC resonator reduces or eliminates these tones in all tested cases. The scalar scenes, pressure and frequency spectrum plots clearly demonstrate the effect of rotating the internal sleeve of the CAC resonator 180 degrees. The differences between the Pre-Production and Production geometries are subtle. The most significant change is in the trailing edge geometry due to the sleeve rotation. This is thought to be the main attributing factor to the dramatic increase in the high frequency noise between geometries. The volume with the larger opening produces the most noticeable flow-generated noise in both geometry cases. Referring to Figure 126 and Figure 127 for a visual representation of the geometry sections, the larger opening is in Section 1 of the Production resonator. The partitioning wall between each section of the resonator becomes the trailing

edge of the volume opening in the direction of flow. This forms a 90 degree edge. With the sleeve rotated in the Pre-Production version, the trailing edge becomes a sharp protruding lip. This, in effect, appears to separate the fluctuating shear layer which forces considerably more fluid flow into the volume itself. As described earlier in this section, the flow re-circulates inside the volume and is then entrained back into the shear layer as vortices, which are transmitted downstream in regular intervals.

The LES CFD simulations of the CAC resonator have enabled detailed flow patterns to be captured and analysed. The geometry responsible for creating large amplitude, high frequency tones has been robustly identified. The geometry which has reduced and often eliminated any flow-generated noise phenomena has also been identified. The CAC Resonator simulations are compared to the CAC Resonator experiments in the following section.

#### 4.2.4.3 CAC Resonator Simulation/Experiment Comparison

The Pre-Production CAC resonator simulation and experimental results are directly compared from an acoustic perspective. The FFT plots for the 30 m/s, 45 m/s and 60 m/s flow velocity cases comparing experimental and simulation frequency distributions immediately downstream of the CAC resonator are shown in Figure 145, Figure 146 and Figure 147 respectively. An additional frequency distribution of the simulated Resonator Section 2 monitor point is included as further detail in Figure 146.

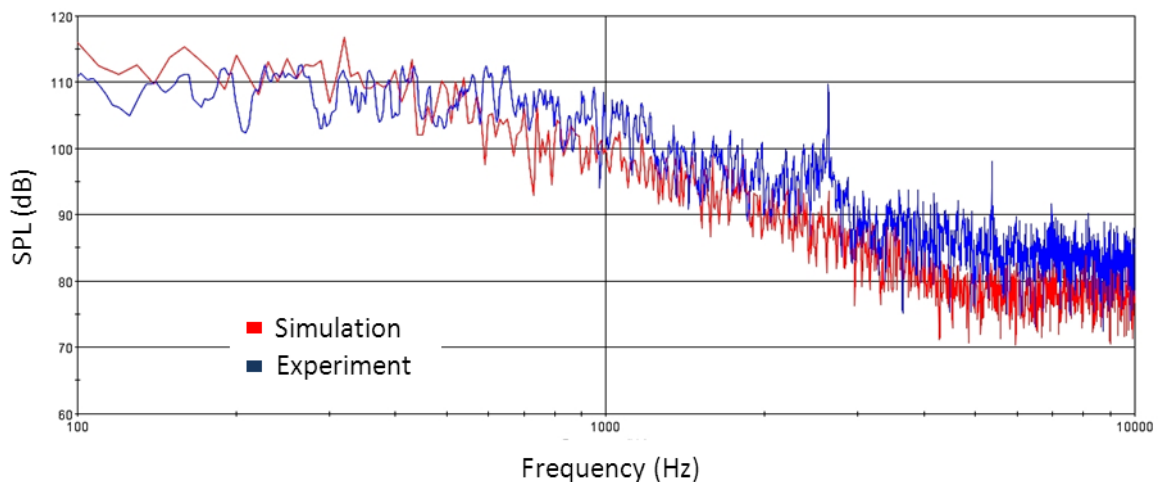


Figure 145: FFT plot - Immediate Downstream location at 30 m/s, simulation and experiment comparison.

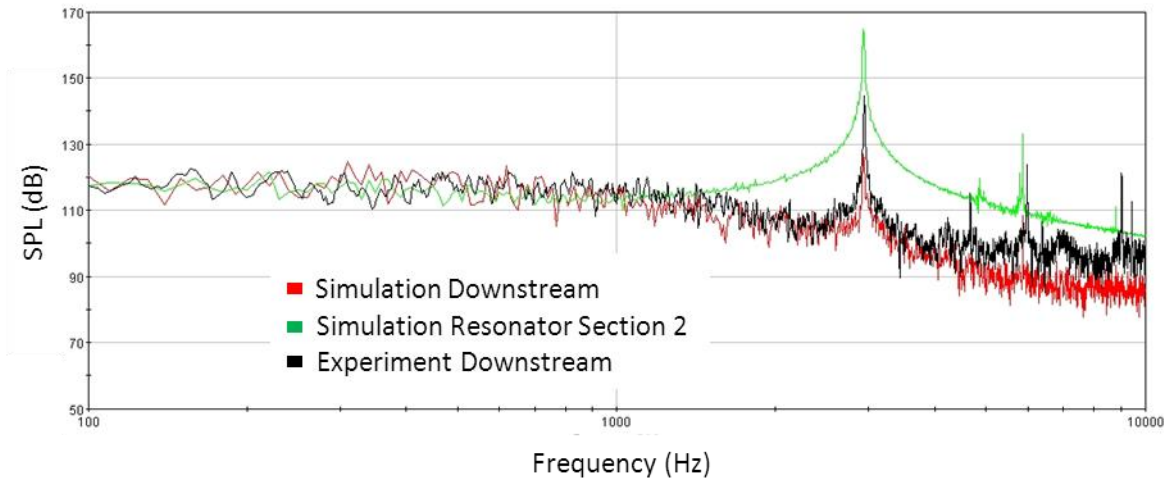


Figure 146: FFT plot - Immediate Downstream and Resonator Section 2 locations at 45 m/s, simulation and experiment comparison.

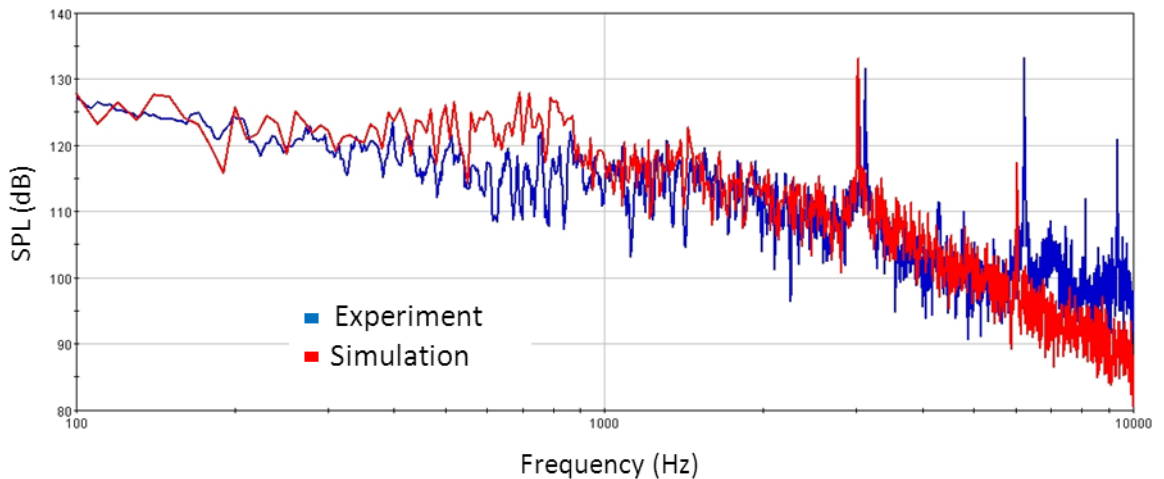


Figure 147: FFT plot - Immediate Downstream location at 60 m/s, simulation and experiment comparison.

Figure 145 compares the acoustic results between experimental and simulation tests at a 30 m/s mean inlet flow velocity. As can be observed, the mean amplitude of the noise immediately downstream of the test piece is very similar between experiment and simulation, taking into account normalisation inaccuracies. However, the experiment produces a low amplitude tone at approximately 2800 Hz which is not picked up in the simulation very clearly. As the tone is of low amplitude, it is not audible from outside of the test section, i.e. in the room surrounding the experiment.

Figure 146 again compares the experiment to simulation but with a 45 m/s inlet flow velocity. Once again, the mean amplitude and frequency distribution between simulation and experiment follow closely. There is a tone produced at around 3000 Hz with an

amplitude of around 40 dB – much higher than the tone produced at a 30 m/s inflow velocity. The amplitude of the tone produced by the CFD is within 1-2 dB of the experiment. As expected, the amplitude of the tone is much higher within the tone production area (Section 2 of the resonator). Interestingly, the experiment picks up higher frequency tones which the simulation does not. The second largest peak appears to be a frequency multiple of the primary frequency, the 2<sup>nd</sup> harmonic. There is also a smaller amplitude peak apparent at approximately 4500 Hz and 9000 Hz present in the experiment noise spectrum and to a lesser extent present in the simulation at the resonator section 2 monitor point. The results suggest these extra peaks, possibly other harmonics of the 3000 Hz, are not transferred downstream.

Figure 147 shows an FFT plot of the same comparisons above but with a 60 m/s inlet flow velocity. Again, the mean amplitudes of the noise in both tests compare well, including the amplitudes of the 1<sup>st</sup> harmonic tone (~3000 Hz). The experiment shows higher amplitudes for what is believed to be the 2<sup>nd</sup> and 3<sup>rd</sup> harmonic tones (6000 and 9000 Hz). It is proposed to be, as appears to be the case with the study at 45 m/s, the higher frequency harmonics are not being propagated downstream in the simulations as effectively as the experiments would suggest should be the case. The frequency of each peak is also offset slightly by 50-100 Hz compared with the experiment frequency analysis. It is likely the inevitable geometrical inaccuracies between the CAD model and the end product could be the cause of this.

Overall, the simulation results align well to experiments. The frequency and amplitude of the 1<sup>st</sup> harmonic tones have been predicted accurately across all tested flow rates. However, the amplitude of the higher harmonic tones are not well represented in the simulations. Finer meshing and adjustments to the sub grid scale model may prevent the higher frequency tones dissipating downstream. The CAC resonator simulations have shown, once again, the advantages of LES as a tool to predict high frequency noise. Turbulent flow patterns can be visualised in a time-marching study. The fundamental origin of high amplitude periodic pressure fluctuations, which translate into noise, can be located and the acoustic tones in the immediate surrounding area have been shown to be very well predicted. To analyse a possible cause of the very high frequency tones (>5000 Hz) which are shown to be dissipated downstream at a higher rate than the experiments would suggest accurate, the Pre-production case is re-meshed with a higher density of cells in the following section.

#### 4.2.4.4 CAC Resonator Mesh Independence

Very fine meshes and preservation of the weak acoustic waves is required because the small amplitudes and the propagative nature of acoustic waves. The use of low dissipation and low dispersion numerical methods to preserve the weak acoustics waves is essential. As a final validation check for the solver and mesh settings of the Large Eddy Simulations, the 45 m/s Pre-Production case is re-meshed with a three-fold increase in the number of cells in the core region. The total mesh count is increased from 4 million cells to 12 million cells by doubling the mesh density in all areas. The resulting mesh is captured in Figure 148. Finer meshing is expected to reduce the effect of the higher frequency tones dissipating downstream.

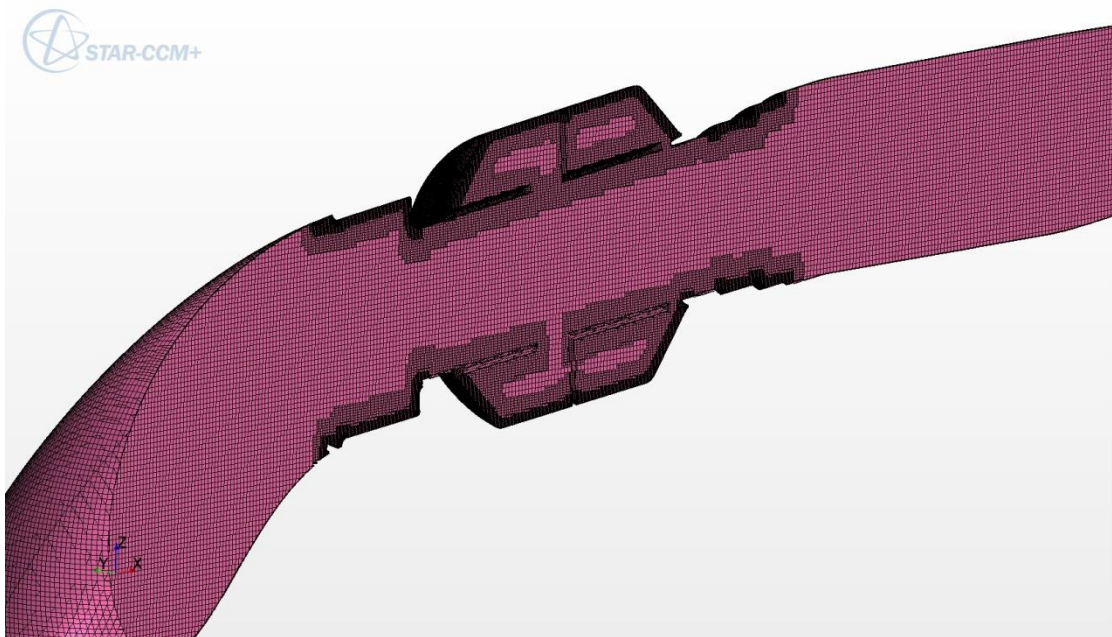
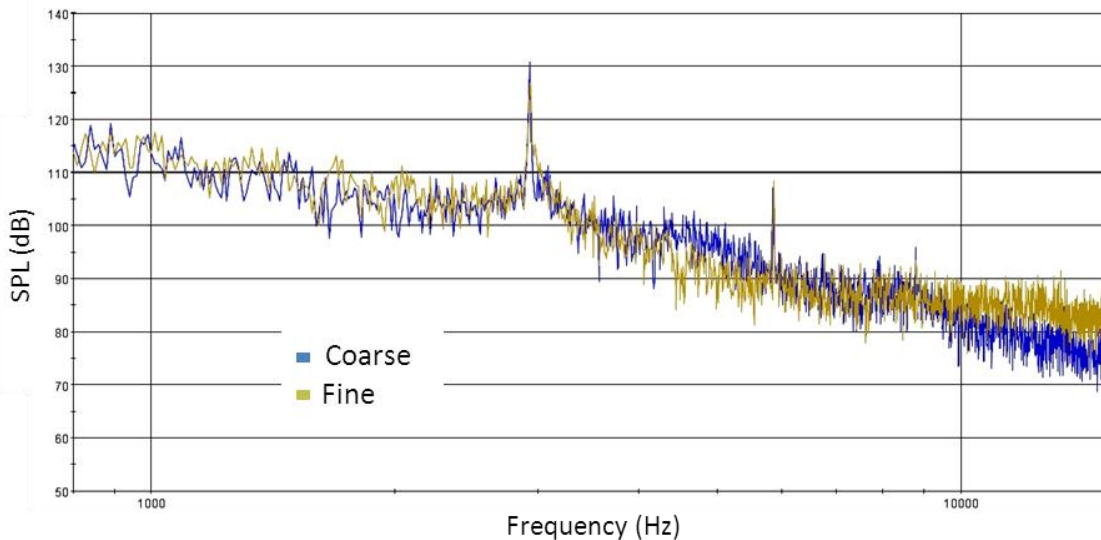


Figure 148: CAC Resonator volume mesh section view



**Figure 149: CAC Mesh Independence – FFT of section immediately downstream of the resonator**

The acoustic frequency spectrum results for the re-meshed case are plotted against the results of the original Pre-Production CAC resonator simulation at 45 m/s in Figure 149. The Immediate Downstream monitor point frequency distributions are compared to analyse how the increased mesh count can affect the high frequency distribution in the areas of interest.

Interestingly, up to around 10 kHz, the frequency distributions for both mesh cases follow very closely. The original mesh simulation (blue) begins to under-predict the mean level of noise beyond this value. This is as expected from the mesh consideration which is detailed in Chapter 3.2. There is a small disparity in the mean noise around 4000 – 5000 Hz. However, this does not influence the peaks in the frequency distributions and could be attributed to the inherent random nature of LES flows. The tonal amplitude and frequencies are almost identical for both cases. Thus, it can be said, for the acoustic spectrum of interest (<10 kHz), the original CAC resonator mesh is adequate to accurately predict the frequency and amplitude of flow-generated tones.

As discussed in the literature review (see Chapter 3.2), Xu et al (Xu, et al., 2007) revealed the dependence of the results on the mesh resolution and on the SGS model. The radiated field induced by the cavity flow was shown to be greatly sensitive to small variations in flow such as the concentration of the coherent structures. Thus, the computation of the correct acoustic levels is a challenging problem. The difficulty in accurately predicting the level of dissipation at high frequencies found in the CAC resonator simulations is therefore anticipated to be due to the Inherent nature of Large Eddy

Simulations. The SGS model provides the balance between construction and dissipation of the turbulent eddy structures. Therefore, this dictates the energy level and dissipation rate of the acoustic waveforms. As the solution in this case has been found to be broadly independent of mesh density, the SGS model and the chosen SGS coefficient has been deduced to be the decisive factor in providing accurate acoustic dissipation levels throughout the geometry. The thesis by Schlatter (Schlatter, 2005) also expresses the importance of the SGS model, particularly in terms of dissipation levels with the use of LES to accurately predict turbulence. Thus, if the problem under study requires a relatively long distance between production and observation of the flow generated noise, it is suggested, with the use of a suitably dense mesh, the SGS model behaviour is a critical area to ensure an accurate acoustic dissipation rate within high Reynolds number flows.

#### **4.2.4.5 Summary**

The premium automotive section of charge inlet tract which is known to produce high frequency tones under certain conditions has been simulated in an aim to replicate the experiments as well as being able to visualise the complex flow phenomenon responsible for the high frequency tones which are shown in Chapter 2. Following on from the QWT investigations, this real-world application of a resonating section helps to further validate the CFD simulations via experimental comparisons. The CAC Resonator which reduced/eliminated the high frequency noise found during vehicle testing and experiments, detailed in Chapter 2.5, was simulated along with the Pre-Production geometry. The CFD analysis was expected to re-create this phenomenon to compare directly to experiments. This would directly assess the capability of LES as a potential design tool to predict unwanted high frequency noise.

The simulations, both visually and numerically, demonstrate the flow-generated noise phenomena present in the corresponding experiments. The acoustic results, in general are shown to give a good correlation between the experiments and LES CFD simulations. A clear difference between the Production and Pre-Production geometry, in terms of flow-generated noise and the flow processes responsible, is demonstrated distinctly by the CFD simulations using LES. The LES CFD simulations of the CAC resonator produced detailed flow patterns which allowed the geometry responsible for creating large amplitude, high frequency tones to be robustly identified. The geometry of interest, which has reduced and often eliminated any flow-generated noise has also been identified. Very good agreement

was found between the experiments and the simulations of the CAC Resonator geometry. The frequency and amplitude of the 1<sup>st</sup> harmonic tones have been predicted accurately across all tested flow rates, generally within 5% of experiment, which is an acceptable tolerance to complete the objectives of this thesis. However, the amplitude of the higher harmonic tones at a reasonable distance away from the source is not as well represented in the simulations. The computation of the correct acoustic levels is a challenging problem. The difficulty in accurately predicting the level of dissipation at high frequencies found in the CAC resonator simulations is concluded to be due to the inherent nature of Large Eddy Simulations. The SGS model is one of the main factors which dictate the energy level and dissipation rate of the acoustic waveforms. As the solution in this case has been found to be broadly independent of mesh density, the SGS model and the chosen SGS coefficient has been deduced to be the decisive factor in providing accurate acoustic dissipation levels throughout the geometry.

The CAC resonator simulations have shown, once again, the advantages of LES as a tool to predict high frequency noise. Turbulent flow patterns can be visualised in a time-marching study. The fundamental origin of high amplitude periodic pressure fluctuations, which translates into noise, can be located and the acoustic tones in the immediate surrounding area have been shown to be very well predicted. The LES CFD simulation analysis of the CAC Resonator provides information on the underlying flow processes which create this high frequency tone. These phenomena, which rely on various geometrical and flow parameters are difficult to prove, understand and visualise through experiments only. Thus, this set of simulations has substantially validated LES as a useful and accurate tool to predict high frequency noise from a practical perspective.

### 4.3 Modelling and Simulation Summary

The simulations have provided further understanding into how a resonator behaves under various flow conditions and geometries. A direct comparison between U-RANS and LES solvers is demonstrated to highlight the benefits of Large Eddy Simulations. The importance of inflow conditions are demonstrated along with a number of mesh independence studies. Significant differences were clear in terms of high frequency noise prediction between U-RANS and LES solvers. The analysis showed the clear advantages of an LES simulation as opposed to U-RANS. The latter U-RANS simulations demonstrated an

inability to capture high frequency noise issuing from the geometries which are central to this thesis. Therefore, LES is essential to enable the prediction of high frequency noise.

A number of LES validation simulations were carried out with a view to replicate a selection of the studies using the U-RANS solver. Further investigations were also carried out with the experiment test geometries. To enhance knowledge of resonant cavity flows, several further parameters were varied which were not practical to investigate experimentally. The LES solutions have been proved to be more useful in providing a greater insight into the processes involved inside and around the resonator. The Large Eddy Simulations have enabled the opportunity to visually inspect the flow processes which are the cause of the noise generated in many of the experimental studies carried out in Chapter 2. CFD simulations using LES have been found to be capable of predicting, with encouraging accuracy, the high frequency flow-generated noise present in several resonating geometries found in many industrial contexts, particularly in the automotive sector.

---

## 5 Conclusion

### 5.1 Thesis Summary

This final chapter presents an overall discussion and conclusion of this thesis. Following the conclusions, directions for future works are suggested.

NVH (noise, vibration and harshness) of automotive systems is receiving an ever increasing level of interest. Industry sectors are facing increasing pressure from customers as well as government authorities to reduce flow noise and its transmission to the interior environment or propagated externally to by passers. The NVH levels are not the only important factor. The *quality* of the noise produced such as the engine note or the exhaust rasp is also a key market area, particularly for luxury/sports car consumers. Resonators play a large part in NVH and sound quality in modern automotive flow system design. An excellent understanding of the complex interaction between the resonators and the effect on the incoming flow is crucial to be able to predict the performance of the designs of these configurations.

Through the design and development of automotive powertrain systems, unusual engine noises, often of high (>1000 Hz) frequency are systematic issues and often discovered late on during a vehicle development programme. Failure mode resolution at this stage in the programme tends to be costly as the vehicle package has been frozen and parts released. Computer Aided Engineering (CAE) is proving to be an increasingly valuable tool to help understand the flow noise generation propagation and transmission mechanisms. Consequently, engineers are able to design against them either by reducing the source or minimising its propagation in the aerodynamic/hydrodynamic domain and the transmission through structures.

Before the last decade, low levels of computational work for production-type geometries were carried out due to the prohibitive computational cost of performing time varying (unsteady) CFD calculations (Mendonca, 2005). With the continued decrease in hardware cost and the increase in performance, Computational Aero-acoustics (CAA) calculations are now being performed by an ever-increasing number of industrial CFD engineers (Piomelli, 2001). Numerical characterisation has the clear benefit of reducing the need for experimental rigs, and potentially provides far greater insight into the flow phenomena involved. The flow can be studied in detail, providing a better understanding. Also many simulations with changing variables can be simulated in a relatively short amount

of time in comparison to real-life. Large Eddy Simulations (LES) is the next stage of this technology advancement. LES solutions are more useful in providing a greater insight into the detailed turbulent flow processes involved inside and around the resonator cavity. In turn, it is able to capture the high frequency unwanted noise which can be created in certain geometries and flows. Time-averaged solvers are unable to capture the high level of turbulence detail required.

The aim of this thesis was to establish the feasibility of industrial application of Large Eddy Simulation (LES) to practical automotive acoustic problems. A Computer Aided Engineering (CAE) tool based around CFD would be utilised in premium automotive applications to allow upfront assessments of the intake/exhaust systems and facilitate cost effective optimisation early on in the vehicle development programme. Furthermore, a CAE tool could be used to aid failure mode resolution at a later stage in the development programme.

As a contribution to knowledge, the primary aim of this study was to gain understanding and scientific insight into the advantages and concerns surrounding the application of LES to industrial acoustic problems for premium automotive applications. In turn, the flow processes which are responsible for the unwanted high frequency noise can be analysed visually and analytically in greater detail than is possible through experimental studies alone. The CAC resonator study in-particular provides a unique insight into the use of LES CFD as a design aid to predict and remove unwanted high frequency aero-acoustic tones. The QWT analysis also provided a unique analytical and visual insight into the importance of geometric tolerances around the neck joint. This study combines the practical aspects of predicting high frequency tones in flows using LES to be applied in the real world complex geometries. The majority of existing studies in industry tend to be RANS based with unique models catered to their specific requirements, primarily due to cost associated with LES. Other studies tend to have a strong theoretical focus with limited industrial transfer. A commercial CFD solver has been utilised in this thesis to replicate the CFD usage within the premium automotive company. This thesis does not aim to code a new solver, nor does it aim to create a theoretical model. The main objective of this thesis has been to assess the capability of LES to predict high frequency noise in complex geometries, with the view to utilise LES as a practical design tool in an industrial context. To accomplish this, several experimental tests were conducted to re-create the unwanted high frequency tones from resonators found in the literature, as well as the examples found during the production phase at Jaguar Land Rover. Several trends were found from the literature, such as the

studies by East (East, 1966), (Panton, 1990), Radavich (Radavich, et al., 2001), and Kannan (Kannan, et al., 2004) (Kannan, et al., 2005). These studies, amongst many others, presented results on the effect of orifice geometry on resonator excitation by grazing flow.

The experiments analysed several side-branch resonator geometries, such as a Variable Volume Helmholtz resonator, a Quarter Wave Tube and a the premium automotive Charge Air Cooler resonator with various in-flow velocities. The aim was to re-create the experiments as numerical simulations using a commercial Computational Fluid Dynamics (CFD) code as validation exercises. The experimental work was also an attempt to gain further understanding into how a resonator behaves under various flow conditions geometries and acoustic signals which can initiate the production of pure tones. The experiments with a side branch consisting of a VVH Helmholtz resonator and an adjustable Quarter Wave Tube (QWT) have been conducted to investigate the effect of various generic side branch configurations. Several parameters were varied such as in-flow rate, resonator volume and resonator neck geometry. The automotive section of charge inlet tract was flowed which was found in prototype testing to produce a high frequency tone. The revised geometry was also tested experimentally.

The experiments have provided an interesting insight into the trends and geometries which can cause high frequency flow-generated noise. Several experiments produced high frequency (>1000 Hz) tones which were found to be semi-independent from the tuned fundamental resonant frequency. Several of the experiments produced clear high frequency tones in many of the geometries tested. These results correlated well with theory and similar published works. The high frequency flow generated noise is primarily related to the resonance between the instabilities in the shear layer of the airflow arising from the wake of the upstream edge of the cavity and the harmonics of the cavity itself.

Computational validations are carried out and further studies are undertaken with the increased information and variability available through CFD. The results have been analysed and compared with the experiments to deduce whether the CFD code is suitable for use as a design tool, and thus could be utilised early on in the product design phase. The LES capability of commercial CFD was assessed by carried out equivalent simulations of the flow rig experiments to model how the acoustic spectrum of turbulent fluid flows can be affected by a resonator inserted in a pipe or attached as a side-branch. Several initial validation simulations were carried out to ensure robust and accurate results were obtained. Robust simulation results are essential to compare to the respective experimental results.

The simulations have provided further understanding into how a resonator behaves under various flow conditions and geometries. A direct comparison between RANS and LES solvers is demonstrated to highlight the benefits of Large Eddy Simulations. The importance of in-flow conditions are demonstrated along with a number of mesh independence studies. Significant differences were clear in terms of high frequency noise prediction between RANS and LES solvers. The analysis showed the advantages of an LES simulation as opposed to RANS. The latter RANS simulations demonstrated an inability to capture high frequency noise issuing from the geometries which are central to this thesis. The VVH noise generation simulations began to show the limitations of U-RANS to predict high frequency flow-generated noise. The lack of detail, visually and numerically, around the flow phenomena which hampers understanding of the flow-acoustic noise generation present. The limitations for U-RANS have been revealed from an aero-acoustics perspective. Therefore, LES has been shown to be essential to enable the prediction of high frequency noise. A number of LES validation simulations were carried out with a view to replicate a selection of the studies using the RANS solver. Further investigations were also carried out with the experiment test geometries. To enhance knowledge of resonant cavity flows, several further parameters were varied which were not practical to investigate experimentally. The LES solutions have been proved to be more useful in providing a greater insight into the processes involved inside and around the resonator. The Large Eddy Simulations have enabled the opportunity to visually inspect the flow processes which are the cause of the noise generated in many of the experimental studies carried out in this thesis.

CFD simulations using LES have been found to be capable of predicting, with encouraging accuracy, the high frequency flow-generated noise present in several resonating geometries found in many automotive applications, the Large Eddy Simulations have produced acoustic results which are generally in very good agreement with the experimental validation results (less than 5% in many cases, compared with experimental data). The computation of the correct acoustic levels has been found to be a challenging problem with the use of LES. The SGS model, which is utilised in LES provides the balance between construction and dissipation of the turbulent eddy structures. Therefore, this dictates the energy level and dissipation rate of the acoustic waveforms. As the solution in this case has been found to be broadly independent of mesh density, the SGS model and the chosen SGS coefficient has been deduced to be the decisive factor in providing accurate acoustic dissipation levels throughout the geometry. Thus, if the problem under study requires a relatively long distance between production and observation of the flow

generated noise, it is suggested, with the use of a suitably dense mesh, the SGS model behaviour is a critical area to ensure an accurate acoustic dissipation rate within high Reynolds number flows.

Overall, this study has enabled a greater understanding of the underlying physical phenomena in automotive cavity flows. The comparison between the computational predictions and the experiments is excellent suggesting that the detailed physics of the flow-generated noise phenomena is captured in the computational analysis using LES. Therefore, the LES CFD code is suitable as a tool to predict high frequency noise. It is suggested the LES function of CFD should be limited to cases of interest due to the increased resource needed to obtain robust results.

## **5.2 Recommendations and Future Work**

The work carried out in this thesis has proven the application of LES is suitable for use as a design tool, and thus could be utilised early on in the product design phase. However, from a practical viewpoint, it is suggested the LES function of CFD should be limited to cases of interest due to the increased resource needed to obtain robust results. A recommendation is to build up a 'best practice' library of suitable geometrical features for specific components through several LES CFD simulations. The use of LES could then be reduced to designs of interest in the near term and used to aid failure mode resolution later on in the programme. As computational resource expands significantly, LES can be phased in to analyse many more design iterations. Applications of LES within automotive internal aero-acoustic flows can also be expanded. Far-field noise modelling through LES is the next logical step for this area of research. For NVH customer satisfaction, the acoustic area of interest is predominantly the region around the driver and passenger's ear location. Therefore, it would be useful to predict which tones would propagate to this area, or be damped out through the various systems in a vehicle.

To accomplish this next stage in LES simulation technology, several areas need to be made more robust. The present research highlighted difficulties in producing the correct level of dissipation of very high frequency tones. The production/dissipation balance is a significant area for further research. Correct modelling of boundary layer has been found to be a very important area. Future work will focus on the near-wall flow-acoustic interactions of internal flow problems. Along with finer meshes, the inflow boundary conditions have

proved to be another significant aspect of robust LES simulation, as discussed in the literature review sections. Synthetic in-flow boundaries which can be applied to acoustic problems, coupled with fully developed flow, would enable more accurate levels of turbulence to be predicted with a minimum level of resource.

To validate the Large Eddy Simulations with greater accuracy, the measurement during experimental studies could be improved for future work. Laser velocimeter/hotwire measurements would enable a greater level of acoustic measurements with minimum intrusion. The monitor points in the simulations can be precisely mapped to the experiments in terms of location absolute pressure levels. As the flow and input noise level was produced in this thesis via a large fan, replicating real world prototype testing by replicating real engine flow pulsations and noise. Ideally a real world internal combustion engine would be incorporated in the test to include pulsations, noise, temperature and pressure which would provide the ultimate validation for any LES simulation.

Furthermore, as LES solvers become more robust with increasing levels of resource, applications of LES throughout the automotive industry can be expanded from a practical perspective to external flows.

## 6 Appendix

### 6.1 Appendix 1

Matlab FFT script in collaboration with Brian Houston, University of Hull Postgraduate Student.

```

%% --- FFT ANALYSIS -- Initial User Input Function
function FFT_SCRIPT ()
% GUI - The code uses
% the provided raw data files and additional information to carry out
a
% FFT of the raw data and calculate acoustic performance.

[Exp_Data_Fname,Exp_Data_Pname] = uigetfile...
  ({'*.*.csv;*.lvm;*.txt','All Excel Files'}, ...
  'Please select the first data file to process',...
  'Raw Data File name');
UI.Exp_Data_File = [Exp_Data_Pname, '',Exp_Data_Fname];
prompt = {'Number of samples to process:', 'Sampling Frequency:', ...
  'Length of Signal:', 'File Extension(csv etc.):', ...
  'Number of header rows:'};
dlg_title = 'Raw data specifications';
num_lines = 1;
answer=inputdlg(prompt,dlg_title,num_lines);
UI.SampleNum = str2double(answer{1});
UI.SampleFreq = str2double(answer{2});
UI.SampleLength = str2double(answer{3});
UI.FileExt = answer{4};
UI.Header_row_num = str2double(answer{5});

%*****
%*****
%This function loads in and processed raw measured data for direct
%comparison
%*****
%*****

iMisc.Sample_No = UI.SampleNum;      %Number of data files to be
processed
Data_path= UI.Exp_Data_File(1:end-6);%Remove the Numerical suffix
from name

%Load raw data
Raw_Data = cell(1,iMisc.Sample_No);
for FileNum=1:iMisc.Sample_No;

if FileNum<10
Import_Suffix=['0',num2str(FileNum)];
else
Import_Suffix=num2str(FileNum);
end %if
Import_path= sprintf('%s%s.%s',Data_path,Import_Suffix,UI.FileExt);

```

```

Raw_Data{FileNum}= importdata(Import_path, ',', UI.Header_row_num);
end %for

%Calculate FRF

Fs = UI.SampleFreq;    % Sampling Frequency
L= UI.SampleLength;    % Length of Signal
Xlim_Max= 500000;    %Cut off Frequency

NFFT = 2^nextpow2(L); %Next power of 2 from length of A&B
iMisc.freq = Fs/2*linspace(0,1,NFFT/2+1);

iMisc.Data_OUTPUT=zeros(length(iMisc.freq),iMisc.Sample_No+1);

for FileNum=1:iMisc.Sample_No;

A=Raw_Data{1,FileNum}.data(:,3);
B=Raw_Data{1,FileNum}.data(:,1);

fft_A = fft(A,NFFT);

Measured_FRF = ((fft_A(1:NFFT/2+1)))

for Value=1:(length(Measured_FRF));
iMisc.Data_OUTPUT(Value,FileNum)=Measured_FRF(Value,1);
end

end

for Value=1:(length(Measured_FRF));
iMisc.Data_OUTPUT(Value,iMisc.Sample_No+1)=mean((iMisc.Data_OUTPUT(Value,:)));
iMisc.Data_OUTPUT(Value,iMisc.Sample_No+2)=iMisc.freq(1,Value);
end

Roi=find(real(iMisc.Data_OUTPUT(:,iMisc.Sample_No+2))<=Xlim_Max);
Max_Index=length(Roi);
iMisc.Mean_Values=zeros(Max_Index,1);
for Value=50:Max_Index;
iMisc.Mean_Values(Value,1)=abs(iMisc.Data_OUTPUT(Value,iMisc.Sample_No+1));
end

a=20*log10(((abs(iMisc.Data_OUTPUT(:,iMisc.Sample_No+1)))/(0.00002)))
;

b=smooth(a);

%plotting
semilogx(iMisc.freq,b,'b'); hold on
grid on
title('FFT plot - ');
xlabel('Frequency (Hz)');
ylabel('dB');
xlim([0 100000]);
h = legend(' ','Downstream Edge','Upstream Edge',3);
end

```

## 6.2 Appendix 2

The statistical error for experiment microphone measurements is summarised in this appendix. Three frequencies from the FFT spectra are chosen for analysis – 1, 2 and 3 kHz. Measurements without air flow are provided for baseline Standard Deviation of the frequency spectrum (FFT) and Standard Deviation of the transfer function (TR). Sound pressures at two microphone positions (with 100 mm interval distance) are recorded with 20 repeated measurements. With the obtained standard deviations, the uncertainties are tabulated against sample flow measurements. The measurements +/- 1 Standard Deviation are provided to give an indication of the likely magnitude of the measurement uncertainties.

*Microphone Test Data*

Dataset Number	Microphone A SPL @ 1000 Hz (dB)	Microphone B SPL @ 1000 Hz (dB)	Microphone A SPL @ 2000 Hz (dB)	Microphone B SPL @ 2000 Hz (dB)	Microphone A SPL @ 3000 Hz (dB)	Microphone B SPL @ 3000 Hz (dB)
1	66.553	63.788	50.545	52.073	46.881	42.554
2	64.066	64.364	52.745	56.201	47.473	40.314
3	66.198	60.413	54.261	51.246	45.771	41.518
4	67.699	66.396	52.531	51.226	48.707	41.578
5	65.991	64.619	53.777	52.639	43.328	44.165
6	67.184	64.646	53.839	53.741	46.245	39.905
7	67.063	62.462	50.548	54.082	43.104	43.308
8	66.619	62.264	54.821	54.560	49.331	41.028
9	68.327	62.368	51.458	54.390	48.958	43.437
10	69.697	60.473	52.387	55.671	47.925	44.968
11	65.546	63.576	49.313	56.201	47.632	40.314
12	65.786	60.413	51.041	54.404	44.393	38.550
13	66.343	60.603	52.181	54.125	49.784	42.959
14	61.155	63.887	49.920	55.273	47.388	42.872
15	66.043	64.694	48.190	53.027	48.083	42.670
16	65.763	63.631	48.862	53.120	46.174	43.750
17	65.270	65.146	52.030	52.408	46.878	45.589
18	64.674	63.127	50.456	51.037	48.471	42.471
19	67.637	63.024	51.167	53.535	48.030	41.545
20	67.471	63.069	50.054	53.566	48.076	41.577
Average (dB)	66.254	63.148	51.506	53.626	47.132	42.254
Average Standard Deviation (dB)		1.727		1.698		1.801
Percentage (%)		2.607		3.297		3.821

*Experimental Data - 30 m/s QWT*

Frequency (Hz)	Volume SPL (dB)	Downstream SPL (dB)	TR (Volume SPL/Downstream SPL)	SD (TR)	TR + SD (TR)	TR - SD (TR)
1000	98.899	93.281	1.060	0.045	1.105	1.015
2000	88.171	82.842	1.064	0.046	1.111	1.018
3000	82.085	74.115	1.108	0.063	1.170	1.045

Frequency (Hz)	Volume SPL + Average Standard Deviation (dB)	Volume SPL - Average Standard Deviation (dB)	Downstream SPL + Average Standard Deviation (dB)	Downstream SPL - Average Standard Deviation (dB)
1000	100.626	97.172	95.008	91.554
2000	89.869	86.473	84.540	81.144
3000	83.886	80.284	75.916	72.314

## 7 Bibliography

A.G Kravchenko, P. M., 1997. On the Effect of Numerical Errors in Large Eddy Simulations of Turbulent Flows. 131(2).

ANSYS, I., 2011. *ANSYS FLUENT User's Guide v14*, Canonsburg: ANSYS, Inc.

Barron, R. F., 2001. *Industrial Noise Control and Acoustics*. New York: Marcel Dekker.

Benamadouche, S., Jarrin, N., Addad, Y. & Laurence, D., 2006. Synthetic Turbulent Inflow Conditions Based on a Vortex-method for Large Eddy Simulation. *Progress in Computational Fluid Dynamics*, Volume 6, pp. 50-57.

Bies, D. A. & Wilson, O., 1957. Acoustic Impedance of a Helmholtz Resonator at Very High Amplitude. *The Journal Of The Acoustical Society Of America*, 29(6), pp. 711-714.

Billson, M., Eriksson, L. & Davidson, L., 2003. *Jet Noise Prediction using Stochastic Turbulence Modeling*. South Carolina, AIAA/CEAS Aeroacoustics Conference and Exhibit.

Boussinesq, J., 1877. Essai sur la thé'orie des eaux courantes (Essay on the theory of water flow).. *Me'moires pre'sente's par divers savants a` l'Acade'mie des Sciences*, Volume 23, pp. 1-680.

Breuer, M., Jovii, N. & Mazaev, K., 2003. Comparison of DES, RANS and LES for the Separated Flow Around a Flat Plate at High Incidence. *International Journal of Numerical Methods in Fluids*, 41(4), pp. 357-388.

Bruggeman, J., 1987. *Flow Induced Pulsations In Pipe Systems*, Netherlands: Eindhoven University of Technology.

Caro, S. et al., 2005. *Aeroacoustic Simulation of the Noise Radiated by an Helmholtz Resonator Placed in a Duct*. Monterey CA, 11th AIAA/CEAS Aeroacoustics Conference.

Cattafesta III, L. N. et al., 2008. Active Control Of Flow-Induced Cavity Oscillations. *Progress in Aerospace Sciences*, 44(7-8), pp. 479-502.

CD-Adapco, 2011. *Star CCM+ 6.02 tutorial guide*, Melville: CD-Adapco.

- Chaudhari, M., Verma, G., Puranik, B. & Agrawal, A., 2009. Frequency Response of a Synthetic Jet Cavity. *Experimental Thermal and Fluid Science*, 33(3), pp. 439-448.
- Chorin, A. J. & Bernard, P. S., 1973. Discretisation of a Vortex Sheet, with an Example of Roll-up. *Journal of Computational Physics*, Volume 13, pp. 423-429.
- Davidson, L., 2010. *Large Eddy Simulation (LES)*. Derby, nafems.org LES Awareness Day.
- Davidson, L., 2013. *Fluid Mechanics, Turbulent Flow and Turbulence*, G teborg: Chalmers University of Technology.
- Davidson, W. K. & Davidson, L., 2004. Role of Initial Conditions in Establishing Asymptotic Flow Behavior. *AIAA*, 42(3), pp. 438-446.
- Davis, D., Stokes, G., Moore, D. & Stevens, G., 1954. *Theoretical And Experimental Investigation Of Mufflers With Comments On Engine-Exhaust Muffler Design*, Washington: National Advisory Committee For Aeronautics.
- Doria, A., 2000. A Simple Method For The Analysis Of Deep Cavity And Long Neck Acoustic Resonators. *Journal of Sound and Vibration*, Volume 232, pp. 823-833.
- Driest, E. R. V., 1956. On Turbulent Flow Near a Wall. *Aeronautical Sciences*, 23(11), pp. 1007-1011.
- Duben, A. P. et al., 2012. Acoustic Flow in the Resonator Throat: Experiment and Computational Modeling. *Acoustical Physics*, 58(1), pp. 69-80.
- Durbin, P. A. & Medic, G., 2007. *Fluid Dynamics with a Computational Perspective*, : Cambridge University Press.
- Dyke, M. V., 1982. *An Album of Fluid Motion*. Stanford, CA: Parabolic Press.
- East, L. F., 1966. Aerodynamically Induced Resonance in Rectangular Cavities. *Journal of Sound and Vibration*, 3(3), pp. 277-287.
- Embleton, T. F. W., 1971. Mufflers. In: *Noise and Vibration Control*. California: McGraw-Hill, pp. 362-405.
- Everest, F. & Pohlmann, K., 2009. *Master Handbook of Acoustics*. 5th ed. New York: McGraw-Hill.

- Ferziger, J. H. & Peric., M., 2002. *Computational Methods for Fluid Dynamics*. 3rd ed. New York: Springer.
- Garnier, E., Adams, N. & P.Sagaut, 2009. *Large Eddy Simulation for Compressible Flows*. : Springer.
- Garnier, E., Pamart, P., Dandois, J. & Sagaut, P., 2012. Evaluation of the Unsteady RANS Capabilities for Separated Flow Control. *Computers & Fluids*, Volume 61, pp. 39-45.
- Georgiadis, N. J. & DeBonis, J. R., 2006. Navier–Stokes Analysis Methods for Turbulent Jet Flows with Application to Aircraft Exhaust Nozzles. *Progress in Aerospace Sciences*, 42(5-6), pp. 377-418.
- Georgiadis, N. J. & DeBonis, J. R., 2007. *Navier–Stokes analysis methods for turbulent jet flows with application to aircraft exhaust nozzles*, Cleveland: Progress in Aerospace Sciences.
- Germano, M., Piomelli, U., Moin, P. & Cabot, W., 1991. A Dynamic Subgrid-Scale Eddy Viscosity Model. *Physics of Fluids*, 3(7), pp. 1760-1765.
- Gloerfelt, X., 2009 (1). Noise from Automotive Components. In: J. Anthoine & J. Christophe, eds. *Aerodynamic Noise from Wall-bounded Flows*. Paris: von Karman Institute.
- Gloerfelt, X., 2009 (2). Cavity Noise. In: J. Anthoine & J. Christophe, eds. *Aerodynamic Noise from Wall-bounded Flows*. Paris: von Karman Institute.
- Go Tuning Unlimited, 2010. *Go Tuning Unlimited*. [Online] Available at: [http://www.gotuning.com/product\\_info.php?products\\_id=1322](http://www.gotuning.com/product_info.php?products_id=1322) [Accessed 6th January 2012].
- Haren, S. V., 2011. *Testing DNS capability of OpenFOAM and Star-CCM+*, Delft: TU Delft Master Thesis.
- Harrison, M., 2004. *Vehicle Refinement: Controlling Noise and Vibration in Road Vehicles*. 1st ed. Oxford: Elsevier.
- Hayes, R. E., Fadic, A., Mmbaga, J. & Najafi, A., 2012. CFD Modelling of the Automotive Catalytic Converter. *Catalysts Today*, 188(1), pp. 94-105.
- Hinze, J., 1975. *Turbulence*. 2nd ed. New York: McGraw-Hill.

Hofmans, G. C. J., 1999. *Vortex Sound in Confined Flows*, s.l.: Eindhoven University of Technology (PhD Thesis).

Howe, M. S., 1975. Contributions to the Theory of Aerodynamic Sound, with Application to Excess Jet Noise and the Theory of the Flute. *Journal of Fluid Mechanics*, 71(4), pp. 625-673.

Howe, M. S., 1984. On the Absorption of Sound by Turbulence and Other Hydrodynamic Flows. *IMA Journal of Applied Mathematics*, Volume 32, pp. 187-209.

Ingard, U., 1953. On the Theory and Design of Acoustic Resonators. *Acoustical Society of America*, 25(6), pp. 1037-1061.

ISO-7235, 1991. *Acoustics - Measurement Procedures for Ducted Silencers - Insertion loss, Flow Noise and Total Pressure Loss*, : International Organization for Standardization.

Jarrin, N., 2008. *Synthetic Inflow Boundary Conditions for the Numerical Simulation of Turbulence*, Manchester: PhD Thesis, University of Manchester (UK).

Jayaraju, S., Komen, E. & Baglietto, E., 2010. Suitability of Wall-Functions in Large Eddy Simulation for Thermal Fatigue in a T-Junction. *Nuclear Engineering and Design*, Volume 240, p. 2544–2554.

Jungowski, W. M., Bortros, K. K. & Studzinski, W., 1989. Cylindrical Side-Branch as Tone Generator.. *Journal of Sound and Vibration*, Volume 131, pp. 265-285.

Kannan, V., Greeley, D., Sovani, S. D. & Khondge, A. D., 2005. *Computational Aero-acoustics Simulation of Whistle Noise in An Automotive Air-Intake System*. Traverse City, Michigan, SAE Noise and Vibration Conference and Exhibition.

Kannan, V., Seifert, J., Golletti, T. & Hanner, D., 2004. *Intake Manifold Whistle Suppression in a Product Development Environment*. Detroit, Michigan, SAE 2004 World Congress & Exhibition.

Karki, K. C. & Patankar, S. V., 1989. Pressure Based Calculation Procedure for Viscous Flows at all Speeds in Arbitrary Configurations. *AIAA Journal*, 27(9), pp. 1167-1174.

Kim, J., Moin, P. & Moser, R., 1986. Turbulence statistics in fully developed channel flow at low Reynolds number. *Journal of Fluid Mechanics*, Volume 177, pp. 133-166.

- Kinsler, L. E., Frey, A. R., Coppens, A. B. & Sanders, J. V., 2000. *Fundamentals of Acoustics*. 4th ed. New York: John Wiley & Sons.
- Kinsler, L., Frey, A., Coppens, A. & Sanders, J., 1982. *Fundamentals of Acoustics*. 3rd ed. New York: Wiley and Sons.
- Klein, M., Sadiki, A. & Janicka, J., 2003. A Digital Filter Based Generation of Inflow Data for Spatially Developing Direct Numerical or Large Eddy Simulations. *Journal of Computational Physics*, 186(2), pp. 652-665.
- Kolmogorov, A. N., 1941. The Local Structure of Turbulence in Incompressible Viscous Fluid for Very Large Reynolds' Numbers. *Doklady Akademii Nauk SSSR*, Volume 30, pp. 301-305.
- Kook, H., 2001. Active Control of Pressure Fluctuations Due to Flow Over Helmholtz Resonators. 255(1).
- Kook, H. & Mongeau, L., 1997. *Analytical Model For The Periodic Pressure Fluctuations Induced By Flow Over A Cavity*. , International Symposium on FSI.
- Kook, H. & Mongeau, L., 2002. Analysis Of The Period Pressure Fluctuations Induced By Flow Over A Cavity. *Journal of Sound and Vibration*, 251(5), pp. 823-846.
- Kriesels, P. et al., 1995. High Amplitude Vortex-Induced Pulsations in a Gas Transport System. *Journal of Sound and Vibration*, 184(2), pp. 343-368.
- Kuttruff, H., 2007. *Acoustics - An Introduction*. Oxon: Taylor & Francis.
- Launder, B. & Spalding, D., 1972. *Mathematical Models of Turbulence*. London, Academic Press.
- Lawson, S. & Barakos, G., 2011. Review of Numerical Simulations for High-speed, Turbulent Cavity Flows. *Progress in Aerospace Sciences*, 47(3), pp. 186-216.
- Lilly, D. K., 1967. The Representation of Small-scale Turbulence In Numerical Simulation Experiments. *Proceedings of IBM Scientific Computing Symposium on Environmental Sciences*, pp. 195-210.

- Lu, H., 2014. Large-eddy Simulation of Turbulent Flows with Applications to Atmospheric Boundary Layer Research. In: J. Awrejcewicz, ed. *Computational and Numerical Simulations*. : InTech, pp. 191-225.
- Marsden, O., Bailly, C., Bogey, C. & Jondeau, E., 2012. Investigation of Flow Features and Acoustic Radiation of a Round Cavity. *Journal of Sound and Vibration*, Volume 331, pp. 3521-3543.
- Mathieu, J. & Scott, J., 2000. *An Introduction to Turbulent Flow*. Cambridge: Cambridge University Press.
- Meissner, M., 2002. Acoustic Modes Induced by Flow in a Pipe with Two Closed Side-branches. *Applied Acoustics*, 63(10), p. 1071–1083.
- Mendonca, F., 2005. *Aeroacoustic Simulation of Double Diaphragm Orifices in an Aircraft Climate Cooling System*, : AIAA.
- Moin, P. & Kim, J., 1982. Numerical Investigation of Turbulent Channel Flow. *Journal of Fluid Mechanics*, Volume 118, p. 341–377.
- Moureau, V., Berat, C. & Pitsch, H., 2005. An Efficient Semi-Implicit Compressible Solver for Large Eddy Simulations. *Annual Research Briefs*, Volume 1, pp. 43-55.
- Munjal, M., 1987. *Acoustics of ducts and mufflers*. New York: John Wiley & Sons.
- Munjal, M. L., 1998. Analysis and Design of Mufflers. *Journal of Sound and Vibration*, 211(3), pp. 425-433.
- Nicoud, F. & Ducros, F., 1999. Subgrid-Scale Stress Modelling Based on the Square of the Velocity Gradient Tensor. *Flow Turbulence and Combustion*, Volume 62, pp. 183-200.
- Pachebat, M. et al., 2008. *Problématique et applications dans le domaine des transports terrestres*. Paris, GDR Bruit des Transports.
- Panton, R., 1990. Effect of Orific geometry on Helmholtz Resonator Excitation by Grazing Flow. *American Institute of Aeronautics and Astronautics (AIAA)*, Volume 28, pp. 60-65.

- Peters, M. C. A. M. & Bokhorst, E. v., 2000. *Flow-Induced Pulsations in Pipe Systems with Closed Side-Branches, Impact of Flow Direction*. Luzerne, Switzerland, Proceedings of the Flow induced vibration 2000 conference.
- Peters, M. & Riezebos, H., 2001. *Analysis Of The Occurrence Of Flow-Induced Pulsations In A Gas Control Station*, Eindhoven: University of Eindhoven.
- Piomelli, U., 1999. Large-eddy Simulation: Achievements and Challenges. *Progress in Aerospace Sciences*, Volume 35, p. 335—362.
- Piomelli, U., 2001. *Large-Eddy and Direct Simulation of Turbulent Flows*. , 9th Annual Conference of the Canadian Society of CFD.
- Piomelli, U., 2008. Wall-layer Models for Large-eddy Simulations. *Progress in Aerospace Science*, 44(6), pp. 437-446.
- Piomelli, U., Balaras, E. & Benocci, C., 1996. Two-Layer Approximate Boundary Conditions for Large-Eddy Simulations. *AIAA*, 34(6), pp. 1111-1119.
- Powell, A., 1964. Theory of Vortex Sound. *Acoustical Society of America* , 36(1), pp. 177-195.
- Radavich, P. M., Selamet, A. & Novak, J. M., 2001. A Computational Approach for Flow–Acoustic Coupling in Closed Side Branches. *Acoustical Society of America*, 109(4), pp. 1343-1353.
- Rai, M. M. & Moin, P., 1993. Direct Numerical Simulation of Transition and Turbulence in a Spatially Evolving Boundary Layer. *Journal of Computational Physics*, Volume 109, pp. 169-192.
- Reynolds, D., 1981. *Engineering Principles of Acoustics*. Boston: Allyn and Bacon.
- Rizzetta, D. & Visbal, M., 2003. Large-Eddy Simulation of Supersonic Cavity Flow-Fields Including Flow Control. *AIAA*, 41(8), p. 1452–1462.
- Rockwell, D., 1983. Oscillations of Impinging Layers. *AIAA*, 21(5), pp. 645-664.
- Rockwell, D. et al., 2003. Shallow Cavity Flow Tone Experiments: Onset of Locked-on States. *Journal of Fluids and Structures*, 17(3), pp. 381-414.

Rockwell, D. & Naudascher, E., 1978. Review-Self-Sustaining Oscillations of Flow Past Cavities. *Journal of Fluids Engineering*, 100(2), pp. 152-166.

Rockwell & Knisely, 1979. The Organised Nature of Flow Impingement up on a Corner. 93(3).

Rogallo, R. S. & Moin, P., 1984. Numerical Simulation of Turbulent Flows. *Annual Review of Fluid Mechanics*, Volume 16, pp. 99-137.

Rossiter, J., 1964. Wind-tunnel experiments on the flow over rectangular cavities at subsonic and transonic speeds.. *Aeronautical Research Council Reports and Memoranda*, October, Issue 3438.

Rouse, H., 1946. *Elementary Mechanics of Fluids*. New York: John Wiley and Sons.

Rowley, C., Colonius, T. & Murray, R., 2000. *POD Based Models of Self-Sustained Oscillations In The Flow Past An Open Cavity*. Pasadena, AIAA.

Russel, D. A., 2005. *Acoustic High-Pass, Low-Pass and Band-Stop Filters*, Flint: GMI Engineering & Management Institute.

S Ziada, S. S., 1999. Strouhal number of flow-excited acoustic resonance of closed side branches. *Fluids Structures*, 13(127), p. 42.

Salim, S. M., Ong, K. C. & Cheah, S. C., 2011. *Comparison of RANS, URANS and LES in the Prediction of Airflow and Pollutant Dispersion*. San Francisco, Proceedings of the World Congress on Engineering and Computer Science 2011 Vol II , pp. 19-21.

Salvador, F. J., Martínez-López, J., Romero, J. V. & Roselló, M. D., 2011. Computational Study of the Cavitation Phenomenon and its Interaction with the Turbulence Developed in Diesel Injector Nozzles by Large Eddy Simulation (LES). *Mathematical and Computer Modelling*, Volume In Press.

Sayma, A., 2009. *Computational Fluid Dynamics*. 1st ed. : BookBoon.com.

Schlatter, P., 2005. *Large Eddy Simulation Of Transition And Turbulence In Wall-Bounded Shear Flow (Thesis)*, Zurich: Swiss Federal Institute Of Technology Zurich.

Schlichting, H., 1955. *Boundary Layer Theory*. London: Pergamon Press.

Schlichting, H., 1979. *Boundary-layer Theory*. 7th ed. New York: McGraw-Hill.

Selamet, A., Kothamasu, V. & Novak, J., 2001. Insertion Loss Of A Helmholtz Resonator In The Intake System Of Internal Combustion Engines: An Experimental And Computational Investigation. *Applied Acoustics*, 62(4), pp. 381-409.

Selamet, A., Kurniawan, D. & Knotts, B. D., 1999. Study Of Whistles With A Generic Sidebranch. *Society of Automotive Engineers, Inc*, 108(6 Part 2), pp. 2988-2998.

Selamet, A., Kurniawan, D., Knotts, B. & Novak, J., 2002. Whistles With A Generic Sidebranch: Production And Suppression. *Journal of Sound and Vibration*, 250(2), pp. 277-298.

Smagorinsky, J., 1963. General Circulation Experiments with the Primitive Equations: Part I, The Basic Experiment. *Monthly Weather Review*, Volume 91, pp. 99-164.

Stoneman, S. A. T., Hourgan, K., Stokes, A. N. & Welsh, M. C., 1988. Resonant Sound Caused by Flow Past Two Plates in Tandem in a Duct. *Journal of Fluid Mechanics*, Volume 192, pp. 455-484.

T Colonius, S. L., 2004. Progress on Nonlinear Problems of Sound Generation. *Computational Aeroacoustics*, Volume 40, pp. 345-416.

Tam, C. et al., 2010. A Computational and Experimental Study of Resonators In Three Dimensions. *Journal of Sound and Vibration*, 329(24), pp. 5164-5193.

Tam, C. et al., 2005. A Computational and Experimental Study of Slit Resonators. *Journal of Sound and Vibration*, Volume 284, pp. 947-984.

Tam, C. K., Ju, H. & Walker, B. E., 2008. Numerical Simulation of a Slit Resonator in a Grazing Flow under Acoustic Excitation. *Journal of Sound and Vibration*, 313(3-5), p. 449-471.

Tang, Y. & Rockwell, D., 1983. Instantaneous Pressure Fields at a Corner Associated with Vortex Impingement. *Journal of Fluid Mechanics*, Volume 126, pp. 187-204.

Torregrosa, A. J., Fajardo, P., Gil, A. & Navarro, R., 2012. Development of Non-Reflecting Boundary Condition for Application in 3D Computational Fluid Dynamics Codes. *Engineering Applications of Computational Fluid Mechanics*, 6(3).

Tracy, M. B. & Plentovich, E. B., 1997. *Cavity Unsteady-Pressure Measurements at Subsonic and Transonic Speeds*, Hampton, Virginia: NASA Technical Paper 3669.

- Tu, J., Yeoh, G. H. & Liu, C., 2012. *Computational Fluid Dynamics - A Practical Approach*. 2nd ed. : Butterworth Heinemann.
- Versteeg, H. K. & Malalasekera, W., 2007. *An Introduction to Computational Fluid Dynamics*. 2nd ed. Harlow: Pearson Education Ltd.
- Vikramaditya, N. & Kurian, J., 2013. Amplitude and Phase Modulation of Cavity Modes in a Supersonic Flow. *European Journal of Mechanics - B/Fluids*, Volume 42, pp. 159-168.
- Villiers, E. d., 2006. *The Potential of Large Eddy Simulation for the Modeling of Wall Bounded Flows*, London: PhD thesis, Imperial College of Science, Technology and Medicine.
- Wagner, C., Huttli, T. & Sagaut, P., 2007. *Large-Eddy Simulation for Acoustics*. : Cambridge University Press.
- Whitehead, T. D., 2005. *The Design of Resonant Absorbers (Thesis)*, Christchurch, New Zealand: University of Canterbury.
- Wilcox, D. C., 2004. *Turbulence Modeling for CFD*. 2nd ed. : DCW Industries, Inc.
- Winterbone, D. & Pearson, R., 2001. *Design Techniques For Engine Manifolds*. U.S.: SAE International.
- Xu, C.-y., Chen, L.-w. & Lu, X.-y., 2007. Large-Eddy and Detached-Eddy Simulations of the Separated Flow Around a Circular Cylinder. *Journal of Hydrodynamics*, 19(5), pp. 559-563.
- Yang, Z. et al., 2014 (Accepted). Numerical Analysis and Passive Control of a Car Side Window Buffeting Noise Based on Scale-Adaptive Simulation. *Applied Acoustics*, Volume 79, pp. 23-34.
- Yasuda, T., Wu, C., Nakagawa, N. & Nagamura, K., 2010. Predictions and experimental studies of the tail pipe noise of an automotive muffler using a one dimensional CFD model. 71(8).
- Ziada, S., 1994. A Flow Visualization Study of Flow-Acoustic Coupling at the Mouth of a Resonant Side-branch. *Journal of Fluids and Structures*, Volume 8, pp. 391-416.
- Ziada, S. & Shine, S., 1999. Strouhal Number of Flow-excited Acoustic Resonance of Closed Side Branches. *Journal of Fluids and Structures*, Volume 13, pp. 127-142.

Zoccola, P., 2004. Effect of opening obstructions on the flow-excited response of a Helmholtz resonator. 19(7).